



**THESE de DOCTORAT DE  
L'UNIVERSITE CLAUDE BERNARD LYON 1**

**Ecole Doctorale N° 52  
Ecole Doctorale de Physique et Astrophysique**

**Discipline** : Physique des Particules

Soutenue publiquement le 24/10/2024, par :

**Sarah Herrmann**

---

**Mesures de la multiplicité des particules chargées vers l'avant et de la dépendance de la production des J/ $\psi$  vers l'avant avec la multiplicité en collisions pp, avec l'expérience ALICE au LHC**

---

Devant le jury composé de :

Augier, Corinne	PR	UCBL Lyon 1	Présidente
Hadjidakis, Cynthia	DR	IJCLAB	Rapporteure
Belikov, Iouri	DR	IPHC	Rapporteur
Zaccolo, Valentina	Pr. associée	INFN	Examinateuse
Uras, Antonio	CR	IP2I	Directeur de thèse
Cheshkov, Cvetan	DR	IP2I	Co-directeur de thèse

---

**Measurements of forward charged-particle  
multiplicity and multiplicity dependence of  
forward  $J/\psi$  production in pp collisions  
with the ALICE experiment at LHC**

---



# Remerciements

Merci à mon copain, Nathan, qui m'a soutenu en continu durant ces trois années qui ont été éprouvantes mais inoubliables.

Merci à ma famille, papa maman mamie Isou et Coco particulièrement, chez qui j'ai toujours pu me réfugier en cas de coup de mou, ou pour me plaindre de mes bugs de code et de mes problèmes de données.

Merci à tous mes ami.e.s doctorant.e.s Max, Elsa, Flo, Yann, Greg, David, Élise, Inès, Benjamin, Alfred, Charles, et tous les autres du labo avec lesquels j'ai pu manger. Grâce à vous mes repas étaient toujours animés et je me sens bien entourée ! J'ai hâte de tou.te.s vous voir devenir Docteurs !

Merci à mes directeurs de thèse, Antonio et Cvetan, qui m'ont accompagnée pendant ces trois ans pour me permettre de réaliser une thèse dont je suis fière, qui ont pris beaucoup de leur temps ces derniers mois pour tout relire et corriger, répondre à toutes mes questions et me préparer à la soutenance. Je leur en suis très reconnaissante !

Merci à Brigitte d'avoir été ma directrice de thèse en première année, merci également à mes autres collègues d'ALICE Lyon, Lucrezia, Robin, Clément et Niveditha, pour l'aide et l'agréable compagnie qu'ils m'ont fournie.

Merci aux membres du service informatique de l'IP2I, Bruno tu nous sauves, nous les doctorants.

Je voudrais également remercier les membres de mon jury qui ont tous fait le déplacement jusqu'à Lyon pour m'écouter, pour leur bienveillance et leur gentillesse. Un très grand merci aux rapporteurs Iouri Belikov et Cynthia Hadjidakis d'avoir pris le temps de lire ma thèse.

I would like to thank the MFT team for their guidance, Stefano, Sarah, Charlotte, Guillaume, Rafael, Shreyasi, Andry, it was a pleasure to work with you on this amazing detector ! A special thanks to Batoul who was always really nice and helpful to me at all times.

I would also like to thank the PWGMM-Mult team, I had the chance to work on this charged particle analysis with you and I learned many things along the way, Valentina, Chiara, thanks a bunch !

Finally, I would like to thank many of my ALICE colleagues who helped me on several topics, Anton Alkin for answering all my O2Physics-related questions (and I had a lot), Ruben Shahoyan for answering all my O2 and detector questions, Sandro Christian Wenzel for his help on O2 and simulations, and Ionut Cristian Arsene for the very nice PYTHIA code he provided.



**Abstract:**

The ALICE experiment at the CERN LHC is primarily dedicated to the study of the Quark-Gluon Plasma, a state of matter in which quarks and gluons are no longer confined within hadrons. This state is produced in particle accelerators during ultra-relativistic heavy-ion collisions. In parallel, proton-proton collisions are used both as a reference for heavy-ion collisions and to understand various phenomena such as particle production mechanisms within the framework of Quantum Chromodynamics (QCD).

In this context the study of the production of heavy mesons such as the  $J/\psi$  is particularly interesting. This particle is a bound state of the charm quark  $c$  and the anti-charm quark  $\bar{c}$ . Charm quarks are produced during semi-hard or hard parton-parton interactions, which can be quite accurately described by perturbative QCD.

The hadronization of  $c - \bar{c}$  pairs into  $J/\psi$ , on the other hand, is a non-perturbative process that requires a phenomenological description. Measuring  $J/\psi$  production as a function of charged particle multiplicity allows for a better understanding of Multi-Parton Interactions (MPI) and quarkonia production models. Results obtained with proton-proton collisions at  $\sqrt{s} = 13$  TeV show a steeper than linear dependence between the production rate of forward  $J/\psi$  and the forward charged particle multiplicity. This result may indicate that a significant portion of  $J/\psi$  is produced by the recombination of charm quarks from two distinct parton interactions. This observation is consistent with results at mid-rapidity. Finally, this measurement challenges the hypothesis that forward  $J/\psi$  production depends less on multiplicity than mid-rapidity  $J/\psi$  production.

The ALICE experiment was equipped with a new detector for the LHC data taking period called Run 3: the Muon Forward Tracker (MFT). This detector allows for more detailed  $J/\psi$  measurements by separating  $J/\psi$  produced directly in the collision from those produced by the decay of  $B$  mesons.

This manuscript presents the work done on implementing software tools to improve the quality of the data provided by the MFT. This work involves developing codes to verify and enhance detector performances during Run 3 data-taking at the LHC. This period, which began in 2022, is characterized by high interaction rates, making the association of a track with the collision from which it originated ambiguous. Indeed, the MFT time resolution does not allow differentiation of tracks originating from collisions less than 5  $\mu\text{s}$  apart, while the nominal collision rate for proton-proton interactions leads to one collision every 2  $\mu\text{s}$ . Several methods have been proposed to reduce collision association ambiguity, notably using the spatial position of collision vertices and matching the MFT with ALICE's fastest detector (the FT0-C). During this study, it became necessary to time-align the MFT with other detectors. The time offset of the MFT was thus evaluated and corrected.

Finally, results of forward charged particle multiplicity as a function of pseudorapidity are obtained. The corresponding measurements were carried out in proton-proton collisions at  $\sqrt{s} = 0.9$  and 13.6 TeV using the MFT detector. This is one of the first measurements in the ALICE experiment with Run 3 data. The results are generally compatible with the hadronic generator PYTHIA8.

**Résumé :**

L'expérience ALICE au LHC du CERN est principalement dédiée à l'étude du Plasma de Quarks et Gluons, un état de la matière dans lequel les quarks et les gluons ne se trouvent

plus confinés dans des hadrons. Cet état est produit en laboratoire en collisions ultra-relativistes d'ions lourds. Les collisions proton-proton, quant à elles, sont utilisées d'une part comme référence par rapport aux collisions d'ions lourds, mais aussi pour comprendre de nombreux phénomènes tels que les mécanismes de production de particules dans le cadre de la Chromodynamique Quantique (Quantum Chromo-Dynamics, QCD).

Dans ce contexte, un sujet particulièrement intéressant est la production de mésons lourds tels que le  $J/\psi$ . Cette particule est un état lié du quark charm  $c$  et de l'antiquark  $\bar{c}$ .

Les quarks charmés sont produits lors des interactions parton-parton semi-dures ou dures, ces processus pouvant être assez précisément décrits par la QCD perturbative.

L'hadronisation des paires  $c - \bar{c}$  en  $J/\psi$  est au contraire un processus non perturbatif, qui nécessite une description phénoménologique. La mesure de la production du  $J/\psi$  en fonction de la multiplicité de particules chargées permet entre autres une meilleure compréhension des Interactions Partoniques Multiples (Multiple Parton Interactions, MPI), et des modèles de production des quarkonia. Les résultats obtenus pour des collisions proton-proton à  $\sqrt{s} = 13$  TeV montrent une dépendance plus que linéaire entre le taux de production des  $J/\psi$  mesurés vers l'avant et la multiplicité des particules chargées vers l'avant. Ce résultat peut indiquer qu'une partie significative des  $J/\psi$  est produite par la recombinaison des quarks charmés provenant de deux interactions partoniques distinctes. Cette observation est en cohérence avec les observations à mi-rapidité. Enfin, cette mesure permet une remise en cause de l'hypothèse selon laquelle la production de  $J/\psi$  vers l'avant dépendrait moins de la multiplicité qu'une production de  $J/\psi$  à mi-rapidité.

L'expérience ALICE a été équipée d'un nouveau détecteur pour la période de collecte des données du LHC appelée Run 3: Le tracker de muons vers l'avant (Muon Forward Tracker, MFT). Ce détecteur permet de réaliser des mesures de  $J/\psi$  plus poussées en séparant les  $J/\psi$  produits directement dans la collision de ceux produits par la désintégration des mésons B. Ce manuscrit présente les travaux réalisés sur l'implémentation d'outils software pour améliorer la qualité des données fournies par le trajectographe MFT. Ces travaux concernent le développement de codes pour vérifier et améliorer les performances du détecteur pendant la prise de données de Run 3 du LHC. Cette période qui a commencé en 2022 se déroule à hauts taux d'interaction, ce qui rend ambiguë l'association d'une trace à la collision dont elle est originaire. En effet, la résolution temporelle du MFT ne permet pas de différencier des traces provenant de collisions à moins de  $5\ \mu s$  d'intervalle, tandis que le taux de collision nominal des interactions proton-proton est d'une collision tous les  $2\ \mu s$ . Plusieurs méthodes ont été proposées pour réduire l'ambiguïté d'association, en utilisant notamment la position spatiale des vertex des collisions et en effectuant une correspondance entre le MFT et le détecteur le plus rapide d'ALICE (le FT0-C). Lors de cette étude, il est apparu nécessaire d'aligner temporellement le MFT avec les autres détecteurs. Le décalage temporel du MFT a donc été évalué et corrigé.

Enfin, des résultats de multiplicité des particules chargées vers l'avant en fonction de la pseudorapidité sont obtenus. Les mesures correspondantes ont été réalisées en collisions proton-proton à  $\sqrt{s} = 0.9$  et  $13.6$  TeV en utilisant le détecteur MFT. Il s'agit d'une des premières mesures dans l'expérience ALICE avec les données du Run 3. Les résultats obtenus sont en général compatibles avec le générateur de collisions hadroniques PYTHIA8.



# Contents

<b>Introduction</b>	<b>1</b>
<b>1 Particle physics in ultra-relativistic collisions</b>	<b>3</b>
1.1 The Standard Model of particle physics . . . . .	3
1.2 QCD under extreme conditions . . . . .	7
1.2.1 Creating the QGP . . . . .	7
1.2.2 Creating QGP in laboratory: ultra-relativistic heavy-ion collisions . . . . .	9
1.2.3 QGP signatures . . . . .	11
1.2.4 QGP-like effects in small systems . . . . .	14
1.3 Quarkonia probes . . . . .	14
1.3.1 Models for charmonium production . . . . .	15
1.3.2 $J/\psi$ polarization . . . . .	18
1.3.3 $J/\psi$ production as a function of charged-particle multiplicity . . . . .	19
1.4 Simulating proton-proton collisions . . . . .	21
1.4.1 The PYTHIA event generator . . . . .	21
1.4.2 EPOS event generator . . . . .	22
<b>2 The Large Hadron Collider and ALICE</b>	<b>23</b>
2.1 The LHC . . . . .	23
2.2 The ALICE detector . . . . .	24
2.2.1 ALICE in Run 2 . . . . .	26
2.2.1.1 The V0 detector . . . . .	27
2.2.1.2 The Muon Spectrometer . . . . .	29
2.2.2 ALICE in Run 3 . . . . .	29
2.2.2.1 Detector upgrades . . . . .	30
2.2.2.2 The Fast Interaction Trigger (FIT) . . . . .	32
2.2.2.3 The Muon Forward Tracker (MFT) . . . . .	33
2.2.3 The Central Trigger System . . . . .	36
2.3 The Online-Offline Computing system $O^2$ . . . . .	37
2.3.1 The $O^2$ analysis framework . . . . .	39
<b>3 Forward <math>J/\psi</math> relative yield versus relative forward multiplicity in pp collisions at <math>\sqrt{s} = 13</math> TeV</b>	<b>41</b>
3.1 Introduction . . . . .	41
3.2 Detectors used in the analysis . . . . .	42
3.3 Analysis . . . . .	42
3.3.1 Analysis strategy . . . . .	42

---

3.3.2	Data sample . . . . .	43
3.3.3	MC samples . . . . .	43
3.3.4	Event selection . . . . .	43
3.3.5	Event triggers . . . . .	44
3.3.6	Track selection . . . . .	44
3.3.7	Dimuon Cuts . . . . .	44
3.4	Multiplicity measurement . . . . .	44
3.4.1	V0C Multiplicity intervals . . . . .	45
3.4.2	Corrections applied to the V0C signal . . . . .	47
3.4.2.1	Signal renormalization and $z_{\text{vtx}}$ correction . . . . .	47
3.4.2.2	Dimuon correction . . . . .	48
3.4.3	Conversion from $N_{\text{V0C}}$ to $N_{\text{ch}}$ . . . . .	50
3.4.3.1	Correction of $\langle N_{\text{ch}} \rangle$ . . . . .	52
3.4.3.2	Systematic uncertainties of the conversion from $N_{\text{V0C}}$ to $N_{\text{ch}}$	53
3.5	Measurement of the relative $\text{J}/\psi$ yield . . . . .	55
3.5.1	$\text{J}/\psi$ signal extraction . . . . .	55
3.5.2	Correction of the $\text{J}/\psi$ yields . . . . .	58
3.5.3	Uncertainties on the dimuon correction . . . . .	60
3.5.4	Total systematic uncertainty of the relative $\text{J}/\psi$ yields . . . . .	61
3.6	Results . . . . .	63
3.7	Comparison with model predictions . . . . .	64
3.8	Discussion of auto-correlation effects from $\text{J}/\psi$ daughters . . . . .	65
3.9	Comparison between forward and midrapidity $\text{J}/\psi$ yields . . . . .	67
3.10	Discussion of the results . . . . .	68
3.11	Conclusion and outlook . . . . .	70
<b>4</b>	<b>Towards physics results with the MFT</b> . . . . .	<b>71</b>
4.1	The MFT Quality Assessment framework . . . . .	71
4.2	Impact of the ITS services on the MFT offset resolution . . . . .	73
4.2.1	Study with an ideal vertex information . . . . .	74
4.2.2	Study with the realistic primary vertex reconstruction . . . . .	79
4.3	MFT track-to-collision association . . . . .	81
4.3.1	The track-to-collision-associator . . . . .	81
4.3.2	The track-to-collision reassociation . . . . .	84
4.4	MFT matching with FT0-C . . . . .	85
4.4.1	FT0-C specifications . . . . .	86
4.4.2	BC range of an MFT track . . . . .	87
4.4.3	Matching procedure . . . . .	87
4.4.4	Illustration of the matching . . . . .	91
4.4.5	Matching efficiency and reliability in MC . . . . .	92
4.5	MFT-FT0-C time alignment . . . . .	96
4.5.1	Context and motivation for time alignment . . . . .	96
4.5.2	Time alignment procedure . . . . .	97
4.5.3	Results . . . . .	98
4.5.4	Summary and conclusion . . . . .	101
4.6	Conclusions and outlook . . . . .	102

<b>5 Measurement of forward charged-particle multiplicity with the MFT</b>	<b>103</b>
5.1 Physics motivations and previously published results	104
5.1.1 Physics motivations	104
5.1.2 Previously published results at LHC	105
5.2 Analysis procedure and selections	110
5.2.1 Datasets and MC simulations	110
5.2.2 Track selection	110
5.2.3 Event selection	111
5.3 Comparison between MC and data	111
5.3.1 p–p collisions at $\sqrt{s} = 0.9$ TeV	111
5.3.2 p–p collisions at $\sqrt{s} = 13.6$ TeV	113
5.4 Correction procedure	115
5.4.1 Track-to-particle correction	116
5.4.2 Selection efficiency correction	117
5.4.3 Calculation of the corrected result	118
5.4.4 MC closure tests	118
5.5 Systematic uncertainties	120
5.5.1 Ambiguous tracks	120
5.5.2 Other systematic uncertainties	121
5.6 Results	123
5.7 Summary and outlook	124
<b>Conclusion</b>	<b>127</b>
<b>A Appendix</b>	<b>129</b>
A.1 Fit functions	129
A.1.1 Double Crystal Ball (CB2)	129
A.1.2 Variable Width Gaussian (VWG)	129
A.1.3 Pol2 $\times$ Exp	129
A.2 Corrections to the number of selected events	130
<b>Bibliography</b>	<b>131</b>
<b>List of Figures</b>	<b>141</b>
<b>List of Tables</b>	<b>146</b>

# Introduction

Particle physics is the branch of physics that studies the fundamental constituents of matter and their interactions, at the subatomic scale. The Standard Model (SM) of particle physics is the theoretical framework that describes the particles and their interactions, encompassing three of the four known fundamental forces in the universe: electromagnetic, weak, and strong interactions, excluding gravity. The strong force, governing the interactions between quarks and gluons, is described by Quantum Chromodynamics (QCD). At very high temperature and density, QCD matter is known to form a phase of Quark Gluon Plasma (QGP). In this medium quarks and gluons, confined in hadrons under “ordinary” conditions of temperature and energy density (i.e. the ones existing in the observable Universe at the current epoch), are asymptotically free. This state is believed to have existed few microseconds after the Big Bang and can be recreated in laboratory in ultra-relativistic heavy-ion collisions, such as those available at the Large Hadron Collider (LHC). The dissociation and the regeneration of the  $J/\psi$  meson, a particle discovered in 1974 consisting of a charm quark and its antiparticle the charm antiquark, is interpreted as one of the most prominent signatures of the QGP formation in ultra-relativistic heavy-ion collisions. Despite significant progress in the recent years, the exact mechanisms behind  $J/\psi$  production, and more generally the production of particles composed of heavy quarks, are not yet fully understood.

For a long time, proton-proton collisions were considered mainly as a baseline for the heavy-ion studies as no QGP formation was expected in collision systems involving only few nucleons in the initial state. As such, pp collisions were used to address QCD processes not implying the formation of any QGP. This includes high-momentum perturbative QCD processes as well as soft low-momentum processes (this second class including for instance the inclusive production of charged particles). Recent discoveries mainly based on LHC data, however, strongly indicated a possible formation of QGP droplets also in proton-proton collisions. This fact boosted even further the interest in proton-proton collisions, and nowadays they are considered an inalienable part of the QGP physics at the LHC.

The ALICE experiment was specifically designed to study the QGP at the LHC. It has a vast physics program with a significant part devoted to measurements in proton-proton collisions. The ALICE detector has excellent tracking and particle identification performances, which allow for a precise reconstruction of  $J/\psi$  via their dimuon or dielectron decay channels. Muons are reconstructed in the forward direction in the tracking chambers of the Muon Spectrometer. The ALICE detector has recently undergone major upgrades to improve its physics performance and keep up with unprecedented collision

rates available at the LHC. One of these upgrades is the installation of the new Muon Forward Tracker (MFT) detector. The MFT is located in front of the Muon Spectrometer, and is the innermost tracking detector at forward rapidity in ALICE. The upgraded ALICE detector including the MFT started taking data in 2022 at the beginning of the LHC Run 3.

This thesis aims to explore first the mechanisms underlying  $J/\psi$  meson production by studying  $J/\psi$  yields as a function of multiplicity in proton-proton collisions with the ALICE detector at the LHC.

The second goal of the thesis is the better understanding of the production mechanisms of charged hadrons at forward pseudorapidity via the study of charged-particle pseudorapidity distribution using the MFT, and develop specific and original tools to better exploit the information coming from this detector. This observable can provide insight into non-perturbative aspects of QCD.

This manuscript is organized as follows. In Chapter 1 an introduction of the Standard Model of Particle Physics is given, with an emphasis on the QCD and briefly reviewing  $J/\psi$  production models. In Chapter 2, the ALICE apparatus is described with its initial design and the upgrades implemented for the Run 3 data taking period. The new software used since 2021 for data acquisition and analysis is also introduced. Chapter 3 describes the measurement of forward  $J/\psi$  yields as a function of forward multiplicity in proton-proton collisions at  $\sqrt{s} = 13$  TeV. Chapter 4 is dedicated to the software developments implemented in view of the MFT physics program, encompassing dedicated performance, matching and time-alignment studies. Finally, Chapter 5 focuses on the first physics measurements obtained using the MFT: the charged-particle pseudorapidity distribution in the forward direction in proton-proton collisions at  $\sqrt{s} = 0.9$  and  $\sqrt{s} = 13.6$  TeV.

# Chapter 1

## Particle physics in ultra-relativistic collisions

### 1.1 The Standard Model of particle physics

The Standard Model (SM) of particle physics is a theoretical framework developed in the early 1970s that categorizes and classifies the elementary constituents of matter, the particles, and describes their fundamental interactions (excluding gravity) and associated symmetries. The interactions between elementary particles can be electromagnetic (mediated by the photon), weak (mediated by the  $Z^0$  or  $W^\pm$ ) or strong (mediated by the gluons). According to the charges they carry, some particles are insensitive to certain interactions: for instance, neutral particles (of electromagnetic charge zero) are not affected by the electromagnetic interaction. In the same way, charges are defined for weak and strong interactions: for the weak interaction, the charge name is weak isospin, and for the strong interaction the charge is named color charge.

Elementary particles can be classified into three categories (see Figure 1.1):

- **Quarks:** fermions with spin  $\pm\frac{1}{2}$  carrying a color charge, a fractional electromagnetic charge, and weak isospin;
- **Leptons:** fermions with spin  $\pm\frac{1}{2}$  lacking color charge, but carrying electromagnetic charge and weak isospin;
- **Vector bosons:** bosons with spin 1, carriers of the fundamental interactions. This group includes the gluons, mediators of the strong interaction between quarks and gluons themselves.

From the theoretical point of view, the standard model is a quantum field theory (QFT) — i.e. a theory combining quantum mechanics and field theory, with a field being a physical quantity defined in every point of space (for example the electromagnetic field) — characterized from the mathematical point of view by the  $SU(3) \times SU(2) \times U(1)$  symmetry group. The  $SU(2) \times U(1)$  structure describes the symmetries of the electroweak theory, while  $SU(3)$  describes the symmetries characterizing the strong interaction. Theories based on symmetries are so-called gauge theories, in which the physical phenomena are invariant under special transformations (in the same way a sphere is invariant, i.e. its properties don't change, under any rotation in space).

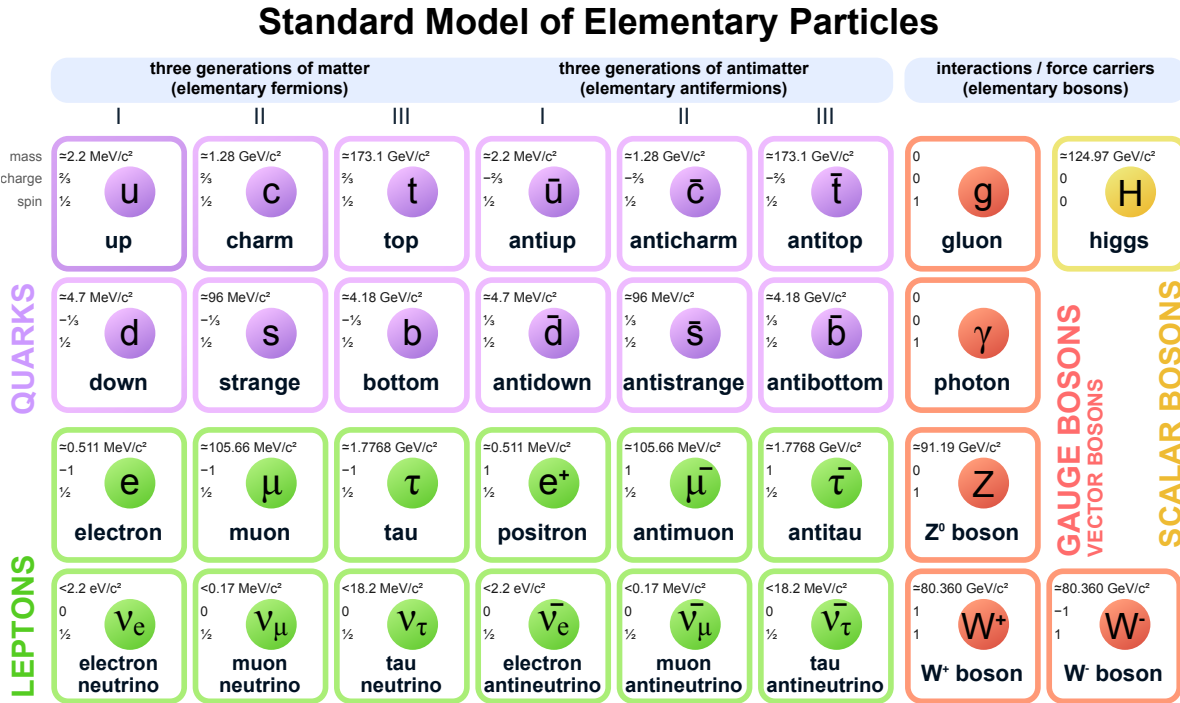


Figure 1.1: Classification of the elementary particles in the Standard Model.

From the mathematical point of view, the sentence “the physical phenomena are invariant under special transformations” translates to: the Lagrangian  $\mathcal{L}$  of the theory is invariant under these special transformations. In other terms, if we consider a theory based on a field  $\phi$  and a transformation which transforms the field  $\phi$  into the field  $\phi'$ , the theory is invariant under this transformation if  $\mathcal{L}(\phi) = \mathcal{L}(\phi')$ .

In the following we will focus on the quarks (see Figure 1.1). Quarks come in six different types called *flavors*: up (u), down (d), strange (s), charm (c), beauty (b) and top (t). The associated anti-quarks are called anti-up ( $\bar{u}$ ), anti-down ( $\bar{d}$ ) etc.... The six quarks are classified into three generations, corresponding to their mass (and then, as a consequence, the chronological order in which they were discovered), each generation having heavier quarks than the previous one.

The main specificity which differentiates quarks from the other elementary fermions of the Standard Model is that they carry a color charge. Color charge is an intrinsic property of quarks and gluons, and the interaction between colored charges is described by Quantum Chromodynamics (QCD). The color charge can take three “values”: blue, red, and green, and three corresponding values for the antiparticles: anti-blue, anti-red, and anti-green. Quarks carry a color charge, antiquarks carry an anticolor charge, and gluons carry both color and anticolor charges. Collectively, quarks, antiquarks, and gluons are referred to as partons. The strong interaction binding quarks and gluons together has a distinctive feature that qualitatively distinguishes it from the electromagnetic interaction: its coupling constant  $\alpha_s$  increases with distance, meaning that the farther apart the color charges are, the stronger their binding force becomes. If one pulls away a quark from a quark-antiquark pair, at some point the binding force becomes so strong that it turns energetically favorable to produce another pair of particles, ending up with more

quark-antiquark pairs. Hence, quarks are always found bound to other quarks by gluons in structures called hadrons, which are color-neutral. This phenomenon is known as confinement, and it prevents quarks or gluons to be studied as isolated particles: as we saw, supplying energy to a quark within a hadron does not free it but rather produces additional quark-antiquark pairs, leading to a cascade of new hadrons, as depicted in Figure 1.2.

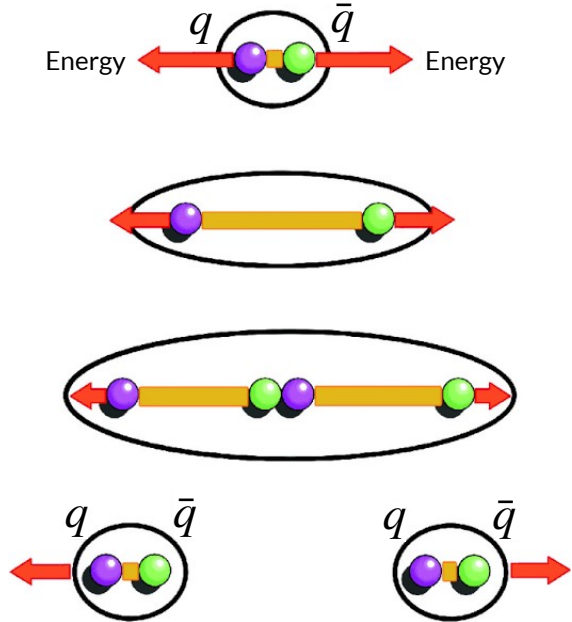


Figure 1.2: A consequence of the confinement phenomenon in QCD [1].

There are three main types of hadrons: mesons, composed of a quark and an antiquark bound together, baryons, composed of three quarks, and antibaryons (three antiquarks). In the following, we briefly summarize the main aspects of the theory of QCD, which describes the strong interaction between color charges.

### Quantum Chromodynamics (QCD)

The QCD lagrangian, invariant under  $SU(3)$  transformations (which can be considered as rotations in the color space) can be expressed as follows:

$$\mathcal{L}_{QCD} = \bar{\psi}_c^f (i\gamma^\mu D_\mu - m) \psi_c^f - \frac{1}{4} G_{\mu\nu}^a G_a^{\mu\nu} , \quad (1.1)$$

where  $\psi_c^f$  is the field corresponding to a quark of flavor  $f$  (that can be  $u, d, s, c, b, t$ ) and of color  $c$  (red, green or blue). The sum on flavors and colors is implicit. The covariant derivative  $D_\mu$  is defined as

$$D_\mu = \partial_\mu + \frac{1}{2} ig G_\mu^a \lambda_a$$

where  $\lambda$  are the Gell-Mann matrices (the 8 generators of the  $SU(3)$  group, see for example in [2]), and  $G_\mu^a$  are the gluon fields. The field strength tensors  $G_{\mu\nu}^a$  are:

$$G_{\mu\nu}^a = \partial_\mu G_\nu^a - \partial_\nu G_\mu^a - g f_{abc} G_\mu^b G_\nu^c ,$$

with  $f_{abc}$  the structure constants of the  $SU(3)$  group.

Equation 1.1 is divided into two parts: the first part describes the quark field (its mass term and kinetic term), along with the quark-gluon interaction term, while the second part encompasses the free-gluon terms with a kinetic term and a self-interaction term, allowing the interaction between 3 and 4 gluon fields. These possible interactions can be described by the Feynman diagrams shown in Figure 1.3.

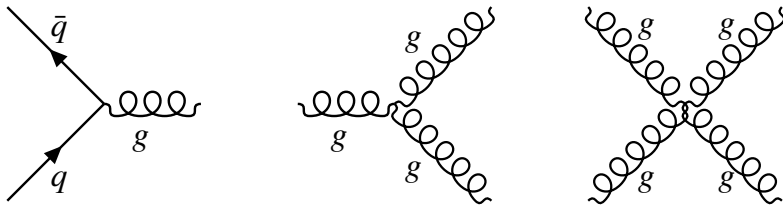


Figure 1.3: Feynman vertices in QCD.

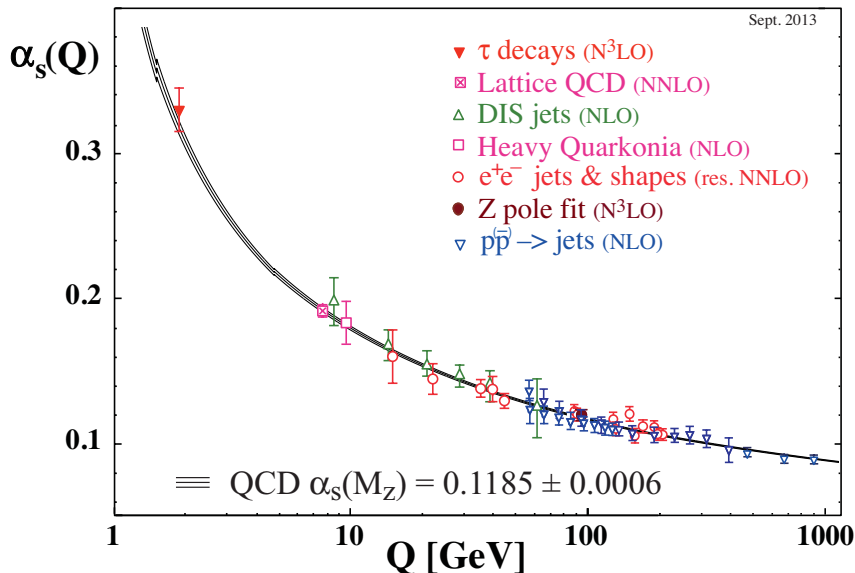


Figure 1.4: The evolution of the strong coupling constant  $\alpha_s$  as a function of the energy scale  $Q$  [3]

The predictions based on the QCD Lagrangian with the coefficient  $g$  — called “bare” coupling parameter — lead to infinite results, which are not physical. This is due to the appearance of several divergences in the calculations, such as the ultra-violet divergences that come into play at very short distances (or very high momentum transfer  $Q$ ). To fix these divergences, a procedure called renormalization is performed, allowing the calculations to provide finite predictions. In practice, the model parameters are redefined and the bare coupling constant is replaced by an effective coupling constant called  $\alpha_s$ , the value of which decreases with the momentum transfer  $Q$  of the processes [2].

The evolution of  $\alpha_s$  with the momentum transfer  $Q$  is reported in Figure 1.4, where two regimes can be identified: the asymptotic freedom at high  $Q$  (the strong interaction becomes weak at short distances), and the confinement at low  $Q$ , characterizing the interactions of quarks and gluons inside the colorless bound states called hadrons.

Since  $\alpha_s \ll 1$  at high  $Q$ , the perturbation theory can be used in this regime, leading to the so-called perturbative QCD. In perturbative QCD, it is assumed that the QCD observables can be expressed as a power expansion of  $\alpha_s$ , starting from the first and second orders of the expansion, named respectively Leading Order (LO) and Next-to-Leading Order (NLO). It is commonly admitted that perturbative QCD is valid when the energy involved in the process is larger than  $\lambda_{QCD} \sim 200$  MeV. At low  $Q$ , the perturbation approach breaks down, and effective models are needed to describe the QCD phenomena.

## 1.2 QCD under extreme conditions

Under extreme conditions of density and temperature, hadrons “melt” and release their contents of quarks and gluons: at short distances and large momentum transfers the strong interaction becomes “weak”, and hadron structures are not possible anymore. Color charges are then deconfined, and this state is called Quark-Gluon Plasma (QGP). QGP represents the deconfined state of QCD matter, visible in the phase diagram shown in Figure 1.5.

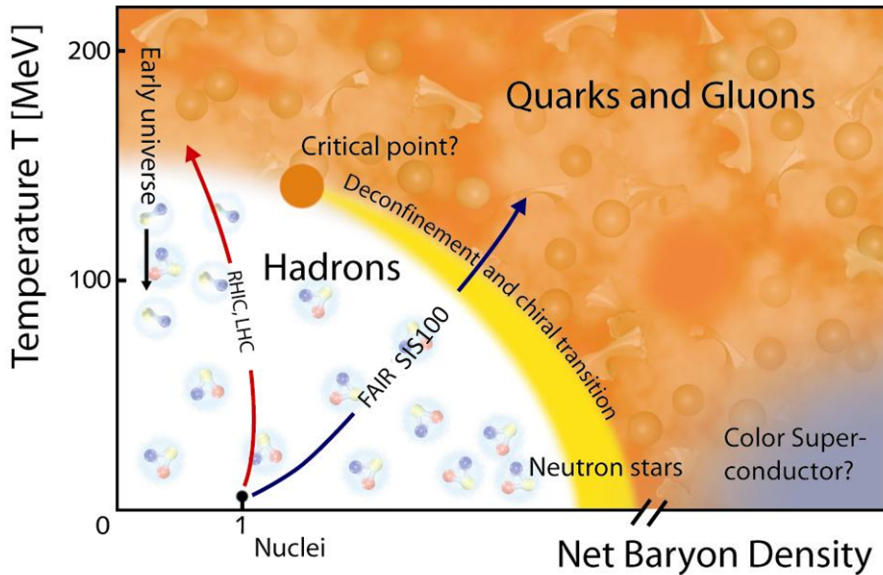


Figure 1.5: QCD phase diagram, from [4].

### 1.2.1 Creating the QGP

There are two ways to create a QGP starting from ordinary hadronic matter, see Figure 1.6:

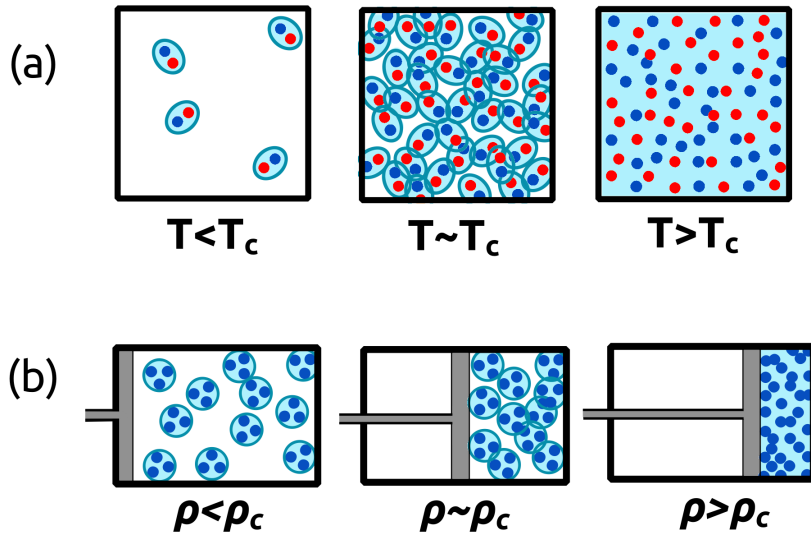


Figure 1.6: Two scenarios of QGP formation, adapted from [5]. Top: at high temperature; bottom: at high net baryon density.

- By increasing the temperature  $T$ : in this case, the QCD vacuum (with zero net baryon density  $\rho_B$ , where  $\rho_B$  is defined as the difference between the number of quarks  $n_q$  and the number of antiquarks  $n_{\bar{q}}$  in the system) is heated within a finite volume. The energy available in this volume allows the production of a large number of  $q\bar{q}$  pairs, increasing the number of color charges per unit volume without increasing the net baryon density. The transition from the QCD vacuum to the QGP can be modeled by passing through a phase of hadron gas. At a certain temperature  $T_c$ , the parton density becomes sufficiently high: color charge is then screened by the surrounding quarks and gluons, and hadronic structures are dissolved (the interaction potential is reduced). The produced QGP has a net  $\rho_B \sim 0$ . The transition temperature between the ordinary hadronic matter and the QGP at  $\rho_B \sim 0$  has been experimentally measured to be  $T_c \approx 160$  MeV, which corresponds approximately to  $1.86 \times 10^{12}$  K.
- By increasing  $\rho_B$ : in this scenario, one can imagine concentrating a large number of baryons in a finite volume, which is adiabatically compressed. The baryons will begin to overlap at a certain critical baryon density  $\rho_c$ , and dissolve into a QGP. In this case, QGP is characterized by a high baryon density ( $n_q \gg n_{\bar{q}}$ ) [5].

These two ways of reaching the QGP phase from ordinary hadronic matter are illustrated in Figure 1.6, where red dots represent antiquarks, blue dots represent quarks, and light blue represents the “sea” of color charges responsible for the strong interaction. This reasoning justifies the existence of QGP under three scenarios: in the early universe, at the center of compact astrophysical objects and in ultra-relativistic collisions of heavy ions.

The hypothesis that the early universe was in a state of QGP, about  $10^{-5}$  s after the Big Bang, is justified by the fact that the universe is expanding and cooling, meaning that in its initial state (going back in time), it was much more dense and hot. The expected net baryon density characterizing the QGP in the early universe is  $\sim 0$ .

### 1.2.2 Creating QGP in laboratory: ultra-relativistic heavy-ion collisions

The study of the QGP necessitates its creation in a well-controlled laboratory environment. The ultra-relativistic collisions of heavy ions offer such an environment with well-defined initial state and the possibility to study the final state with particle detectors. In practice, before being collided the heavy ions are accelerated to a speed very close to the speed of light by means of gigantic accelerators such as the Large Hadron Collider (LHC). During collisions of heavy ions at ultra-relativistic energies (at the LHC the center-of-mass energy per nucleon pair ranges between 2.76 TeV and 5.36 TeV), each incident nucleus appears in the laboratory as a disk contracted by the relativistic length contraction effect, by a factor proportional to  $\frac{1}{\gamma}$  where  $\gamma$  is the Lorentz factor. For large nuclei like Pb, the diameter of the disk is about 14 fm, and its width is  $\frac{14}{\gamma}$  with  $\gamma = 2500$  for collisions at the LHC [6].

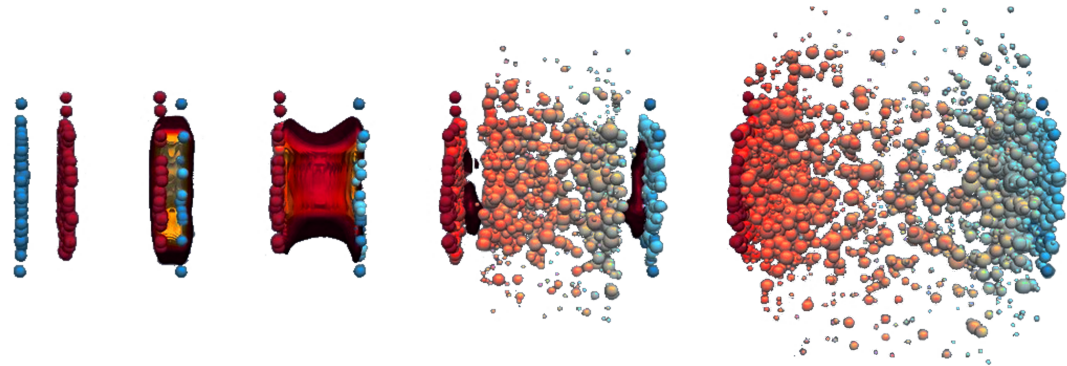


Figure 1.7: Evolution of an heavy-ion collision - adapted from [MADAI collaboration, Hannah Petersen and Jonah Bernhard].

During the collision, different stages occur. This is illustrated in Figure 1.7, which depicts the temporal evolution of a collision between two heavy ions. The time increases from left to right. In this figure one can see the initial stage of the collision, which consists of two Lorentz-contracted heavy ions, intermediate stages where QGP is represented as a continuum medium, and the final stage where numerous hadrons are produced.

These different stages can be best described using a spatio-temporal diagram shown in Figure 1.8, where the following stages are illustrated:

- Pre-equilibrium: at relativistic energies, interactions occur at the partonic level (i.e., between quarks and gluons), producing a fireball in an excited state. The constituents of the fireball frequently further interact, establishing a local equilibrium state. The time taken to establish a local thermodynamic equilibrium is called the thermalization time.
- Expansion: at equilibrium, quarks and gluons are in a deconfined state, i.e. in QGP state. This system has a thermal pressure that acts on the surrounding vacuum, causing the volume of the fireball to undergo hydrodynamic expansion. As it expands, the energy density decreases, and the volume cools down.

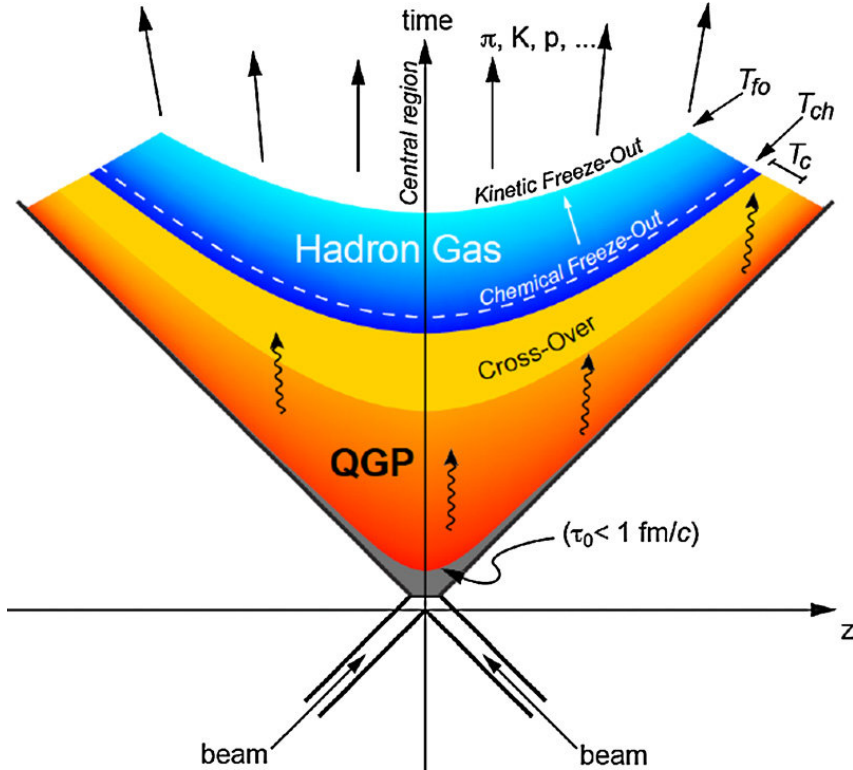


Figure 1.8: Spatio-temporal diagram of the evolution of a heavy-ion collision. [7].

- Hadronization: below a certain temperature, deconfined quarks and gluons will hadronize, meaning that they will arrange themselves into hadrons. During this stage, the size of the fireball increases rapidly, while the temperature remains approximately constant.
- Chemical freeze-out: the hadrons formed during the hadronization phase undergo elastic and inelastic collisions until the number of inelastic collisions (collisions that change the identity of the hadrons) is no longer sufficient, due to expansion, to significantly change the proportions between the different hadronic species. This stage is called chemical freeze-out: the proportions between the hadronic species are approximately fixed after this stage, but elastic collisions (energy and momentum exchange between hadrons) remain possible.
- Kinetic freeze-out: when the mean free path of hadrons in the hadron gas becomes larger than the typical dimensions of the volume occupied by the gas, even elastic collisions become very rare: local equilibrium is broken, and the kinematic distributions of the hadrons are fixed. This is the stage of kinetic freeze-out [8].

### Centrality in heavy-ion collisions

An important parameter to characterize heavy-ion collisions is the centrality, which is an observable related to the transverse distance  $b$  between the centers of the colliding nuclei. In Figure 1.9, the two nuclei are represented just before the collision (on the left), and just after their interaction (on the right). As suggested by the schema, the smaller the  $b$

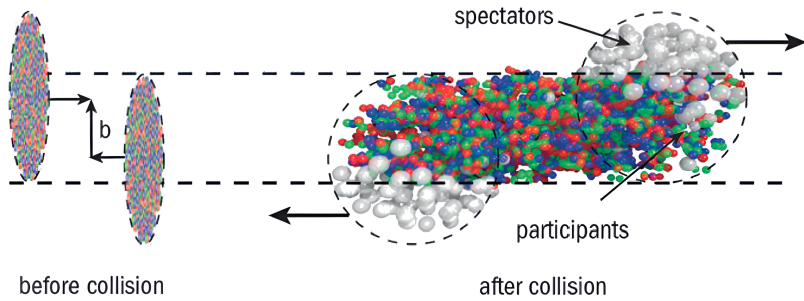


Figure 1.9: A semi-central collision, with some nucleons participating in the collision, and others being spectators. Figure from [9].

the more nucleons will participate to the collision. The collisions with the smallest  $b$  are called central collisions, and the collisions with large  $b$  are called peripheral collisions. In central collisions, the number of charged particles produced is larger than in peripheral collisions, which can be explained by the higher number of nucleon-nucleon interactions. In proton-proton collisions, the notion of centrality is not so well-defined, as the fluctuations related to the internal structure of the colliding protons become too important. Nevertheless, a classification of pp collision can be made based on the number of charged particles produced in the final state. This observable is frequently used and is called **multiplicity**, defined as the total number of charged particles produced in a collision.

### 1.2.3 QGP signatures

The creation of a QGP medium during the intermediate stages of a heavy-ion collision alters the environment in which particle production and propagation take place: studying these effects, we can probe the nature of the plasma and characterize the interaction of single partons and hadrons with the deconfined medium. The probes are typically classified as “soft” or “hard” and are sensitive to different properties of the created QGP medium. Among soft probes one can mention light-flavor hadron yields, enhancement of strange-particle production and hydrodynamic flow. The hard probes are mainly related to electromagnetic radiation, production of heavy quarkonium and open heavy flavors, and jets, providing insight on the temperature of the medium and the interactions of heavy and high- $p_T$  partons with it. In the following, the soft and hard QGP probes will be introduced, along with the QGP properties they allow to study.

#### Soft QGP probes

It has been observed that the production of particles in heavy-ion collisions can be successfully described by assuming hadronization to be a statistical process. The most established model based on this approach is called Statistical Hadronization Model (SHM), an effective model which describes the process of hadron formation in high energy collisions at energy (or distance) scales where perturbative QCD is no longer applicable. In this model, as the collision evolves, large massive and colorless objects called *clusters* are produced [10]. In heavy-ion collisions, the SHM assumes the system to be described according to the rules of the canonical ensemble, namely a hadron gas in thermal equilibrium with conserved baryon number, characterized by a the temperature  $T$  and a baryochemical potential  $\mu_B$ .

The temperature of this system is obtained at the chemical freeze-out by fitting the SHM model to the experimental data of hadron yields. The value of the temperature is found to be  $T_{CF} = 156.5 \pm 1.5$  MeV [11]. A value of  $\mu_B = 0.71 \pm 0.45$  MeV has been measured by the ALICE collaboration using net baryon yields [12]. The measurement of the hadron yields in Pb-Pb collisions in ALICE are in very good agreement with the predictions of the SHM [13], comforting the hypothesis that the system formed by heavy-ion collisions reaches a thermal equilibrium before hadronizing.

Another success of the SHM model is the prediction of a phenomenon called strangeness enhancement, i.e. the enhancement of strange particle production when going from p-p, p-A to A-A collisions (A indicating a nuclear species). Strangeness enhancement has been successfully measured in ALICE [14] and is interpreted within the SHM model as a suppression of strangeness in small collision systems due to a reduction of phase-space available for particle production [15].

Concerning its bulk properties, the QGP has been found to behave as a fluid with very low viscosity, its evolution in a heavy-ion collision being well described by hydrodynamics [8]. One of the most prominent aspects of the hydrodynamics picture is the possibility to naturally account for the observed collective behavior of the medium. Under this scenario, the observation of radial and anisotropic flow has become one of the signature of the creation of a QGP. The flow induces long-range correlations between the momenta of final-state particles. More specifically, particle distribution as a function of the azimuthal angle  $dN/d\varphi$  can be studied by means of a Fourier decomposition to extract flow coefficients  $\nu_n = \langle \cos[n(\varphi - \Psi_n)] \rangle$ , where  $\Psi_n$  is the azimuthal angle of the symmetry plane of the overlap region of the two colliding nuclei, and  $\varphi$  is the azimuthal angle of the particle momentum.  $\nu_0$  is called radial flow,  $\nu_1$  - directed flow and  $\nu_2$  - elliptic flow. In most heavy-ion collisions, the overlap region has an ellipsoidal shape, which makes the elliptic flow  $\nu_2$  the dominant coefficient in the Fourier expansion. The origin of this flow is the presence of spatial anisotropies in the overlap region of the two colliding nuclei, which then translates in the final state into a momentum anisotropy [16]. The elliptic flow is illustrated in Figure 1.10.

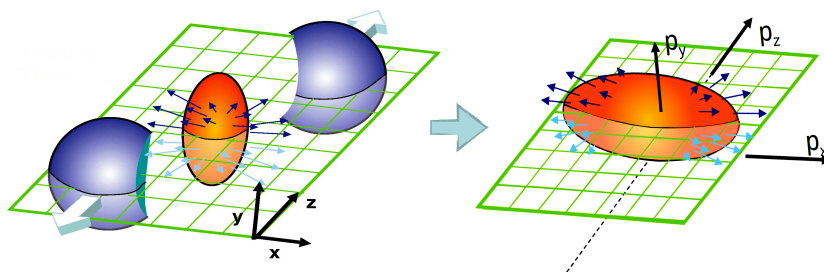


Figure 1.10: Elliptic flow: spatial anisotropies in the initial state are transferred to a momentum anisotropy of the final state particles.

### Hard and electromagnetic probes

Hard and electromagnetic probes include a variety of signature involving heavy and high- $p_T$  parton production, as well as photon emission from the medium. As an example of the first class of probes, we briefly mention here the case of quarkonium production. The production of bound  $q\bar{q}$  states such as charmonia  $c\bar{c}$  and bottomonia  $b\bar{b}$  is predicted to be sensitive to the medium temperature. A Debye screening effect leading to the suppression

of quarkonia in the presence of a hot and dense state was indeed predicted in 1986, and this mechanism was proposed as a direct proof of the QGP formation [17]. In the hot medium, the binding potential of the state decreases due to the high density of color charges surrounding the  $q\bar{q}$  state, as schematized in Figure 1.11. The Debye length  $\lambda_D$ , the maximal distance allowing for the formation of a bound  $q\bar{q}$  state, is inversely proportional to the temperature.

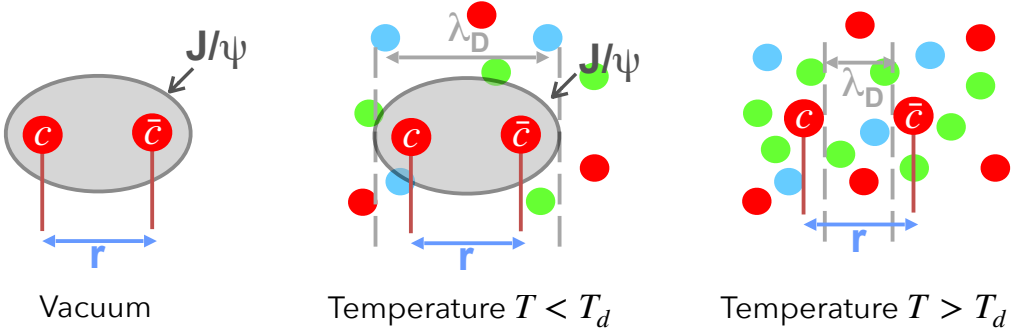


Figure 1.11:  $J/\psi$  state dissociation at increasing temperature due to the Debye screening effect,  $T_d$  being the dissociation temperature at which  $\lambda_D < r$ . Figure adapted from [18].

If the Debye length is lower than the binding radius of the bound quarkonium state, the bound state is dissociated and its yield is suppressed. Since the binding radii of the quarkonium states are different, the suppression is expected to follow a sequential trend with temperature: as the temperature increases, the first state that dissociates is the one with the largest binding radius, and the other states follow. The suppression of the different quarkonium states can then be exploited to set up a “thermometer” of the QGP medium [19]. For the  $c\bar{c}$ , however, the measurements at the LHC provide evidences of another mechanism coming into play: the regeneration of  $c\bar{c}$  states, that combine because of the large number of  $c$  and  $\bar{c}$  quarks produced in the QGP at the LHC energies. According to this picture, the final number of  $c\bar{c}$  states after hadronization will account for the initial number of  $c\bar{c}$  bound states, minus those who were dissociated, plus those who were recombined [20].

The regeneration effect does not come into play for bottomonium  $b\bar{b}$  states since the  $b$  quark production cross section is too small even at the LHC energies and hence the amount of produced  $b$  quarks is insufficient for sizable recombination effects (but conditions for a similar mechanism in the beauty sector may be reached at higher energies).

Among the electromagnetic (and electroweak) probes, one interesting example is given by the electromagnetic radiation emitted by the medium, from which several properties of the QGP can be estimated: photons do not interact strongly with the medium, and are therefore probes of the stages of the collision at which they were produced. Direct photons, in particular, those not originating from hadron decays, are especially interesting and deliver information about the temperature, collective flow and space-time evolution of the medium. In the most central Pb-Pb collisions in ALICE, in the low- $p_T$  region, up to  $p_T \approx 2$  GeV/c, an excess of the direct photon signal was observed. This excess was in agreement of models assuming the formation of a QGP and allowed for the extraction of an effective QGP temperature  $T_{eff} = 297 \pm 12(stat) \pm 41(sys)$  MeV [21].

### 1.2.4 QGP-like effects in small systems

In the standard paradigm dominating heavy-ion physics until the first results from the LHC experiments, it was assumed that QGP formation is only possible in large collision systems (A-A collisions of sufficiently large nuclei), p-p collisions being only considered as a reference for in-medium effects. However, since the start of the operation of the LHC, leading to a drastic increase of the available collision energy with respect to previous accelerators, evidence for collective effects was reported for the first time in p-A and in p-p collisions. Measurements of azimuthal correlations and anisotropic flow, for instance, indicate that similar collective effects take place in small and large collision systems. Non-zero flow coefficients of various particles were indeed measured at the LHC, for instance in ATLAS in p-p collisions [22] and in CMS in p-Pb collisions at high multiplicity [23]. The continuous increase of strange hadron yields with multiplicity, across various collision systems [14], suggests that multiplicity is a more relevant scaling parameter than collision system for characterizing the transition from vacuum to in-medium physics in hadronic collisions. One of the possible explanation for the strangeness enhancement in small systems explicitly assumes the formation of a small QGP droplet at high multiplicity [24]. The presence of QGP-like effects in p-p collisions led to a renewed interest in these collisions: along their traditional usage as a reference for heavy-ion collisions and (perturbative) QCD studies, high-multiplicity p-p collisions are now also customarily used to probe the onset of collectivity in small systems, improving our understanding of complex QCD systems by constraining the available phenomenological models [16].

## 1.3 Quarkonia probes

Quarkonia are very interesting hadrons, successfully described by non-relativistic models in some cases, studied profusely, yet not completely understood. A short introduction of their theoretical description is given in this section.

Both c and b quarks are heavy with respect to the three lightest quarks u, d and s, with  $m_c \approx 1.3 \text{ GeV}/c^2$  and  $m_b \approx 4.2 \text{ GeV}/c^2$ : this allows them to be theoretically described with non-relativistic potential, the Cornell potential [25]. This potential describes the bound state of  $q$  and  $\bar{q}$  as a function of the quark-antiquark distance  $r$  according to the following relation:

$$V(r) = \sigma r - \frac{\alpha}{r}, \quad (1.2)$$

with  $\sigma$  being the confining strength and  $\alpha$  being the Coulomb-like coupling constant. This potential can be added in a Schrödinger's equation and its solutions are resonances, representing the possible bound states. Similarly to the case of the hydrogen atom in atomic physics, a quarkonium system is characterized by several quantum numbers, among them the orbital angular momentum quantum number  $L$  (integer) and the spin angular momentum quantum number  $S$  (can be  $S = 0$  or  $S = 1$ ). The total angular momentum quantum number  $J$  is also an integer that can take values in  $[|L - S|, L + S]$ . A physical quarkonium state can be represented by the notation  $^{2S+1}L_J$ , or by its  $J^{PC}$  numbers, with  $P = (-1)^{L+1}$  the parity of the quark-antiquark state and  $C = (-1)^{L+S}$  the charge-conjugation eigenvalue [26]. The bound states of the charmonium family are represented in Figure 1.12. A similar figure can be derived for the bottomonium states, with the equivalent of  $J/\psi$  being the  $\Upsilon$  ground state.

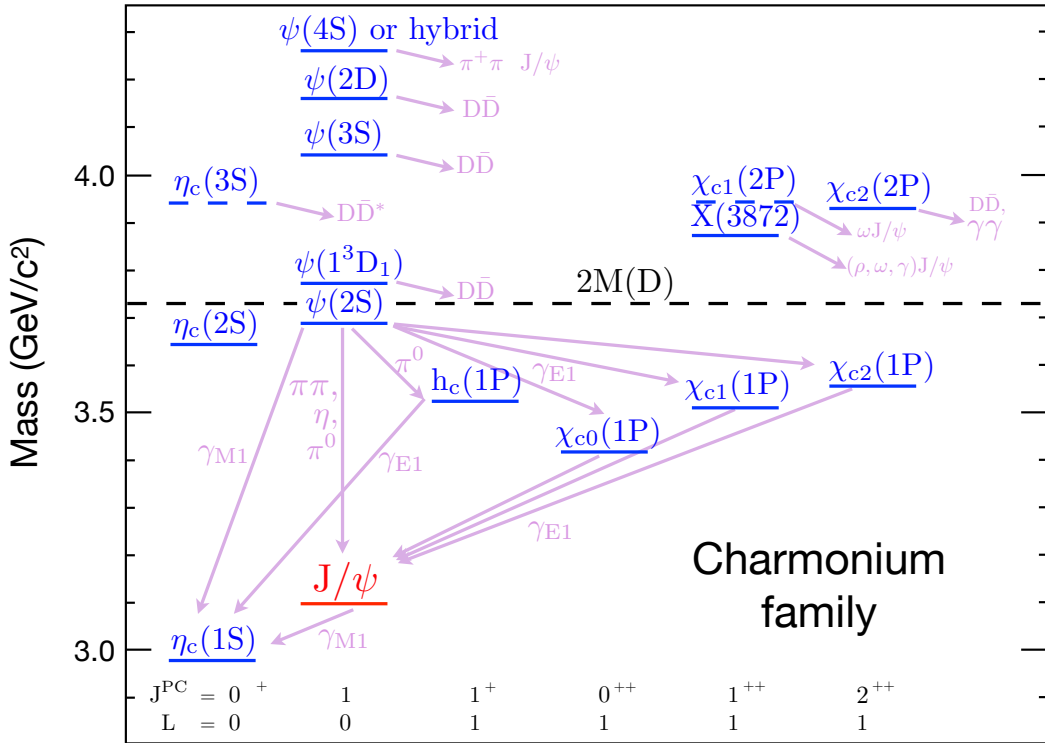


Figure 1.12: Charmonium resonances, their quantum numbers  $J^{PC}$  and decays. Adapted from [26] by Batoul Diab.

While the following discussion will focus on this particular state, the general concepts concerning the production models also apply to the other quarkonium states.

The mass of the  $J/\psi$  has been precisely measured by several experiments, and its current experimental value is [27]

$$m_{J/\psi} = 3096.900 \pm 0.006 \text{ MeV}/c^2.$$

The main decay modes of the  $J/\psi$  have the following probabilities, also called Branching Ratios (BR) [27]:

$$\text{BR}(\text{ } J/\psi \rightarrow \text{Hadrons}) = 87.7 \pm 0.5\%$$

$$\text{BR}(\text{ } J/\psi \rightarrow e^+ e^-) = 5.971 \pm 0.032\%$$

$$\text{BR}(\text{ } J/\psi \rightarrow \mu^+ \mu^-) = 5.961 \pm 0.033\%$$

The  $J/\psi$  has been discovered 50 years ago, and though our understanding of this particle has greatly improved, with extremely precise measurements of its mass and lifetime, some of its characteristics are still unknown. The production of  $J/\psi$  in hadronic collisions remains poorly understood, with several models failing to fully describe this production process. The main available models for  $J/\psi$  production are introduced in the following section.

### 1.3.1 Models for charmonium production

The  $J/\psi$  yields observed in experiments include two contributions: the  $J/\psi$  which are directly produced during the collision, i.e. prompt production, and the  $J/\psi$  produced as

a decay daughter (mainly of b-hadrons), called non-prompt production.

The prompt production of charmonium states involves two stages: the production of a  $c\bar{c}$  pair (perturbative process), and its non-perturbative evolution into the hadronic states. The final hadronic state is colorless, i.e. in a color-neutral state: the treatment of the color neutralization is a central issue in the different models of charmonium (and in more general terms, quarkonium) production, models which will be shortly introduced in the following. More details on these models can be found in references [28] and [29].

### The Color Evaporation Model

Historically, the first model of quarkonia production is the Color Evaporation Model (CEM). The main assumption of CEM is that the production rate of a quarkonium state is proportional to the production rate of a  $Q\bar{Q}$  pair, regardless of the quantum numbers of the  $Q\bar{Q}$  pair or the considered quarkonium state. The proportionality factor,  $F_Q$ , where  $Q$  indicates the quarkonium state, is the parameter describing the evolution of the  $Q\bar{Q}$  state into the bound state. During this evolution, the  $Q\bar{Q}$  pair is assumed to neutralize its color through several non-perturbative (soft) gluon interactions, hence the term *color evaporation* [28].

In the CEM, the quarkonium mass lies between  $2m_Q$  and the mass of a pair of the lightest open-charm hadrons  $2M_H$ . In the case of the  $J/\psi$ ,  $m_Q = m_c$  and  $M_H = M_D$ , the mass of the D meson.

The  $J/\psi$  production cross section in this model can be then factorized as follows:

$$\sigma(J/\psi + X) = F_{J/\psi} \int_{2m_c}^{2M_D} \frac{d\sigma_{c\bar{c}}}{dm_{c\bar{c}}} dm_{c\bar{c}}, \quad (1.3)$$

with  $\sigma_{c\bar{c}}$  the cross section for  $pp \rightarrow c\bar{c} + X$  and  $F_{J/\psi}$  the universal factor for  $J/\psi$ .

### The Color Singlet Model

In the Color Singlet Model (CSM), the quark-antiquark pair is produced already in a color-singlet state, and then hadronizes keeping its colorless state. The assumption is that the quantum states of the pair does not evolve between its production and its hadronization, neither in spin, nor in color. It was introduced in the 1980s [30, 31] and became the leading model for quarkonia production in the 1990s. The  $J/\psi$  production cross section in this model is expressed as follows [32]:

$$d\sigma[J/\psi + X] = \sum_{i,j} \int f_i(x_i) f_j(x_j) d\sigma_{i+j \rightarrow c\bar{c}+X} |\psi(0)|^2$$

with  $f_{i,j}(x)$  being the parton densities in the colliding hadrons, and  $|\psi(0)|$  the probability that the  $c\bar{c}$  pair hadronizes into the  $J/\psi$  state. This model has successfully described experimental data at low center-of-mass energy but fails to predict  $J/\psi$  production at the LHC energies in its original form.

### NRQCD

Quarkonium states such as charmonia ( $c\bar{c}$ ) or bottomonia ( $b\bar{b}$ ) involve a quark mass  $m_Q$  larger than the typical hadronic scale  $\Lambda_{QCD}$ . The typical relative velocity of the heavy

quark inside the bound state decreases as the mass  $m_Q$  increases [33]. As a consequence, the heavy quark-antiquark pair is produced with low velocity in the center of mass frame. In this regime, the evolution of the pair can then be considered to be non-relativistic. The production of the pair (dominated by gluon fusion) can be considered as a perturbative process, but then its hadronization is not, making the study of heavy quarkonia a multi-scale problem. The fact that direct QCD calculations in multi-scale problems are very challenging motivated the development of an effective field theory based on QCD, called NRQCD. This theory is equivalent to QCD at the energy scale relevant for the formation of heavy quarkonia states [34]. The NRQCD effective Lagrangian is derived from the QCD Lagrangian by neglecting all states of momenta much larger than the heavy quark mass and adding new interaction terms [35].

In the NRQCD framework, the production cross section of a quarkonium state  $H$  can be factorized into short-distance coefficients  $F_n$  (dependent on the kinematic variables of the production process, but independent of the quarkonium state  $H$  [36]) and operators describing long-distance effects called Long Distance Matrix Elements (LDMEs). These elements encompass the probability for a  $Q\bar{Q}$  pair to evolve into a quarkonium state.

$$\sigma(H) = \sum_n \frac{F_n(\Lambda)}{m_Q^{d_n-4}} \langle 0 | O_n^H(\Lambda) | 0 \rangle ,$$

where  $\Lambda$  is the ultraviolet cutoff of the effective theory,  $n$  is the order up to which one wants to calculate the cross section,  $\langle 0 | O_n^H(\Lambda) | 0 \rangle$  are the LDMEs and  $O_n^H$  are four-fermion operators, whose mass dimensions are  $d_n$ .

### Non-prompt production

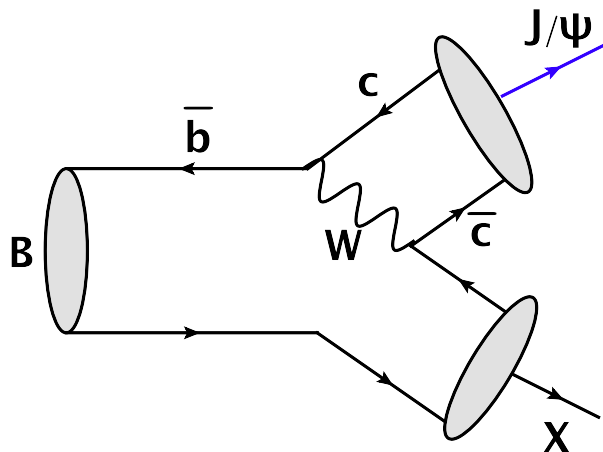


Figure 1.13: Feynman diagram of a B hadron weak decay into a  $J/\psi$  [37].

The non-prompt  $J/\psi$  are mainly produced from the weak decay of the B-hadrons, an example of such decay diagram at leading order being shown in Figure 1.13.

The lifetime of the B-hadron is such that the decay happens at a distance  $c\tau \approx 500\mu m$  from the production point of the B-hadron.

The fraction  $f_b$  of non-prompt  $J/\psi$  in the total yield at mid-rapidity has been measured by several experiments at the LHC and the Tevatron [38]. The results of these measurements are shown in Figure 1.14. In the  $J/\psi$  transverse momentum interval  $1.3 < p_T < 3$  GeV/ $c$  the non-prompt fraction is about 10 % and rises as the  $p_T$  of the  $J/\psi$  increases.

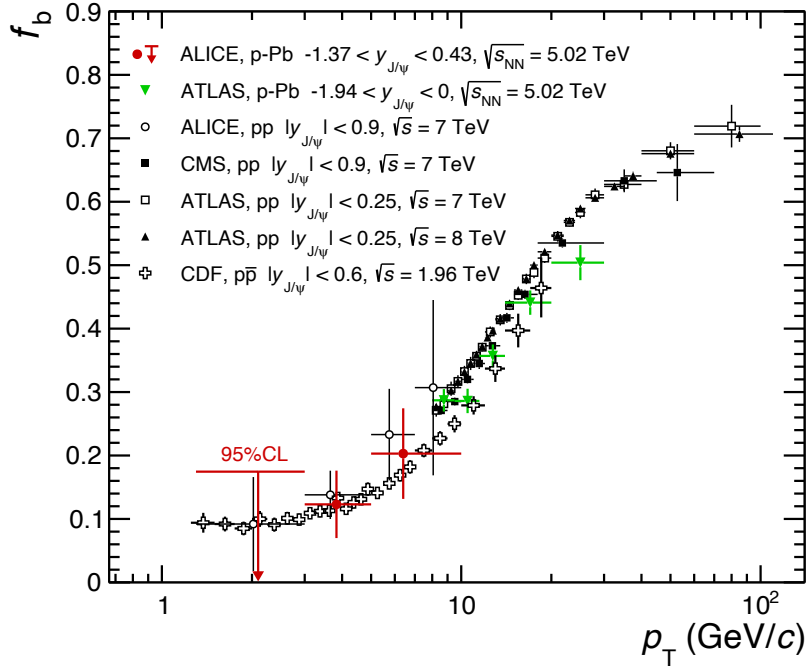


Figure 1.14: Fraction of non-prompt  $J/\psi$  as a function of  $p_T$  for different collision energy and systems [38].

### 1.3.2 $J/\psi$ polarization

The studies of the  $J/\psi$  polarization are complementary to the measurements of the  $J/\psi$  production cross section. They can help to further constrain the theoretical models. Experimentally, the  $J/\psi$  polarization is measured in the dilepton decay channel based on the angular distribution of the decay leptons in the  $J/\psi$  rest frame [39]

$$W(\cos \theta, \varphi) \propto \frac{1}{3 + \lambda_\theta} (1 + \lambda_\theta \cos^2 \theta + \lambda_\varphi \sin^2 \theta \cos 2\varphi + \lambda_{\theta\varphi} \sin 2\theta \cos \varphi), \quad (1.4)$$

where  $\theta$  and  $\varphi$  are the polar and azimuthal angles between the lepton and a given reference axis, respectively, and  $(\lambda_\theta, \lambda_\varphi, \lambda_{\theta\varphi})$  are the three polarization parameters. In hadronic collisions, the most commonly used references axes are the helicity and Collins-Soper axes. The helicity axis is given by the  $J/\psi$  flight direction in the rest frame of the colliding hadrons, while the Collins-Soper axis is given by the direction of the relative velocity of the colliding hadrons in the  $J/\psi$  rest frame. The two extreme set of values of the polarization parameters  $(\lambda_\theta, \lambda_\varphi, \lambda_{\theta\varphi})$  are  $(1, 0, 0)$  and  $(-1, 0, 0)$ . They correspond to the so called transverse and longitudinal polarizations, respectively.

Next-to-Leading Order calculations based on CSM and NRQCD models predict partial transverse or longitudinal polarization of  $J/\psi$  in pp collisions at the LHC [40]. In general, the predicted values of the polarization parameters depend on the transverse momentum of the  $J/\psi$  and the chosen reference axis. Other NRQCD calculations incorporating both color-singlet and color-octet contributions to the  $J/\psi$  production predict zero or small longitudinal polarization at high  $p_T$  [41]. The experimental results clearly show very small or zero polarization in pp collisions at 7 and 8 TeV [42–44]. The observed tensions between the experimental data and theoretical models put strong additional constraints

on the existing theoretical models and indicates that more studies, both theoretical and experimental, are needed in order to acquire a full understanding of the  $J/\psi$  production in hadronic collisions.

### 1.3.3 $J/\psi$ production as a function of charged-particle multiplicity

In this section, the experimental results on  $J/\psi$  production as a function of charged-particle multiplicity are shortly reviewed, covering different center-of-mass energies and different collision systems.

The idea of measuring  $J/\psi$  production as a function of charged-particle multiplicity was introduced in 2011 in [45]. One of the interest of this measurement is to improve our understanding of high-multiplicity p-p collisions, especially the role of Multi-Parton Interactions. The  $J/\psi$  is a probe of choice in this context, because its production involves a complex interplay between soft and hard components (see section 1.3.1 for more details). A very important concept to be mentioned when discussing high-energy p-p collisions is the one of “Multi Parton Interactions” (MPI), referring to multiple parton hard-scatterings taking place within a single hadron collision, i.e. events in which two or more independent hard parton interactions occur simultaneously in a single hadron-hadron collision. MPIs are possible due to the composite nature of hadrons. These interactions are not yet completely understood and play a role in several measurements [46].

The first measurement of  $J/\psi$  production as a function of relative charged-particle multiplicity in proton-proton collisions was performed in 2012 by the ALICE collaboration [47]. This result, reported in Figure 1.15, already gave indications that the relative  $J/\psi$  yield does not have the same mid-rapidity multiplicity dependence when the  $J/\psi$  is measured at in the forward rapidity region  $2.5 < y < 4$  or in the central rapidity region  $|y| < 0.9$ , the increase in the  $J/\psi$  relative yield being steeper for  $J/\psi$  produced at mid-rapidity. It is worth noting that this measurement has been made exploiting all inelastic events (INEL events).

Later measurements of  $J/\psi$  relative yield as a function of relative charged-particle multiplicity were made for the INEL>0 event class, corresponding to inelastic events with at least one charged primary particle in  $|\eta| < 1$ : the results are summarized in Figure 1.16, which also includes the first result at  $\sqrt{s} = 7$  TeV for forward  $J/\psi$ . The  $J/\psi \rightarrow e^+e^-$  results at  $\sqrt{s} = 13$  TeV are taken from [48].

All these results follow a similar pattern: the relative yield of  $J/\psi$  produced at forward rapidity follows an almost linear dependence as a function of the multiplicity measured at mid-rapidity , whereas the relative yield of  $J/\psi$  produced at mid-rapidity has a steeper dependence with the respect to the same reference.

One can wonder to what extent the rapidity region of the  $J/\psi$  has an impact on the dependence, making a forward  $J/\psi$  less sensitive to multiplicity effects. To investigate further this question, it was proposed to study the production of forward  $J/\psi$  as a function of the relative multiplicity also measured in the forward region. This study and its results are presented and discussed in chapter 3.

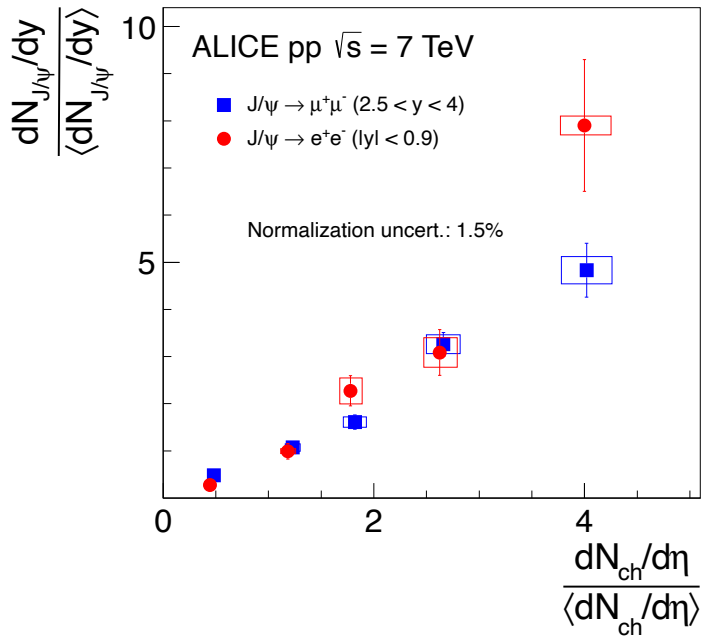


Figure 1.15: Forward and mid-rapidity  $J/\psi$  relative yield as a function of relative multiplicity at mid-rapidity at  $\sqrt{s} = 7$  TeV, for inelastic events [47].

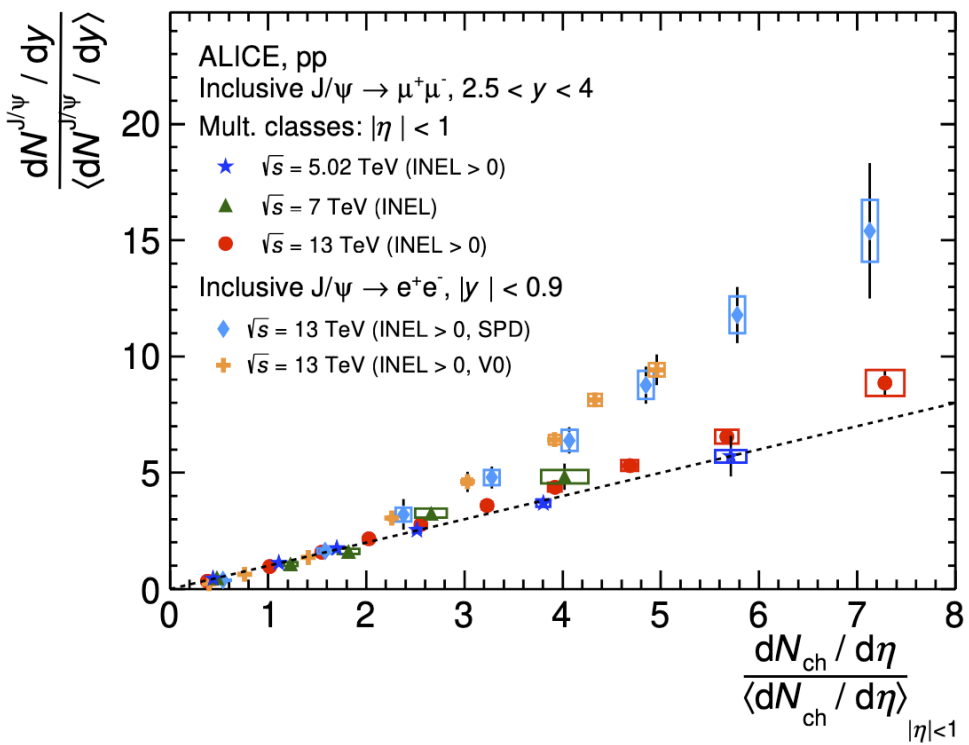


Figure 1.16: Forward and mid-rapidity  $J/\psi$  relative yield as a function of relative multiplicity at mid-rapidity [49].

## 1.4 Simulating proton-proton collisions

In experimental particle physics, a crucial step is to understand the detector effects affecting the measurements, in order to disentangle them when investigating the physics underlying the observations: this is done using simulations. Simulations in high-energy particle physics usually foresee two different steps : first, primary particles are “created” using generators implementing specific models for the kinematic distributions, exploiting perturbative calculations or phenomenological approaches, and their decays are simulated; second, non-decayed primary particles and any other decay product are propagated through the modeled detector volumes simulating any relevant interaction with matter: this step is usually performed using transport codes such as GEANT4 [50]. In both steps, the Monte Carlo approach is exploited to take into account the probabilistic nature of the simulated processes.

In the following, two of the main general-purpose generators used to simulate high-energy hadronic collisions are introduced: PYTHIA and EPOS.

### 1.4.1 The PYTHIA event generator

PYTHIA [51] is a complex event generator implementing perturbative QCD and phenomenological models of soft interactions, parton showers and Multiple Parton Interactions along with decays.

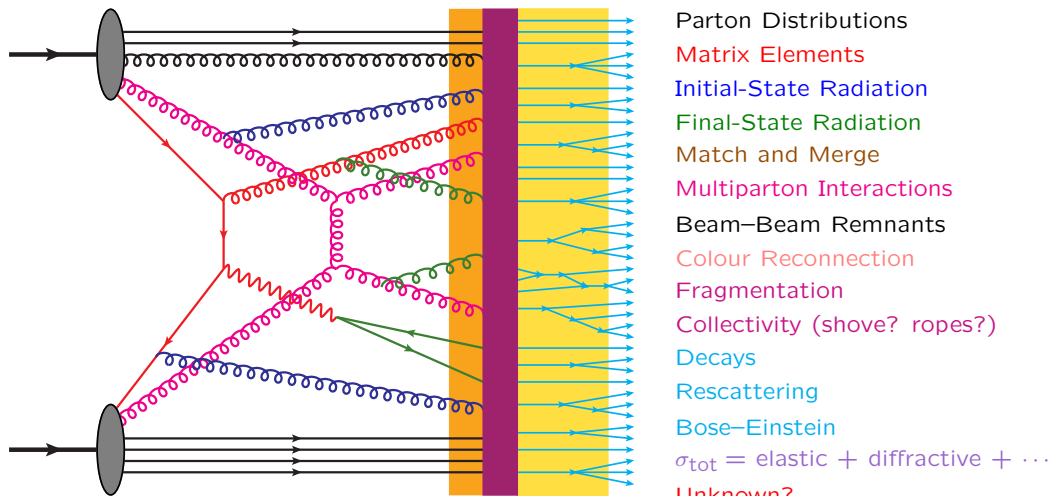


Figure 1.17: View of a hadron-hadron collision in PYTHIA [52].

Each proton-proton interaction simulated in PYTHIA is divided into several steps: the hard-scattering process usually described by perturbative QCD, the initial- and final-state radiation based on parton shower models and MPIs, and finally the hadronization described by the Lund string model [53]. In this model, the strong confining force is treated as a flux tube with potential energy increasing with the distance between quark and anti-quark. These strings then fragment into hadrons.

Some of the aforementioned steps cannot be derived from first principles, and rely on the adjustment of the main relevant parameters based on experimental data. The hadronization, especially, involves non-perturbative phenomena and is therefore described in PYTHIA

using effective models involving free parameters adjusted on the available experimental data. Different tunes for these parameters are possible in PYTHIA, leading to different final results.

Since the total number of parameters is large, some of them being correlated, specific tunes are proposed as a reference and released. In this thesis, PYTHIA8 will be used exclusively with the Monash 2013 tune: this is the default tune for pp simulations, implementing the most accepted reference for the initial-state-radiation, multiparton-interactions and beam-remnants aspects [51].

### 1.4.2 EPOS event generator

EPOS [54] is an event generator originally created to modelize jet production along with their complete event description. The acronym stands for “Energy conserving quantum mechanical approach, based on Partons, parton ladders, strings, Off-shell remnants and Splitting of parton ladders”.

It is a general purpose event generator, meant to describe any observable in high-energy hadron interactions, aiming at behaving better than PYTHIA in the low- $p_T$  region.

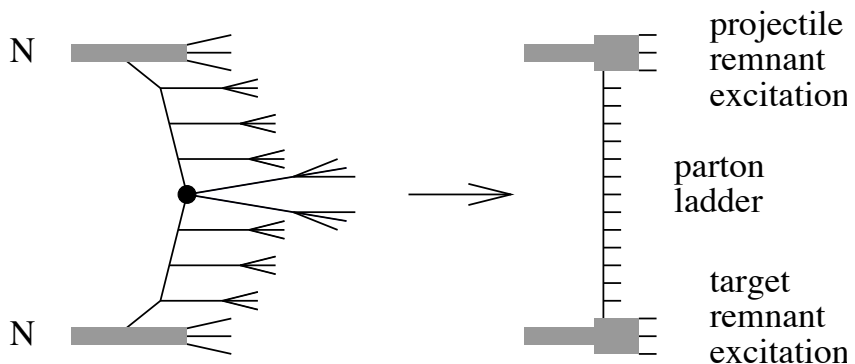


Figure 1.18: Schematic view of the parton ladder and the beam remnants in EPOS [55].

Since the creation of the EPOS generator in 2010, which successfully described RHIC data, different versions were developed to suit different types of experimental conditions, the later versions implementing hydrodynamics (EPOS3, EPOS4). Among the available versions, EPOS-LHC is one specifically tuned to describe the available observations at the LHC energies.

The main concept behind EPOS-LHC is the assumption of a core-corona behavior of the system created during collisions. The core undergoes collective evolution and hadronization, and can be understood as high-density thermalized matter or in other terms a quark-gluon plasma (QGP) volume. Surrounding the core is a corona where isolated parton interactions occur without influence from neighboring partons, meaning there is no collective behavior. These parton interactions in the corona also contribute to hadronization [56].

EPOS is then able to simulate different collision systems, from p-p to A-A, and is able to accurately predict an extensive number of observables such as the flow in p-Pb collisions [57] and the transverse momentum spectra of final-state hadrons [58]. MPIs are also implemented in EPOS, and are modeled as multiple-pomeron exchanges.

# Chapter 2

## The Large Hadron Collider and ALICE

In this Chapter the Large Hadron Collider (LHC) will be introduced and the experimental apparatus of A Large Ion Collider Experiment (ALICE) will be described.

### 2.1 The LHC

The LHC is the largest particle accelerator and collider in the world, with a circumference of nearly 27 km. It is located underground near Geneva, at the France-Switzerland border. It accelerates and collides protons as well as heavy nuclei up to center-of-mass energies of  $\sqrt{s} = 13$  TeV for proton–proton collisions in the data taking period called Run 2, and up to  $\sqrt{s} = 13.6$  TeV in the most recent data taking period, Run 3 (the corresponding center-of-mass energy per nucleon pair in Pb-Pb collisions in Run 3 so far is  $\sqrt{s_{NN}} = 5.36$  TeV).

Before particles start circulating inside the LHC infrastructure, they are accelerated by several linear and circular accelerators, from LINAC to PS (Proton Synchrotron) and SPS (Super Proton Synchrotron). Their trajectories are constantly guided using magnetic dipoles. In the LHC, the two beams are accelerated inside two separate rings in opposite directions, and collide in well-identified points located inside underground experimental caverns where particle detectors are installed.

A sketch of the layout of the LHC is shown in Figure 2.1, with the 4 main interactions points, corresponding to the 4 main LHC detectors: ATLAS (A Toroidal LHC Apparatus), CMS (Compact Muon Solenoid), LHCb (Large Hadron Collider beauty experiment) and ALICE.

ATLAS and CMS serve as general-purpose detectors with a focus on investigating the Standard Model and searching for signals of Beyond Standard Model physics. Their primary objectives include studying fundamental particles like the Higgs boson to understand their properties and looking for new particles or deviations from Standard Model predictions for known particles, hinting to physics beyond the Standard Model. This encompasses searches for phenomena such as dark matter particles.

The LHCb experiment focuses on the investigation of the matter-antimatter asymmetry through the study of CP violation, with special emphasis on the beauty sector.

ALICE is an experiment dedicated to the study of hadronic matter at the TeV energies, and in particular the Quark-Gluon Plasma (QGP) phase. This experiment and its

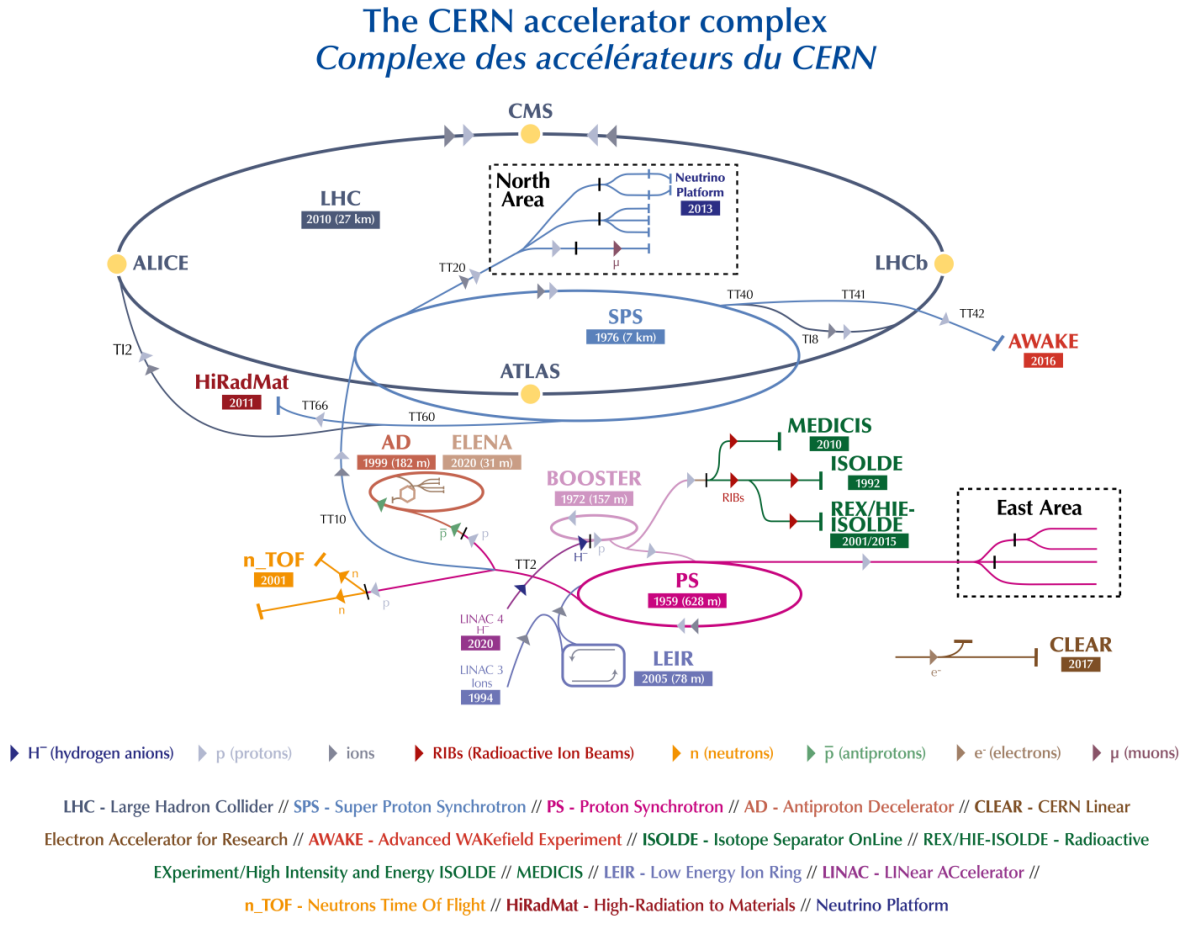


Figure 2.1: The layout of the LHC and the CERN accelerator complex [59]

detectors will be described in detail in this Chapter.

Particles in the LHC beams are grouped into packets of protons (or ions) called bunches, the time distance between two bunches being 25 ns in standard LHC operations. This time unit called Bunch Crossing (BC) is used in this thesis to define time duration. The interacting bunches can be more or less spaced in time (by an integer number of BCs), and their distribution in time, called the bunch filling scheme, can vary from one data taking period to another. The default proton-proton filling scheme is 3564 BCs long, representing the time it takes for a proton to complete a full turn of the LHC ring. This period is called orbit, and during one continuous data taking period called run, the proton beams go through several orbits. The rate at which the proton or Pb ion bunches interact is called the Interaction Rate (IR).

## 2.2 The ALICE detector

The ALICE detector is located at the second interaction point of the LHC, called P2. Looking towards the center of the LHC ring, the two sides of the ALICE detector along the beam axis are called C-side on the right (negative  $z$  coordinate)- towards the CMS

Interaction point (IP) - and A-side on the left (positive  $z$  coordinate) - towards the ATLAS IP.

A sketch of the ALICE coordinate system is shown in Figure 2.2. In this figure, the  $(x, y, z)$  axes are shown together with the spherical coordinates used to describe the trajectory of particles in ALICE,  $(r, \theta, \varphi)$ .

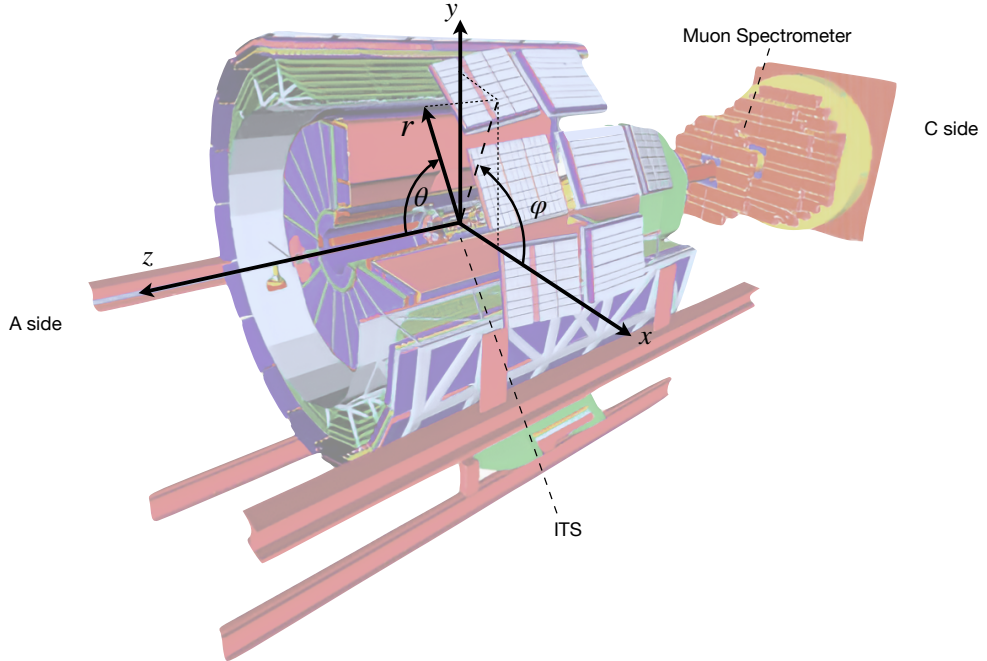


Figure 2.2: The ALICE detector (solenoid magnet not shown) with its coordinate system.

In experimental particle physics, the transverse momentum  $p_T$  and the rapidity  $y$ <sup>1</sup> are used abundantly to characterize the produced particles. The transverse momentum  $p_T$  of a particle is the norm of its momentum in the plane perpendicular to the beam axis and is defined as:

$$p_T = \sqrt{p_x^2 + p_y^2}.$$

The rapidity  $y$  is defined as:

$$y = \frac{1}{2} \ln \left( \frac{E + p_z}{E - p_z} \right)$$

Easier to compute and equivalent to the rapidity for light relativistic particles, the pseudorapidity  $\eta$  is commonly used when dealing with non-identified particles or geometrical acceptance:

$$\eta = -\ln \left( \tan \frac{\theta}{2} \right)$$

This section provides a description of the ALICE detector and its evolution from LHC Run 1-2 to Run 3. It begins with an overview of the ALICE sub-detectors during the Run 2 data-taking period (2015-2018, relevant for the first analysis discussed in this thesis), then

---

<sup>1</sup>The symbol  $y$  also denotes the  $y$  in cartesian coordinates, but in this thesis most of the  $y$  are the rapidity

outlines the upgrades implemented during the Long Shutdown 2 of the LHC (LS2), and finally describes the current version of the detector used in Run 3 (2022-2026, relevant for the second analysis presented in this thesis) [60].

### 2.2.1 ALICE in Run 2

A schematic view of the ALICE detector in Run 2 is shown in Figure 2.3. It is composed of several sub-detectors outlined in the figure, each serving a specific function.

THE ALICE DETECTOR

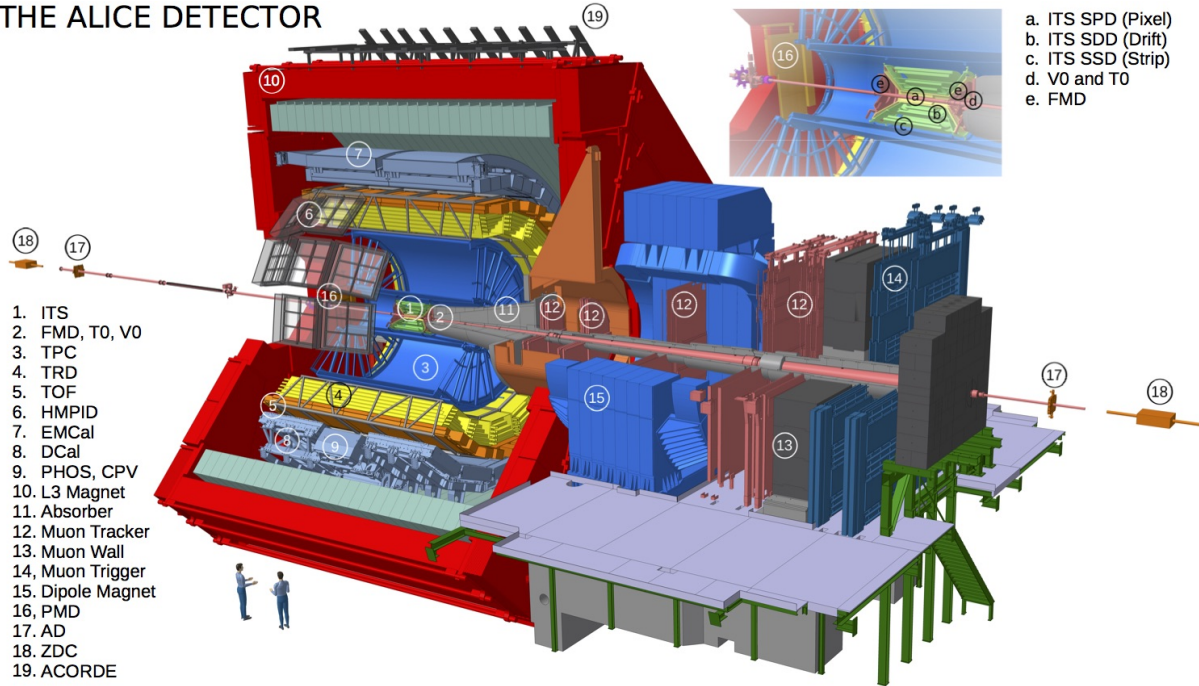


Figure 2.3: The ALICE detector in Run 2 [61].

### Central Barrel Detectors

The central part of the ALICE detector, known as the central barrel, is located inside an octagonal solenoid magnet called L3. This magnet bends the trajectories of the charged particles propagating inside its inner volume. The central barrel covers the full azimuthal range at mid-rapidity ( $\eta$  close to 0) and contains several detectors which are presented in the following:

The **Inner Tracking System (ITS)** is a silicon tracking system composed of six cylindrical layers. It covers the pseudorapidity range  $|\eta| \leq 0.9$ . Its main goal is to identify the position of the primary vertex with a resolution better than  $100 \mu\text{m}$  and provide tracking of charged particles down to  $p_T = 100 \text{ MeV}/c$ . The two layers closest to the beam pipe form the Silicon Pixel Detector (SPD), this sub part of the ITS covers the pseudorapidity region  $|\eta| < 1.4$ . This subdetector is sometimes used independently of the full ITS for vertex reconstruction.

The **Time Projection Chamber (TPC)** is designed for charged-particle tracking and identification. It consists of a large drift volume of gas and its end-caps are equipped with Multi-Wire Proportional Chambers.

The **Time Of Flight (TOF)** detector exploits Multigap Resistive Plate Chambers to perform time-of-flight measurements, providing an important input for particle identification.

The **Transition Radiation Detector (TRD)** is composed of proportional gas chambers and radiators used to identify and track hadrons and electrons.

The **High-Momentum Particle Identification Detector (HMPID)** consists of Cherenkov counters and serves as a particle identification detector for high- $p_T$  tracks, with  $p_T > 1 \text{ GeV}/c$ .

The **Electromagnetic Calorimeter (EMCal)** is a Pb-scintillator calorimeter that identifies electrons and performs photon and pion measurements in the pseudorapidity region  $|\eta| > 0.7$ . It is also used as a jet trigger.

The **Photon Spectrometer (PHOS)** is an electromagnetic calorimeter composed of PbWO<sub>4</sub> crystals responsible of photon identification. It is also used as a high-energy photon trigger.

In summary, these central detectors are used for precise tracking and identification of charged particles, as well as for particle momentum and energy measurements.

### Forward sub-detectors

The ALICE detector in Run 2 is equipped with several forward sub-detectors, such as the V0 detector, the Forward Multiplicity Detector (FMD) consisting of several layers of silicon strip detectors at a distance of 70-150 cm from the interaction point, and the Zero-Degree Calorimeter (ZDC) composed of neutron and proton calorimeters. These detectors cover a wide range of pseudorapidities and are essential for studying particle production in the forward direction and for triggering specific classes of events.

ALICE also has a dedicated part of the detector for the tracking and identification of muons, the Muon Spectrometer. It is located outside the central barrel, in the forward region. This detector is described in more details in subsection 2.2.1.2.

The sub-detectors used more specifically in the analysis based on the Run 2 data covered in this thesis are described in more details in the following subsections.

#### 2.2.1.1 The V0 detector

The V0 is a forward detector made of two disks, one on the A-side called V0-A and covering the pseudorapidity region  $2.8 < \eta < 5.1$ , and one on the C-side called V0-C covering the region  $-3.7 < \eta < -1.7$  (Figure 2.4).

The V0-A is located 329 cm away from the IP ( $z = 0 \text{ cm}$ ) whereas the V0-C is located at  $z = -88 \text{ cm}$ .

Both V0-A and V0-C are composed of 32 and 48 scintillators (cells) respectively, divided in 4 rings and 8 sectors corresponding to 32 distinct channels which are numbered as can

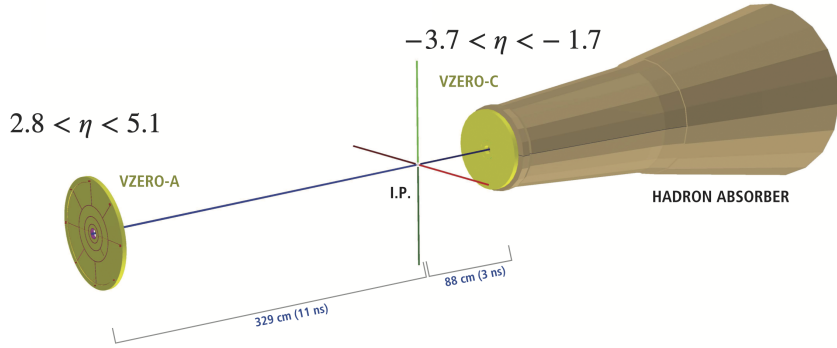


Figure 2.4: The V0 detector with its two detection disks, adapted from [62].

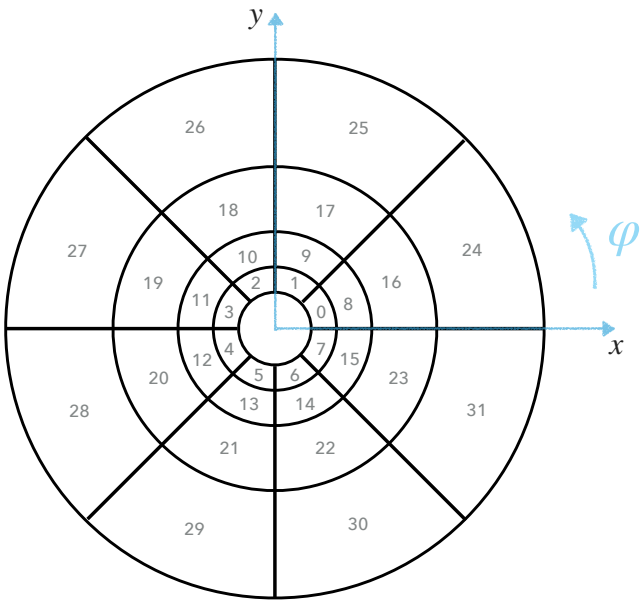


Figure 2.5: V0-C channels and their numbering.

be seen for the V0-C in Fig.2.5. Each sector corresponds to an azimuthal angle range of  $\pi/4$  and each ring corresponds to a specific range in  $\eta$ .

The V0 detector plays a crucial role in the ALICE experiment. First, the V0 detector provides the minimum-bias trigger in various collision systems including p-p, p-Pb, and Pb-Pb, requiring a coincidence of signals in both V0-A and V0-C within a specific time window. It provides beam-gas rejection via the correlation of the timing information from V0-C and V0-A and thanks to its time resolutions of 450 ps for V0-A and 350 ps for V0-C. Finally, it is used as the main detector for centrality estimation in Pb-Pb collisions by summing up the energy deposited in V0-C and V0-A and fitting the result using a Glauber model.

This detector operates as follows: charged particles passing through the scintillator cells produce scintillation light, which is converted by wavelength shifting fibers and transmitted to photomultipliers through clear optical fibers [63]. The amplitude of the scintillation signals recorded by the photomultipliers is proportional to the energy deposited by the

charged particles, allowing for an estimation of particle multiplicity based on the knowledge of the average energy deposited by a minimum-ionizing particle.

### 2.2.1.2 The Muon Spectrometer

The Muon Spectrometer is installed on the C-side of the ALICE experiment. It covers the pseudorapidity region  $-4 < \eta < -2.5$  and the azimuthal region  $0 < \varphi < 2\pi$ . Its goal is to study open heavy-flavor production ( $D$  and  $B$  mesons) through single muon measurements, and quarkonia production ( $J/\psi$ ,  $\psi'$  and  $\Upsilon(1S)$ ,  $\Upsilon(2S)$  and  $\Upsilon(3S)$ ) via their dimuon decay channel, down to zero  $p_T$ . It also allows for the study of the low-mass vector mesons such as  $\rho$ ,  $\omega$  and  $\phi$ .

The Muon Spectrometer is composed of different parts [64]. Going from left to right in Figure 2.6, the particles cross first an absorber (mainly composed of carbon and concrete) designed to absorb the hadrons emerging from the interaction point. Beyond the absorber, the muons traverse five tracking stations equipped with multi-wire proportional chambers [65] and are deflected by the magnetic field provided by a warm dipole magnet, allowing for the determination of their momentum. The next part is the muon filter, an iron wall designed to reduce the background in the trigger chambers by absorbing secondary hadrons and low-momentum muons [66]. Finally, the muons reach the trigger system (in pink in the figure) made of two stations equipped with Resistive Plate Chambers characterized by a time resolution of around 1 ns.

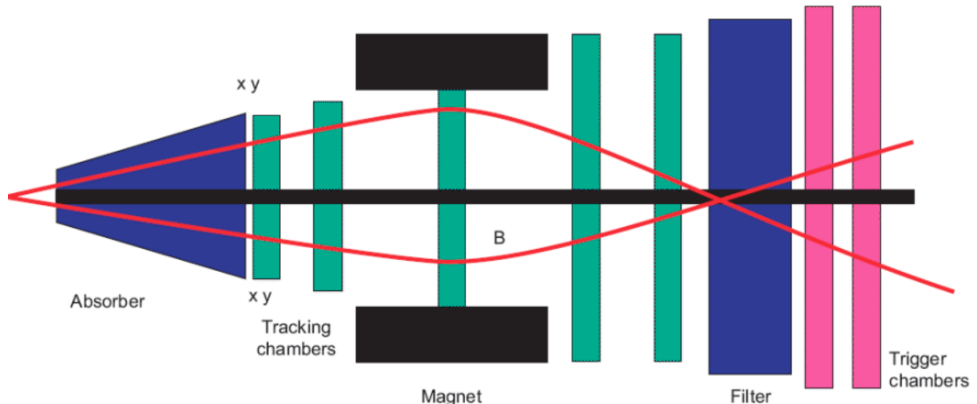


Figure 2.6: The Muon Spectrometer and its different parts [67].

### 2.2.2 ALICE in Run 3

In view of LHC Run 3, ALICE has deployed a strategy aimed at enhancing its capabilities for a large panel of physics measurements. This includes achieving a 50 kHz Pb-Pb event readout rate, a significant increase from the previous rate of approximately 1 kHz in the central barrel in Run 1 and 2. The physics goals for this period encompass a broad range of phenomena. ALICE aims to study heavy-flavour mesons and baryons down to very low  $p_T$ , as well as charmonium states down to zero  $p_T$ . Additionally, the experiment will focus on thermal dileptons and direct photons originating from QGP radiation and low-mass vector mesons. Furthermore, ALICE aims to conduct high-precision measurements of light and

hyper-nuclei to deepen our understanding of nuclear matter properties [68]. Because of the complex combination of signal identification and background discrimination characterizing some of these measurements (especially at low  $p_T$ ), it is not favorable to create a dedicated hardware trigger. The strategy is then to use a minimum-bias readout (reading every event) at the highest possible rate, opposed to the Run 2 strategy of reading only triggered events.

### 2.2.2.1 Detector upgrades

To meet the requirements for the foreseen physics goals, the ALICE detector underwent several upgrades during the Long Shutdown 2 (LS2). These upgrades needed to be implemented before the Run 3 data taking period, which commissioning started in 2021. A timeline of the different LHC shutdown and data-taking periods between 2016 and 2026 is given in Figure 2.7.

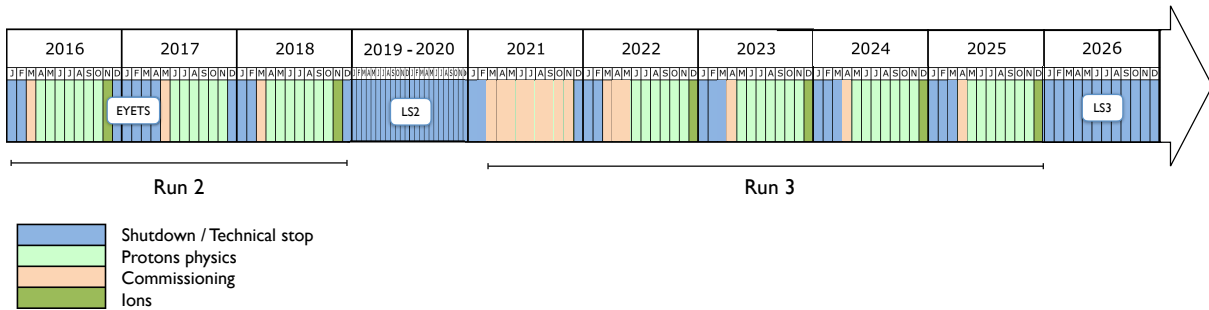


Figure 2.7: The LHC timeline from Run 2 to Run 3, adapted from [69].

The upgrade program included the installation of an improved Inner Tracking System and a new Muon Forward Tracker for faster and more precise particle tracking and vertexing, also thanks to a smaller diameter beampipe. New timing detectors called Fast Interaction Triggers (FIT) replace the forward detectors used in Runs 1 and 2. Additionally, the existing Multi-Wire Proportional Chambers (MWPC) were replaced by quadruple Gas Electron Multiplier (GEM) chambers as readout chambers of the Time Projection Chamber (TPC): this replacement was motivated by the requirement to preserve the excellent particle identification capabilities of the TPC at significantly higher interaction rates, and to allow for a continuous read-out in p-p and Pb-Pb collisions. Finally, a new Online and Offline framework (O2) was developed to manage the increased data throughput of around 1TByte/s, along with new readout electronics.

The new ITS, called ITS2, has an improved spatial resolution thanks to its lower material budget. It consists of an inner and outer barrels, composed respectively of 3 and 4 layers, for a total surface of  $10 \text{ m}^2$  of silicon pixel sensors with a spatial resolution of  $5 \mu\text{m}$  [70]. The sensors equipping the ITS2 are called ALPIDE and are also used for the MFT; more details on them will be given in section 2.2.2.3. The ITS2 is visible in light green in the zoomed view of Figure 2.8, next to the MFT.

Like in Run 2, the standalone ITS tracks along with ITS and TPC/TOF matched tracks are used to determine the primary vertex of each collision.

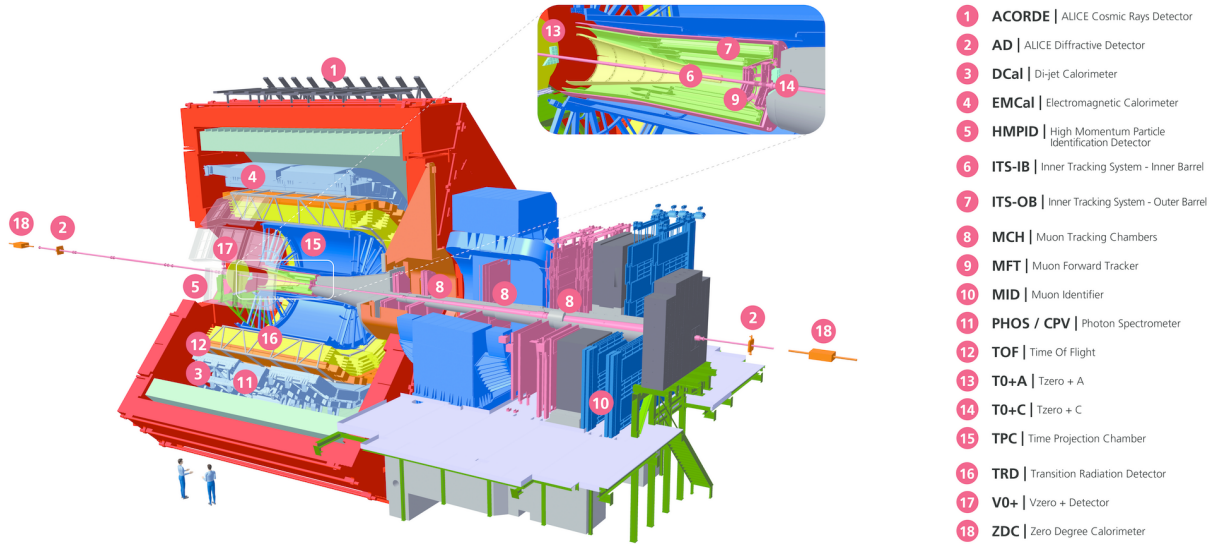


Figure 2.8: The ALICE detector in Run 3.

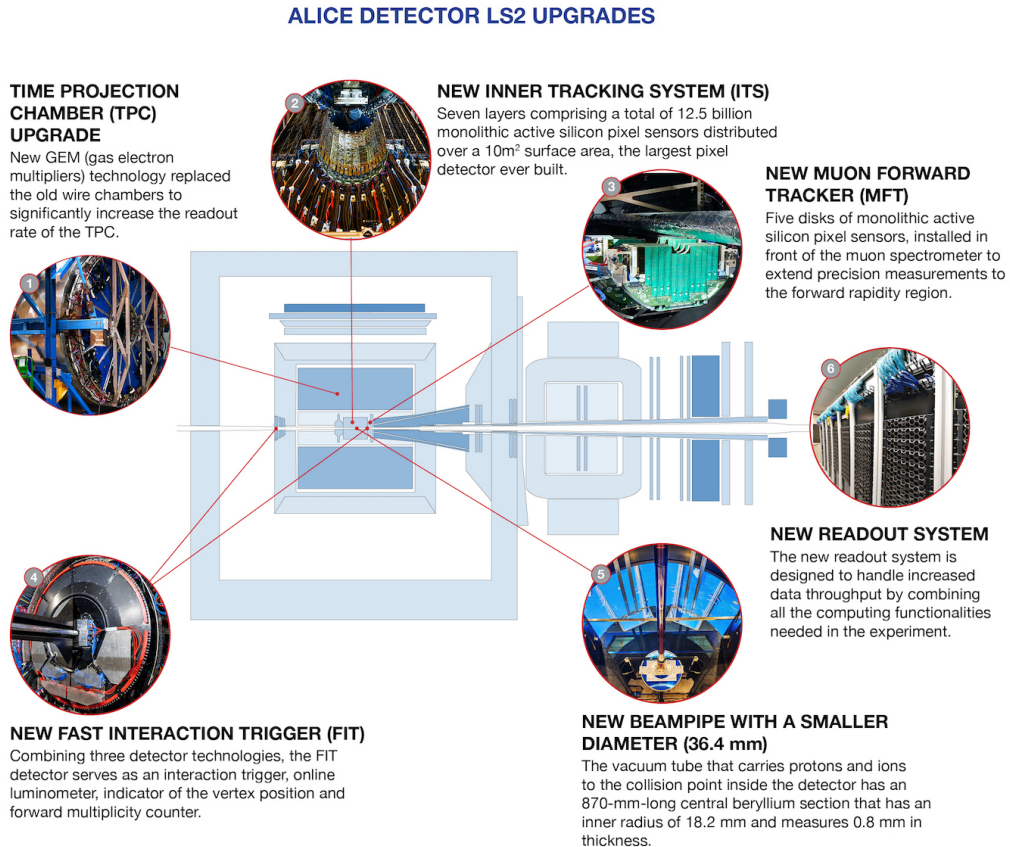


Figure 2.9: The different detector upgrades implemented during Long Shutdown 2 (LS2) [71].

These upgrades are summarized in Figure 2.9, their goal is to improve ALICE capabilities down to low- $p_T$  by reducing the material budget in the volumes crossed by the particles emerging from the interaction point, and to keep up with the increased interaction rate and data volume in Run 3 and 4. The upgrades that are the most relevant to this thesis will be described in more details in the following.

### 2.2.2.2 The Fast Interaction Trigger (FIT)

Since in Run 3 ALICE operates with continuous readout, a new fast system is needed to make online selection of events: the Fast Interaction Trigger (FIT). This system replaces the set of T0 V0, FMD, PMD and AD (the ALICE Diffractive detector) detectors used during Run 1 and 2 [72].

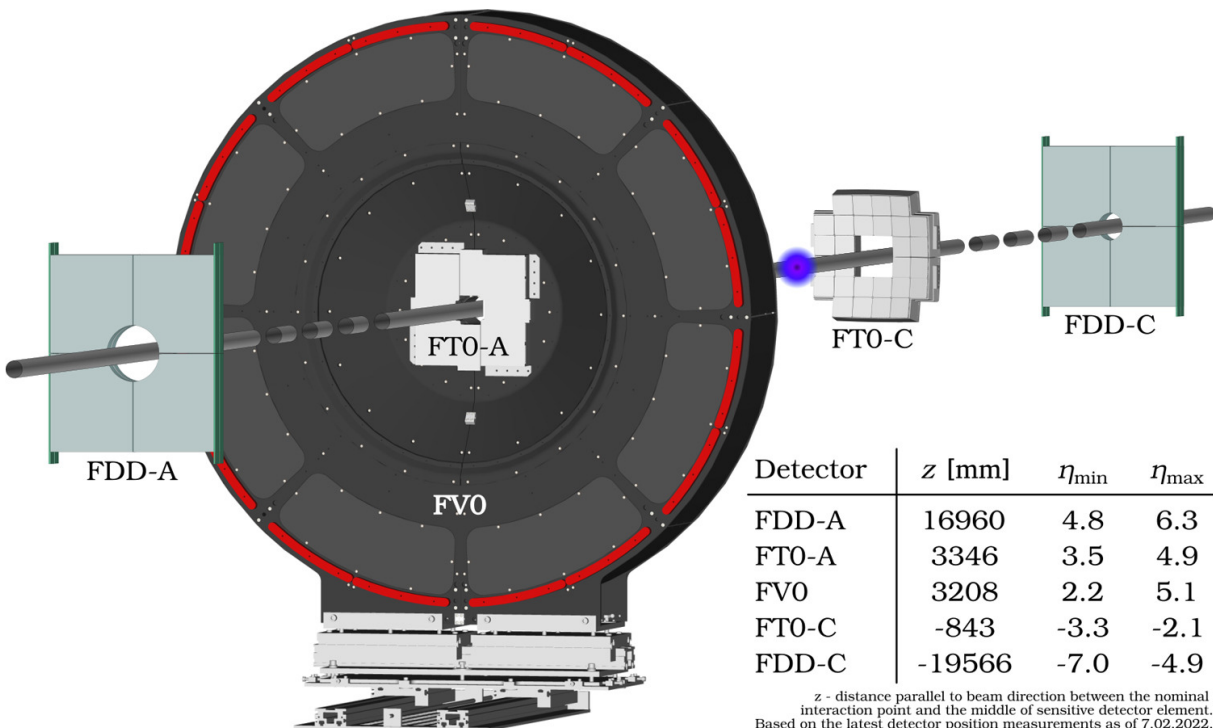


Figure 2.10: The FIT detectors [73].

The FIT consists of three detectors: the FV0, FT0 and FDD, all of which are represented in Figure 2.10. Both FT0 and FDD are made of two parts, one on the A-side (FT0-A and FDD-A), and one on the C-side (FT0-C and FDD-C) allowing for a wide pseudorapidity coverage in the forward and backward directions. The FV0 is made of plastic scintillators connected to photomultipliers and is used to determine centrality in Pb-Pb collisions. It is located where the previous V0-A detector was in Run 2. The V0-C, on the other hand, has been replaced by the FT0-C, located 84cm from the IP on the C-side and made of an array of Cherenkov modules divided in quadrants. The FT0-A has the same structure and is located 3.5m away from the IP on the A side. Each module of the FT0 detectors is made of 4 quartz radiators optically coupled to a photosensor. This technology leads to a very good intrinsic time resolution of 13 ps, making this detector the fastest one in ALICE.

The FT0 is used to generate minimum-bias triggers and to reject the beam-gas background by requiring signals in both FTO-A and FTO-C with timings compatible with beam-beam interaction close to the nominal IP. The FTO is also employed as a luminometer.

The Forward Diffractive Detector (FDD) detector is made of two arrays surrounding the beam pipe at +17 m and –19.5 m from the nominal IP. Each array consists of two layers of plastic scintillators connected to photomultipliers. The FDD contributes to diffractive cross section measurements and studies of ultra-peripheral Pb–Pb collisions.

### 2.2.2.3 The Muon Forward Tracker (MFT)

The MFT is a silicon pixel tracker installed as a part of the upgrade campaign of the ALICE detector during the LHC Long Shutdown 2.

#### Physics motivations

The MFT has been designed to allow for a clean identification of prompt/displaced muon sources, resulting in particular in the possibility of having charm/beauty separation in the heavy-flavor sector and background reduction in the light-flavor sector. Among the key measurements allowed by the MFT is the study of charmonium dissociation and regeneration mechanisms by measuring prompt  $J/\psi$  and  $\psi'$ , and the estimation of the degree of thermalization of heavy quarks via the measurement of the elliptic flow of charmonia and single muons from decays of heavy-flavor hadrons. The MFT also aims to investigate the medium density and the parton energy loss via the observation of beauty production yields using  $J/\psi$  from b-hadron decays for instance. Furthermore, the MFT extends the tracking of charged particles to the forward region, which was not possible in ALICE before its installation.

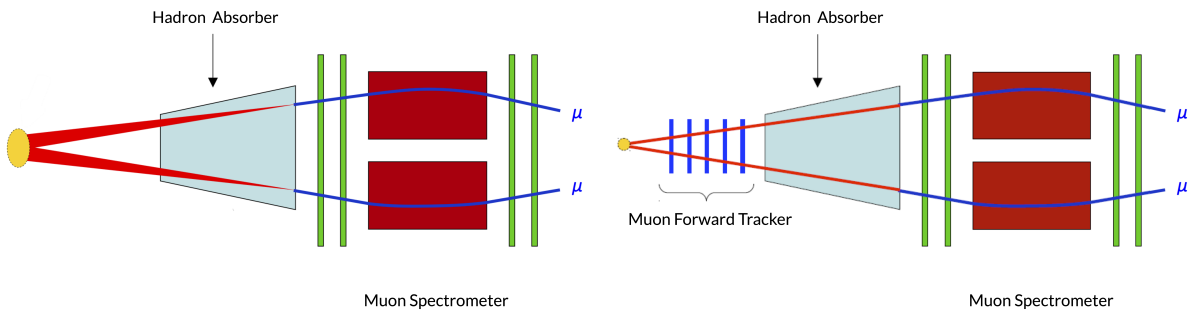


Figure 2.11: Muon tracks with (right) and without (left) the MFT matching.

To fulfill its physics goals, the MFT is required to separate prompt and non-prompt  $J/\psi$  and  $\psi'$ , which is not possible using the Muon Spectrometer (MS) alone: due to the large distance of the tracking stations from the primary vertex, and the multiple scattering induced on the muon tracks by the front absorber [74], the MS offset resolution is not sufficient to perform the separation. After matching the MS and the MFT information for the muon tracks (matching based on a  $\chi^2$  criterion or machine learning algorithms), the separation will be possible. The improvement in the spatial resolution provided by the MFT is sketched in figure 2.11.

The MFT has been installed in the ALICE cavern at the end of 2020 and is located between the ITS and the muon absorber. It is made of 2 half-cones (bottom-top), each cone containing five detection half-disks perpendicular to the beam axis, between  $z = -460$  mm and  $z = -768$  mm ( $z = 0$  representing the interaction point), each consisting of a front and a back detection plane called layers [75] and covering the pseudorapidity region  $-3.6 < \eta < -2.5$ . The half-disk and layer structure is illustrated in figure 2.12a. The MFT provides a pointing resolution down to few tens of  $\mu\text{m}$  for muons at forward rapidity, as well as secondary vertexing for muon pairs, by matching the tracks reconstructed in the Muon Spectrometer to those reconstructed in the MFT.

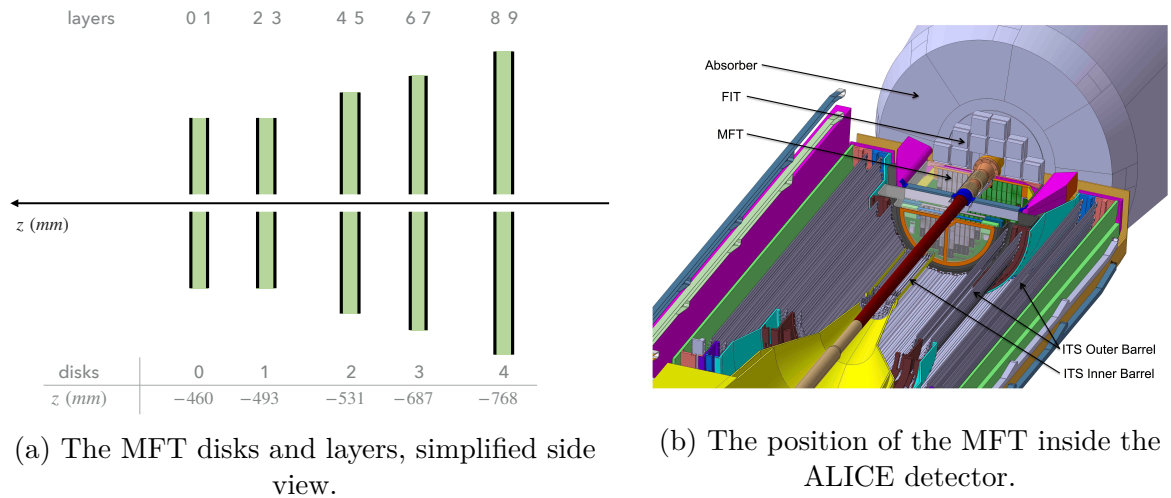


Figure 2.12: The MFT geometry and location.

The MFT exploits a silicon pixel chip called ALice PIxel DEtector (ALPIDE) for the detection of charged particles. These sensors are made of a Complementary Metal-Oxide Semiconductor (CMOS) using the Monolithic Active Pixel Sensor (MAPS) system technology that was specifically developed for the ALICE ITS2 and MFT [76]. The various ALPIDE chips are glued on flexible printed circuits to form ladders, which are then assembled onto the half-disks. A total of 936 ALPIDE chips equip the MFT, covering a total surface of around  $0.4 \text{ m}^2$ .

The CMOS technology has the particularity of integrating both sensor and read-out electronics in the same volume [70], reducing the material budget with respect to the hybrid silicon pixel technology. The specific ALPIDE chip is characterized by a space resolution of  $5 \mu\text{m}$  and a time resolution lower than  $5 \mu\text{s}$ . It is the first large-scale application of the CMOS technology in an LHC experiment.

The digital signals gathered by the ALPIDE chips are transmitted to Common Readout Units (CRUs), where they are regrouped, compressed and sent to First Level Processors (FLP) for further processing. The signals from adjacent pixels are combined into clusters, those provide information on the position of the crossing points between the particles trajectories and ALPIDE sensors. The clusters themselves are grouped into Read-Out Frames (ROF), which are time windows with a width corresponding to 198 BCs. The time separation between BCs being 25 ns, the MFT ROF is  $4.95 \mu\text{s}$  long.

## Tracking

The purpose of tracking algorithms is to “convert” the cluster information into track information, with the reconstructed tracks being the best possible approximation of the real trajectory of the particles crossing the detector. The MFT tracking algorithm can be separated into two steps: the track finding and the track fitting. For the track finding, two methods are used. The first one is called Linear Track Finder (LTF): as its name suggests, it looks for clusters aligned along a straight line, within a given radial tolerance  $R_{\text{cut}}$  (figure 2.13). Due to the forward position of the MFT and the direction of the magnetic field, the curvature induced on the MFT tracks by the ALICE solenoid magnet can be neglected at least at high- $p_T$ , hence supporting the choice of a LTF for such tracks.

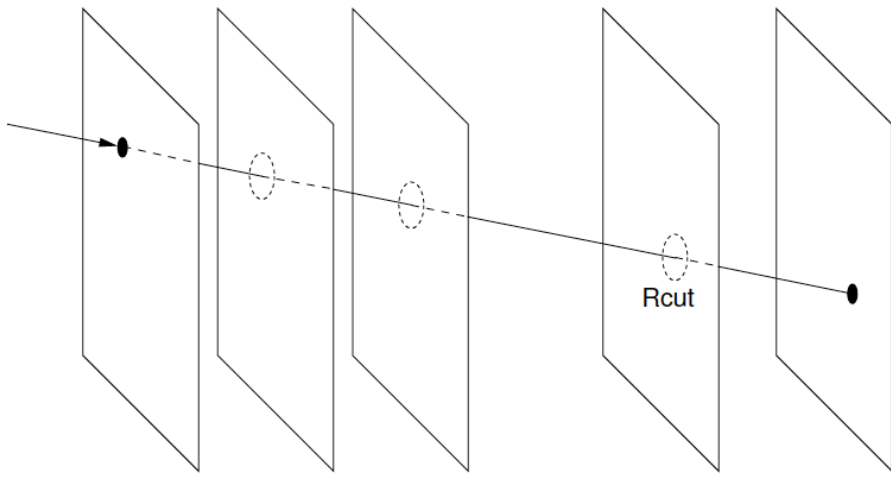


Figure 2.13: Linear Track Finder schematic using the  $R_{\text{cut}}$  parameter (maximum distance for a cluster to be attached to a straight line) [75].

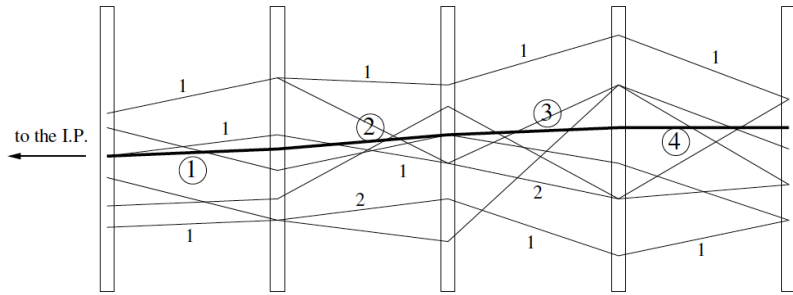


Figure 2.14: The Cellular Automaton method [75].

All clusters are considered by the LTF algorithm, and the ones that are attached to tracks are then removed from the list of available clusters considered in the further steps. At the end of the track finding with the LTF algorithm, the remaining clusters are then injected into the second track finding algorithm, based on a Cellular Automaton (CA) approach.

The Cellular Automaton is particularly suited for low-momentum tracks, sensitive to multiple scatterings, and is based on a propagation and joining of “segments”. A segment is a portion of line connecting two clusters from two consecutive disks of the MFT, and must point to the primary vertex within some angular cuts. The CA starts from one given segment having a cluster in the first MFT disk and adds further segments towards the last MFT disks imposing track continuity conditions, as depicted in figure 2.14. Such chains of segments are then considered as track candidates.

When the track candidates are found by the combination of the LTF and CA algorithms, a track fitting algorithm is applied in order to extract the kinematic parameters of each track. This procedure exploits a Kalman filter, an algorithm having a large number of applications, allowing for the estimation of the parameters of a dynamic system based on a set of measurements and their corresponding uncertainties. In the specific case of the MFT track fitting, the Kalman filter initializes the track parameters, predicts the track spatial and momentum coordinates considering material effects, updates the parameters based on measurements. The process is repeated for each track cluster, starting from clusters in the MFT layers farthest from the interaction point and propagating inward. The algorithm refines the estimates until the last cluster, the closest one to the interaction point, is reached.

### 2.2.3 The Central Trigger System

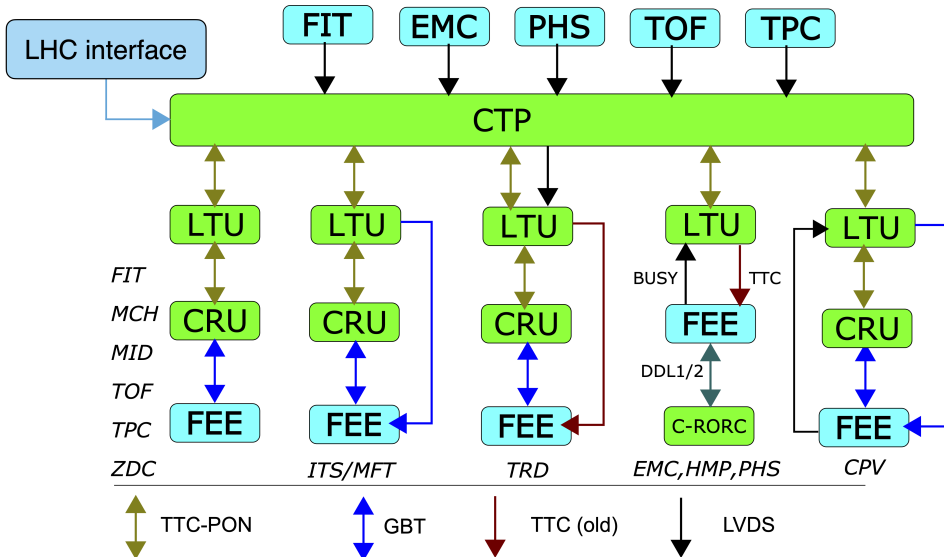


Figure 2.15: The Central Trigger System in Run 3, adapted from [77].

The Central Trigger System (CTS) in ALICE consists of the Central Trigger Processor (CTP) and the Local Trigger Unit (LTU) boards. Its main role is to centralize trigger signals from the trigger detectors and to distribute trigger and clock signals to the rest of the ALICE detectors. For each ALICE detector, an LTU board serves as communication interface between that specific detector and the CTP: the CTP distributes clock and triggers to the LTU and receives detector input, LHC clock and Bunch Filling scheme via the LHC interface.

In Run 1 and Run 2, trigger detector systems provided logic signals to the CTP indicating the presence of specific signal in this detector corresponding to a potentially interesting physics event (presence of muons of high- $p_T$ , coincidence of V0-A and C, high multiplicity, etc...) [78]. The CTP transmitted trigger signals with different latencies which were classified under four levels of trigger: LM (Level Minus, 650 ns of latency), L0 (Level 0, 900 ns of latency), L1 (Level One, 6.5  $\mu$ s), and L2 (Level 2, 88  $\mu$ s).

In Run 3 the readout is continuous, so trigger signals are not required for the data acquisition to start. However, the CTP is still very useful as it provides time-stamps to synchronize data from different detectors and continuous trigger signals to the detectors that do not implement an upgraded readout system [77].

The CTS in Run 3 is illustrated in Figure 2.15, where one can see the role of the Common Readout Units (CRU) developed for Run 3, which are interfaces between the detector Front End Electronics (FEE) and the LTUs. The technology of the links between the different CTS subsystems are also indicated, see for instance the GigaBit Transceiver (GBT) technology used for the ITS and MFT CRU to FEE transmission.

## 2.3 The Online-Offline Computing system $O^2$

In Run 3, all the data are stored to disk, contrarily to Run 2 where only triggered data (with specific triggers for different types of events) were stored. This causes a drastic increase of the data volume, prompting the ALICE collaboration to redesign its computing system. In this context  $O^2$  was created, the software framework for Run 3 and Run 4 of ALICE, developed in collaboration with the FAIR Software Group at GSI (Center for heavy ion research in Germany).  $O^2$  stands for Online Offline computing system, as it integrates both the data readout and its subsequent processing. It combines different required functionalities such as detector read-out, event building, data recording, detector calibration, data reconstruction, physics simulation and analysis [79]. The analysis part is separated in a sub-framework called O2Physics, which uniquely deals with the processing of Analysis Object Data called AO2D in Run 3. The process is schematically represented in Figure 2.16: it is worth noting that O2Physics is a part of  $O^2$ , but for clarity they have been separated on the figure.

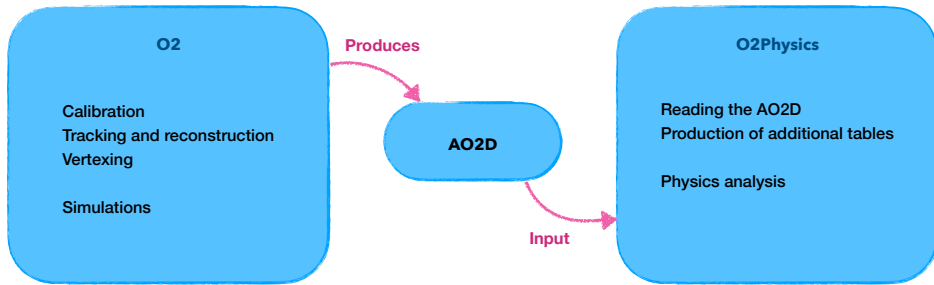


Figure 2.16: The different roles of  $O^2$  and O2Physics.

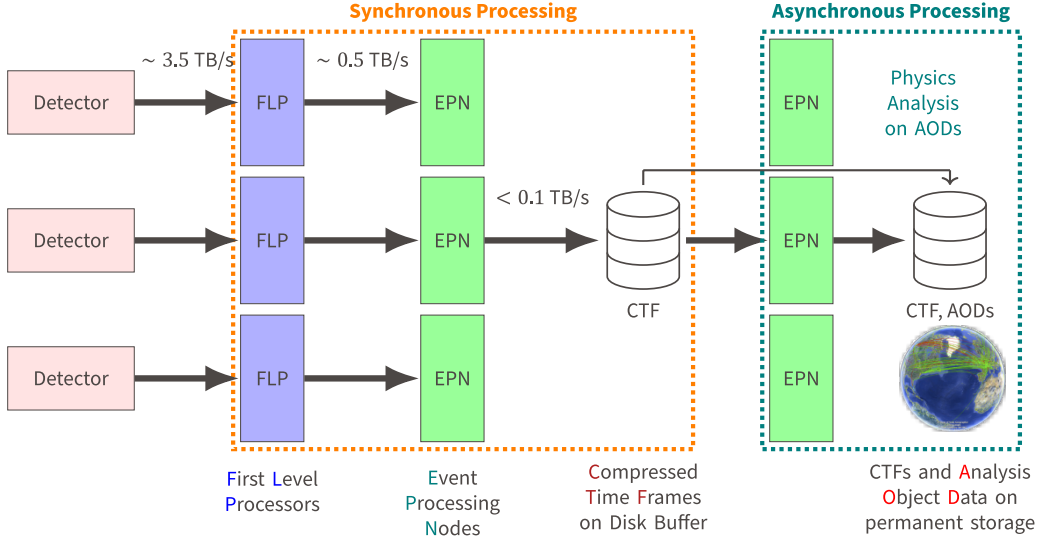


Figure 2.17: The synchronous and asynchronous part of the data flow in ALICE  $O^2$  [80].

The  $O^2$  framework is structured into three layers [81]:

1. The transport layer which features data transportation using FairMQ messages;
2. The Data Model Layer which defines message descriptions in a language-agnostic manner, accommodating various data formats (ROOT objects for instance);
3. The Data Processing Layer (DPL) which acts as a translator, converting user codes into a panel of message-exchanging FairMQ devices (actors which communicate through message exchange) [82].

Each step of the data treatment in  $O^2$  (reconstruction, calibration, simulation) is based on this processing model and takes place in different computing infrastructures : the computing farm of ALICE called  $O^2$  farm and the worldwide LHC-Grid infrastructure. The  $O^2$  package can also be installed as a framework by ALICE users to run small-scale local reconstructions.

The  $O^2$  farm is composed of two types of computational devices: the First Level Processors (FLPs) and the Event Processing Nodes (EPNs), both equipped with the  $O^2$  framework. The tasks performed by these various computers are assigned hierarchically, since the raw data are processed by the FLPs first, and then by the EPNs. As an example, for the MFT, the signal compression and readout quality control take place in FLPs, whereas the clusterization and the MFT tracking are done on EPNs.

The  $O^2$  data processing can be separated into two steps: synchronous (happening in real-time during data taking) and asynchronous (happening at a later stage). Both processes of  $O^2$  are depicted in figure 2.17.

In the synchronous part of the framework, raw data arrive from the detector and are first compressed by Common Readout Units (CRUs) inside the First level Processors (FLPs). The CRU acts as the interface between the front-end electronics and  $O^2$ , allowing for a two-way communication [83]. The data are divided into Sub-Time Frames (STFs). These STFs are then transferred to the EPNs where they are merged into complete Time Frames (long

of roughly 10 ms each) and further compressed (via clustering and tracking for instance) and calibrated. The overall compression factor is more than 30. The Compressed Time Frames (CTFs) are stored into a disk buffer.

These CTFs are then asynchronously processed: in this phase, data reconstruction and final calibrations are performed using the information from the Condition and Calibration Data Base (CCDB), both on EPNs and on the Worldwide LHC Computing Grid. The output is then permanently stored in the AOD format, and the analysis can subsequently be performed.

### 2.3.1 The $O^2$ analysis framework

The analysis framework of ALICE in Run 3 ( $O^2$ Physics) processes data in the AOD format (AODs are in practice interconnected tables in ROOT trees [84]), using C++ codes with additional classes and methods defined inside the  $O^2$  framework.

The AODs are processed by specific analysis codes called tasks, performing table filtering, concatenation, histogram filling etc, and which output can be subsequently used to derive physics results. These tasks are translated by the Data Processing Layer (DPL) to an ensemble of FairMQ devices such as readers and mergers [82]. This process is summarized in Figure 2.18.

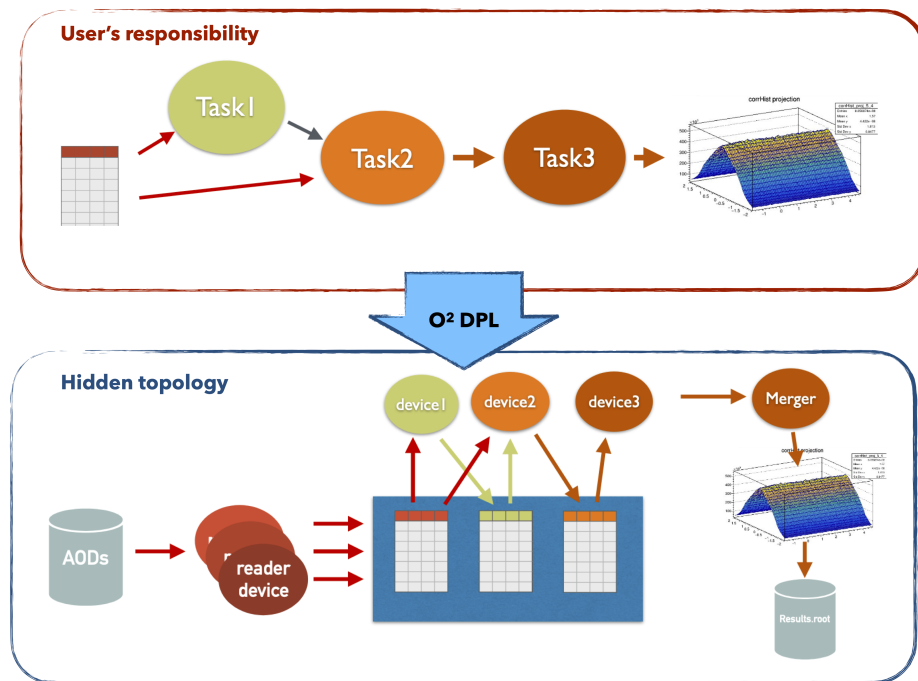


Figure 2.18: The role of the Data Processing Layer (DPL) in the analysis framework of ALICE [81].

$O^2$  being a completely new software framework, data calibration and further software developments are crucial to ensure the data quality and readiness, and the smooth transition to Run 3 physics results in ALICE.



# Chapter 3

## Forward $J/\psi$ relative yield versus relative forward multiplicity in pp collisions at $\sqrt{s} = 13$ TeV

This Chapter describes the analysis performed to study the relative  $J/\psi$  yield, measured using the Muon Spectrometer in the forward direction, as a function of the relative multiplicity also at forward rapidity, estimated with the V0C detector. The analysis is based on data from proton-proton collisions taken by the ALICE experiment from 2016 to 2018. The results are compared to theoretical models and their interpretation is discussed.

### 3.1 Introduction

The ALICE collaboration has studied  $J/\psi$  production as a function of charged-particle multiplicity at midrapidity in proton-proton collisions, both at midrapidity, in the  $J/\psi \rightarrow e^+e^-$  [48] decay channel, and at forward rapidity ( $-4 < y < -2.5$ ) in the  $J/\psi \rightarrow \mu^+\mu^-$  channel [49]. While in both cases the  $J/\psi$  production has been found to increase with multiplicity, the trends are rather different — steeper than linear at midrapidity and close to linear at forward rapidity.

It is known that the results of multiplicity dependence measurements for particle production in proton-proton collisions are in general dependent on the choice of the rapidity ranges of the involved particles: in our case the  $J/\psi$  (the signal), the charged particles used to obtain the event multiplicity, and the charged particles whose number is used to define the multiplicity classes. In the cases where the rapidity range considered for the signal or for the multiplicity measurement overlaps with the one of the multiplicity class selection, there can be significant auto-correlation effects leading to biases in the measured multiplicity dependence. So far, the measurements at midrapidity and forward rapidity have only been performed as a function of the midrapidity multiplicity, and thus the observed differences can also originate from auto-correlation effects. In order to investigate this point and shed more light on the production mechanisms of  $J/\psi$ , measurements as a function of multiplicity at forward rapidity are also needed.

In this Chapter, the measurement of relative  $J/\psi$  yield measured at forward rapidity ( $-4 < y < -2.5$ ) in the muon spectrometer via the  $J/\psi \rightarrow \mu^+\mu^-$  decay channel, as a

function of the relative multiplicity in the V0-C detector in proton-proton collisions at  $\sqrt{s} = 13$  TeV, is reported.

## 3.2 Detectors used in the analysis

The main ALICE detectors used in this analysis are the following (their description can be found in Chapter 2):

- The Muon Spectrometer, for muon triggering and tracking, allowing the extraction of the  $\mathbf{J}/\psi$  signal;
- The V0 for the definition of the Minimum Bias trigger condition, the V0-C for multiplicity class selection and charged-particle multiplicity determination;
- The Silicon Pixel Detector (SPD) for the determination of the primary vertex position of events and for event selection.

## 3.3 Analysis

The relative forward  $\mathbf{J}/\psi$  yield as a function of the forward relative multiplicity is measured using the procedure described in this section<sup>1</sup>.

### 3.3.1 Analysis strategy

The multiplicity classes considered in the analysis are determined in Minimum Bias (MB) events using the V0C signal distribution. These classes corresponds to intervals in the distribution of the V0C signal, from low signal corresponding to low multiplicity events to high signal corresponding to high multiplicity events. The number of events in the  $i$ -th class is noted as  $n_{\text{ev}}(i)$ , and the total number of Minimum Bias events (integrated in multiplicity) is noted as  $N_{\text{ev}}$ .

In dimuon events (triggered using the Muon Spectrometer)  $\mu^+$  and  $\mu^-$  tracks are reconstructed and their invariant mass is computed. The dimuon invariant mass spectrum is then built in each chosen V0C interval. By fitting these spectra the number of  $\mathbf{J}/\psi$  in each V0C interval, noted as  $n^{\mathbf{J}/\psi}(i)$ , is obtained. By fitting the dimuon invariant mass in the whole sample of dimuon events, the total number of  $\mathbf{J}/\psi$   $N^{\mathbf{J}/\psi}$  can also be computed. The relative  $\mathbf{J}/\psi$  yield (also called self-normalized  $\mathbf{J}/\psi$  yield) in the multiplicity class  $i$  is then given by:

$$\frac{dN_{\mathbf{J}/\psi}/dy(i)}{\langle dN_{\mathbf{J}/\psi}/dy \rangle} = \frac{n^{\mathbf{J}/\psi}(i)}{n_{\text{ev}}(i)} \times \frac{N_{\text{ev}}}{N^{\mathbf{J}/\psi}}. \quad (3.1)$$

Since the V0C signal is not a physical observable itself, it is converted into a number of primary charged particles (following the ALICE definition of primary particles [85]) using MC simulation. The average number of primary charged particle per event is then obtained in each V0C interval (multiplicity class) and in the whole MB sample. In the

---

<sup>1</sup> In this section, the procedure is only outlined, while the full procedure is broken down into steps and detailed in the following sections

following, these quantities will be denoted as  $dN_{\text{ch}}/d\eta(i)$  and  $\langle dN_{\text{ch}}/d\eta \rangle$  respectively. The relative multiplicity (also called self-normalized multiplicity) in the multiplicity class  $i$  is given by:

$$\frac{dN_{\text{ch}}/d\eta(i)}{\langle dN_{\text{ch}}/d\eta \rangle} = \frac{n_{\text{ch}}(i)}{n_{\text{ev}}(i)} \times \frac{N_{\text{ev}}}{N_{\text{ch}}}, \quad (3.2)$$

with  $n_{\text{ch}}(i)$  being the number of charged particles in the events of multiplicity class  $i$  and  $N_{\text{ch}}$  the total number of charged particles in all Minimum Bias events.

### 3.3.2 Data sample

The analysis is based on data sample of proton-proton collisions at  $\sqrt{s} = 13$  TeV taken from 2016 to 2018 during the LHC Run 2. Employing the event selection mentioned in section 3.3.4, 1.167 billion selected Minimum Bias events are used.

### 3.3.3 MC samples

Three different MC samples are used. They are produced with different generators and will be referred in the text by their period tag, LHCxx:

- LHC17d18, a MC simulation using the PYTHIA8 generator tuned on 2016 run conditions;
- LHC16d3, a MC simulation using the EPOS-LHC generator;
- LHC20a4, a charmonia-enriched MC simulation used to evaluate the  $J/\psi$  acceptance and fit parameters, tuned on 2018 run conditions.

### 3.3.4 Event selection

Both  $J/\psi$  yield and  $dN_{\text{ch}}/d\eta$  are measured for  $\text{INEL} > 0$  events, which are defined as inelastic collisions having at least one charged particle within  $|\eta| < 1$ . The same selections are applied in data and MC simulations.

Commonly used Physics Selections (PS) were applied to the collisions. They include:

- Beam-induced background rejection by requiring the coincidence of V0 signals on A and C sides;
- Rejection of events too close in time to be distinguished from one another (pile-up rejection);
- Selection of collisions with primary vertex with longitudinal  $z_{\text{vtx}}$  coordinate in the range  $|z_{\text{vtx}}| < 10$  cm.

Moreover, the selected events are required to pass vertex quality assurance cuts (noted vtxQA in the following):

- Presence of a reconstructed Silicon Pixel Detector (SPD) vertex;
- Resolution on the SPD  $z$  vertex position smaller than 0.25 cm.

In addition to the pileup cuts applied within the Physics Selection, a cut depending on the number of SPD tracks is applied as follows:

- The events with a reconstructed number of SPD tracks smaller than 40 must have at least 3 SPD tracks contributing to the vertex;
- The events with a reconstructed number of SPD tracks larger than 40 must have at least 5 SPD tracks contributing to the vertex.

This additional selection has been used by default in many multiplicity dependent analyses [86] and is used in this analysis for consistency.

### 3.3.5 Event triggers

Three different triggers were used in this analysis. The first one is a Minimum Bias (MB) trigger based on the coincidence of signals in the A and C side of the V0 detector. The second and the third ones are muon triggers: a single-muon trigger selecting single muons with a  $p_T > 1$  GeV/ $c$ , and a dimuon trigger selecting events with two muons of opposite charge both having a transverse momentum  $p_T > 1$  GeV/ $c$ . Each trigger is used for different purposes. The MB event sample is used to derive the  $N_{V0C}$  distributions, the  $\langle N_{V0C} \rangle_{\text{run}}$  used for the renormalization of the V0C signal (see section 3.4.2.1), and the  $N_{V0C}$  multiplicity intervals. The single-muon event sample allows us to compute the correction to the V0C signal removing the muons coming from the  $\mathbf{J}/\psi$ , as explained in more details in section 3.4.2.2. Finally, the dimuon trigger is used to reconstruct the  $\mathbf{J}/\psi$  through their dimuon decay channel.

### 3.3.6 Track selection

Commonly used quality cuts are applied to the reconstructed muon tracks. First, the tracks are required to be in the pseudorapidity acceptance of the MS  $-4 < \eta^\mu < -2.5$ . Then, each track reconstructed in the muon tracking chambers of the MS is required to match a corresponding track segment in the muon trigger stations. Finally, muon tracks crossing the thickest sections of the absorber are rejected by requiring their radial distance from the  $z$  axis at the exit of the absorber ( $R_{\text{abs}}$ ) to be between 17.6 and 89.5 cm.

### 3.3.7 Dimuon Cuts

The dimuon pairs retained as  $\mathbf{J}/\psi$  candidates are required to pass the following selection criteria: the two muons have to be of opposite signs, the rapidity of the muon pair must be in the range  $-4.0 < y_{\mu\mu} < -2.5$ , and the invariant mass of the must be within the interval  $2 < M_{\mu\mu}^{\text{inv}} < 5$  GeV/ $c^2$ .

## 3.4 Multiplicity measurement

In the following, the event-by-event V0C signal will be called V0C multiplicity, and will be noted  $N_{V0C}$ . The multiplicity intervals and the mean relative V0C multiplicity in any

given interval  $i$ ,  $\frac{N_{\text{V0C}}(i)}{\langle N_{\text{V0C}} \rangle}$ , are estimated using MB events. The employed procedure is described in more details in the following sections.

### 3.4.1 V0C Multiplicity intervals

The V0C multiplicity intervals are determined based on the following percentile ranges (from low to high multiplicities): 100-70%, 70-50%, 50-40%, 40-30%, 30-20%, 20-15%, 15-10%, 10-5%, 5-1%, 1-0.5%, 0.5-0.25%, 0.25-0%.

In each event, the corresponding multiplicity percentile is computed from the total V0C signal, after the correction for the  $z_{\text{vtx}}$  dependence of the signal, and the anti-aging correction compensating the decrease of the average V0C signal over time. More details on these corrections are available in 3.4.2. After the corrections are applied, each data run has the same average V0C signal with no dependence as a function of  $z_{\text{vtx}}$ .

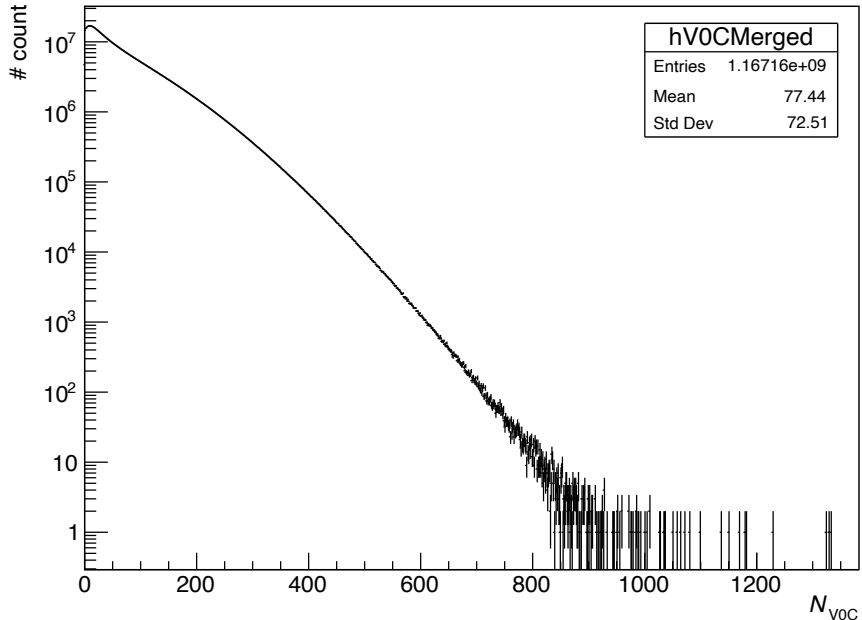


Figure 3.1:  $N_{\text{V0C}}$  distribution in MB events.

After these corrections are applied, the V0C distributions from all data periods considered in the analysis can be merged. It is then the merged V0C distribution, reported in Figure 3.1, that is used to determine the different multiplicity intervals. The ratios of the corresponding distributions for each period, over the merged distribution, are shown in Figure 3.2. It is worth noting that the distributions corresponding to the single periods show no significant deviation from the merged distribution beyond the expected statistical fluctuations.

The resulting V0C intervals are given in Table 3.1, together with the corresponding percentile ranges and the number of selected MB events (also called kINT7 events by the name of their tag in the ALICE software framework) in each range.

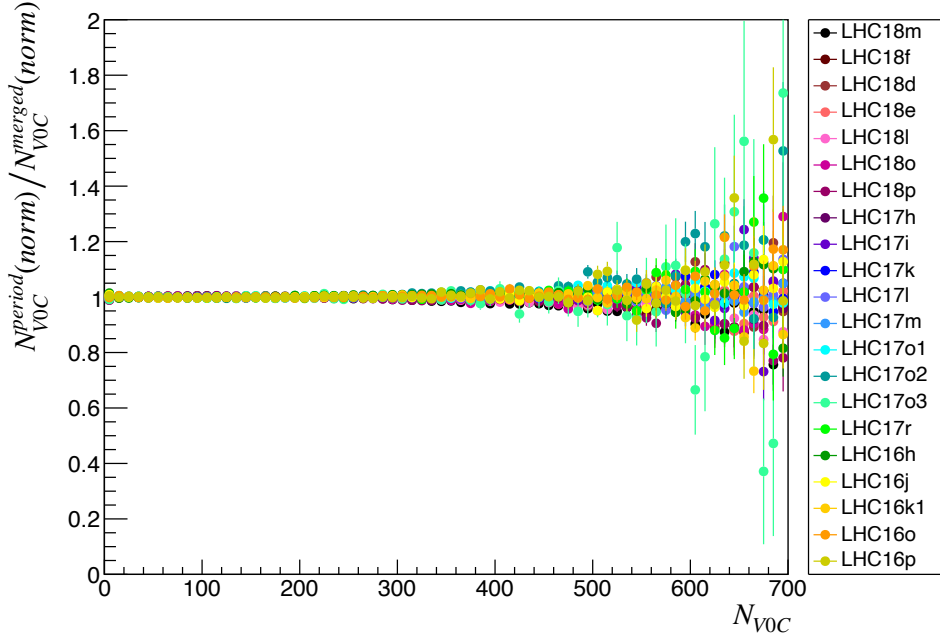


Figure 3.2: Ratio of V0C distributions per period over merged V0C distribution. The distributions are normalized by their integrals.

Interval number $i$	$N_{V0C}$ range	$N_{V0C}(i)/\langle N_{V0C} \rangle$	Percentile range, %	$n_{\text{ev}}^{\text{selkINT7}}$
1	[0.0,28.7]	0.187	100-70	$3.51 \times 10^8$
2	[28.7,54.7]	0.527	70-50	$2.33 \times 10^8$
3	[54.7,72.6]	0.817	50-40	$1.17 \times 10^8$
4	[72.6,95.5]	1.079	40-30	$1.16 \times 10^8$
5	[95.5,127.1]	1.425	30-20	$1.17 \times 10^8$
6	[127.1,148.8]	1.776	20-15	$5.9 \times 10^7$
7	[148.8,178.1]	2.099	15-10	$5.8 \times 10^7$
8	[178.1,225.3]	2.573	10-5	$5.8 \times 10^7$
9	[225.3,324.5]	3.397	5-1	$4.7 \times 10^7$
10	[324.5,364.4]	4.419	1-0.5	$5.8 \times 10^6$
11	[364.4,403.9]	4.931	0.5-0.25	$2.9 \times 10^6$
12	[403.9,697.0]	5.856	0.25-0.02	$2.7 \times 10^6$

Table 3.1: Multiplicity intervals obtained from the V0C signal  $N_{V0C}$  distribution.

### 3.4.2 Corrections applied to the V0C signal

#### 3.4.2.1 Signal renormalization and $z_{\text{vtx}}$ correction

In the data, a run-by-run variation of the mean V0C signal is observed, due to the aging of the detector [48] [86]. Such aging effects are often observed in case of scintillator-based detectors and are usually due to the aging of the scintillator material after prolonged irradiation with ionizing particles. In the case of the V0 detector, however, the aging is mainly due to the degradation of the photo-multiplier response with the increase of the accumulated charge during the data taking [87]. It is worth noting that the aging of the V0 detector is not taken into account in the MC simulations, and therefore needs to be corrected in the data. The correction of the run-by-run variation of the mean V0C signal is computed with respect to a reference value  $\langle N_{\text{V0C}} \rangle_{\text{ref}}$ , corresponding to the mean  $N_{\text{V0C}}$  signal in a reference data-taking period of 2018<sup>2</sup>. The  $N_{\text{V0C}}$  signal in any given run is thus renormalized in the following way:

$$N_{\text{V0C}}^{\text{renorm}} = \frac{\langle N_{\text{V0C}} \rangle_{\text{ref}}}{\langle N_{\text{V0C}} \rangle_{\text{run}}} \times N_{\text{V0C}},$$

with  $\langle N_{\text{V0C}} \rangle_{\text{run}}$  being the mean  $N_{\text{V0C}}$  multiplicity in a specific run. This correction effectively ensures that all runs and all periods have the same average V0C signal  $\langle N_{\text{V0C}} \rangle = \langle N_{\text{V0C}} \rangle_{\text{ref}} = 77.5$ . The precision with which the correction is implemented is of 0.2%, which is neglected.

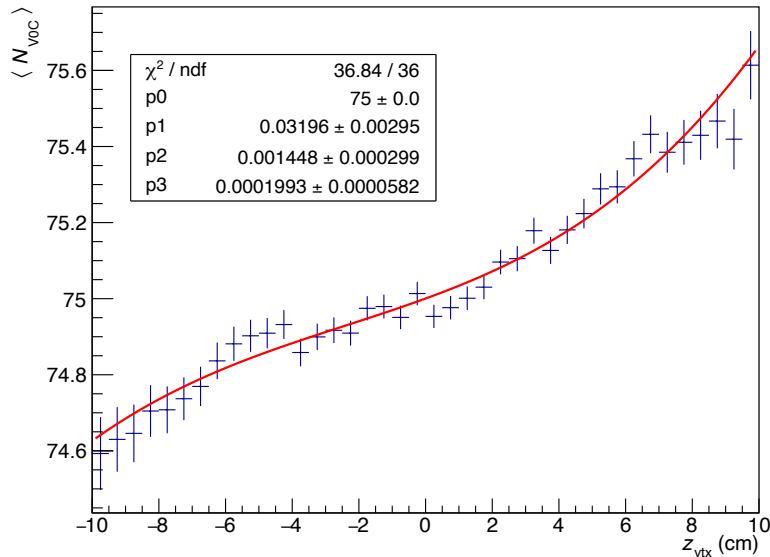


Figure 3.3: Average  $N_{\text{V0C}}$  versus  $z_{\text{vtx}}$  before the corrections for the residual  $z_{\text{vtx}}$  dependence in period LHC18m. The red curve represents the fit used to obtain the correction function described in the text.

The V0C signal in a given event also has a dependence on the  $z_{\text{vtx}}$  of the corresponding primary vertex, and the ALICE analysis frameworks contains a default correction for this

<sup>2</sup> The reference period corresponds to the beginning of 2018 data-taking campaign, just after the initial calibration of the V0 detector and before the appearance of any sizable aging effects.

dependence. Nevertheless, some residual  $z_{\text{vtx}}$  dependence remains, which is corrected for by applying a correction function extracted from a fit of the  $z_{\text{vtx}}$  profile of  $N_{\text{V0C}}$  in each period. In Figure 3.3, one can see an example of such a profile. The correction function is defined as  $f_{\text{corr}}^{\text{zvtx}}(z) = 1 + Az + Bz^2 + Cz^3$ , and the corrected  $N_{\text{V0C}}^{\text{final}}$  for an event having the primary vertex with longitudinal coordinate  $z$  is obtained as:

$$N_{\text{V0C}}^{\text{final}} = \frac{N_{\text{V0C}}^{\text{renorm}}}{f_{\text{corr}}^{\text{zvtx}}(z)},$$

where  $N_{\text{V0C}}^{\text{renorm}}$  is the run-by-run renormalized  $N_{\text{V0C}}$  signal as explained above.

### 3.4.2.2 Dimuon correction

The  $\mathbf{J}/\psi$  is measured in the dimuon channel using the muon spectrometer, which has a large acceptance overlap in pseudorapidity with the V0C. Consequently, the two muons coming from the  $\mathbf{J}/\psi$  decay can produce a signal in the V0C, leading to an increase in the multiplicity of the event measured by the V0C. In order to avoid this auto-correlation effect and associate the event in which the  $\mathbf{J}/\psi$  is measured to the correct multiplicity interval, the signal left by the two muons in the V0C should be subtracted. We call this correction the dimuon correction.

As explained in Chapter 2, section 2.2.1.1, the V0C is divided into 4 rings and 8 sectors corresponding to 32 channels which are numbered from 0 to 31. The outermost ring of the V0C (composed of the channels identified by numbers between 24 to 31) falls outside the Muon Spectrometer (MS) acceptance.

Every year at the start of the data taking in Run 1 and Run 2, the V0 detector was calibrated to ensure that each detector channel had the same predefined response to a minimum-ionizing particle (MIP). However, due to the limited precision of the calibration procedure, some residual channel-by-channel differences persisted: the dimuon correction must then be tuned channel by channel. The procedure to estimate the correction is described in the following.

First of all, 32  $(\eta, \varphi)$  histograms (one per V0C channel) are defined, with a  $4 \times 8$  binning corresponding to the  $4 \times 8$  channels of the V0C detector. Then, in single-muon events, the histogram corresponding to the V0C channel crossed by the muon track reconstructed in the event is updated, filling each bin with the signal of the V0C channel corresponding to that bin. After normalization to the total number of events, the average signal in a given channel  $j$  for events where the muon crossed the channel  $i$  will be  $\langle s_i[j] \rangle$ . An example of such a histogram can be seen in Figure 3.4, where one can see for instance that the V0C channel 3 ( $\frac{3\pi}{4} \leq \varphi \leq \pi$ ,  $-3.7 \leq \eta \leq -3.2$ , the bin framed in red) has an average signal  $\langle s_{16}[3] \rangle = 5.1$  in single-muon events where the muon hits the V0C channel 16.

The largest values for the  $\langle s_i[j] \rangle$  quantities are expected when  $i = j$ , due to the signal of the muon tracks.

In single-muon events, the average signal in any given channel hit by the muon is a sum of the muon signal and the signal from charged particles from the underlying event. A simple procedure can then be defined in order to estimate the impact of the specific signal of the muons for each V0C channel, in order to be able to subtract it in the rest of the analysis. In the following we want to determine the excess signal due to one muon in channel  $i$ . To this end, let us consider the 2D histogram corresponding to single-muon events in which the muon hits channel  $i$ : in this histogram, the average signal in channel  $i$  is  $\langle s_i[i] \rangle$ . Let us

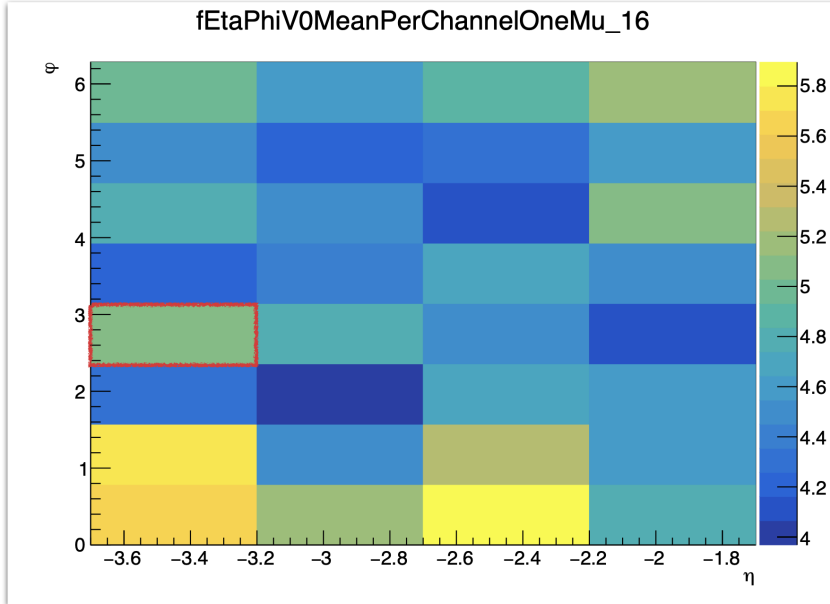


Figure 3.4: Average signal in the V0C channels in events where a single muon has hit channel 16. The bin framed in red corresponds to the V0C channel 3.

also consider the 2D histograms corresponding to single-muon events in which the muon hits the channels  $j$  and the channel  $k$  which are located in the same ring as channel  $i$ , but at  $\varphi_i \pm \frac{\pi}{2}$  in the azimuthal direction (see Figure 3.5). In these two histograms, one can obtain  $\langle s_j[i] \rangle$ , the average V0C signal in channel  $i$  in single-muon events in which the muon hits the channels  $j$ , and  $\langle s_k[i] \rangle$ , the average V0C signal in channel  $i$  in single-muon events in which the muon hits the channels  $k$ . One can assume that the average of both these values give us a reliable estimate of the signal from charged particles from the underlying event in channel  $i$ . We can then use the difference between the quantities

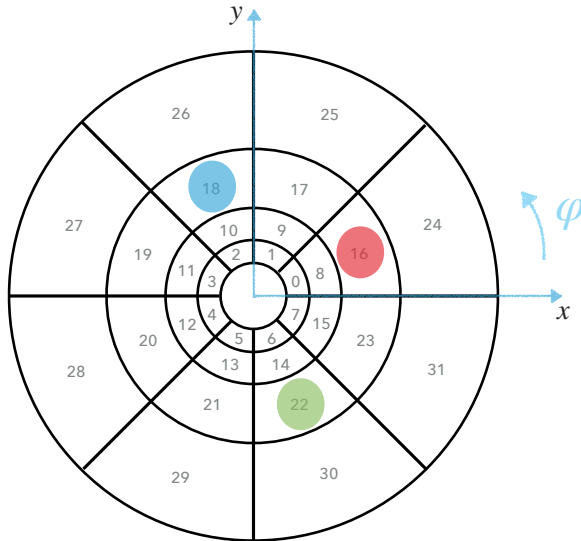


Figure 3.5: Channels  $k = 18$  and  $j = 22$  are located in the same ring as channel  $i = 16$ , but at  $\varphi \pm \frac{\pi}{2}$  in the azimuthal direction.

$\langle s_i[i] \rangle$ ,  $\langle s_j[i] \rangle$  and  $\langle s_k[i] \rangle$  to estimate the excess signal due to the presence of a muon in channel  $i$ ,  $e[i]$ :

$$e[i] = \langle s_i[i] \rangle - \frac{\langle s_j[i] \rangle + \langle s_k[i] \rangle}{2}$$

When studying the underlying event signal in a given channel, channels located in the same ring and at  $\pm \frac{\pi}{2}$  in azimuth provide the less biased reference:

- channels in other rings would need pseudorapidity dependence effects to be taken into account. Indeed the multiplicity of the underlying event can depend on the pseudorapidity of the muon present in the event;
- channels in the same ring but adjacent to the channel  $i$  or located at a distance  $\sim \pi$  in azimuth would introduce a bias related to possible short-range correlations originating from jets or particle decays.

The  $e[i]$  quantities are estimated period by period, and are then used in dimuon events to correct the V0C signal in the channels hit by a muon. To determine which channel has been hit the kinematic variables  $\eta^\mu, \varphi^\mu$  of each muon are simply being translated into a V0 channel position. The trajectory of the muon is extrapolated as a straight line toward the V0C plane. If channel  $i$  is hit by a muon in a dimuon event, the corrected signal in channel  $i$  is then simply taken to be

$$s_{corr}[i] = s[i] - e[i],$$

with  $s[i]$  being the signal in channel  $i$  in the dimuon event and  $e[i]$  the excess previously derived. If both muons hit the V0C (one in channel  $i_1$ , the other in channel  $i_2$ ), the total V0C multiplicity with dimuon correction is taken to be:

$$N_{V0C}^{\text{corr},\mu\mu} = N_{V0C} - e[i_1] - e[i_2]$$

The  $N_{V0C}^{\text{corr},\mu\mu}$  obtained in this way is then corrected for the  $z_{\text{vtx}}$  dependency and aging following the different procedures described in section 3.4.2.

### 3.4.3 Conversion from $N_{V0C}$ to $N_{\text{ch}}$

In order to obtain results that can be discussed independently of the ALICE detector, the  $N_{V0C}$  signal must be transformed into a number of primary charged particles in  $-3.7 < \eta < -1.7$ , noted  $N_{\text{ch}}$ .

To do so, one needs to ensure that the V0C detector response is sufficiently well simulated in MC. To this end, the distributions of the  $N_{V0C}$  signal in data and PYTHIA8 MC simulation are compared in Figure 3.6. The comparison shows an excellent agreement within  $\pm 10\%$  between data and MC. The largest discrepancies are observed at low event multiplicity. Similar discrepancies were already observed with the central barrel at midrapidity [88] and therefore are most likely due to the limited precision in the modeling of low-multiplicity collisions in PYTHIA, rather than to the limited quality of the detector simulation, in particular the V0C response.

The correlation between  $N_{V0C}$  and  $N_{\text{ch}}$  is studied with MC simulations using both PYTHIA and EPOS-LHC event generators, and is shown in Figure 3.7.

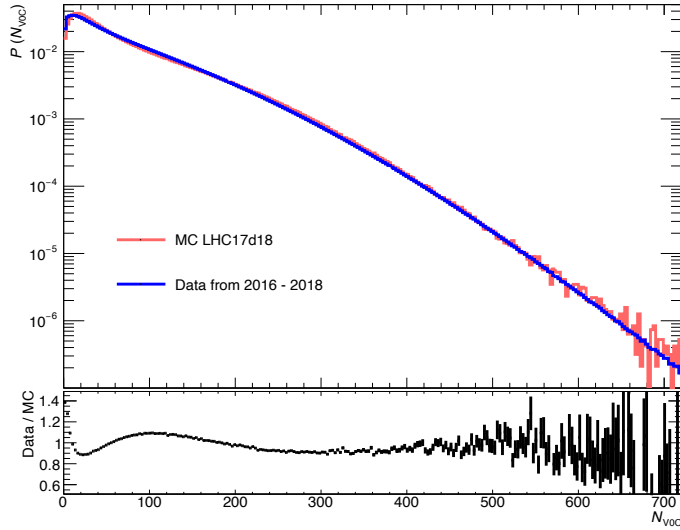


Figure 3.6:  $N_{\text{VOC}}$  distributions in LHC17d18 MC (PYTHIA8 event generator) and in data (top), and ratio of data over MC (bottom).

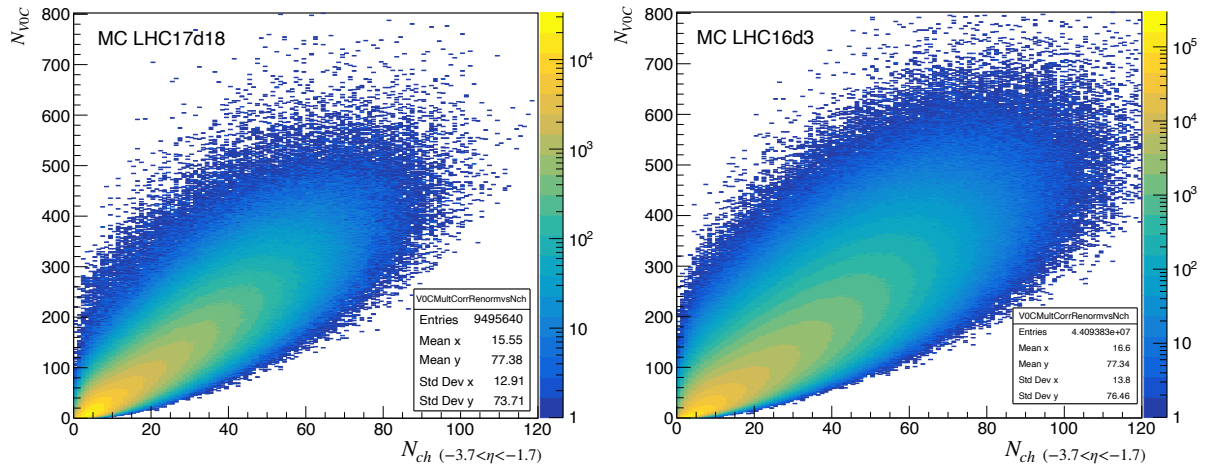


Figure 3.7:  $N_{\text{VOC}}$  versus  $N_{\text{ch}}$  in MC simulations generated with PYTHIA8 (left panel) and EPOS-LHC (right panel).

The average multiplicity  $\langle N_{\text{ch}} \rangle$  versus  $N_{\text{VOC}}$  from PYTHIA8 and EPOS-LHC in selected events is then fitted with an empirical function  $g$  defined as:

$$g(x) = A \left( 1 - \exp \left( - \frac{(x - \alpha)^2}{(\beta x + \gamma)^2} \right) \right).$$

The definition of the fit function has no physical meaning, its functional form has been retained among other possible functions because it fits well the profile up to the highest available multiplicities. It should be also noted that the residual discrepancies between the profiles and the fit function are significantly smaller than the differences between the profiles obtained with PYTHIA8 and EPOS-LHC. The results of the fits for the two different event generators can be seen in Figure 3.8. The fits are performed starting from

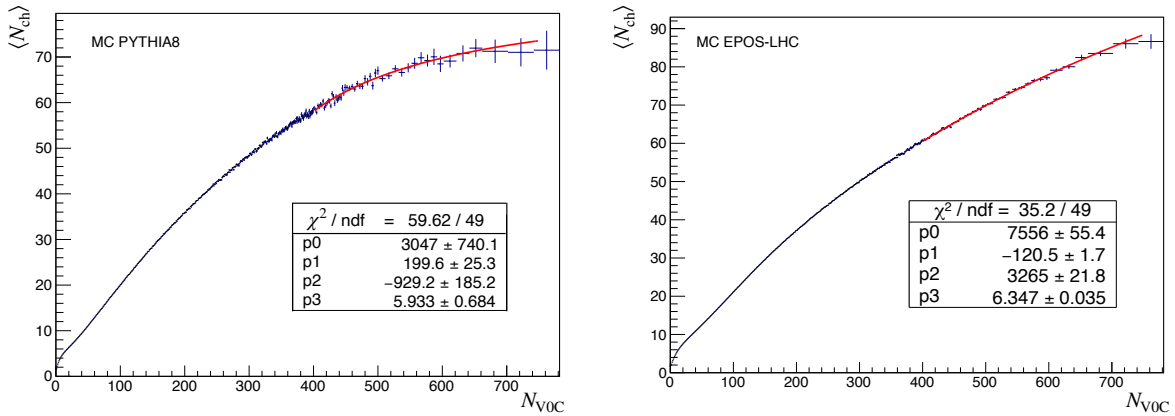


Figure 3.8:  $\langle N_{ch} \rangle$  versus  $N_{V0C}$  in PYTHIA8 (left panel) and EPOS-LHC (right panel) fitted with the function  $g$  (see text).

$N_{V0C} = 403.85$  (the lower boundary of the last multiplicity interval), below which the distribution of  $N_{ch}$  is directly used thanks to the large available statistics in the MC. For a given  $N_{V0C}$  value, the corresponding average  $\langle N_{ch} \rangle$  is then given by:

$$g_{N_{ch}}(N_{V0C}) = \begin{cases} \langle N_{ch} \rangle & \text{if } N_{V0C} < 403.85 \\ A \left( 1 - \exp \left( -\frac{(N_{V0C} - \alpha)^2}{(\beta N_{V0C} + \gamma)^2} \right) \right) & \text{else} \end{cases} \quad (3.3)$$

Then, for every  $N_{V0C}$  range  $i$ , the data-weighted average multiplicity  $\langle N_{ch} \rangle_i$  is computed in the following way:

$$\langle N_{ch} \rangle_i = \frac{\sum_{j=1}^{N_{\text{bins}}} n_{\text{evt}}^j \times g_{N_{ch}}(N_{V0C}^j)}{\sum_{j=1}^{N_{\text{bins}}} n_{\text{evt}}^j}, \quad (3.4)$$

where  $N_{\text{bins}}$  is the total number of bins in the range  $i$  of the  $N_{V0C}$  distribution (see Figure 3.1),  $j$  a generic bin inside this range,  $n_{\text{evt}}^j$  the number of events in bin  $j$ , and  $N_{V0C}^j$  the  $N_{V0C}$  value in bin  $j$ .

The relative multiplicity in the range  $i$  is then:

$$\frac{dN_{ch}/d\eta(i)}{\langle dN_{ch}/d\eta \rangle} = \frac{\langle N_{ch} \rangle_i}{\langle N_{ch} \rangle}, \quad (3.5)$$

with  $\langle N_{ch} \rangle_i$  defined above, and  $\langle N_{ch} \rangle$  the data-average multiplicity in the whole  $N_{V0C}$  range, calculated in the same way as  $\langle N_{ch} \rangle_i$ .

### 3.4.3.1 Correction of $\langle N_{ch} \rangle$

The average multiplicity  $\langle N_{ch} \rangle_i$  defined above is computed considering the selected events, satisfying the Minimum Bias trigger called kINT7, the Physics Selection (PS) and the vtxQA cuts. Therefore, one needs to correct the  $\langle N_{ch} \rangle_i$  values in order to obtain the corresponding ones for  $\text{INEL} > 0$  events. To do so, let us define the correction factors  $\epsilon_{N_{ch}}^i$  for each multiplicity bin  $i$  in the following way:

$$\epsilon_{N_{ch}}^i = \frac{\langle N_{ch} \rangle_i ((\text{kINT7} + \text{PS}) + \text{vtxQA})}{\langle N_{ch} \rangle_i (\text{INEL} > 0)},$$

where  $\langle N_{\text{ch}} \rangle_i$  is the mean number of primary charged particles per event in the  $N_{\text{V0C}}$  range  $i$  in the event class specified within parenthesis: either the selected events, i.e. ((kINT7 + PS) + vtxQA), or INEL > 0 events.

$N_{\text{V0C}}$ range	$\epsilon_{N_{\text{ch}}}$ or $\epsilon_{N_{\text{ch}}}^i$	$\epsilon_{N_{\text{ch}}} / \epsilon_{N_{\text{ch}}}^i$
integrated	1.048	1
[0, 28.7]	1.076	0.974
[28.7, 54.7]	1.008	1.040
[54.7, 72.6]	1.007	1.041
[72.6, 95.5]	1.005	1.043
[95.5, 127.1]	1.002	1.046
[127.1, 148.8]	1.001	1.047
[148.8, 178.1]	$\approx 1$	1.048
[178.1, 225.3]	$\approx 1$	1.048
[225.3, 324.5]	$\approx 1$	1.048
[324.5, 364.4]	$\approx 1$	1.048
[364.4, 403.9]	$\approx 1$	1.048
[403.9, 697.0]	$\approx 1$	1.048

Table 3.2: The  $\epsilon_{N_{\text{ch}}}$  and  $\epsilon_{N_{\text{ch}}}^i$  correction factors as obtained using MC.

Similarly, the correction factor for integrated multiplicity is given by:

$$\epsilon_{N_{\text{ch}}} = \frac{\langle N_{\text{ch}} \rangle ((\text{kINT7} + \text{PS}) + \text{vtxQA})}{\langle N_{\text{ch}} \rangle (\text{INEL} > 0)}.$$

The values of  $\epsilon_{N_{\text{ch}}}$  and  $\epsilon_{N_{\text{ch}}}^i$  are obtained from MC simulation. They are summarized in Table 3.2. The relative average multiplicity in INEL > 0 events  $\frac{dN_{\text{ch}}/d\eta(i)}{\langle dN_{\text{ch}}/d\eta \rangle}(\text{INEL} > 0)$  is then obtained as<sup>3</sup>:

$$\frac{dN_{\text{ch}}/d\eta(i)}{\langle dN_{\text{ch}}/d\eta \rangle}(\text{INEL} > 0) = \frac{dN_{\text{ch}}/d\eta(i)}{\langle dN_{\text{ch}}/d\eta \rangle}(\text{sel}) \times \frac{\epsilon_{N_{\text{ch}}}}{\epsilon_{N_{\text{ch}}}^i}$$

The  $\epsilon_{N_{\text{ch}}}$  correction is the only correction applied to the  $N_{\text{ch}}$  values after the conversion from  $N_{\text{V0C}}$ .

The values of the obtained relative average multiplicity in INEL > 0 events can be found in the third column of Table 3.3.

### 3.4.3.2 Systematic uncertainties of the conversion from $N_{\text{V0C}}$ to $N_{\text{ch}}$

Since the conversion from  $N_{\text{V0C}}$  to  $N_{\text{ch}}$  is dependent on the considered MC model, it is necessary to estimate the associated systematic uncertainty. For this purpose, the following variations of the conversion procedure are considered:

- two different MC generators (PYTHIA8 and EPOS-LHC) are used to obtain the correlation between  $N_{\text{V0C}}$  and  $N_{\text{ch}}$  (see section 3.4.3);

<sup>3</sup> Hereafter, the charged-particle multiplicity  $N_{\text{ch}}$  will also be presented in terms of charged-particle multiplicity density  $dN_{\text{ch}}/d\eta$  which is obtained dividing  $N_{\text{ch}}$  by the pseudorapidity range covered by the V0C detector, and which is equivalent to  $N_{\text{ch}}$  within the present analysis of relative multiplicities.

Interval $i$	$\langle N_{\text{V0C}} \rangle_i / \langle N_{\text{V0C}} \rangle$	$\frac{dN_{\text{ch}}/d\eta(i)}{\langle dN_{\text{ch}}/d\eta \rangle}$ (INEL > 0)	$\sigma_{\text{stat}}(\%)$	$\sigma_{\text{conv,sys}}(\%)$
1	0.187	0.333	0.0002 (0.07 %)	0.013 (3.95 %)
2	0.527	0.658	0.0004 (0.05 %)	0.024 (3.68 %)
3	0.817	0.904	0.0004 (0.04 %)	0.010 (1.07 %)
4	1.079	1.136	0.0004 (0.03 %)	0.009 (0.79 %)
5	1.425	1.443	0.0003 (0.02 %)	0.019 (1.34 %)
6	1.776	1.743	0.0002 (0.01 %)	0.027 (1.57 %)
7	2.099	2.005	0.0002 (0.01 %)	0.032 (1.62 %)
8	2.573	2.359	0.0005 (0.02 %)	0.040 (1.72 %)
9	3.397	2.905	0.0030 (0.10 %)	0.055 (1.89 %)
10	4.419	3.494	0.0103 (0.29 %)	0.069 (1.98 %)
11	4.931	3.749	0.0152 (0.41 %)	0.073 (1.96 %)
12	5.856	4.141	0.0180 (0.44 %)	0.062 (1.50 %)

Table 3.3: Summary of the relative V0C signal, the relative charged-particle multiplicity and its statistical and systematic uncertainties for the multiplicity intervals considered in the analysis.

- $N_{\text{V0C}}$  is scaled with three different factors  $f_{\text{V0C}} = 0.9, 1.0$  and  $1.1$  before the conversion is applied.

The factors  $f_{\text{V0C}}$  applied to  $N_{\text{V0C}}$  directly enter Eq 3.4 as follows:

$$\langle N_{\text{ch}} \rangle_i = \frac{\sum_{j=1}^{N_{\text{bins}}} n_{\text{evt}}^j \times g_{N_{\text{ch}}} (f_{\text{V0C}} \cdot N_{\text{V0C}}^j)}{\sum_{j=1}^{N_{\text{bins}}} n_{\text{evt}}^j} \quad (3.6)$$

These factors are introduced in order to take into account the discrepancies observed between the data and MC for what concerns the charged-particle multiplicity. In the present analysis, the MC  $N_{\text{V0C}}$  distribution is renormalized to the same reference value as the data. The resulting distribution, shown in Figure 3.6, is in a very good agreement with the data at intermediate and high multiplicities. Nevertheless, there are discrepancies at low multiplicity and the average charged-particle multiplicity in PYTHIA8 is found to be about 10% lower with respect to the measured charged-particle multiplicity in INEL > 0 collisions [89].

The final value of the relative multiplicity in each V0C interval  $i$  is calculated as the average of the results obtained with the 6 variations mentioned above:

$$\frac{dN_{\text{ch}}/d\eta(i)}{\langle dN_{\text{ch}}/d\eta \rangle} = \frac{1}{6} \sum_{j=1}^6 \left[ \frac{dN_{\text{ch}}/d\eta(i)}{\langle dN_{\text{ch}}/d\eta \rangle} \right]_j, \quad (3.7)$$

where  $j$  is the index of the variation. The systematic uncertainty  $\sigma_{\text{conv,sys}}$  is taken as the RMS of the distribution of  $\left[ \frac{dN_{\text{ch}}/d\eta(i)}{\langle dN_{\text{ch}}/d\eta \rangle} \right]_j$ :

$$\sigma_{\text{conv,sys}}(i) = \sqrt{\frac{1}{6} \sum_{j=1}^6 \left( \left[ \frac{dN_{\text{ch}}/d\eta(i)}{\langle dN_{\text{ch}}/d\eta \rangle} \right]_j - \frac{\langle dN_{\text{ch}}/d\eta \rangle_i}{\langle dN_{\text{ch}}/d\eta \rangle} \right)^2}. \quad (3.8)$$

The obtained systematic uncertainties are summarized in Table 3.3.

Finally, it is found that the values of the relative multiplicity in all the data periods employed in the analysis differ by at most 0.3% and therefore no associated systematic uncertainty is considered.

## 3.5 Measurement of the relative $J/\psi$ yield

As a reminder, in each V0C interval  $i$ , the relative  $J/\psi$  yield is given by:

$$\frac{dN_{J/\psi}/dy(i)}{\langle dN_{J/\psi}/dy \rangle} = \frac{n^{J/\psi}(i)}{n_{ev}(i)} \times \frac{N_{ev}}{N^{J/\psi}}, \quad (3.9)$$

with  $n_{J/\psi}(i)$  being the number of  $J/\psi$  in dimuon events belonging to the V0C interval  $i$ ,  $n_{ev}(i)$  the number of MB-triggered events in the same interval  $i$ ,  $N^{J/\psi}$  the total number of  $J/\psi$  in the total sample of dimuon events passing the event selection, and  $N_{ev}$  the total number of MB events passing the event selection.

Both dimuon and MB events are required to pass the event selections described in section 3.3.4.

As it will be described in the next section,  $n^{J/\psi}(i)$  and  $N^{J/\psi}$  are extracted from the dimuon invariant mass spectra, corrected for the Acceptance  $\times$  Efficiency of the muon spectrometer.

### 3.5.1 $J/\psi$ signal extraction

In order to correct the number of  $J/\psi$  for the acceptance and efficiency of the muon spectrometer, each dimuon invariant mass spectrum is filled with a weight  $w = 1/[A \times E(p_T, y)]$ , where  $p_T$  and  $y$  are the dimuon transverse momentum and rapidity, respectively, and  $A \times E$  is the  $J/\psi$  Acceptance  $\times$  Efficiency. The  $A \times E$  correction is applied on dimuons within the  $J/\psi$  invariant mass region to take automatically into account the variation of the  $A \times E$  with multiplicity. Indeed, the average  $J/\psi$   $p_T$ ,  $\langle p_T^{J/\psi} \rangle$  increases with multiplicity [49] and so does the  $A \times E$ . This correction method is more straightforward than correcting the number of  $J/\psi$  because the  $J/\psi$   $A \times E$  does not need to be computed in the different multiplicity intervals, and it was showed that it lead to the same results. The considered  $J/\psi$  Acceptance  $\times$  Efficiency is shown in Figure 3.9: it is derived using a  $J/\psi$  MC simulation properly anchored to all the data taking periods considered in the present analysis. In each multiplicity interval, the weighted dimuon invariant mass is then fitted using different signal and background functions. For the  $J/\psi$  and  $\psi(2S)$  peaks, a double Crystal Ball (CB2) function is used (see definition in Appendix A.1.1), with the tail parameters  $\alpha$ ,  $\alpha'$ ,  $n$  and  $n'$  fixed to two sets of values summarized in Table 3.4. Eight variations of the fit parameters are considered:

- two different sets of CB2 tail parameters (see Table 3.4);
- two different background functions, namely a Pol2  $\times$  Exp and a Variable Width Gaussian (VWG), defined in Annex A.1.3 and A.1.2;
- two different invariant-mass fit ranges, namely 2.3–4.9  $\text{GeV}/c^2$  and 2.1–4.7  $\text{GeV}/c^2$ .

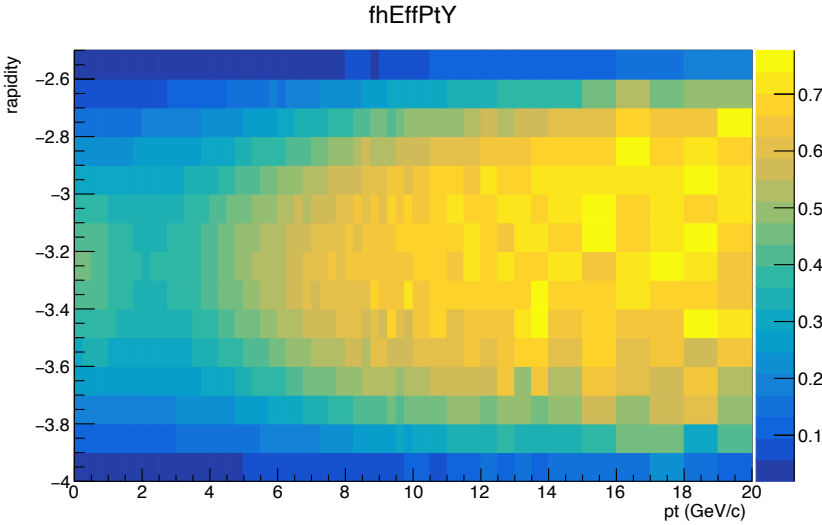


Figure 3.9:  $\mathbf{J}/\psi$  Acceptance  $\times$  Efficiency for the  $\mathbf{J}/\psi$  measurement in the dimuon channel.

Tail parameter	Run 2	MC
$\alpha$	0.883	0.993
$\alpha'$	1.832	2.182
$n$	9.940	2.9075
$n'$	15.323	3.122

Table 3.4: Tail parameters extracted from a fit to all available Run 2 dimuon data and from the corresponding anchored MC.

Figure 3.10 shows examples of the invariant mass fits for different multiplicity intervals. The relative  $\mathbf{J}/\psi$  yields are then obtained for each of these eight ( $2 \times 2 \times 2$ ) variations of the fit conditions. Each time, the same fit conditions are applied to both the dimuon invariant mass spectra in the various V0C intervals, and to the dimuon invariant mass spectrum integrated in multiplicity. In this way, the final result in each multiplicity bin  $i$  can be estimated averaging the results of the eight variations:

$$\frac{dN_{\mathbf{J}/\psi}/dy(i)}{\langle dN_{\mathbf{J}/\psi}/dy \rangle} = \frac{1}{8} \sum_{j=1}^8 \left[ \frac{dN_{\mathbf{J}/\psi}/dy(i)}{\langle dN_{\mathbf{J}/\psi}/dy \rangle} \right]_j , \quad (3.10)$$

where  $j$  is the index running over the considered variations.

The statistical uncertainty of the relative  $\mathbf{J}/\psi$  yield  $\left[ \frac{dN_{\mathbf{J}/\psi}/dy(i)}{\langle dN_{\mathbf{J}/\psi}/dy \rangle} \right]_j$  corresponding to any given variation  $j$  is calculated as follows:

$$\sigma_{\text{stat}}^j(i) = \left[ \frac{dN_{\mathbf{J}/\psi}/dy(i)}{\langle dN_{\mathbf{J}/\psi}/dy \rangle} \right]_j \times \sqrt{\left( \frac{\sigma_{n(i)}^j}{n_j^{\mathbf{J}/\psi}(i)} \right)^2 + \left( \frac{\sigma_N^j}{N_j^{\mathbf{J}/\psi}} \right)^2} ,$$

where  $\sigma_{n(i)}^j$  and  $\sigma_N^j$  are the statistical uncertainties on  $n_{\mathbf{J}/\psi}(i)_j$  and  $N_j^{\mathbf{J}/\psi}$ , respectively. These uncertainties are computed taking into account the covariance matrix of the invariant-

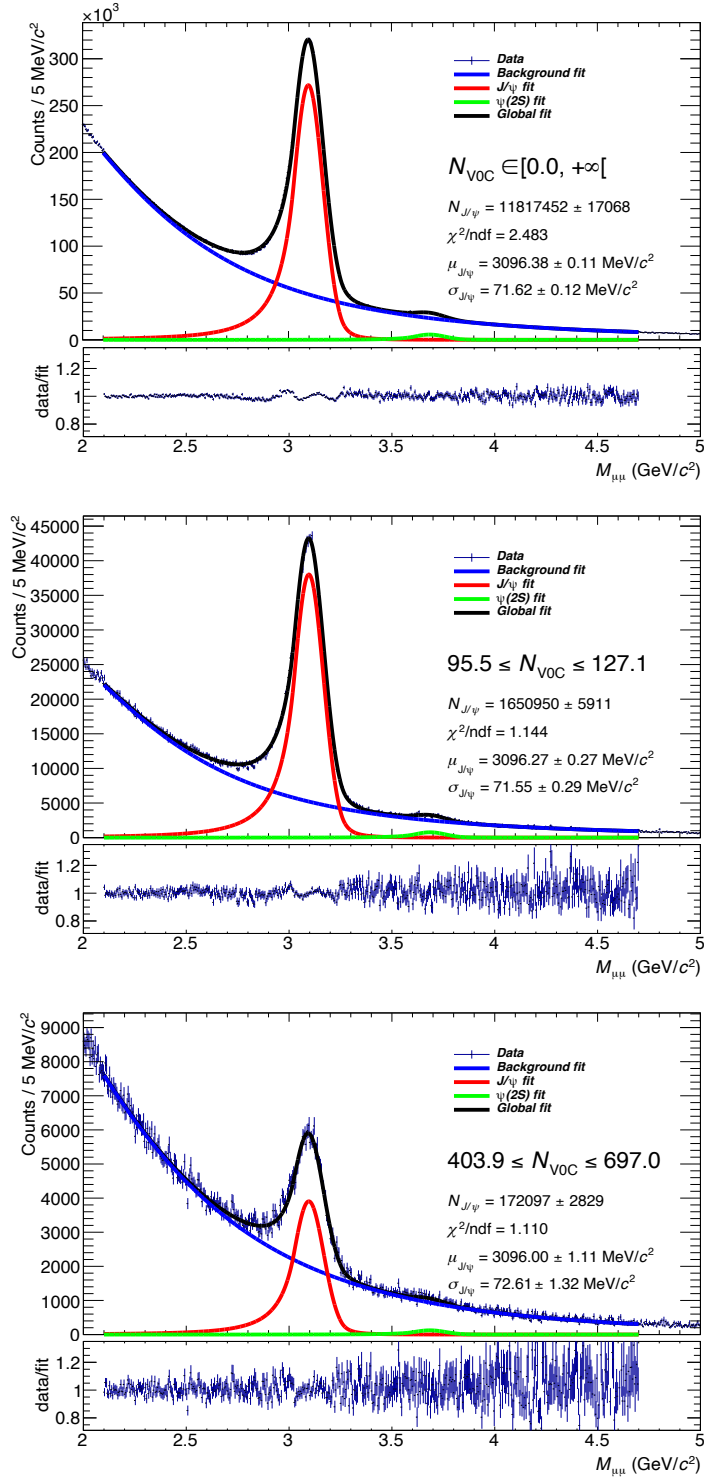


Figure 3.10: Fit of the dimuon invariant mass spectra for the multiplicity-integrated sample (top), in multiplicity interval 5 (middle), and in multiplicity interval 12 (bottom). The CB2 tails are taken from the anchored MC. The background is fitted with a VWG function. The fit range is defined between  $2.1$  and  $4.7$   $\text{GeV}/c^2$ .

mass fit. The statistical uncertainties on  $n_{\text{ev}}(i)$  and  $N_{\text{ev}}$  are negligible given the high number of MB events.

The statistical uncertainty of the relative yields corresponding to any given multiplicity interval  $i$  is then taken conservatively as the mean of the statistical uncertainties of the variations  $j$ :

$$\sigma_{\text{sig,stat}}(i) = \frac{1}{8} \sum_{j=1}^8 \sigma_{\text{stat}}^j(i) \quad (3.11)$$

The systematic uncertainty  $\sigma_{\text{sig,sys}}$  of the relative yields is taken as the RMS of the distribution of the values  $\left[ \frac{dN_{\text{J}/\psi}/dy(i)}{\langle dN_{\text{J}/\psi}/dy \rangle} \right]_j$ :

$$\sigma_{\text{sig,sys}}(i) = \sqrt{\frac{1}{8} \sum_{j=1}^8 \left( \left[ \frac{dN_{\text{J}/\psi}/dy(i)}{\langle dN_{\text{J}/\psi}/dy \rangle} \right]_j - \frac{dN_{\text{J}/\psi}/dy(i)}{\langle dN_{\text{J}/\psi}/dy \rangle} \right)^2}. \quad (3.12)$$

A compilation of the extracted  $\mathbf{J}/\psi$  relative yields and their statistical and systematic uncertainties is given in Figure 3.11: as one can see, the systematic uncertainties related to the signal extraction are negligible with respect to the corresponding statistical uncertainties.

### 3.5.2 Correction of the $\mathbf{J}/\psi$ yields

The calculation of the  $\mathbf{J}/\psi$  yields (numerator and denominator on the left side of Eq. 3.9) is based on the number of events triggered with the MB trigger (kINT7) and passing the selection described in section 3.3.4. Corrections are needed to convert these number of events into a corresponding number of  $\text{INEL} > 0$  events. Let us introduce three correction factors:  $\epsilon_{\text{INEL}>0}^{\text{MB}}$ ,  $C_{\text{INEL}=0}$  and  $\epsilon_{\text{vtxQA}}$ , defined as follows:

$$\epsilon_{\text{INEL}>0}^{\text{MB}} = \frac{N_{\text{ev}}(\text{INEL} > 0 + (\text{kINT7} + \text{PS}))}{N_{\text{ev}}(\text{INEL} > 0)},$$

where  $N_{\text{ev}}(\text{INEL} > 0 + (\text{kINT7} + \text{PS}))$  is the number of  $\text{INEL} > 0$  events triggered by the kINT7 trigger and passing the Physics Selection (PS), and  $N_{\text{ev}}(\text{INEL} > 0)$  is the number of  $\text{INEL} > 0$  events with no further selection;

$$C_{\text{INEL}=0} = \frac{N_{\text{ev}}(\text{INEL} = 0 + (\text{kINT7} + \text{PS}))}{N_{\text{ev}}(\text{kINT7} + \text{PS})},$$

where  $N_{\text{ev}}(\text{INEL} = 0 + (\text{kINT7} + \text{PS}))$  is the number of  $\text{INEL} = 0$  events triggered by the kINT7 trigger and passing Physics Selection, and  $N_{\text{ev}}(\text{kINT7} + \text{PS})$  is the total number of events triggered by the kINT7 trigger and passing the Physics Selection;

$$\epsilon_{\text{vtxQA}} = \frac{N_{\text{ev}}((\text{kINT7} + \text{PS}) + \text{vtxQA})}{N_{\text{ev}}(\text{kINT7} + \text{PS})},$$

where  $N_{\text{ev}}((\text{kINT7} + \text{PS}) + \text{vtxQA})$  is the total number of events triggered by the kINT7 trigger and passing the Physics Selection and the vertex quality-assurance selection.

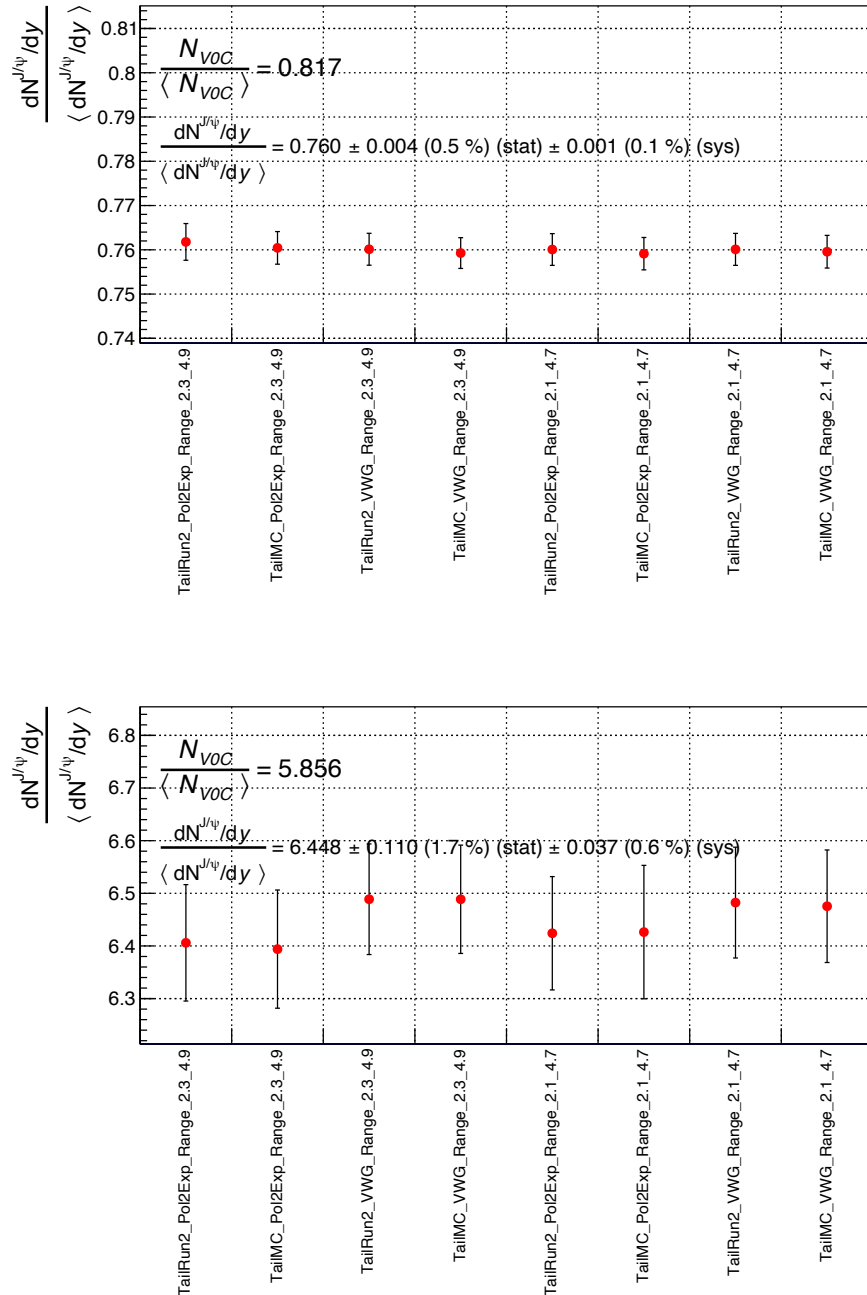


Figure 3.11:  $J/\psi$  relative yields and their uncertainties in the multiplicity interval 3 (top) and 12 (bottom).

The correction factors are computed for each multiplicity interval and for the multiplicity-integrated sample.  $\epsilon_{\text{INEL}>0}^{\text{MB}}$  and  $C_{\text{INEL}=0}$  are computed using MC simulation, while  $\epsilon_{\text{vtxQA}}$  is calculated using data. The values of the correction factors are summarized in Table 3.5.

The number of events for each multiplicity class and the integrated number of events is

$N_{\text{V0C}}$ range	$\epsilon_{\text{INEL}>0}^{\text{MB}}$	$\epsilon_{\text{vtxQA}}$	$C_{\text{INEL}=0}$
integrated	0.943	0.960	0.019
[0, 28.7]	0.866	0.906	0.048
[28.7, 54.7]	0.958	0.965	0.016
[54.7, 72.6]	0.975	0.983	0.006
[72.6, 95.5]	0.986	0.991	0.003
[95.5, 127.1]	0.994	0.996	0.001
[127.1, 148.8]	0.997	0.998	0.0003
[148.8, 178.1]	0.999	0.999	0.0001
[178.1, 225.3]	1.0	1.0	$\approx 0$
[225.3, 324.5]	1.0	1.0	$\approx 0$
[324.5, 364.4]	1.0	1.0	$\approx 0$
[364.4, 403.9]	1.0	1.0	$\approx 0$
[403.9, 697.0]	1.0	1.0	$\approx 0$

Table 3.5: Correction factors applied on the  $\mathbf{J}/\psi$  yields.

then corrected in the following way:

$$N_{\text{ev}}(\text{INEL} > 0) = \frac{1}{\epsilon_{\text{INEL}>0}^{\text{MB}}} \frac{1}{\epsilon_{\text{vtxQA}}} \times (1 - C_{\text{INEL}=0}) \times N_{\text{ev}}((\text{kINT7} + \text{PS}) + \text{vtxQA}),$$

with  $N_{\text{ev}}((\text{kINT7} + \text{PS}) + \text{vtxQA})$  being the number of the events selected for the analysis, and  $N_{\text{ev}}(\text{INEL} > 0)$  the number of events in the  $\text{INEL} > 0$  class chosen for the normalization (see Appendix A.2 for the details).

Once all the corrections are taken into account, the relative  $\mathbf{J}/\psi$  yield for  $\text{INEL} > 0$  events is given by equation 3.13.

$$\frac{dN_{\mathbf{J}/\psi}/dy(i)}{\langle dN_{\mathbf{J}/\psi}/dy \rangle} = \frac{n^{\mathbf{J}/\psi}(i)}{N^{\mathbf{J}/\psi}} \times \frac{N_{\text{ev}}}{n_{\text{ev}}(i)} \times \frac{\epsilon_{\text{INEL}>0}^{\text{MB},i}}{\epsilon_{\text{INEL}>0}^{\text{MB}}} \times \frac{\epsilon_{\text{vtxQA}}^i}{\epsilon_{\text{vtxQA}}} \times \frac{1 - C_{\text{INEL}=0}^i}{1 - C_{\text{INEL}=0}}. \quad (3.13)$$

The systematic uncertainties of the relative  $\mathbf{J}/\psi$  yields are conservatively estimated as the differences between the results with and without the application of the correction factors described above. In the following, these uncertainties will be noted as  $\Delta_{\text{INEL}>0}$ ,  $\Delta_{\text{INEL}=0}$  and  $\Delta_{\text{vtxQA}}$ .

### 3.5.3 Uncertainties on the dimuon correction

As explained in section 3.4.2.2, the dimuon correction is estimated from the analysis of single muon events, computing the different average signals in each V0C channel and isolating the excess signal corresponding to a muon crossing the channel. The correction is obtained and applied separately for each data period. However, the excess signal can differ run-by-run within a given period. This can lead to a systematic effect that has to be taken into account. It is known that within a given period, the runs at the beginning of the period and the runs at the end differ the most, due to the aging of the V0C detector during one period. Therefore, in order to estimate the corresponding systematic effect, the excess muon signal is calculated for runs at the beginning and at the end of any given

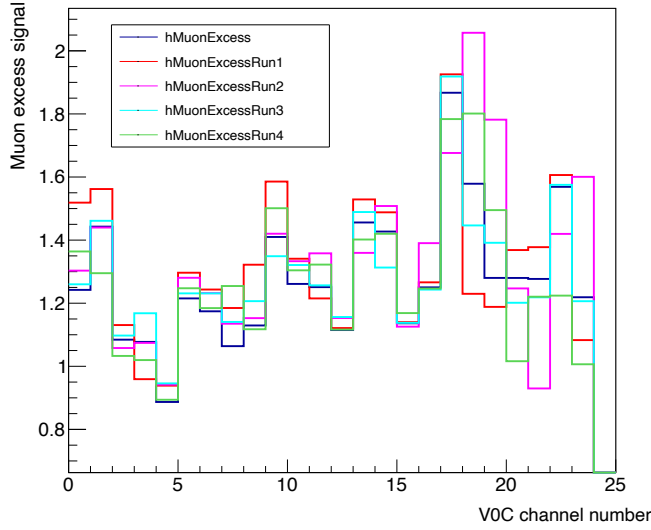


Figure 3.12: Excess signal due to the passage of a muon in the different V0C channels. The excess averaged over the analyzed periods is in dark blue, the other histograms are the excess in different runs of the LHC18m period.

period, as represented in Figure 3.12 for the LHC18m data-taking period. It is found that in general the excess muon signal ranges between 0.5 and 2. These two extreme values are used as the excess muon signal for all V0C channels in order to obtain the relative  $J/\psi$  yields. The systematic uncertainties  $\Delta_{\mu\mu}$  are then computed as the average of the differences between the nominal yields and the yields obtained with these extreme values of the excess muon signal:

$$\Delta_{\mu\mu}^{\text{low}} = |Y_{\text{nominal}}^i - Y_{\text{low}}^i|,$$

$$\Delta_{\mu\mu}^{\text{high}} = |Y_{\text{nominal}}^i - Y_{\text{high}}^i|,$$

$$\Delta_{\mu\mu} = \frac{\Delta_{\mu\mu}^{\text{low}} + \Delta_{\mu\mu}^{\text{high}}}{2},$$

where  $Y_{\text{nominal}}^i$ ,  $Y_{\text{low}}^i$  and  $Y_{\text{high}}^i$  denote the  $J/\psi$  relative yield  $\frac{dN_{J/\psi}/dy(i)}{\langle dN_{J/\psi}/dy \rangle}$  in the multiplicity interval  $i$  obtained with the nominal and the extreme values of the excess muon signal, respectively.

### 3.5.4 Total systematic uncertainty of the relative $J/\psi$ yields

The systematic uncertainties of the relative  $J/\psi$  yields arise from five different sources:

- The systematic uncertainties of the signal extraction  $\sigma_{\text{sig,sys}}$ . These uncertainties are found to be practically negligible;
- The systematic uncertainties related to the yield corrections  $\Delta_{\text{INEL}>0}$ ,  $\Delta_{\text{vtxQA}}$  and  $\Delta_{\text{INEL}=0}$ ;

- The systematic error of the dimuon correction  $\Delta_{\mu\mu}$ .

These systematic uncertainties are considered to be uncorrelated and therefore the total systematic uncertainty on the relative  $\mathbf{J}/\psi$  yields is obtained as their quadratic sum:

$$\sigma_{\text{sys}}^{\text{total}} = \sqrt{\sigma_{\text{sig,sys}}^2 + \Delta_{\text{INEL}>0}^2 + \Delta_{\text{vtxQA}}^2 + \Delta_{\text{INEL}=0}^2 + \Delta_{\mu\mu}^2}.$$

Table 3.6 summarizes the values of the systematic uncertainties. It is worth noting that for all sources, the systematic uncertainties are the highest for the first multiplicity interval. Indeed, the dimuon correction is the most significant in the first interval because at low multiplicity, the relative impact of removing two muons is high. For the other uncertainties, the efficiency corrections affect mainly the low multiplicity events because with a low number of tracks present, it is easier to mistake the class of events (INEL=0, INEL>0 or INEL) and to reconstruct a vertex with poor vtxQA.

$\frac{dN_{\text{ch}}/d\eta(i)}{\langle dN_{\text{ch}}/d\eta \rangle}$ (INEL > 0)	$\frac{dN_{\mathbf{J}/\psi}/dy(i)}{\langle dN_{\mathbf{J}/\psi}/dy \rangle}$	$\Delta_{\mu\mu}$	$\Delta_{\text{INEL}>0}$	$\Delta_{\text{vtxQA}}$	$\Delta_{\text{INEL}=0}$	$\sigma_{\text{sys}}^{\text{total}}$
0.333212	0.143530	0.010 (7.0 %)	0.013 (8.9 %)	0.009 (6.0 %)	0.004 (3.0 %)	0.019 (13.2 %)
0.657568	0.472803	0.007 (1.6 %)	0.007 (1.6 %)	0.002 (0.5 %)	0.001 (0.3 %)	0.011 (2.3 %)
0.903716	0.799477	0.005 (0.6 %)	0.026 (3.3 %)	0.019 (2.3 %)	0.010 (1.3 %)	0.034 (4.3 %)
1.135551	1.118095	0.004 (0.3 %)	0.049 (4.4 %)	0.035 (3.1 %)	0.018 (1.6 %)	0.063 (5.6 %)
1.443043	1.554435	0.008 (0.5 %)	0.080 (5.1 %)	0.056 (3.6 %)	0.028 (1.8 %)	0.102 (6.5 %)
1.743123	1.989077	0.009 (0.5 %)	0.108 (5.4 %)	0.076 (3.8 %)	0.037 (1.9 %)	0.137 (6.9 %)
2.005480	2.376568	0.015 (0.6 %)	0.133 (5.6 %)	0.093 (3.9 %)	0.045 (1.9 %)	0.169 (7.1 %)
2.359330	2.977255	0.032 (1.1 %)	0.170 (5.7 %)	0.119 (4.0 %)	0.057 (1.9 %)	0.217 (7.3 %)
2.905211	4.017696	0.056 (1.4 %)	0.229 (5.7 %)	0.161 (4.0 %)	0.076 (1.9 %)	0.295 (7.4 %)
3.494474	5.276262	0.097 (1.8 %)	0.301 (5.7 %)	0.211 (4.0 %)	0.100 (1.9 %)	0.393 (7.5 %)
3.749348	5.934679	0.167 (2.8 %)	0.338 (5.7 %)	0.237 (4.0 %)	0.113 (1.9 %)	0.460 (7.7 %)
4.141169	7.119549	0.232 (3.3 %)	0.406 (5.7 %)	0.285 (4.0 %)	0.135 (1.9 %)	0.565 (7.9 %)

Table 3.6: Summary of the systematic uncertainties of the relative  $\mathbf{J}/\psi$  yield.

## 3.6 Results

The results of the  $J/\psi$  relative yield as a function of the relative multiplicity measured in the V0C acceptance  $-3.7 < \eta < -1.7$  are shown in Figure 3.13. The black vertical error bars are the statistical uncertainties of the relative  $J/\psi$  yields, while the red boxes correspond to the total systematic uncertainties of the relative  $J/\psi$  (vertical size) yields and the relative multiplicity (horizontal size). One should stress that the systematic uncertainties on the relative  $J/\psi$  yields and the relative multiplicity are correlated across the multiplicity intervals. This is an important point to be taken into account in the comparisons with models or event generators.

The results clearly show a rapidly increase of the  $J/\psi$  yield as a function of the forward multiplicity.

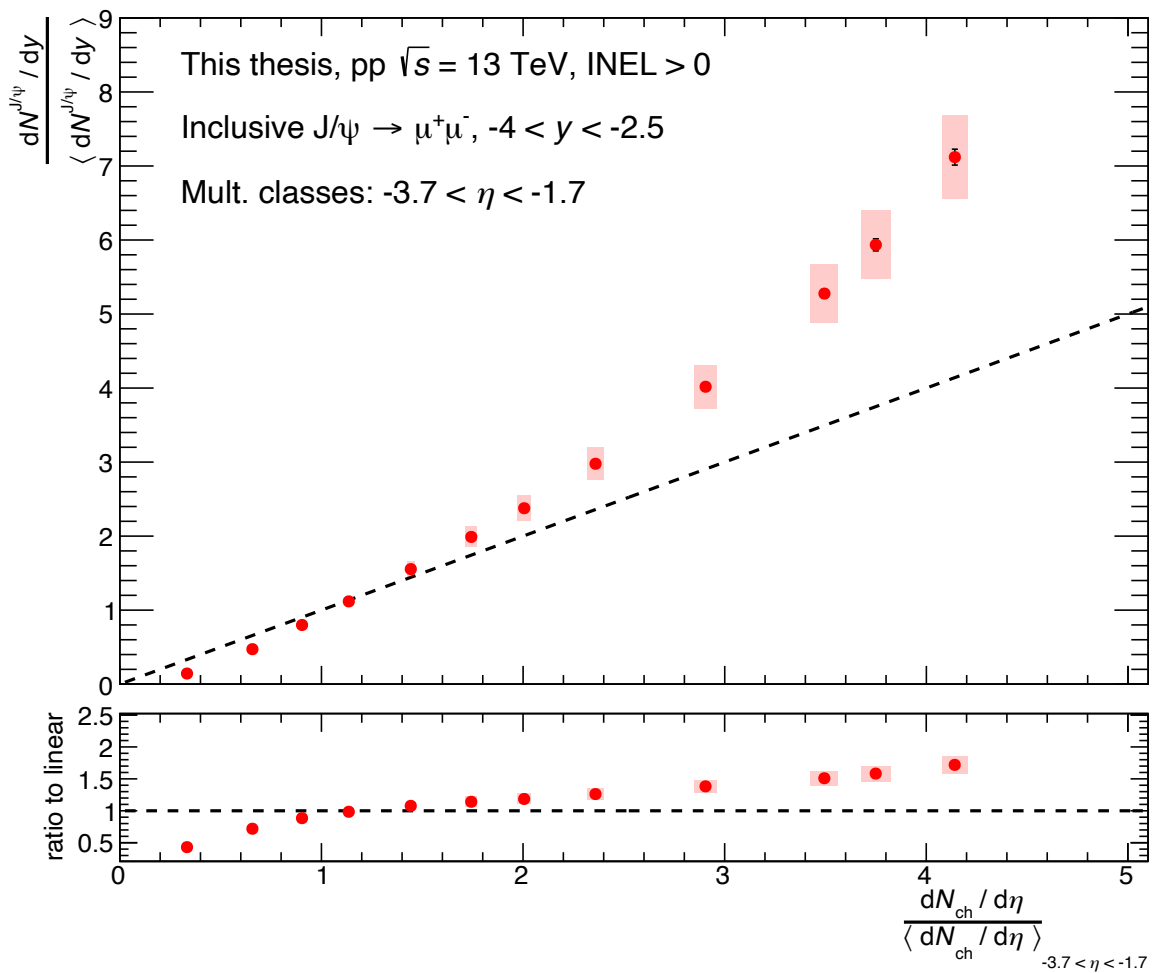


Figure 3.13:  $J/\psi$  relative yield as a function of the relative multiplicity measured in the V0C acceptance  $-3.7 < \eta < -1.7$ .

### 3.7 Comparison with model predictions

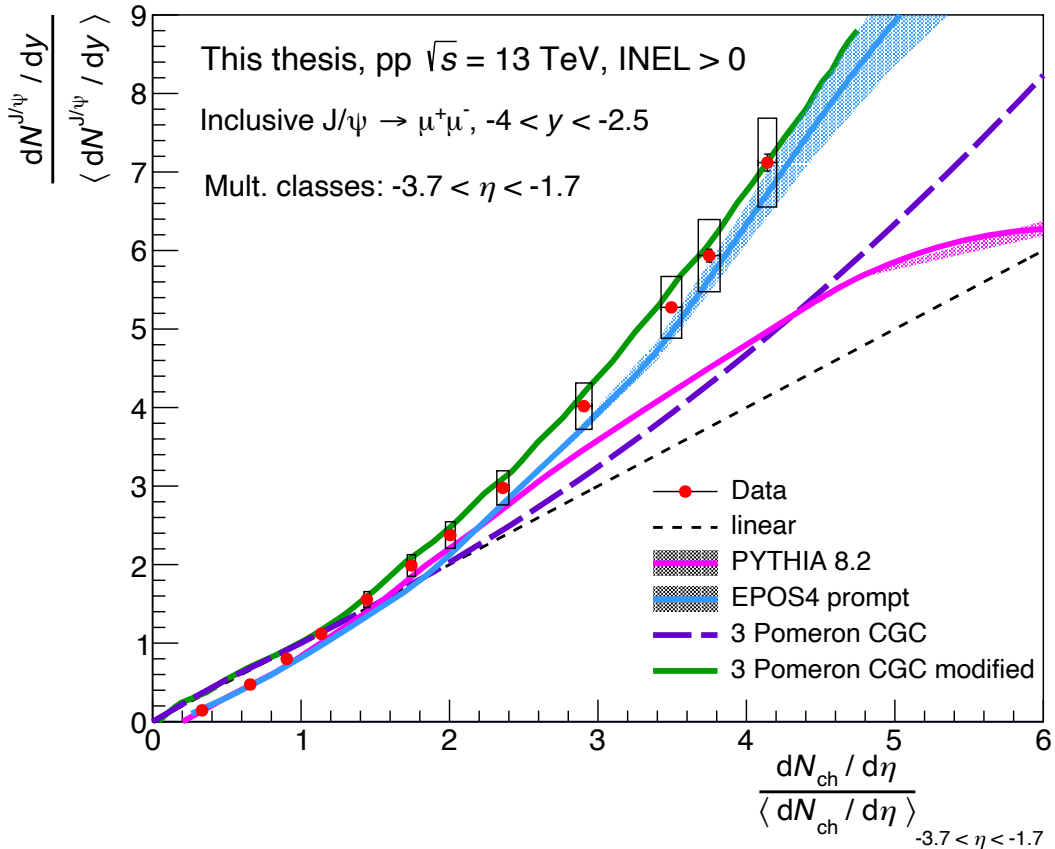


Figure 3.14:  $\mathbf{J}/\psi$  relative yield as a function of the relative multiplicity in the V0C acceptance  $-3.7 < \eta < -1.7$  compared with PYTHIA 8.2, EPOS4HQ [90] and two 3-Pomeron CGC (Color Glass Condensate) model predictions [91, 92].

The results obtained for the forward  $\mathbf{J}/\psi$  relative yield as a function of the forward relative multiplicity are compared with several model predictions in Figure 3.14. The predictions are from PYTHIA 8.2, EPOS4HQ, and CGC models. PYTHIA 8.2 calculations consider both prompt and non-prompt  $\mathbf{J}/\psi$  production, while EPOS4HQ and CGC models consider prompt  $\mathbf{J}/\psi$  production only. EPOS4HQ is an EPOS version featuring hydrodynamics mechanisms and core-corona separation. EPOS4HQ is an extension of EPOS4 designed to properly model the production of charm quarks [90]<sup>4</sup>. Both the considered 3-Pomeron CGC models describe the  $\mathbf{J}/\psi$  production using the color-singlet contribution of NRQCD using 3-Pomeron (or gluon) fusion and Color Glass Condensate (CGC) calculations. In the CGC theory, initial-state nucleons in ultra-relativistic collisions are described in terms of a very dense and highly-saturated gluonic matter, each gluon carrying a very low fraction [93] of the total momentum of the nucleon. The difference between the 3-Pomeron CGC model developed in [91] and the modified 3-Pomeron CGC model described in [92] is that in the latter higher-order gluon interactions are included when describing  $\mathbf{J}/\psi$  production.

<sup>4</sup> The specific version used for the predictions presented here is EPOS4.0.2e7

It is important to note that the comparisons are not straightforward: in all the models except PYTHIA, the predictions only take into account prompt  $J/\psi$  production, whereas the experimental result include prompt and non-prompt  $J/\psi$ . On the other hand, models and the experimental result agree in excluding the  $J/\psi$  daughters from the counting of the multiplicity in the events containing a  $J/\psi$ .

As one can see in Figure 3.14, PYTHIA 8.2 underestimates the results at intermediate and high multiplicity, whereas EPOS4 and the modified 3-Pomeron CGC model predictions are consistent with the data. Interestingly, the former 3-Pomeron CGC model accurately describes the measurements of both midrapidity  $J/\psi$  versus midrapidity multiplicity and forward  $J/\psi$  versus midrapidity multiplicity [49], but does not describe the results from the present analysis of the forward  $J/\psi$  versus forward multiplicity.

## 3.8 Discussion of auto-correlation effects from $J/\psi$ daughters

As already mentioned, in the present analysis the  $J/\psi$  daughters were removed from the V0C signal by using the dimuon correction (see section 3.4.2.2). Indeed, including these daughters leads to an auto-correlation effect in the measurement. In order to estimate this effect, the results with including and excluding the  $J/\psi$  daughters are compared in Figure 3.15. As one can note, the differences are nevertheless small and are at maximum 3.4% in the highest multiplicity interval.

The comparison of the results with including and excluding  $J/\psi$  daughters was also recently established in the case of the measurement of midrapidity  $J/\psi$  yields as a function of the midrapidity multiplicity. The same trend was observed: the dependence when including the  $J/\psi$  daughters in the estimation of the multiplicity is steeper. The effect of excluding the daughters is however more significant than in the present analysis. In order to further investigate the effect of the presence of the  $J/\psi$  daughters on the multiplicity of  $J/\psi$  events, a specific study is carried out with PYTHIA 8.2. 1.500 billion MB events are generated, forcing  $J/\psi$  to decay into two muons, and the relative yield of forward  $J/\psi$  as a function of the relative forward multiplicity is derived in three different cases:

1. Using multiplicity classes in the V0C acceptance  $-3.7 < \eta < -1.7$  including the  $J/\psi$  daughters (also called “legs”) in the counting of particles in the events with a  $J/\psi$ ;
2. Using multiplicity classes in the V0C acceptance  $-3.7 < \eta < -1.7$  excluding the  $J/\psi$  daughters that are falling in the V0C acceptance;
3. Using multiplicity selection classes based on the number of charged particles in  $|\eta| < 1$ . In this case, the  $J/\psi$  daughters do not have any impact as they are not contributing to the multiplicity in the  $|\eta| < 1$  region. The  $J/\psi$  yields are plotted as a function of the relative multiplicity in  $-3.7 < \eta < -1.7$ .

The outcome of this study can be seen in Figure 3.16. The removal of the  $J/\psi$  daughters has a significant impact on the steepness of the curve, especially above a relative multiplicity of  $\sim 4$ . This observation is in contrast with the relatively small effect of daughter removal seen in the experimental data. As explained previously, at a relative multiplicity

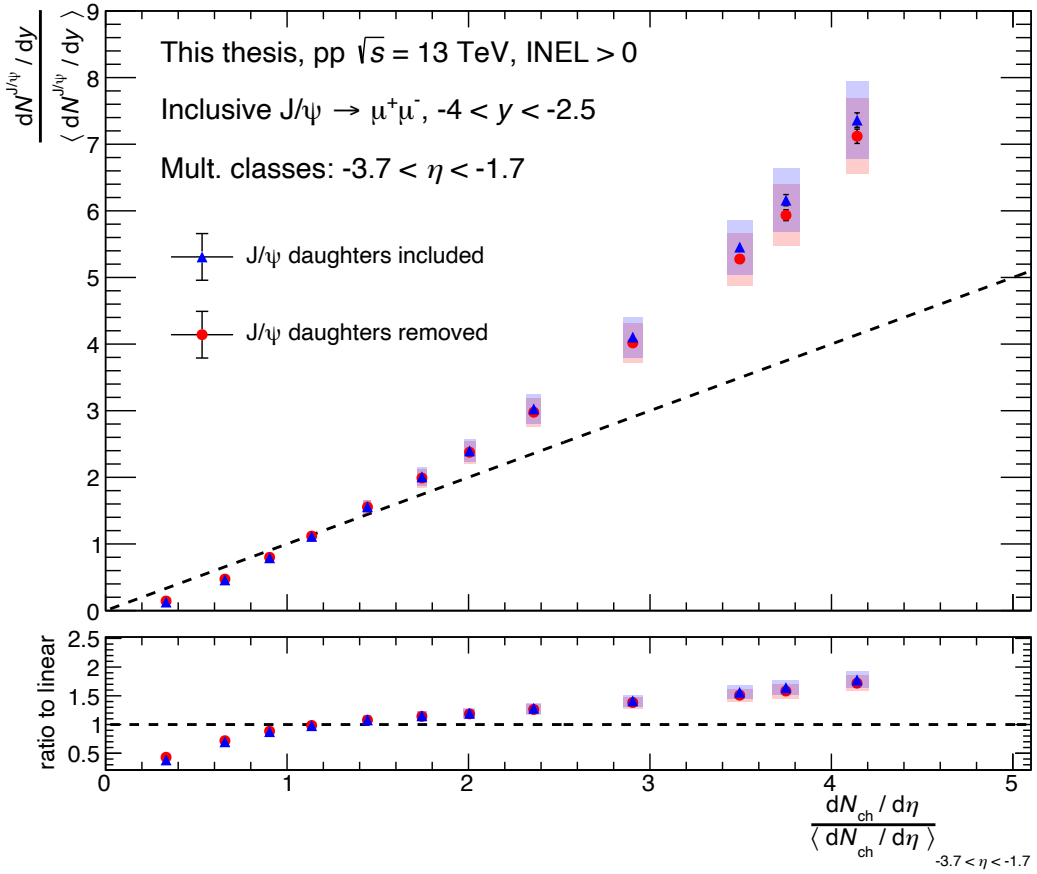


Figure 3.15:  $\mathbf{J}/\psi$  relative yield as a function of the relative multiplicity in the V0C acceptance  $-3.7 < \eta < -1.7$  with and without the dimuon correction.

around 4.1 the relative yield in data changes by only 3.4% when muon daughters are excluded, while in PYTHIA8 the corresponding effect is of the order of 13%. This difference can be explained by the working principle of the V0 detector, which delivers an output signal proportional to the energy deposited by charged particles in its scintillator layer. The detector is calibrated so that the signal of amplitude 1 corresponds to the energy deposit of a minimum-ionizing particle (MIP). As it can be seen in Figure 3.12, muons produce in average a signal corresponding to about 1.5 MIPs<sup>5</sup>. This is because at forward rapidity in the MS acceptance, the muon  $p$  at  $p_T = 1$  GeV/c is between 6 and 27 GeV/c, while a muon MIP in a plastic scintillator has  $p \in [0.1, 1]$  GeV/c. Most charged particles produced in the collisions reaching the V0 detector deposit energy which is significantly larger than the one expected for a MIP. In addition, the V0 detector is also sensitive to secondary particles produced by interactions of primary particles with the material located close to the detector. From the correlation between  $N_{ch}$  and  $N_{V0C}$  (see Figures 3.8) it was determined that a signal in the V0C of around 400 in amplitude corresponds to 60 primary charged particles. Therefore, the effect of simply removing two muons is  $2 \times 1.5/400 = 0.75\%$  in terms of  $N_{V0C}$ , whereas the corresponding effect in terms

<sup>5</sup> The large channel-by-channel variations seen in the figure are mainly due to the limited precision of the V0 calibration procedure and statistical uncertainties.

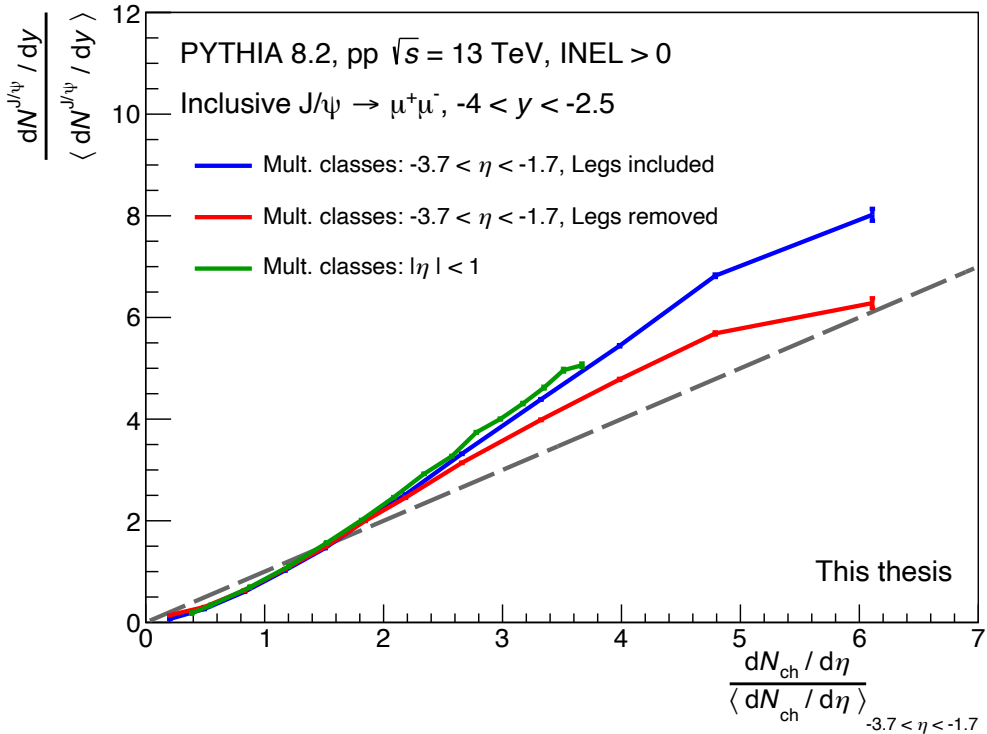


Figure 3.16:  $J/\psi$  relative yield as a function of the relative multiplicity in the V0C acceptance  $-3.7 < \eta < -1.7$  obtained with PYTHIA 8.2 simulations with including or excluding the  $J/\psi$  daughters from the multiplicity estimation, and with a different multiplicity selection based on the number of charged particles in  $|\eta| < 1$ .

of number of charged particles is  $2/60 = 3.3\%$ . This means that removing the signal of two muons from the V0C signal has 4.4 times less impact than removing two muons from the charged-particle multiplicity and explains why in PYTHIA the effect of removing the daughters leads to a difference of 13% whereas in the data the difference is only 3.4%.

In Figure 3.16, it is also interesting to note that the result with the multiplicity selection in  $|\eta| < 1$  is very close to the result with the multiplicity selection in  $-3.7 < \eta < -1.7$  and with the inclusion of  $J/\psi$  daughters. The same observation was made in the data based on measurements  $J/\psi$  yields at midrapidity (see Figure 3.17, left): the results with the inclusion of the daughters as a function of the midrapidity multiplicity, with a midrapidity-based multiplicity selection, coincide with the results with the V0-based multiplicity selection (i.e. using charged-particle multiplicity in the acceptance of V0A and V0C detectors).

### 3.9 Comparison between forward and mid-rapidity $J/\psi$ yields

In Figure 3.17, the previously published measurements of forward and midrapidity  $J/\psi$  relative yield as a function of the relative multiplicity in  $|\eta| < 1$  are compared with the results presented in this thesis (in red). Two observations can be made. First, the forward

rapidity  $\mathbf{J}/\psi$  yields versus forward multiplicity have the same steeper-than-linear trend as the midrapidity  $\mathbf{J}/\psi$  yields versus midrapidity multiplicity. Second, the multiplicity dependence of the forward rapidity  $\mathbf{J}/\psi$  yield is significantly steeper as a function of forward multiplicity than as a function of midrapidity multiplicity. In other words, it seems that there is a stronger dependence of the  $\mathbf{J}/\psi$  relative yield with the relative multiplicity when the  $\mathbf{J}/\psi$  is measured in a rapidity interval overlapping with the one where the multiplicity is defined.

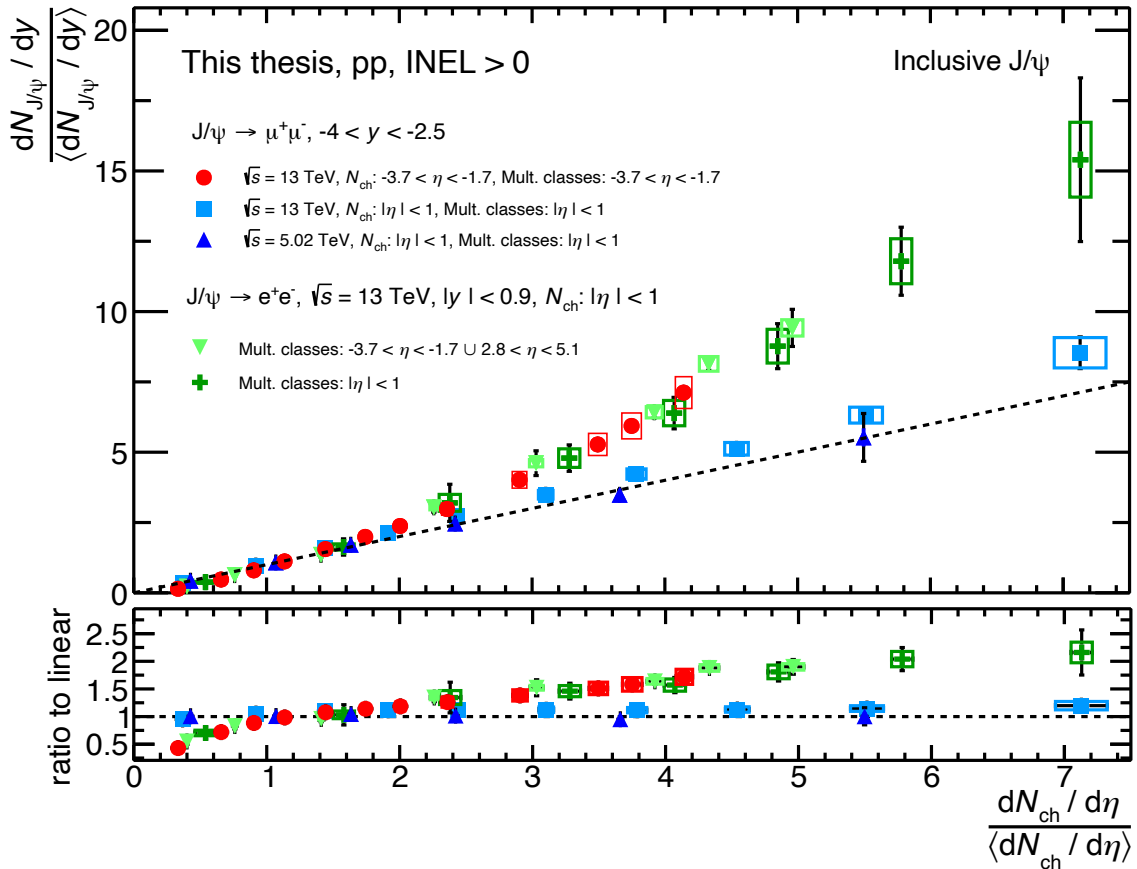


Figure 3.17: Forward and midrapidity  $\mathbf{J}/\psi$  relative yields as a function of relative multiplicity in  $|\eta| < 1$  (blue and green) [49], compared with forward  $\mathbf{J}/\psi$  relative yields as a function of relative multiplicity in  $-3.7 < \eta < -1.7$  (red). The bottom panel shows the ratio of each result to the linear  $y = x$  reference.

### 3.10 Discussion of the results

In the following, the results will be discussed in the framework of the PYTHIA modeling of high-energy proton-proton collisions. In PYTHIA8, there are three sources of inclusive  $\mathbf{J}/\psi$  production [94]:

- Pairs of charm and anti-charm quarks are created in hard scattering processes, like gluon fusion, quark-antiquark annihilation or gluon splitting. The description of these processes is implemented within the NRQCD framework. The produced pairs

are in either color-singlet or color-octet state, and the latter transitions to a color-singlet state via the emission of a gluon;

- Through the “cluster collapse” mechanism,  $J/\psi$  are produced via recombination of charm and anti-charm quarks at the hadronization stage. In case of presence of MPIs and enabled Color Reconnection (CR)<sup>6</sup> mechanism, the two quarks can come from two distinct hard-scattering processes;
- Non-prompt  $J/\psi$  are produced in decays of beauty hadrons.

The  $J/\psi$  yields from the NRQCD mechanisms and non-prompt sources show in general a close-to-linear dependence as a function of the number of MPIs, while the “cluster collapse” yields have a quadratic dependence in case the CR is enabled.

On the experimental side, the charged-particle event multiplicity is widely used as a proxy for the number of MPIs. While this approach is in general well justified, it has some limitations that can impact the interpretation of the results. It is well known, in fact, that in small collision systems (i.e. those that feature few colliding nucleons), local multiplicity fluctuations and the presence of jets lead to significant selection biases [95]. This results in a weaker correlation between the number of MPIs and the multiplicity, affecting the measured particle species abundances and spectra [96]. In general, the range spawn in multiplicity is significantly wider compared to that in the number of MPIs, and the collisions characterized by the highest multiplicities correspond to multi-jet final states [97].

The  $J/\psi$  yields from the three sources described above exhibit rather different behavior as a function of the charged-particle multiplicity.

The NRQCD ones show a close-to-linear dependence similar to that as a function of the number of MPIs. The weaker correlation between the number of MPIs and the multiplicity is possibly compensated by the presence of associated hadrons that increase the multiplicity of the events containing  $J/\psi$ , resulting in a steeper dependence. It is worth noting that recent measurements of the  $J/\psi$  production in jets [98, 99] indicate that PYTHIA underestimates hadron production associated with high- $p_T$   $J/\psi$ .

The  $J/\psi$  yields from “cluster collapse” show a somewhat less steep dependence on the multiplicity, compared to the dependence on the number of MPIs.

Finally, the non-prompt  $J/\psi$  yields show significantly steeper dependence versus multiplicity compared to that versus the number of MPIs. The reason is that these  $J/\psi$  are produced together with associated particles from the b-quark fragmentation, the b-hadron decay and the eventual recoil jet.

The above considerations also depend on whether the multiplicity selection is performed in the same rapidity range as  $J/\psi$ . In general, both  $J/\psi$  yields and charged-particle multiplicity spawn smaller range when done using multiplicity selection in different rapidity ranges. This is very well illustrated via the measurements of midrapidity  $J/\psi$  yields versus midrapidity multiplicity performed with multiplicity selections at mid- and forward rapidity (light blue and yellow points in Fig.3.17, left). While the observed trends are similar, the multiplicity selection based on the forward V0 detector results in significantly smaller range in both the  $J/\psi$  relative yields and the relative charged-particle multiplicity.

---

<sup>6</sup> Color Reconnection is a mechanism that describes the interactions occurring between color fields during the hadronization.

The results presented in this thesis show a steeper-than-linear increase of the forward  $\mathbf{J}/\psi$  yield as a function of the forward multiplicity, in contrast to the measurement performed of the forward  $\mathbf{J}/\psi$  yield versus midrapidity multiplicity and using selection on midrapidity multiplicity (red points in Figure 3.17, left). This may indicate that the linear dependence seen in the latter measurement could be due to the significantly wider range spawn in the relative multiplicity axis, and to the fewer auto-correlation effects, rather than to a major difference in the production mechanisms of  $\mathbf{J}/\psi$  at forward rapidity. It is clear that the current results still need to be complemented by other studies before more firm conclusions to be drawn. For example, the measurement of midrapidity  $\mathbf{J}/\psi$  yields versus forward pseudorapidity multiplicity could help clarify the situation.

## 3.11 Conclusion and outlook

To conclude, the forward relative  $\mathbf{J}/\psi$  yields has been measured as a function of the relative multiplicity at forward rapidity, in proton-proton collisions at  $\sqrt{s} = 13$  TeV. The results show a steeper-than-linear increase, which can be interpreted within the PYTHIA event generator as an indication that Color Reconnection mechanism is at play in the production of  $\mathbf{J}/\psi$ . The results also show a good agreement with the EPOS4HQ and the considered 3-Pomeron CGC models.

In the future, this analysis could greatly benefit from the MFT tracking information. First of all, the MFT enables particle tracking at forward rapidity. This would allow to filter out most of secondary particles, providing a more accurate measurement of charged-particle multiplicity. The measurement would also be significantly less MC-model dependent compared to present study performed using the V0C detector. In addition, the MFT will provide the possibility to study separately prompt and non-prompt  $\mathbf{J}/\psi$  production. This would be very important to establish a more appropriate comparison with theoretical models describing separately the two contributions, or describing prompt  $\mathbf{J}/\psi$  production only.

Studying the relative  $\mathbf{J}/\psi$  yield dependence as a function of the relative multiplicity in the transverse region (i.e. in the azimuthal region  $\pi/3 < |\varphi - \varphi_{\mathbf{J}/\psi}| < 2\pi/3$ ) was proposed in [94] to further investigate the role of possible auto-correlation effects from associated hadroproduction. Calculations performed with PYTHIA8 have indeed demonstrated that the usage of the transverse region diminishes the auto-correlations. This approach remains of interest today, as no such measurement has yet been published using ALICE data.

Finally, it is clear that more differential analyses are needed in order to better understand the mechanisms of the  $\mathbf{J}/\psi$  production in high-energy proton-proton collisions. One recently introduced observable is the event flattenicity. In the recent reference [100], flattenicity is proposed as an additional tool in the selection of high-multiplicity events, avoiding the biases arising from local multiplicity fluctuations and auto-correlation effects. Moreover, within the PYTHIA8 model, flattenicity can provide a proper selection of collisions with a high number of MPIs. Studying the  $\mathbf{J}/\psi$  yield as a function of both multiplicity and flattenicity can be therefore very useful to disentangle various effects involved in  $\mathbf{J}/\psi$  production.

# Chapter 4

## Towards physics results with the MFT

The MFT being a new detector of ALICE and O<sup>2</sup> being a new software framework for the experiment, several code developments were needed before this detector was ready to contribute to the ALICE physics program. These developments encompass for instance quality control, optimization of track-to-collision association and MFT time alignment with the FT0-C detector. These implementations were required to ensure the quality and usability of the MFT data and the related MC simulations.

This section covers the implementation of the various software development projects mentioned above, from the creation of a workflow that assesses the quality of MFT tracks and the application of this workflow to estimate the MFT spatial resolution, to the creation of specific codes to associate a given track to its collision and the matching of MFT tracks with the FT0-C information.

### 4.1 The MFT Quality Assessment framework

As any other ALICE sub-detectors, the MFT has a dedicated workflow for quality control purposes, called asynchronous Quality Control. This workflow stores histograms such as the ones for the kinematic distributions of MFT tracks, the *x-y* position of reconstructed clusters, the number of tracks per ROF (Read-Out Frame), using 10% of the statistics of the data taking period of which the quality is being assessed. Depending on the run, this limited statistics is sometimes not enough to spot software or detector issues: a workflow working on larger samples is then required.

This workflow was called MFT Assessment workflow and is designed to help assessing the quality of the MFT data and the related MC simulations, and to derive performance and simulation plots. This workflow can run on both A02D files and intermediate files, and produces several performance histograms as an output. It was used as a complement to the asynchronous Quality Control, exploiting the full statistics to have a more precise estimation of the information already available from the Quality Control, and provide additional information. In this Section, a few example of such histograms and their use will be discussed.

Since the MFT first reconstructed objects are clusters (groups of adjacent fired pixels in a same chip), looking at the distribution of clusters in a disk can give us information about possible inactive regions of the disk. As such, the *x-y* distribution of all MFT clusters

in a disk is a useful input, see for instance the corresponding histogram for disk 3 in Figure 4.1a. When an MFT chip is working fine, the corresponding area in the MFT disk is fully covered with clusters: the distribution shown in Figure 4.1a shows that during the specific run the data are taken from, a few chips in disk 3 were not working. In a second step, one can try to see which of the reconstructed MFT clusters are used to build tracks: plotting the  $x$ - $y$  distribution of the clusters that are part of an MFT track can give us a valuable insight, as shown in Figure 4.1b for disk 3 in the same run as in 4.1a, where one can see some white lines and rectangles that are due either to chips not sending data, or to acceptance loss in the edges of the detector due to the tracking restrictions (requiring MFT tracks to have at least one cluster in 4 different MFT disks, and at least 5 clusters in total).

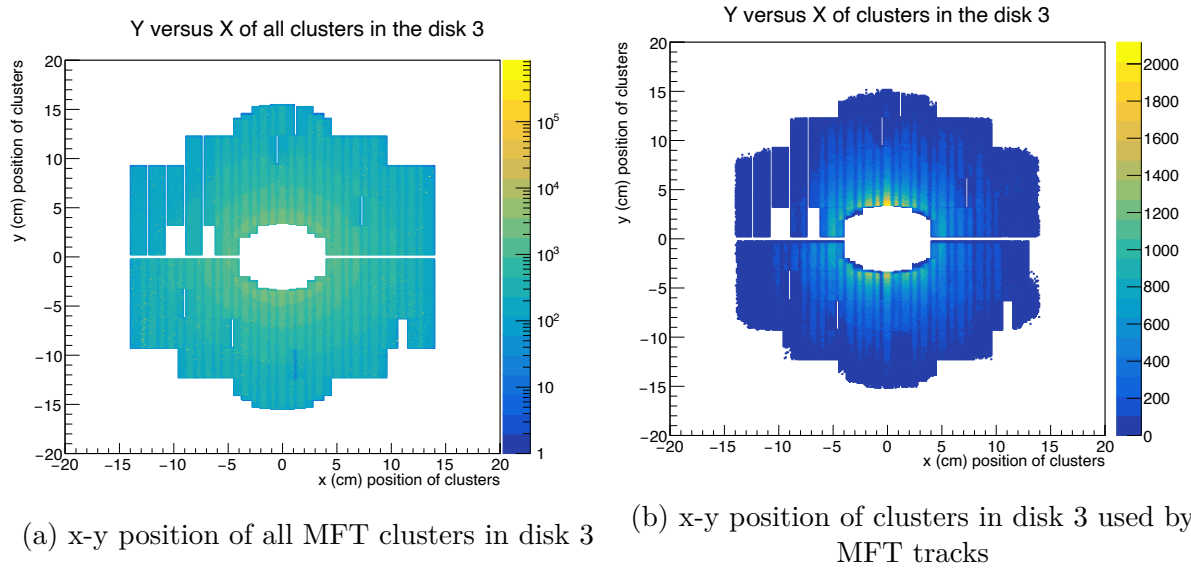


Figure 4.1: Cluster positions in disk 3

This type of histogram allows the analyzer to monitor data quality and will be particularly useful to check for example whether the MC simulations correctly reproduce the detector status in terms of inactive chips. The impact of a few chips can indeed create some holes in the detector acceptance as a function of  $(\eta, \varphi)$ , which must be reproduced by the MC. The number of clusters per track is also monitored (see Figure 4.2a), as it is an important parameter for several reasons, the most important one being that the number of clusters directly affects the quality of the reconstructed track: a higher number of clusters generally implies better spatial resolution and tracking precision, resulting in a more accurate reconstruction of the particle trajectory. Furthermore, monitoring the number of clusters per track helps when analyzing different options for the tracking algorithm optimization, making it easier to choose the optimization with the highest number of clusters per track. This is particularly relevant in Pb-Pb collisions, where the number of track candidates is very large.

Finally, the  $(\eta, \varphi)$  distribution of MFT tracks is also stored, giving us information on the acceptance of the detector and allowing to monitor the effect of alignment, which directly impacts the shape of this 2D distribution. In Figure 4.2b, for instance, one can see areas in the the  $(\eta, \varphi)$  plane which are in average less populated with tracks with

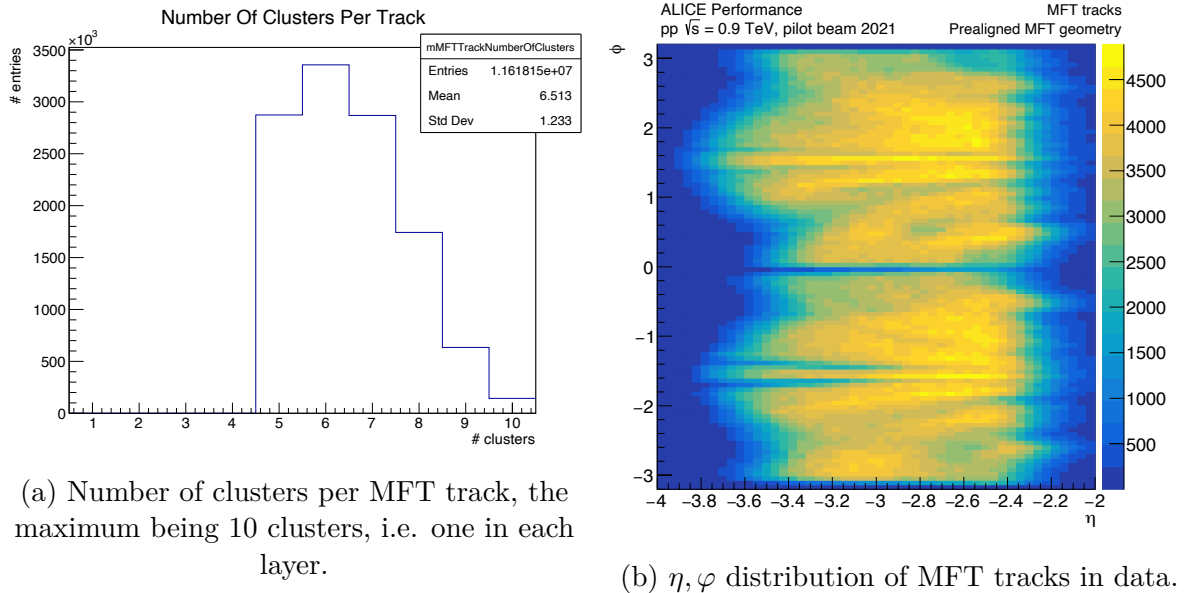


Figure 4.2: More histograms obtained with the MFT assessment workflow.

respect to the neighboring regions: these structures appear as horizontal or vertical lines in the  $x$ - $y$  plane, corresponding to chips that should be overlapping but aren't because of a misalignment of disks and chips, which leads to a loss of aligned clusters and therefore tracks in these specific regions.

A similar workflow was written to analyze MFT tracks matched with muon tracks, and is called the Global Forward Assessment workflow. It contains additional matching information but will not be developed further in this manuscript.

## 4.2 Impact of the ITS services on the MFT offset resolution

As mentioned in section 2.2.2.3, the strongest physics cases of the MFT are the measurements where the detector acts as a secondary vertexer for the Muon Spectrometer, allowing for instance to discriminate between prompt and non-prompt  $J/\psi$ . The spatial resolution of the MFT is then a critical parameter: as for any other vertex detector, this parameter is highly sensitive to the volumes sitting between the primary vertex and the first tracking disks. For this reason, the composition of the different support volumes of the ITS inner barrel, which is installed right in front of the MFT, had to be mindfully optimized. The endcap of the ITS inner barrel plays a particularly important role in this context, since the particles emerging from the interaction point region have to traverse this volume before reaching the MFT. In order to limit the impact on the traversing particles, especially in terms of multiple scattering, at the time of the preparation of the MFT Technical Design Report (TDR) [75] this volume, called “flange”, was designed to be composed of carbon fibers, element which has a low atomic number, a characteristics which allows to minimize multiple scattering effects. For reasons related to specific mechanical constraints, however, the flange (visible in figure 4.3) ended up to be made

of an aluminum alloy, an element with a larger atomic number than the foreseen carbon ( $Z = 13$  for Aluminum, instead of 6 for Carbon). Consequently, the impact of this volume on the MFT spatial resolution and on the global muon tracks resolution needed to be re-assessed in order to understand the possible degradation of the performance with respect to the studies reported in the TDR.

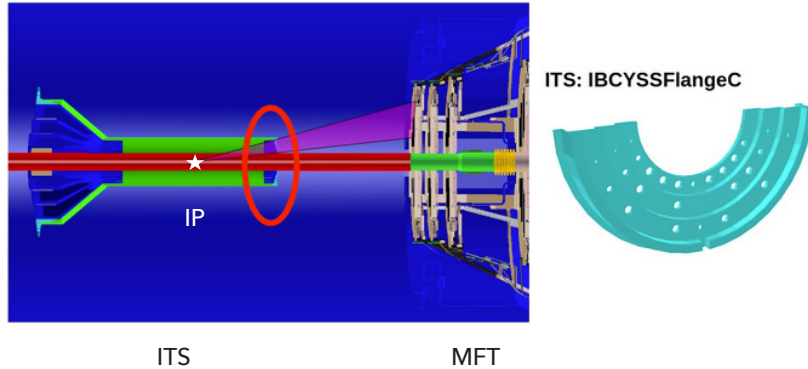


Figure 4.3: Picture of the support structures of the ITS and the MFT, the Interaction Point (IP) is represented with a white star, the flange volume is circled in red and represented on the right panel. The particles going towards the MFT cross this volume, which is 1.5 mm thick.

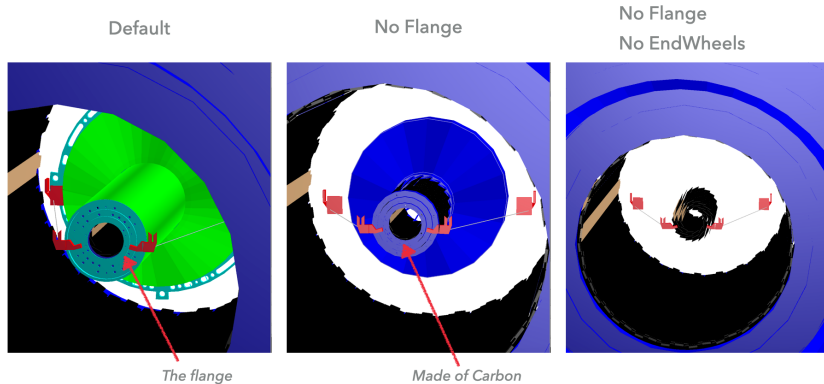


Figure 4.4: The different configurations of the detector used for the simulations

This study was performed in two steps: in the first one, the effect of the volumes on muon and charged tracks were studied considering an ideal information for the primary vertex of the collision, exploiting the analysis tools available in the “MFT assessment workflow”; in the second one, the study was refined considering realistic reconstruction conditions for the primary vertex, and a specific `O2Physics` analysis task.

#### 4.2.1 Study with an ideal vertex information

For this study, simulations of muons with a flat  $p_T$  distribution have been performed on the grid, embedded in a background of proton-proton collisions at  $\sqrt{s} = 13.6$  TeV and employing three distinct configurations for the detector setup. A box generator has been

used for muons, and PYTHIA8 for the pp background. The geometries corresponding to the aforementioned detector configurations are shown in figure 4.4. They correspond to :

1. the default setup encompassing all components of the detector;
2. a configuration excluding the flange volume;
3. a configuration excluding both the flange and the ITS end-wheels.

The analysis of the results corresponding to these configurations was carried out exploiting both the MFT “assessment workflow” and the Global Forward “assessment workflow”. For each configuration, a Monte Carlo simulation dataset has been exploited, containing approximately  $1.8 \times 10^5$  MFT standalone tracks (corresponding to unidentified charged particles) and  $1.6 \times 10^5$  muon tracks.

The considered workflows filled histograms containing the residuals (offsets)  $x_{\text{res}}$  and  $y_{\text{res}}$  of the extrapolated track to the true production vertex of the corresponding particle, the procedure to obtain these residuals is rather standard and can be described as follows: First of all, we define the true production vertex of a given particle, identifying its coordinates as  $(v_x^{\text{gen}}, v_y^{\text{gen}}, v_z^{\text{gen}})$ . This particle is reconstructed into a track exploiting the standard tracking tools. This track is then propagated inwards to the  $z$  position of its true production vertex  $v_z^{\text{gen}}$ , using an helix propagation that takes the curvature of the tracks with the magnetic field into account. This track propagation leads to 2 coordinates:  $(x_{\text{prop}}, y_{\text{prop}})$ , allowing for the definition of the residuals of the tracks at the true production vertex as:

$$x_{\text{res}} = x_{\text{prop}} - v_x^{\text{gen}}$$

$$y_{\text{res}} = y_{\text{prop}} - v_y^{\text{gen}}$$

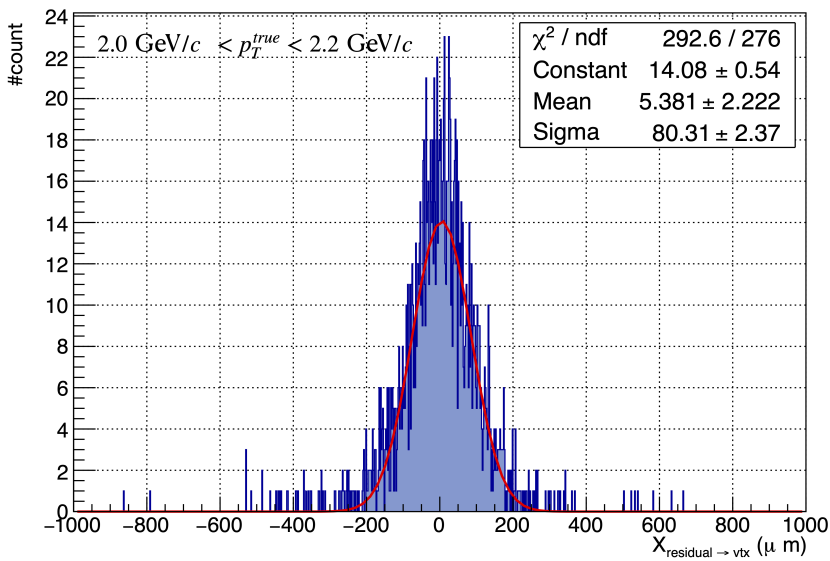


Figure 4.5: Distribution of residuals (offsets) along  $x$  for the MFT standalone tracks, for the simulations with no flange and no end-wheels.

The distributions of  $x_{\text{res}}$  and  $y_{\text{res}}$  are studied as a function of the generated  $p_T$  and  $\eta$ , respectively the transverse momentum and the pseudorapidity of the generated MC particle corresponding to the reconstructed track. An example of such a distribution is shown in the histogram in figure 4.5, fitted with a Gaussian curve.

To estimate the detector offset resolution, each distribution of  $x_{\text{res}}$  and  $y_{\text{res}}$  is fitted with a Gaussian function, and the  $\sigma$  parameter is taken as the best estimate of the resolution. This parameter is extracted as a function of  $p_T$ , for the three detector setups and for both standalone MFT tracks (unidentified charged particles) and global muon tracks (exploiting the matched information of MFT and Muon Spectrometer).

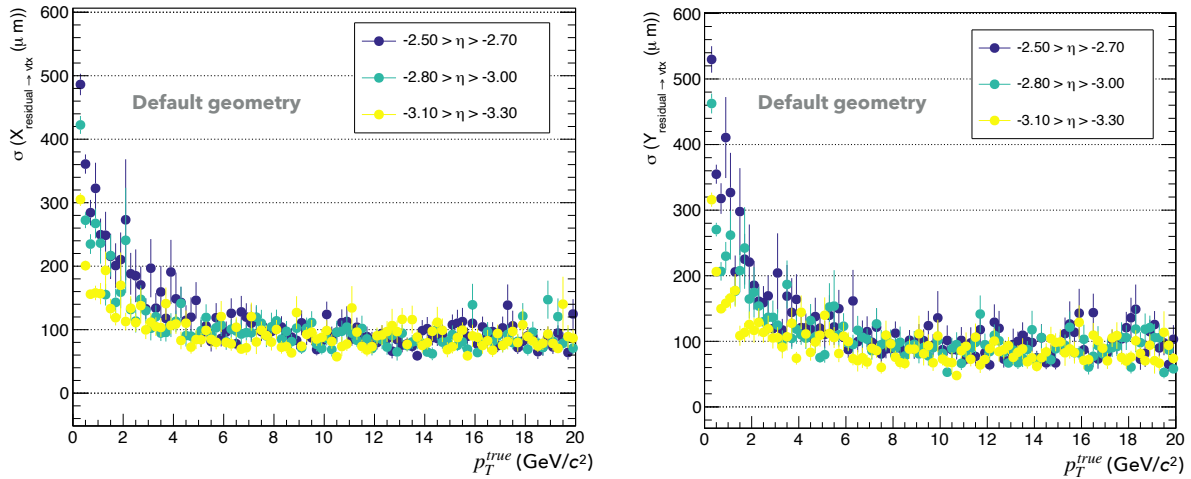


Figure 4.6: Offset resolution for standalone MFT tracks (unidentified charged particles) along the  $x$  (left) and  $y$  axis (right) as a function of the true  $p_T$ , with the default detector geometry.

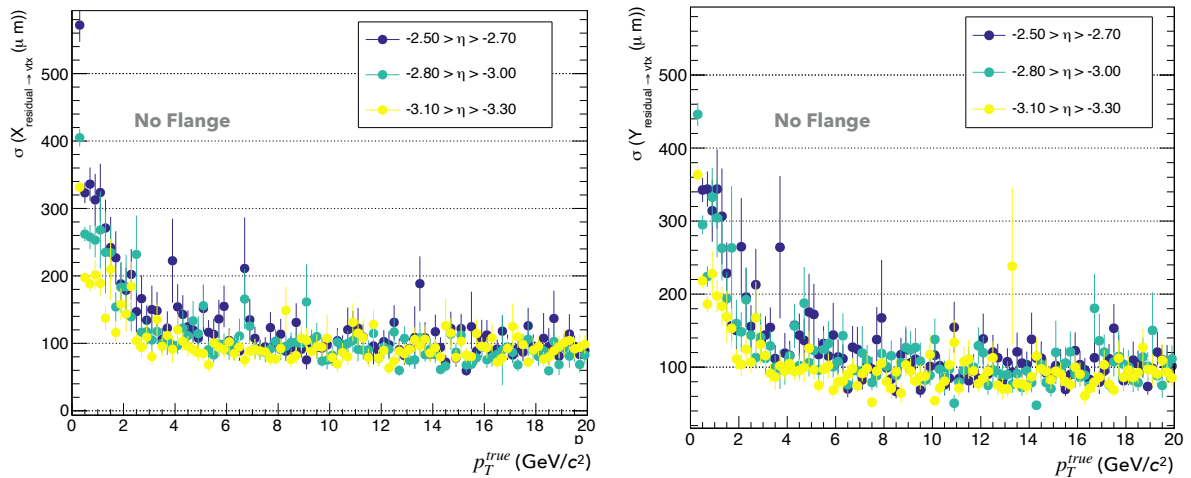


Figure 4.7: Offset resolution for standalone MFT tracks (unidentified charged particles) along the  $x$  (left) and  $y$  axis (right) as a function of the true  $p_T$ , with the detector geometry without the flange.

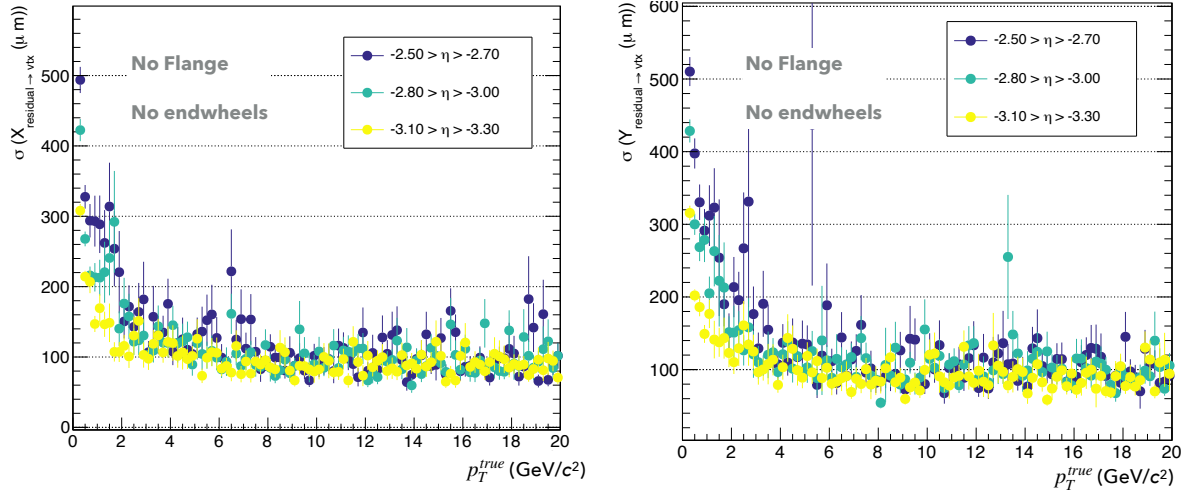


Figure 4.8: Offset resolution for standalone MFT tracks (unidentified charged particles) along the  $x$  (left) and  $y$  axis (right) as a function of the true  $p_T$ , with the detector geometry without the flange and the end-wheels.

The results of the MFT offset resolution are visible in figures 4.6, 4.7 and 4.8. It can be concluded that the presence of the flange or the end-wheels don't impact the MFT spatial resolution, as there is no significant difference between the resolution, as a function of  $p_T$ , in the three considered detector scenarios.

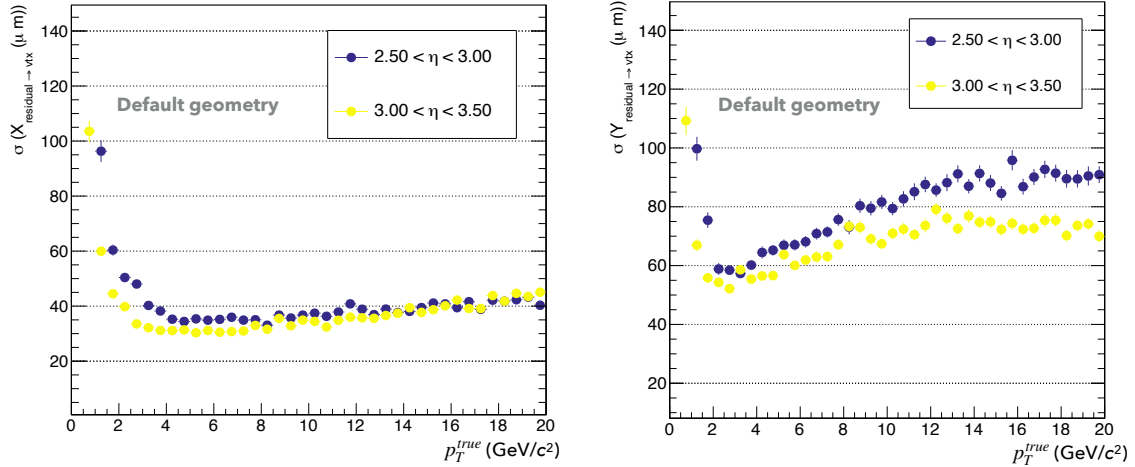


Figure 4.9: Offset resolution for global muon tracks (combining the information of the MFT and the Muon Spectrometer) along the  $x$  (left) and  $y$  axis (right) as a function of the true  $p_T$ , with the default detector geometry.

The same study is performed on the simulated sample of global muon tracks, and the

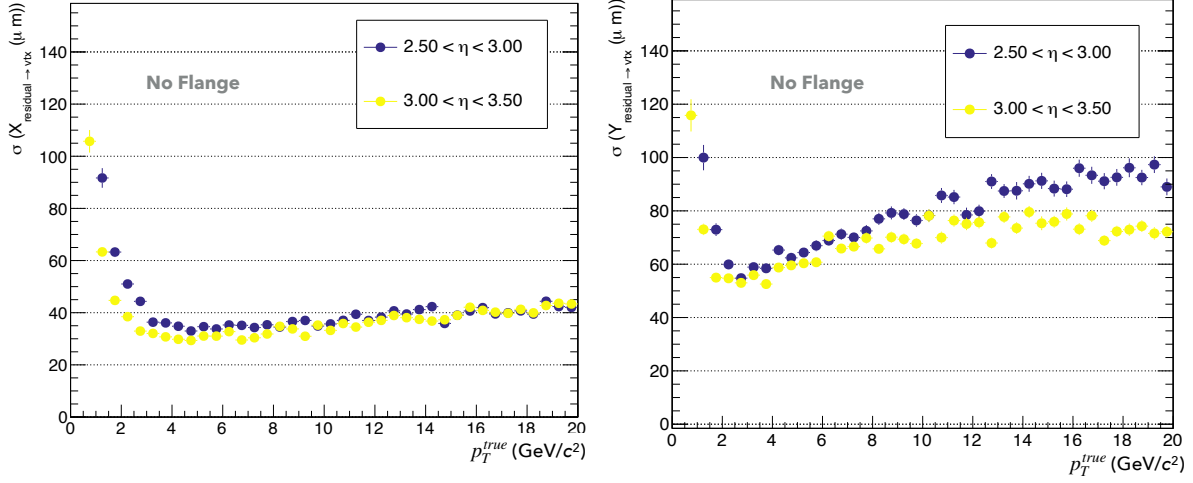


Figure 4.10: Offset resolution for global muon tracks (combining the information of the MFT and the Muon Spectrometer) along the  $x$  (left) and  $y$  axis (right) as a function of the true  $p_T$ , with the detector geometry without the flange.

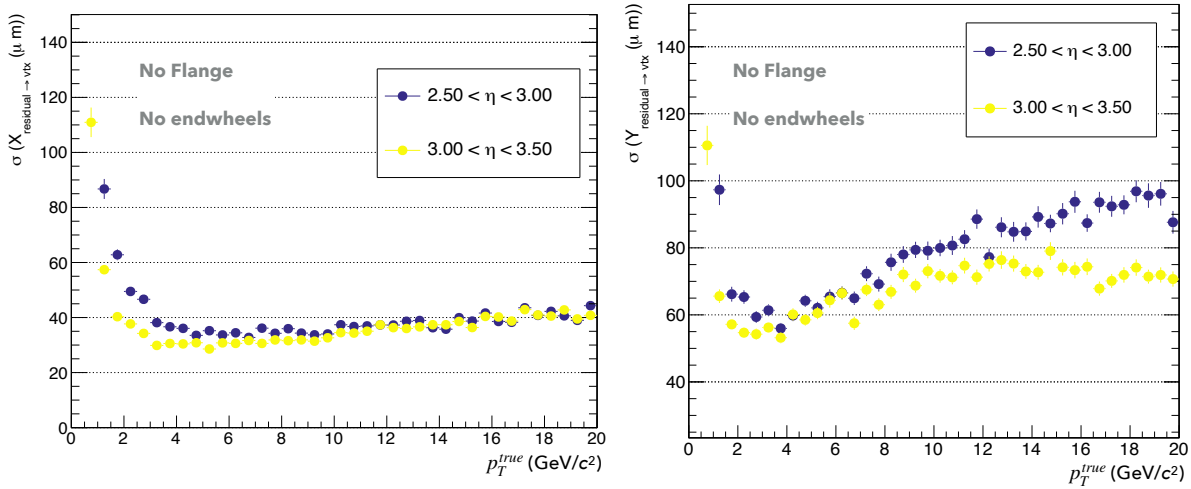


Figure 4.11: Offset resolution for global muon tracks (combining the information of the MFT and the Muon Spectrometer) along the  $x$  (left) and  $y$  axis (right) as a function of the true  $p_T$ , with the detector geometry without the flange and the end-wheels.

results are shown in Figures 4.9, 4.10 and 4.11, reporting the offset resolution for the

three detector scenarios. In this case, too, no significant worsening of the offset resolution can be noticed, and the derived resolution along  $x$  for global muon tracks is similar to the one reported in the MFT TDR [75], i.e. smaller than  $40 \mu\text{m}$  above  $p_T \sim 4 \text{ GeV}/c$ .

### 4.2.2 Study with the realistic primary vertex reconstruction

Simulations of proton-proton collisions at 13.6 TeV were performed for the study with the realistic primary vertex reconstruction, employing two distinct detector configurations: with the default detector setup, and with the setup without the flange.

Some differences must be mentioned with respect to the study presented in section 4.2.1, the first one being that the track propagation is now performed towards the reconstructed primary vertex of the collision, instead of the production vertex of the particle. Since both primary and secondary particles are produced in the MC simulation, in order to have comparable results between the two detector setups (and isolate the impact of the additional volume on the pointing resolution) only primary particles are considered, i.e. those which originate from the primary vertex. Moreover, in Run 3, some tracks can be ambiguous. i.e. the track time window overlaps with the time window of several collisions (these collisions are called the compatible collisions to that track), making the association of tracks to collisions ambiguous when simulating a realistic scenario for the data taking (section 4.3 describes in more details ambiguous tracks and their treatment). Each collision having a priori a different primary vertex, their  $z_{\text{vtx}}$  is also different, and the choice of which  $z_{\text{vtx}}$  the track should be propagated to has a direct impact on the pointing resolution. To keep this study independent of this specific aspect, only the tracks having only one compatible collision are considered here. Finally, the simulations are not muon-enriched.

Overall, for all the above reasons, this second study of the impact of the ITS services on the MFT offset resolution is more realistic than the one presented in the previous section. Once again, the goal of this study is not to provide a quantitatively precise estimation the MFT pointing resolution, but rather to isolate and estimate the effect of the flange on this quantity on the objects stored at the AOD level, which is the level at which physics results are derived.

Similarly to the previous part of the analysis, let's define the reconstructed primary vertex of one collision, which a given primary particle originates from, using the coordinates  $(v_x^{\text{rec}}, v_y^{\text{rec}}, v_z^{\text{rec}})$ . The considered particle is then reconstructed into a track. This track (which must be associated to one unique collision) is then propagated inwards to the  $z$  position of its primary vertex  $v_z^{\text{rec}}$ , using a linear propagation. The track propagation leads to 2 coordinates:  $(x_{\text{prop}}, y_{\text{prop}})$ . The residuals  $x_{\text{res}}$  and  $y_{\text{res}}$  can be defined as follows:

$$\begin{aligned} x_{\text{res}} &= x_{\text{prop}} - v_x^{\text{rec}} \\ y &= y_{\text{prop}} - v_y^{\text{rec}} \end{aligned}$$

In that case, these residuals coincide with the projections of the Distance of Closest Approach (DCA) of the track to the vertex, along  $x$  and  $y$ . Histograms of  $x_{\text{res}} = \text{DCA}_x$  and  $y_{\text{res}} = \text{DCA}_y$  are filled as a function of  $p_T^{\text{true}}$  and fitted with a sum of two Gaussians, as can be seen in Figure 4.12. The narrower Gaussian describes the core of the distribution, and its sigma parameter  $\sigma_1$  will be taken as the offset resolution for this particular  $p_T$  range.

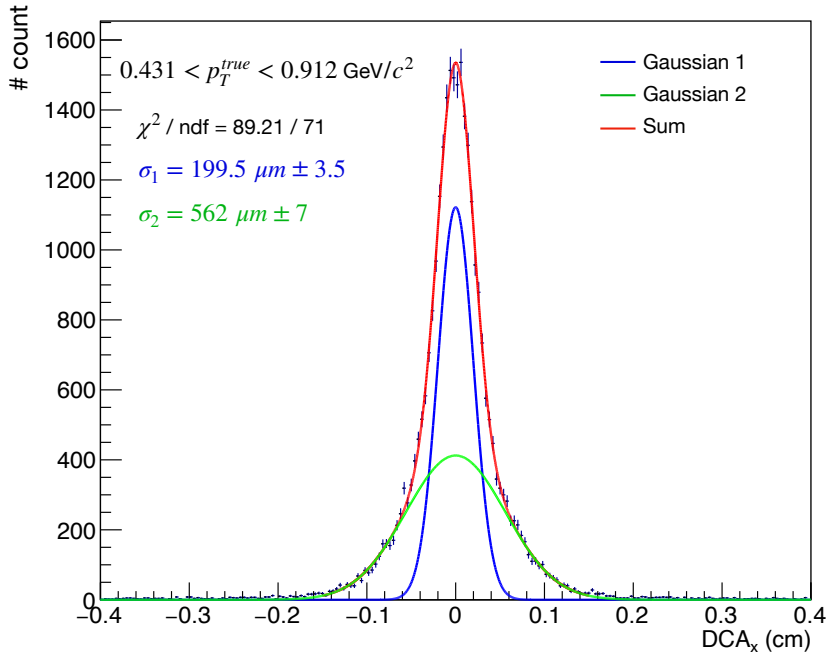


Figure 4.12:  $\text{DCA}_x$  of MFT tracks from primary particles and only non-ambiguous tracks, fitted with the sum of 2 Gaussians. The wider gaussian is used to better describe the distribution tails, while the narrower one is used for the resolution determination.

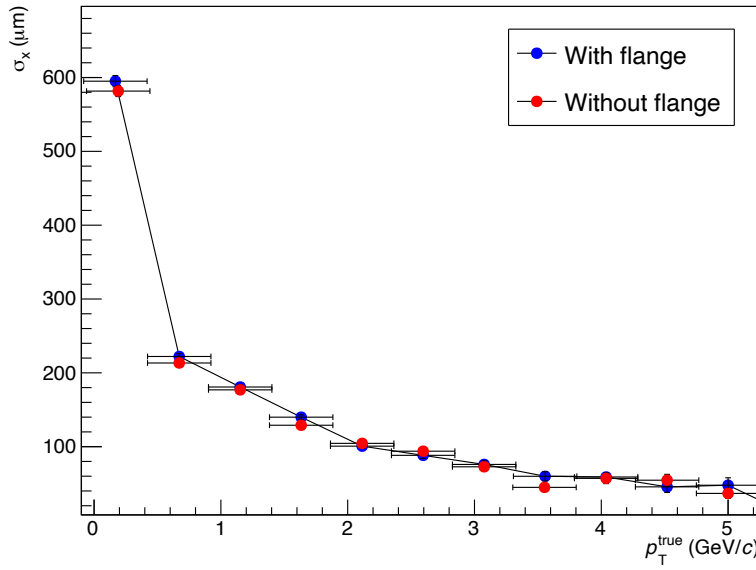


Figure 4.13: MFT offset resolution along the  $x$  axis as a function of the  $p_T$  of the MC particle.

The comparison between the MFT offset resolution along  $x$  with the flange and without the flange as a function of  $p_T$  is reported in Figure 4.13, where one can see that the impact of the flange is luckily very limited.

To conclude, the impact of the ITS service volumes on the MFT offset resolution is very small, both in simulations of single muons on top of a pp background, and in more realistic pp PYTHIA8 simulations based on A02D and realistic vertex reconstruction. The impact on the secondary vertex discrimination for displaced dimuons is then expected to be negligible, a very positive news for any analysis aiming to discriminate between prompt and non-prompt  $J/\psi$ .

## 4.3 MFT track-to-collision association

In Run 3, at the interaction rate (IR) chosen for the pp physics program in ALICE (up to 500 kHz, ten times higher than the one in Pb-Pb collisions), the time window corresponding to a reconstructed track overlaps with multiple collisions. The time window associated to a given track is determined either by the Read-Out frame (ROF) to which the clusters associated to the track belong, for detectors that collect clusters in ROF such as the ITS and the MFT, or by the approximate time and time resolution of a track for the other detectors. For example, the ITS and MFT considered as standalone detectors have a default ROF length of  $\approx 4.95 \mu s$  in proton-proton collisions, corresponding to 198 bunch crossings (BC). With an Interaction Rate (IR) of 500 kHz (the nominal interaction rate in pp collisions in ALICE), there is in average one collision every  $2 \mu s$ , meaning that the readout window associated to a given standalone ITS or MFT track overlaps with  $\approx 2.5$  collisions on average. The number of collisions overlapping with one readout window depends on the IR of the data-taking period, and more specifically on the filling scheme of that period.

Knowing the specific time window in which the particle corresponding to the reconstructed track crosses the detector, and the time associated to the different collisions (i.e. to the different reconstructed primary vertices), one can associate a track to the different collisions it is time-compatible with.

### 4.3.1 The track-to-collision-associator

In the 02 framework, after the tracks are reconstructed, the vertex reconstruction takes place, based on the available ITS-TPC tracks. These tracks are grouped into contributor tracks, i.e. tracks that are compatible with the same primary vertex. The next step consists in associating the other tracks (the non-contributor ITS-TPC tracks, which are not used for the determination of the primary vertices, and the tracks reconstructed in other detectors like the MFT) to the reconstructed primary vertices: by definition, all the tracks associated to a given primary vertex come from the same collision.

This procedure is performed in 02 by means of a track-to-vertex association, based on the time information of the track and the available primary vertices. In case more than one vertex is time-compatible with the reconstructed track, the algorithm associates the track, by default, to the first time-compatible collision. This information is passed to the last stage of the data reconstruction, where the data are registered in the format called Analysis Object Data (A02D): as a result, the standalone MFT track table (as well as the other track tables) contains for each track the index to one compatible collision, which is the first collision in time compatible to this track [101]. Of course, when several time-compatible collisions are available for a given track (their quantity depending on the

track time window and the IR), there is no specific reason for the collision that created the track to be the first collision among the compatible ones. Since at the A02D level only the first compatible collision index is stored in the track table, it is then necessary to create a code which can process the A02D information, recover for each track the list of all compatible collisions, and choose wisely which collision is the most likely to be the one associated to the track.

This association is done in `O2Physics` using two different tasks for the different types of tracks:

- `o2-analysis-track-to-collision-associator`, for the tracks reconstructed in the central barrel;
- `o2-analysis-fwdtrack-to-collision-associator` for the tracks reconstructed in the forward direction, i.e. muons and MFT tracks.

Both tasks are based on the same code that loops over each track, and for each track loops over all the available collisions. For efficiency purposes, a loose cut is applied on the BC difference  $|BC_{\text{track}} - BC_{\text{coll}}|$ , where  $BC_{\text{track}}$  is the BC of the middle of the time window of the track and  $BC_{\text{coll}}$  the BC of the collision  $coll$ , to avoid processing a collision if it is too far (in time) from the considered track.

The selection must be cautiously configured as a compromise between avoiding the elimination of possible time-compatible collisions for a specific track, and including in the loop collisions that are significantly far from the track in time. For the MFT, this loose cut has been configured such that the collisions having their  $BC_{\text{coll}}$  more than 460 BC away from  $BC_{\text{track}}$  are eliminated. If a given collision passes this first, loose cut, then a second, stricter one (also based on the time difference between the collision and the track) is applied, as described below.

The second cut is implemented in a different way for tracks reconstructed by detectors characterized by sharp readout windows, or detectors characterized by a gaussian-like time resolution.

For detectors that reconstruct tracks associating them to sharp readout windows, such as the ITS and the MFT,  $t_{\text{track}}$  is defined as the center of the track readout window, and its associated time uncertainty is defined as  $\sigma_{\text{track}} = \frac{\text{readout window size}}{2}$ .  $t_{\text{track}}$  is then associated to a box-like time error, meaning that the track crossed the detector in the time range  $[t_{\text{track}} - \sigma_{\text{track}}, t_{\text{track}} + \sigma_{\text{track}}]$ , as shown in Figure 4.14.

For the other detectors, the time resolution of the track is gaussian-like, meaning that the track has crossed the detector around the time  $t_{\text{track}}$ , with a gaussian standard deviation  $\sigma_{\text{track}}$  (see Figure 4.15).

For each collision  $coll$  passing the first cut, one can define  $t_{\text{coll}}$  as the time at which this collision occurred and its associated gaussian time uncertainty as  $\sigma_{\text{coll}}$ . One can then compute the time difference between the track and the collision as  $\Delta t = |t_{\text{track}} - t_{\text{coll}}|$ . The collision is considered compatible in time with the track if  $\Delta t < \Delta_{th}$ , where the threshold  $\Delta_{th}$  is defined as:

- $\Delta^{th} = \sigma_{\text{track}} + n_{\sigma} \times \sigma_{\text{coll}}$ , for tracks characterized by a box-like time uncertainty;
- $\Delta^{th} = n_{\sigma} \times \sqrt{\sigma_{\text{track}}^2 + \sigma_{\text{coll}}^2}$ , for tracks characterized by a gaussian-like time uncertainty,

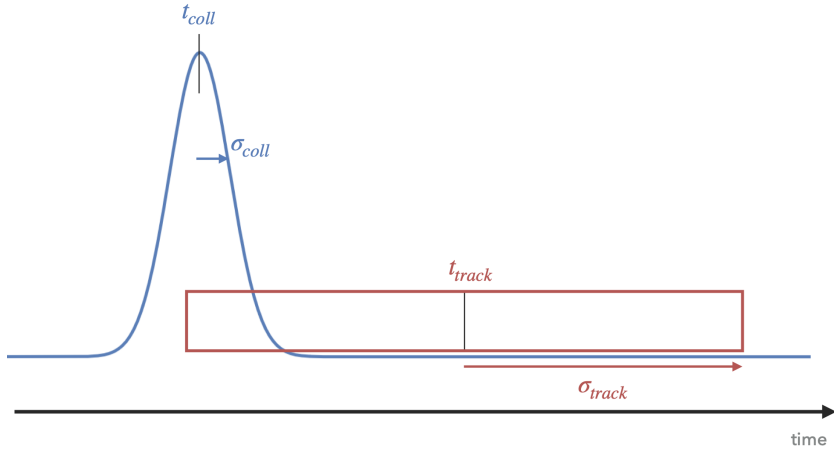


Figure 4.14: Track time for detectors characterized by a sharp readout window, and collision time.

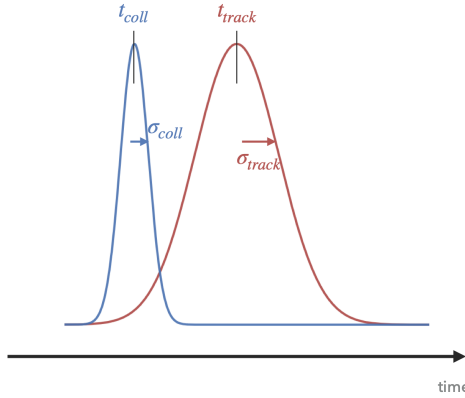


Figure 4.15: Track time for detectors characterized by a gaussian resolution, and collision time.

with  $n_\sigma$  being a configurable  $\geq 1$  set to 4 by default.

This configurable can be changed by the analyzer, the higher its value is, the less likely it is to miss the track's true collision. The downside is that the number of compatible collisions per track increases with  $n_\sigma$ , since  $\Delta^{th}$  increases.

The results showed in the following were computed with  $n_\sigma = 4$ .

The task then fills a table containing for each track the list of their compatible collisions. Any track that has more than one compatible collision is then identified as an ambiguous track.

Figure 4.16 shows the number of compatible collisions per MFT track for one run of the LHC22o data taking period. For this particular run the IR was 658 453 Hz, which corresponds to one collision each  $1.519 \mu\text{s}$  on average: one expects to have each MFT track compatible to 3.3 collisions on average, which is close to the mean of the histogram. For proton-proton collisions at  $\sqrt{s} = 13.6 \text{ TeV}$ , the nominal IR in ALICE was chosen to be 500 kHz, corresponding to one collision each  $2 \mu\text{s}$  in average. Under these conditions the percentage of ambiguous MFT tracks is then rather high (about 90% of all MFT tracks

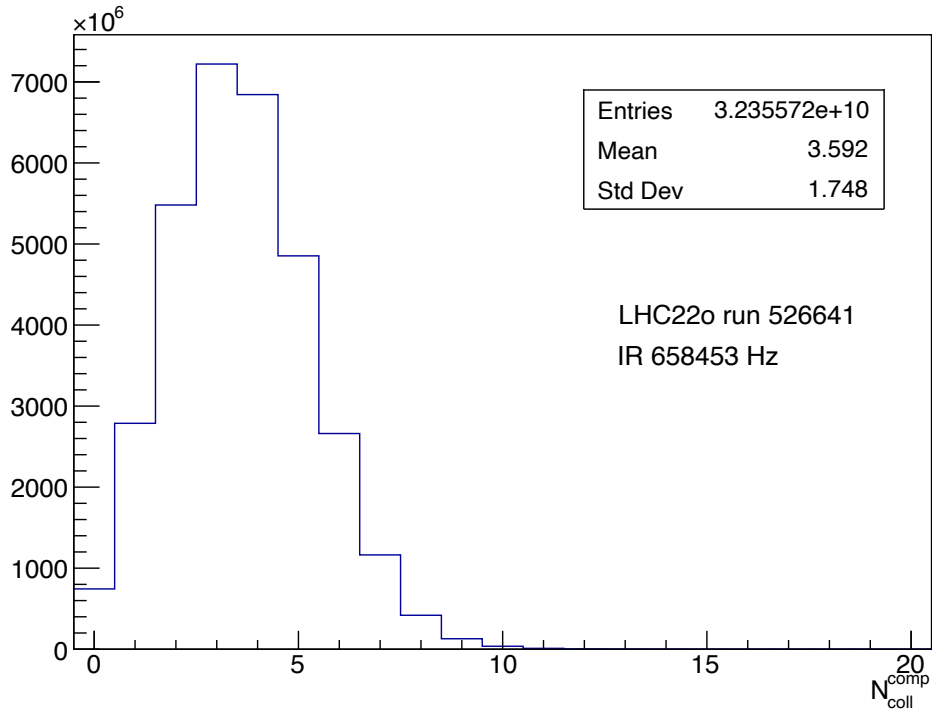


Figure 4.16: Histogram of the number of compatible collisions per standalone MFT track for one run of the LHC22o data taking period (pp collisions at  $\sqrt{s} = 13.6$  TeV). The total number of processed MFT tracks is  $3.23 \times 10^{10}$ .

are ambiguous for the dataset LHC22o), and one needs to wisely choose which collision the track should be associated to. The way this step is performed also depends on the type of analysis one wants to carry: for some analyses the analyzer may need a unique collision for each track, for others they may want to consider all compatible collisions. The process of associating a track to its collision is especially crucial if one wants to study particular processes involving exclusive particle production: a prime example is the study of  $J/\psi$  production, where the analyzer will need to characterize as best as possible the environment accompanying the production of the  $J/\psi$  particle, the primary vertex of the collision, the particles produced alongside the  $J/\psi$ , and other parameters. All of these requirements can only be met if one knows which tracks originate from which collisions.

### 4.3.2 The track-to-collision reassociation

One of the most robust methods to perform a reliable track-to-collision association is based on the computation of the Distance of Closest Approach (DCA) between the track and all the compatible collisions, these collisions being determined using the `track-to-collision-associator` workflow (section 4.3.1). The idea underlying this method is to assign each track to the collision minimizing the  $DCA_{xy}$  of the considered track.

Since the largest fraction of the reconstructed tracks correspond to particles originating from a primary vertex, this method is particularly fitted to associate any ambiguous track to the collision it most likely originates from.

To describe in more details how the algorithm works, let's consider one ambiguous MFT

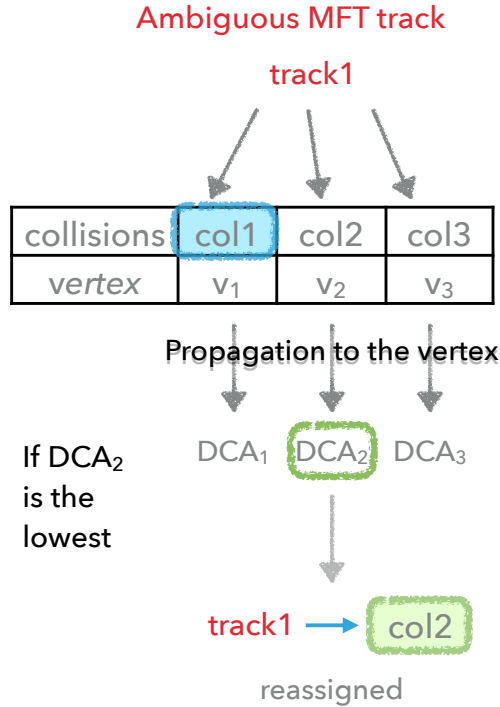


Figure 4.17: Schematic of the different steps of the algorithm leading to the reassociation of an MFT track to the collision with the smallest  $DCA_{xy}$ . “col1”, “col2” and “col3” are the collisions compatible with this track, obtained with the fwdtrack-to-collision-associator.

track. This track is compatible to several collisions  $coll_i$ , each corresponding to a primary vertex  $v_i$  with coordinates  $(v_i^x, v_i^y, v_i^z)$ . The track parameters are then propagated to each  $v_i^z$  using a helix propagation taking into account the magnetic field of the L3 magnet. Let's call the propagated parameters of the track  $(x_p, y_p)$ . We can then define the DCA along the  $x$  and  $y$  axis, and the  $DCA_{xy}$  for the collision  $coll_i$ :

$$DCA_{x,i} = x_p - v_i^x$$

$$DCA_{y,i} = y_p - v_i^y$$

$$DCA_{xy,i} = \sqrt{DCA_{x,i}^2 + DCA_{y,i}^2}$$

The best fitted collision for a given track is then the one which provides the smallest  $DCA_{xy,i}$ . As a final step of the algorithm, a table is built containing the track indices and the index of their respective reassigned collision. The reassociation process is schematically illustrated in Figure 4.17 for an ambiguous MFT track “track1”.

## 4.4 MFT matching with FT0-C

Given that the MFT is a relatively slow detector, the concept of pairing its tracks with signals from much faster detectors appears promising. The perfect candidate for this

pairing is the FT0-C detector, which combines high time resolution and an appropriate location, between the MFT and the muon absorber.

In the following, the FT0-C will be described in more details and the matching procedure of MFT tracks to FT0-C signals will also be explained. In this section, the FT0-C and MFT are considered time-aligned. As we will explain in section 4.5, it is not the case in data but it is the case in MC simulations.

#### 4.4.1 FT0-C specifications

The FT0-C is a quartz Cherenkov detector located  $-82.6$  cm away from the Interaction Point (IP) behind the MFT along the  $z$  axis, covering the pseudorapidity region  $-3.4 \leq \eta \leq -2.3$ . It is a very fast detector, part of the FIT (Fast Interaction Trigger) with a time resolution close to 13 ps.

The FT0-C is divided into 28 modules, each divided in 4 channels (also called quadrants) [102] [103]. Each channel is identified by an integer number, the ChannelID, going from 96 to 207, as one can see in Figure 4.18, and has a size of  $2.65 \times 2.65$  cm $^2$ .

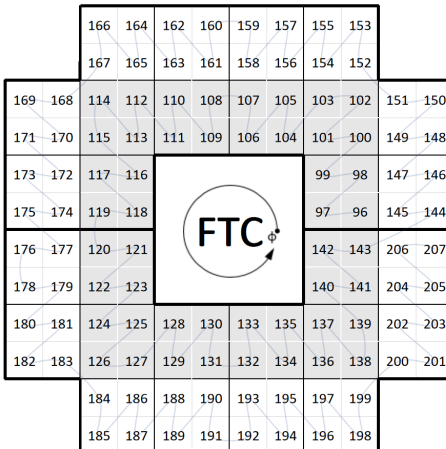


Figure 4.18: FT0-C channel map (view from IP)

In the AO2D, the FT0-C signals are stored in a table which contains the globalBC of the signal (information on the BC and orbit in which it occurred) and the ChannelID of the quadrants that received non-zero amplitudes. Knowing the ChannelID, one can then obtain the position of the center of the channel that received a signal.

As mentioned previously, the FT0-C is located between the MFT and the muon absorber, therefore there is almost no material budget between the two detectors, making the propagation of MFT tracks towards the FT0-C straightforward. The only limitation to the matching comes from the FT0-C dead zones.

Indeed, due to the geometry of the FT0-C and the position of the different modules, some specific regions are not covered by the active volumes of the detector, as explained in section 4.4.3.

#### 4.4.2 BC range of an MFT track

MFT tracks are grouped into Readout Frames (ROFs), which represent predefined time intervals that contain the time at which the tracks crossed the detector. The width of each ROF takes into account the time resolution of the chip and of the readout chain. In proton-proton datasets, each MFT ROF is 198 Bunch Crossings (BC) long, or  $198 \times 25 \text{ ns} = 4.95 \mu\text{s}$  (in a few datasets the ROF length was larger, but in the study presented here we will only focus on datasets with a ROF length of 198 BC).

The FT0 (A or C) data stored in AO2D files contain the information of the BC and orbit each signal occurred in, so that one can identify all of the FT0-C signals corresponding to a particular BC and orbit. The pair (BC, orbit) is encoded in the globalBC integer identifier.

For each MFT track it is then possible, starting from the range of globalBC corresponding to its time window, to gather all of the FT0-C signals that occurred within its ROF.

#### 4.4.3 Matching procedure

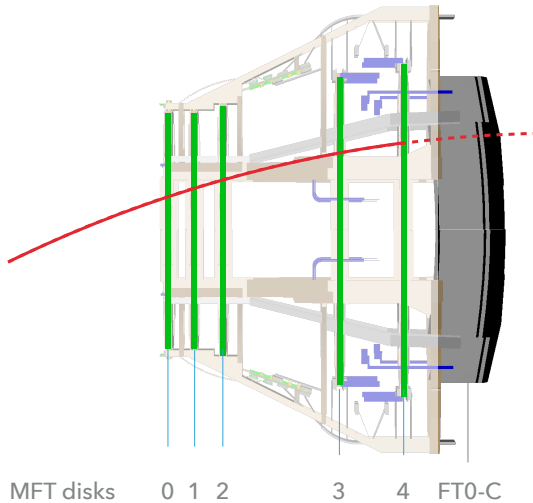


Figure 4.19: Extrapolation of one MFT track towards FT0-C

The MFT-FT0-C matching procedure is based on the comparison between the spatial position of the extrapolated MFT track and the position of the time-compatible FT0-C hits.

The procedure involves the following steps (we will consider only one MFT track and its associated ROF in the following, but the steps are repeated for each MFT track):

- First, all MFT tracks are extrapolated to the average  $z$  position of FT0-C quadrants, at  $z = -82.6 \text{ cm}$ , using an helix propagation. The inputs used for this operation are the B field in the propagation region and the track parameters.
- After the track has been propagated, all FT0-C signals that occurred during the MFT ROF are gathered, as explained in section 4.4.2, and their positions are extracted via their ChannelID. The FT0-C signals which are time-compatible with

the MFT track can occur in different BCs, and a given FT0-C channel can be fired several times during the MFT ROF (i.e. several of the selected FT0-C signals can correspond to the same FT0-C channel).

- Let's note  $(x_e, y_e, -86.2)$  the extrapolated coordinates (in cm) of the MFT track at the FT0-C average  $z$ . If the point identified by these coordinates falls within the volume of a fired FT0-C quadrant (time-compatible with the MFT track ROF), the MFT track is **matched** with that FT0-C signal. The point is declared to fall inside the volume of a given FT0-C quadrant if its distance from the center of the quadrant is smaller than a cutoff  $r$ . The value of  $r$  is determined with MC simulations, studying the distribution of the distance between the extrapolated MFT track and the center of the fired FT0-C quadrant, for MC particles leaving signals both on the MFT track and the FT0-C.

Simulations of around 1 Million minimum-bias proton-proton events with PYTHIA8-Monash generator were needed, with the full detector simulation and reconstruction. These simulations were tuned to the 2022 data taking period LHC22o in order to consider realistic interaction rate and reconstruction conditions. Studying this MC sample had two main purposes: to determine the cutoff  $r$  to be used in the MFT-FT0-C matching procedure, and to estimate the matching efficiency and purity.

## Determining the matching cutoff

The determination of the matching cutoff imposed the analysis of intermediate reconstruction objects in the output of the MC simulations, meaning objects available before the production of AO2D, and not propagated to the AO2D. In these intermediate objects, each FT0 signal has one or several MC-labels pointing to the MC particle(s) that left these signals. This is also the case for MFT tracks. By imposing the MC-label of the MFT track to be the same as the MC-label of the FT0 signal, one can identify the cases in which the same particle produced the MFT track and the FT0-C signal: MFT tracks satisfying this condition are called **MC-matched** MFT tracks.

The first quantity to study for MC-matched MFT tracks is the distance  $D$  between the position of the propagated MFT track at the FT0-C average  $z$ , represented by the coordinates  $(x_e, y_e, -86.2)$ , and the center of the FT0-C channel sharing the same MC-label as the track, identified by the coordinates  $(x_c, y_c, z_c)$ :

$$D = \sqrt{(x_c - x_e)^2 + (y_c - y_e)^2 + (z_c - 86.2)^2} \quad (4.1)$$

The distribution of this distance  $D$  (in cm) is represented in Figure 4.20, showing that almost every match corresponds to a distance between the propagated track and the FT0-C channel center  $D < 2$  cm. For this reason,  $r = 2$  cm has been retained as the value for the cutoff of the matching condition between the extrapolated MFT tracks and the corresponding FT0-C quadrants.

## FT0-C dead zones

The FT0-C geometry consists of modules, which are separated in the transverse plane. Consequently, the peripheral zones of each module have limited efficiency, and often in

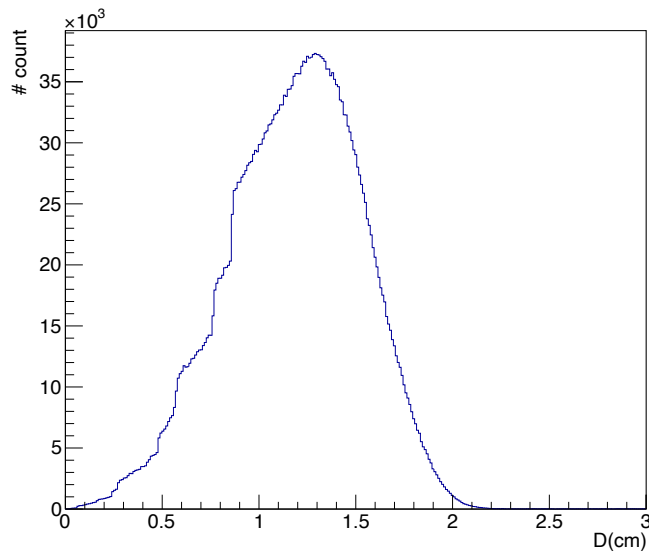


Figure 4.20: Distribution of the distance  $D$  (in cm) between the extrapolated MFT track and the center of the FT0-C channel sharing the same MC-label as the track

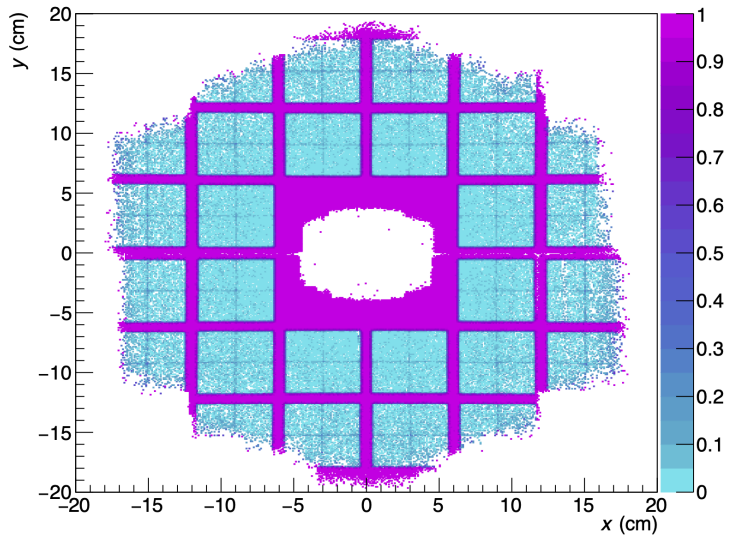


Figure 4.21: Probability for MFT tracks **not** to match with any FT0-C signal. The central rectangular FT0-C hole is clearly visible in pink, together with the inefficient peripheral zones of the different FT0-C modules. The white areas correspond to zones without MFT tracks (the shape of the MFT detection planes results in the circular hole at the center).

these regions the signal is lost. This effect is visible when looking at the probability for MFT tracks **not** to match with any FT0-C signal, see Figure 4.21. This probability is computed by calculating the difference between the total number of MFT tracks and the number of MFT-FT0-C MC-matched tracks, divided by the total number of MFT tracks.

The MFT tracks falling in the central hole of the FT0-C can be easily excluded by removing MFT tracks with extrapolated positions fulfilling this condition :

$$|x_e| < 6.365 \text{ cm AND } |y_e| < 6.555 \text{ cm}$$

In order to only keep tracks benefiting from a good matching efficiency, one then needs to exclude the MFT tracks falling into the inefficient regions in the periphery of each modules. Conveniently, these regions are very well defined in space with a structure consisting of vertical and horizontal bands. Thanks to this specificity, the regions to be excluded can be defined by projections of the 2-dimensional matching efficiency and can just be excluded with a few lines of code. The excluded regions are defined as the ones where the matching efficiency, computed as the ratio between the number of MC-matched MFT tracks and the number of MFT tracks, is lower than 0.65 for a given extrapolation coordinate  $x_e$  or  $y_e$ . The matching efficiency as a function of  $x_e$  is represented in Figure 4.22, together with the threshold of 0.65 and the regions to be excluded on the  $x$  axis. The same strategy is repeated with the matching efficiency as a function of  $y_e$ .

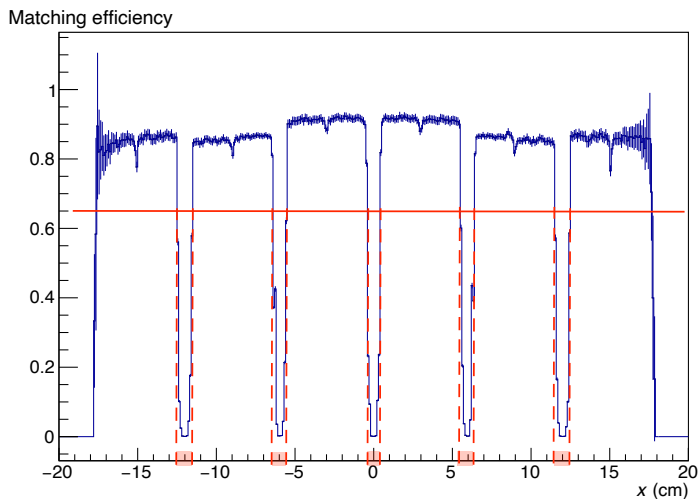


Figure 4.22: MFT-FT0-C MC-matching efficiency as a function of the extrapolated  $x$  position of the track: the  $x$  regions highlighted in red are the regions that will be excluded.

The matching efficiency was also computed on data to check that the removal of dead zones was adequate. To do this check, the matching efficiency  $N_{\text{tracks}}^{\text{matched}}/N_{\text{tracks}}$  was obtained as a function of the extrapolated MFT tracks  $x$  and  $y$  coordinates, with the MFT extrapolated tracks falling into the peripheral zones of modules excluded or not. The result of this check is visible on Figure 4.23 and was evaluated with a time shift of 47 BC (see subsection 4.5 for the definition of this BC shift).

The matching efficiency after removing the boundary regions between FT0-C modules can be seen on the right panel of Figure 4.23. The inefficient horizontal and vertical bands of the FT0-C, in blue-green on the left panel, were successfully excluded. In most of the quadrants, the matching efficiency is higher than 94 %, leading to a very reliable matching procedure and opening the ground to physics analysis using these MFT-FT0C tracks.

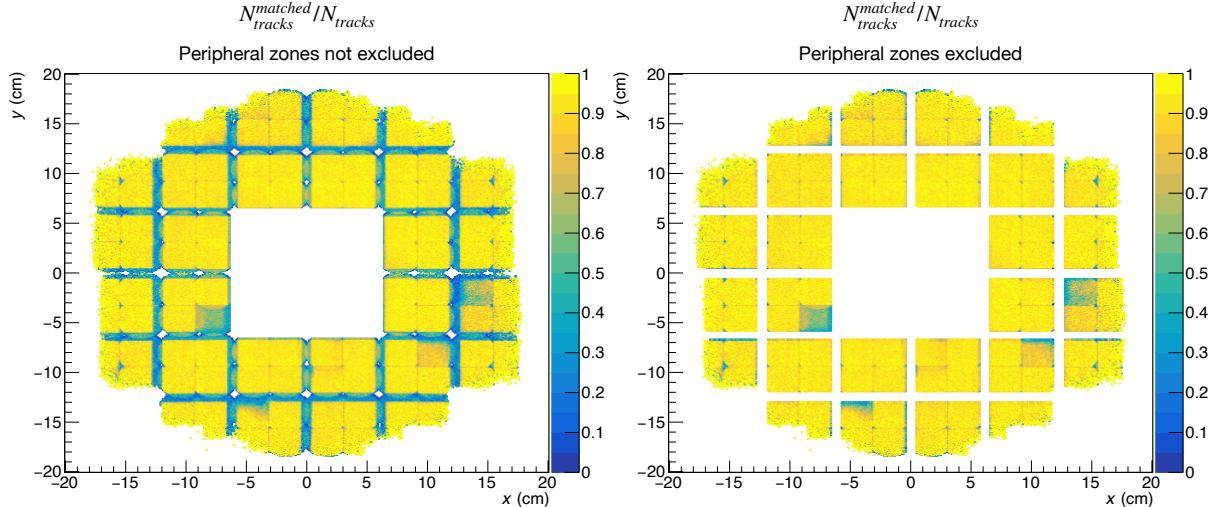


Figure 4.23: MFT-FT0-C matching efficiency before and after excluding inefficient regions

#### 4.4.4 Illustration of the matching

Because the matching procedure and the corresponding results are non trivial, a visual illustration is presented in this section, based on MC simulations.

A single MFT track is considered here, that has been propagated to the FT0-C plane ( $z = -86.2$  cm). The FT0-C signals that occurred within the MFT track ROF are gathered and their ChannelIDs are determined. One can then represent each fired FT0-C channel within the MFT ROF on the FT0-C plane, as seen in the left panel of Figure 4.24. Each FT0-C quadrant (or channel) is represented as a square with a black outline. If the channel has been fired during the MFT ROF, its interior will be filled with light gray, on top of which will be a square of color that corresponds to the BC of the fired signal (see legend). One channel can be fired multiple times during one MFT ROF, hence one quadrant can be filled with different colored squares.

The BC number in the legend is just an index, BC 0 being the first BC (within the MFT ROF) with an FT0-C signal corresponding to it.

The extrapolated coordinates of the MFT track are represented with a red star.

In the zoom box of Figure 4.24, one can see that the channel that was hit by the MFT extrapolated track (bottom left quadrant) has been fired during BC 1 and BC 3. The distance between the extrapolated track and the center of that FT0-C channel being smaller than 2 cm, the MFT track is **matched**.

Once an MFT track has been matched with FT0-C signals the time window of the track can be subsequently reduced. In the right panel of Figure 4.24, the focus is on the same track as on the left panel, which has matches with two FT0-C signals in two different BCs (BC 1 and BC 3). One can then suppose that the MFT track was produced in one of these two BCs, and it was checked that in this case the particle that left the MFT track had indeed been created during BC 3. The track time window associated to the MFT track is consequently reduced from one ROF (by default 198 BCs long in p-p collisions) to 2 BCs, assuming that the BC of the original particle is unknown.

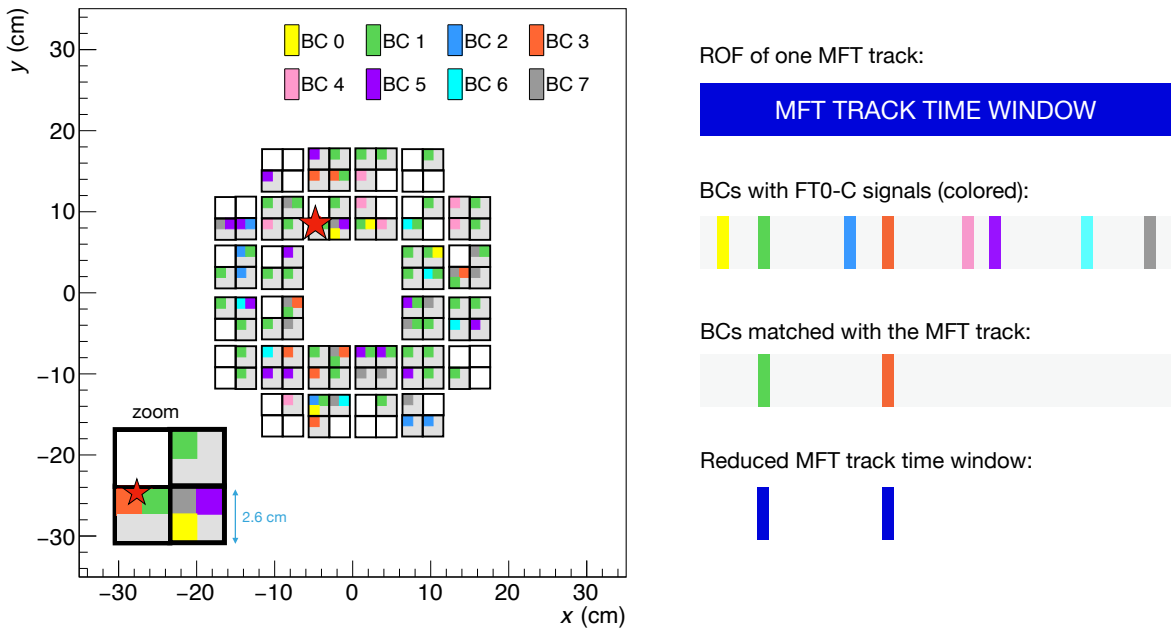


Figure 4.24: On the left: Extrapolation of one MFT track towards FT0-C, the FT0-C and extrapolated MFT track coordinates (marked by a red star) are visible in the  $xy$  plane of  $z$  coordinate  $-82.6$  cm. On the right: reduction of that MFT track time window.

#### 4.4.5 Matching efficiency and reliability in MC

Using the same MC simulations mentioned above, and having established the cutoff radius for the matching of an MFT with an FT0-C signal ( $r = 2$  cm), and identified the zones to be excluded for the matching to be efficient, the matching probability was further studied considering several parameters:

1. The percentage of **matchable** tracks, defined as the percentage of MFT tracks that fall within the FT0-C geometrical acceptance (i.e. excluding the FT0-C dead zones) and that have their origin BC inside the MFT ROF<sup>1</sup>. This percentage is  $N_{\text{matchable}}^{\text{tracks}}/N_{\text{tracks}}^{\text{total}}$ , with  $N_{\text{tracks}}^{\text{total}}$  the total number of MFT tracks excluding fake tracks and tracks coming from electronic noise. In the MC simulations considered, this percentage was found to be 54.1%. This low efficiency is due to the FT0-C dead zones.
2. The percentage of **MC-matched** tracks, defined as the ratio between the number of MFT tracks with FT0-C signals with the same MClabel and the number of matchable tracks. This percentage was found to be 92.5% in the considered MC. It is not 100% since the MC simulation takes into account the inefficiency of the FT0-C detector.

<sup>1</sup>It was noted that in some cases, the particle was generated after the end of the ROF, but the track was still stored in the ROF.

3. The ratio between the number of **matched** MFT tracks (i.e. the number of MFT tracks that find a signal in an FT0-C channel within 2 cm of the track extrapolated position and within the corresponding MFT ROF) and the number of matchable tracks. This ratio, which can be interpreted as an intrinsic efficiency of the MFT-FT0-C matching in MC simulations, has been found to be 96.2%. This ratio is higher than the percentage of **MC-matched** tracks because some of these matches are occurring with FT0-C signals not originating from the same particle as the MFT track (fake matches). Again, this percentage is lower than 100% due to the inefficiency of the FT0-C implemented in the MC.

These numbers show that when the MFT tracks cross the FT0-C geometrical acceptance, a very high percentage of them are matched. This strengthens the interest of the MFT-FT0-C matching.

It is also necessary to study the reliability of the matching. As a reminder, the goal of this matching is to estimate the time of creation of the particle that left an MFT track, with a better resolution than the one corresponding to the MFT ROF. By checking that among the FT0-C signals matched with the track, at least one of them corresponds to the same BC as the BC of the original particle, one can study the reliability of the matching. To this end, the MFT matchable tracks will be separated into two categories:

- The tracks in the first category are matchable tracks that don't find any FT0-C signal within 2 cm of the extrapolated position (and within the MFT track ROF), meaning that these tracks are not matched with any FT0-C signal. This condition corresponds to a probability of  $3.8\% = 100\% - 96.2\%$ : these tracks have not been matched because the particle responsible for the track did not leave an FT0-C signal.
- The tracks in the second category are matchable tracks **with** matches with FT0-C signals. As mentioned previously, these tracks represent 96.2 % of the matchable sample, and within these tracks 98.5 % of them have a match with an FT0-C signal corresponding to the same BC of the particle creation. In other words, 94.7 % of the matchable tracks have an FT0-C match that has the same BC as the BC of the particle corresponding to the MFT track. It is important to keep in mind that though this fraction is really high, one MFT track can match several FT0-C signals in different BCs, due to the length of the MFT ROF. In the MC studied here featuring proton-proton collisions at 500 kHz, one MFT track is matched with 1.35 FT0-C signals on average.

The average number of matched BC per matchable track depends on the FT0-C occupancy within the MFT ROF (which depends on the interaction rate and the charged particle multiplicity of the specific collisions), and is 1.35 in the particular MC simulations studied as mentioned previously, with 1.2 % of matchable tracks having 4 or more matched BCs. This means that the MFT-FT0-C track time is still ambiguous in some cases. In Figure 4.25 the fraction of matchable tracks is represented as a function of the number of BC matched per track, the latter is obtained by gathering the FT0-C channels matched with the track, and obtaining the BCs at which they were fired during the MFT ROF. In this simulation, 65.19 % of matchable MFT tracks have only one matched BC, meaning that for these tracks we have access to the track time with a precision of 1 BC.

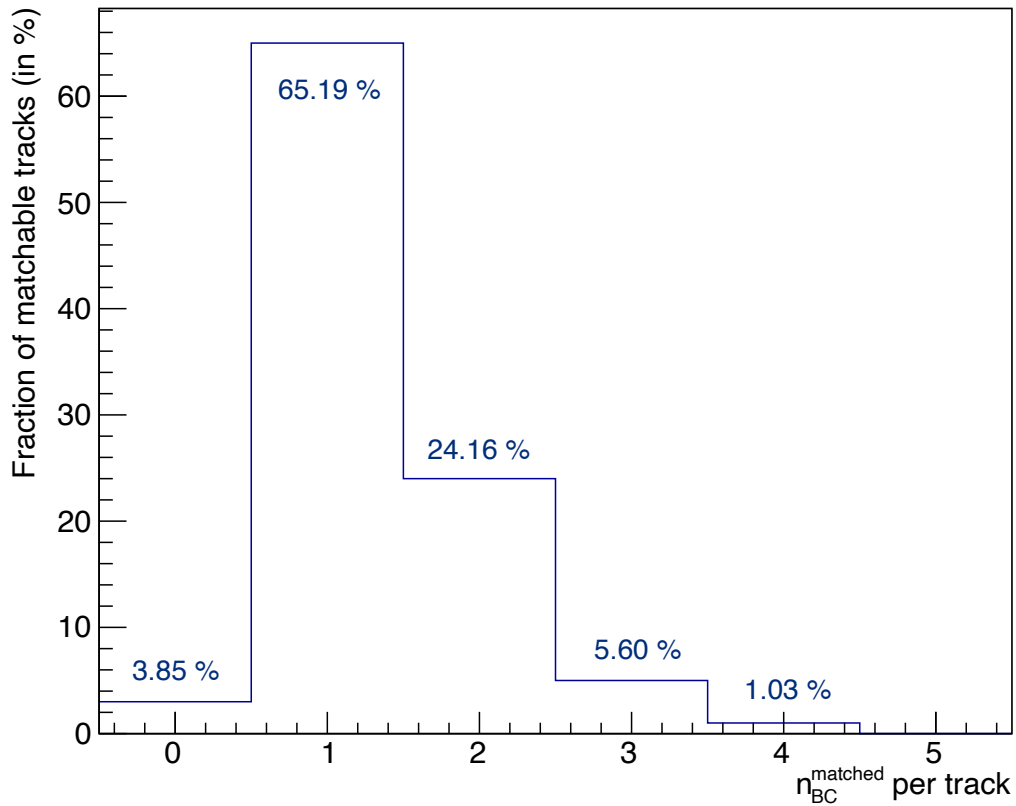


Figure 4.25: Fraction of matchable tracks as a function of the number of BC matched with FT0-C signal per MFT track

This MC study provides strong arguments in favor of performing the MFT-FT0-C matching, firstly because the vast majority of matchable MFT tracks indeed have a match in the FT0-C detector, secondly among these matchable tracks, 92.5 % are MC-matched (i.e. MFT track and FT0-C signal have the same MC-label). 94.7% of matchable tracks have an FT0-C match with the BC of the original particle (fake matches are included). Furthermore, after the matching with FT0-C, most of the matchable MFT tracks (65.19%) end up with a time window of only 1 BC, compared to the 198 BCs default of the MFT ROF in proton-proton collisions.

In conclusion, the matching with the FT0-C greatly improves the time resolution of an MFT track. This feature will be extremely helpful to correctly associate a given MFT track to a collision: one can indeed imagine that among the few BCs corresponding to the FT0-C signals matching the MFT track, only some of them will be associated to a collision, with the possibility to further reduce the residual ambiguity by considering the DCA between the track and each collision vertex.

The possibility to have an MFT track associated to a small time window is also useful in studies of MFT-MCH matching for muons. This particular matching procedure is way more complex than the MFT-FT0-C matching because the track can undergo multiple scattering inside the muon absorber, changing the trajectory of the particle: an improved timing information for the MFT track can thus help to exclude some MFT-muon

track candidates, using the MCH time resolution and the narrow MID time resolution ( $\sim 4$  BCs).

However, in the matching between MFT and FT0-C there is a key point that needs further investigation: all the matching-reliability studies and the visualization of Figure 4.24 were based on MC simulations in which MFT and FT0-C are perfectly synchronized in time; this scenario does not correspond to the real detector conditions, and the way to take this point into account will be further discussed in the next section.

## 4.5 MFT-FT0-C time alignment

### 4.5.1 Context and motivation for time alignment

At the LHC, and particularly in Run 3, the rate of events is very high making a proper timing of the reconstructed signals a crucial issue for the experiment. The LHC clock gives the BC and orbit of each interaction and is transmitted to the Central Trigger Processor of ALICE. Each detector or piece of detector has its own internal clock that is turned on when the detector is powered: this internal clock then needs to be synchronized and offset so that it displays the same time as the LHC clock. In other terms, for two clocks to display the same time, it is necessary that they have the same cycle duration (i.e. one BC lasts the same exact duration for both clock, at all times), and that the initial time  $t_0$  at which they start incrementing is the same.

Phase-locked loops are used to ensure that the detectors in ALICE and the LHC clock have exactly the same cycle duration [77].

Because the local internal clock starts when the detector is turned on, its initial time  $t_0^{local}$  differs from the initial time of the LHC clock  $t_0$ . The offset between these two  $t_0$  therefore needs to be calculated and subtracted for the clocks to display the same time.

In the following we will say that two detectors are aligned in time if the internal (or local) clocks of the detectors both have the same cycle duration and the same  $t_0$ , i.e. they display the same time, all the time.

For the FT0, which is part of the fast detectors that provide trigger information to the Central Trigger Processor, the synchronisation is done in the following way: the LHC interface sends the filling scheme to the FT0 at the start of each LHC fill. In this filling scheme some BCs are "filled" i.e. contain collisions, some are empty. The filled BCs then lead to signals in both FT0-A and FT0-C, and the offset between  $t_0$  and  $t_0^{FT0}$  is determined. The result is that if LHC indicates that there is an interaction in ALICE at BC = 1, the interaction detected by FT0 also has BC = 1. There are constant controls to cross-check what BC numbers the FT0 detects collisions in and what BC numbers are published by LHC as collision-BCs, and to ensure their compatibility.

For the MFT, each ALPIDE chip possesses an internal clock and the synchronization happens in the following way: the Central Trigger Processor sends trigger messages containing BCID and Orbit to the MFT Front End Electronics. When that signal is received by the MFT, the local clock of each ALPIDE chip then resets its BC and orbit counter (which previously indicated a random BC and orbit) to the BCID and Orbit provided and starts incrementing from there. No offset is implemented.

The total latency from the interaction to the front end electronics has been evaluated to be close to 1210 ns [104] in continuous readout mode (LM trigger) and for trigger distribution via GBT links (both MFT and ITS receive trigger messages from the CTP via GBT links). This latency was later reevaluated to be closer to 1500 ns, which corresponds to  $\approx 60$  BCs. This time propagation encompasses CTP and LTU processing times and the transmission of trigger messages via the long optical cables linking CTP to MFT/ITS.

This evaluation is nevertheless theoretical and the time alignment of MFT and LHC clocks needs to be estimated in real data.

Because of the proximity of MFT and FT0-C and the very high time precision of FT0, it is logical to try to align in time MFT and FT0, not to mention that in order to match the signals from the FT0-C and the MFT as described in the previous section, the time

misalignment between the two detectors needs to be computed and corrected. Since, as explained above, the FT0-C is already aligned in time with the Central Trigger Processor and LHC clock, synchronizing the MFT and the FT0-C automatically ensures the MFT internal clocks to be aligned in time with the LHC clock.

### 4.5.2 Time alignment procedure

In order to estimate the time shift between MFT and FT0-C I proposed and implemented a method consisting in counting the number of MFT tracks matched with FT0-C signals, as a function of a shift in BC applied to the beginning of the MFT Readout Frames. The main idea behind this method is that the probability to have one MFT track matched with its corresponding FT0-C signal (meaning that the same particle left the track and the signal) should have a peak when MFT and FT0-C are perfectly time-aligned, corresponding to the situation observed in MC simulations discussed in section 4.4.5. However if the window in which we gather the FT0-C signals is not the actual window in which the MFT tracks occurred, (because of a time misalignment between the two detectors) the probability to have MFT-FT0-C matches is reduced.

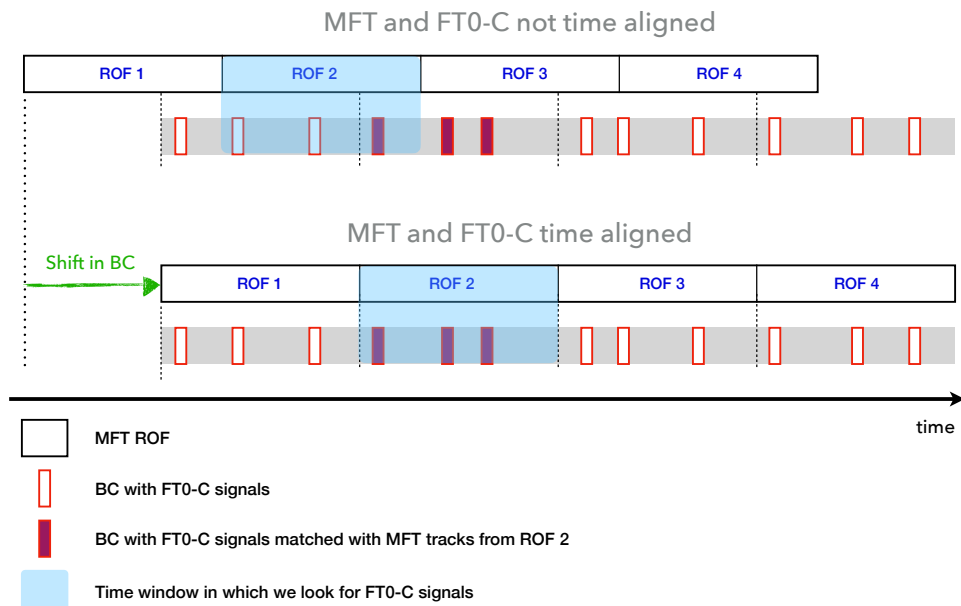


Figure 4.26: MFT-FT0-C time alignment, the green arrow representing the time shift added between the two detectors to recover a correct time alignment.

There is of course the possibility to match a given MFT track with a wrong FT0-C signal (meaning that the particle that left the track and the particle that left the FT0-C signal are different), the matched FT0-C signals coming from tracks in another time windows, from other tracks in the same time window, or just from noise. The probability to have fake MFT-FT0-C matches should however not depend on the time shift applied to the beginning of MFT ROFs, it will just depend on the occupancy of the FT0-C detector in

the considered time window. The occupancy itself depending on the collision type, the filling scheme and the IR.

Following the above argument, one can thus expect that the highest proportion of MFT tracks matched with FT0-C signals is found when a proper shift between the FT0-C and the MFT clocks is applied, recovering the time alignment between the two detectors. Figure 4.26 illustrates two different scenarios: the top panel represents the initial, uncorrected situation with the MFT and FT0-C not time-aligned, while in the bottom panel the MFT and FT0-C are time-aligned thanks to a shift in BC applied to the MFT signal. These scenarios represent of course a very simplified sketch of the real situation: as explained above, it is possible to have fake matches between MFT tracks from ROF 2 with FT0-C signals which did not originate from the same particle; these fake matches are supposed however to happen with a uniform probability, and are not represented.

In the bottom panel scenario, the MFT ROFs were shifted by a certain number of BCs with respect to their initial position: this time shift is represented by the green arrow, and its duration in BCs will be called  $n_{align}$ . As explained above, the strategy to determine  $n_{align}$  is to shift the beginning of MFT ROFs by  $n$  BCs,  $n$  being a positive or negative integer. For each value of  $n$  one will look at the number of MFT tracks finding a match with the FT0-C inside this new (shifted) ROF. In the performed study,  $n$  is incremented by steps of one unit by default, and the fraction of unmatched MFT tracks  $f_u(n)$  is computed for each  $n$ , defined as

$$f_u(n) = \frac{\text{Number of unmatched MFT tracks}}{\text{Number of matchable MFT tracks}} \Big|_{\text{MFT ROFs shifted by } n \text{ BCs}} \quad (4.2)$$

With “Number of unmatched MFT tracks” being the number of matchable MFT tracks with no match in the FT0-C within the shifted MFT ROFs. Only matchable MFT tracks are of course considered here, meaning that the MFT tracks falling into the FT0-C dead zones (see subsection 4.4.3) are excluded from this study.

When scanning a sufficiently large range for  $n$ , the fraction of unmatched MFT tracks can be represented as a function of the BC shift applied to the ROFs. The minimum of this curve will then correspond to the shift in BC leading to the maximum of matched MFT track, and the corresponding abscissa will then indicate the time shift needed to time-align MFT and FT0-C, i.e.  $n_{align}$  BCs.

This fraction is computed on different periods and runs having different BC filling schemes and interaction rates. The BC with FT0-C signals considered were also required to have **at least one hit in the FT0-A in the BC duration**. This selection was implemented to try to select only the BCs with collisions and to cut out FT0-C noise. It is important to note that this selection doesn't change much the result of the minima found for the  $f_u(n)$  function.

### 4.5.3 Results

In Figure 4.27a the fraction of unmatched MFT tracks versus time shift is represented for one particular run of the period LHC22q, which had an interaction rate of 2.1 kHz. As expected, the fraction of unmatched MFT tracks versus time shift does have a minimum. The minimum of  $f_u$  is obtained for  $n \in [28, 63]$ .

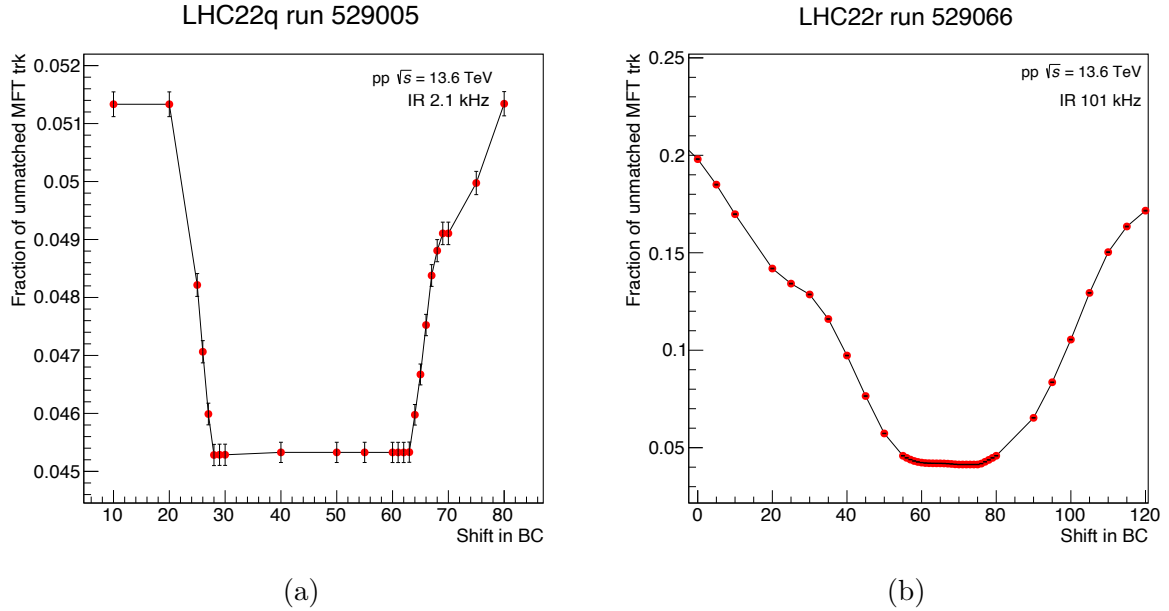


Figure 4.27: Fraction of unmatched tracks as a function of the shift in BC applied to the beginning of the MFT ROFs for two different runs, at relatively low IR compared to the nominal IR in Run 3.

The distribution of colliding BCs inside one LHC orbit (i.e., the filling scheme) plays a crucial role in the precision of this method. If the colliding BCs are widely spaced, the proportion of matched (or unmatched) MFT tracks will exhibit a plateau for a large range of  $n$ -BC shifts, even when the shift is incremented by 1 BC at a time. This is schematized in Figure 4.28: in the left panel the MFT ROF 2 is shifted by three different numbers of BCs, and in the right panel the corresponding fraction of unmatched MFT tracks versus the shift in BC is represented. This scenario explains the presence of a plateau in Figure 4.27a: in the analyzed run, the filling scheme was sparse. For reference, this filling scheme is represented in the top panel of Figure 4.29, where the smallest duration between 2 filled BCs is 40 BCs.

The dataset analyzed in Figure 4.27a does not provide sufficient precision to determine the time shift necessary to time-align the two detectors. The study was reproduced with several other datasets with different BC filling schemes and IR. The BC filling scheme of LHC22o run 527826 with nominal IR is represented in the bottom of Figure 4.29, where one can see that the number of colliding bunch crossings is way higher than in the top panel. This filling scheme will then lead to a better precision in the determination of the time shift between the MFT and the FT0-C. The results for three different IR are represented in Figures 4.27b, 4.30a and 4.30b. In all these figures we can clearly see the evolution of the fraction of unmatched MFT tracks as a function of the time shift, following the same trend in each dataset: first a decrease, then a minimum, more or less narrow, then an increase.

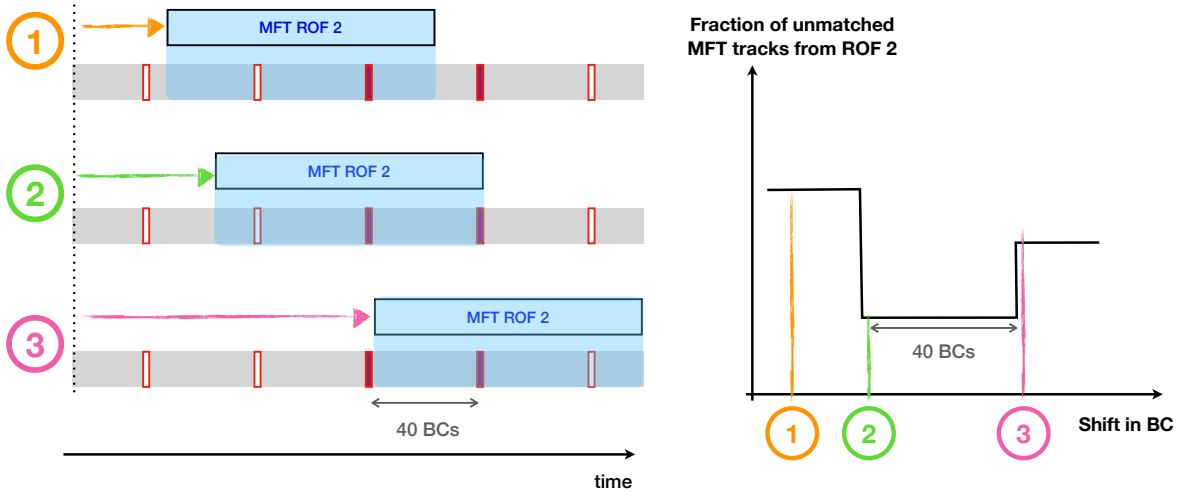


Figure 4.28: Fraction of unmatched tracks as a function of the shift in BC applied to the beginning of the MFT ROF 2 in case of a sparse filling scheme. The legend is the same as in figure 4.26. In this figure one implicitly assumes that all BCs corresponding to FT0-C signals have an associated collision.

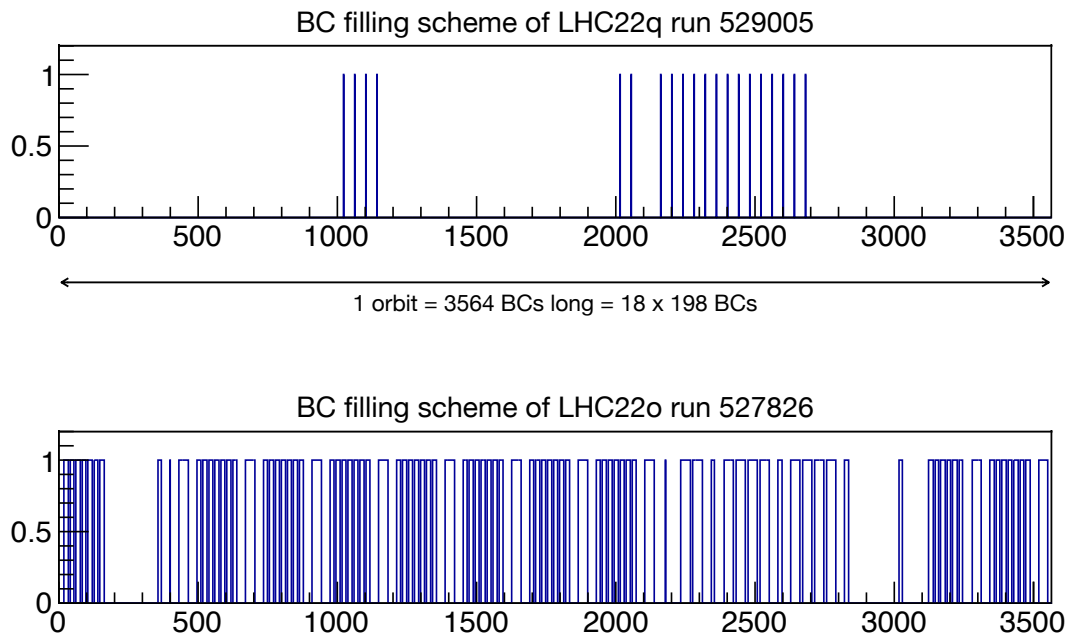


Figure 4.29: Filling schemes of two runs in Run 3

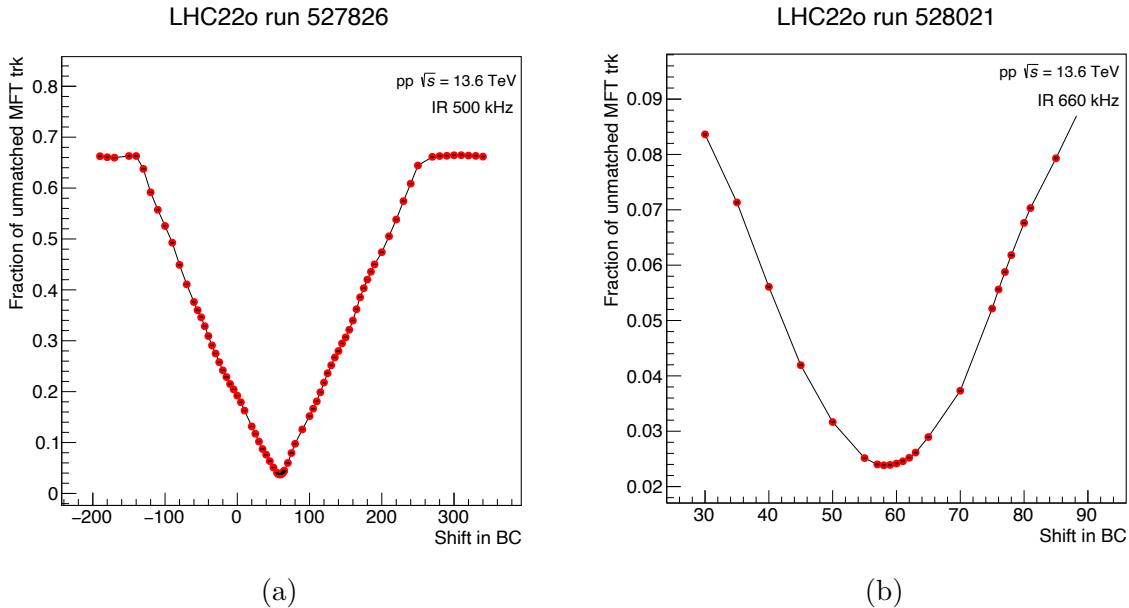


Figure 4.30: Fraction of unmatched tracks as a function of the shift in BC applied to the beginning of the MFT ROFs for two different runs of LHC22o, close to the nominal IR for p-p collisions in Run 3.

#### 4.5.4 Summary and conclusion

Table 4.1 summarizes the different results of the time shift  $n_{align}$  BC that leads to the maximum of MFT tracks matches with FT0-C signals. A fiducial range is given for  $n_{align}$ : its width depends both on the width of the minimum found for the  $f_u$  function, and the uncertainty associated to the value of the function itself (an uncertainty of 0.1% has been considered in this case). The last line corresponds to a run at very high IR: the corresponding result needs to be taken with caution, because the occupancy of the FT0-C is high in such run conditions.

Dataset	IR (kHz)	$n_{align}$ in
LHC22q run 529005	2.1	[28, 63]
LHC22r run 529066	101	[60, 75]
LHC22o run 527826	500	[57, 61]
LHC22o run 528021	660	[57, 61]
LHC22o run 526926	986	[50, 62]

Table 4.1: Summary table of the results for the time alignment between MFT and FT0-C for various IR conditions characterizing the ALICE pp data taking in Run 3

From the analysis of the values reported in table 4.1 it was chosen to use  $n_{align} = 60$ , corresponding to a time shift of 60 BCs, as the value of the time offset between the MFT clocks and the FT0 clock (which is equivalent to the LHC clock). Some of the  $n_{align}$  ranges are not completely overlapping, which could be attributed to some systematic uncertainty to be associated to the limits of these ranges. Indeed, it was determined that for ITS, the

different internal clocks inside ALPIDE chips have a time misalignment among themselves of  $\approx 10$  BCs<sup>2</sup>. Since the MFT has the same ALPIDE chips and almost the same cable length from CTP to front-end electronics as the ITS, this value of 10 BCs can reasonably be taken as the uncertainty on  $n_{align}$ .

To conclude, the offset between the MFT clocks and the LHC clock has been determined to be  $60 \pm 10$  BCs. After this work, this offset has been implemented in O2 and the AO2D reconstruction, so that the MFT ROFs start with the BCID and OrbitID provided by the LHC clock, without latency. Thanks to this implementation, the track-to-collision association is more reliable, because the MFT ROFs are now shifted to their right positions. This ensures that the collision time (determined by the FT0) and the MFT ROF time window are time-aligned.

It is worth noting that the ITS has measured an offset of 64 BCs, and that both these offsets are compatible with the predicted value of CTP  $\rightarrow$  MFT/ITS latency of  $\approx 1500$  ns.

## 4.6 Conclusions and outlook

In conclusion, participation in several activities was undertaken to study and develop codes to check and improve the quality of MFT data. Crucial software developments were carried out by providing a list of compatible collisions for each MFT track, using DCA methods and matching with a faster detector, the FT0-C. This work required to develop and implement a procedure to estimate the time offset between FT0 and MFT, enabling the alignment of the two detectors in time.

Now that the MFT is time-aligned with the FT0, more studies of the reduction of ambiguity needs to be performed in both data and MC. For instance, one could use a combination of MFT-FT0-C matching and DCA methods to associate an even lower number of collisions to one MFT track. Another method can also be to use the FT0VTX trigger, the trigger which is used to determine if there is a collision in one BC: it requires hits in FT0-A and C in coincidence (in a very small time window of a few ns) and would help discriminating even better the BCs. This further development could lead to a drop in the number of BCs matched with FT0-C signals per MFT track shown in Figure 4.25, because only the FT0-C signals in FT0VTX triggered BCs would be considered. Less BCs would of course translate into less collisions candidates for the association with an MFT track.

As mentioned previously, having an MFT track with a reduced time window is also useful in studies of MFT-MCH matching for muons. This matching can be quite challenging because of the high number of MFT tracks candidates per MCH track. Having a precise time information could drastically reduce the number of candidates.

In more general terms, for every analysis that requires an unique track to collision association, the tools developed in this thesis will be essential.

---

<sup>2</sup>Ruben Shahoyan, private communications.

# Chapter 5

## Measurement of forward charged-particle multiplicity with the MFT

Charged-particle pseudorapidity distribution, also called charged-particle pseudorapidity density, is defined as the number of primary charged particles per collision and unit of pseudorapidity. It can be understood as primary charged-particle multiplicity in intervals of pseudorapidity. A primary particle in ALICE is defined as a particle with a mean proper lifetime  $\tau$  larger than  $1 \text{ cm}/c$ , which is either a) produced directly in the main interaction, or b) from decays of particles with  $\tau$  smaller than  $1 \text{ cm}/c$ , excluding particles produced in interactions with materials [85]. This observable, noted  $dN_{\text{ch}}/d\eta$ , is crucial in understanding particle production mechanisms in high-energy hadronic collisions, ranging from proton-proton to heavy-ion systems. The measurement of the production of charged hadrons in high-energy proton-proton interactions allows to better characterize the global properties of the collisions. Indeed, since both soft and hard QCD processes are at play in high-energy hadronic collisions, and soft processes can only be modeled phenomenologically, these measurements provide additional constraints to models and event generators.

In this Chapter, the physics motivations of the study of charged-particle pseudorapidity distributions will be presented first, along with previously published results at the LHC. The analysis procedure will then be described following the order the various steps were performed. Given that the measurement is using corrections based on MC simulations, the first step in the analysis was to ensure a sufficient quality for the MC, and in particular a good agreement between data and MC. The results of the comparison between data and MC will be shown. The correction procedure will then be described along with a MC closure test which was performed to check its validity. The study of the systematic uncertainties will be presented. While the uncertainty due to ambiguous tracks has been successfully estimated, other systematic uncertainty (Diffraction content and model dependence, extrapolation to zero  $p_T$  and material budget) were not due to MC simulations with specific conditions still missing at the time of the writing of the manuscript. Finally, the results for the forward charged-particle pseudorapidity distributions in p-p collisions at  $\sqrt{s} = 0.9$  and  $13.6 \text{ TeV}$  will be shown.

## 5.1 Physics motivations and previously published results

### 5.1.1 Physics motivations

As mentioned above, charged-particle pseudorapidity distributions provide constraints to models and particle event generators. These measurements can be done in different classes of events corresponding to different types of proton-proton interactions. In general, proton-proton collisions can be elastic or inelastic. Elastic collisions correspond to interactions in which the colliding protons exchange kinetic energy only, and the final state remains the same as the initial state. At the LHC, the most interesting interactions are those in which new particles are produced in the interaction of the two initial protons: these interactions are called inelastic collisions, see Figure 5.1. Inelastic collisions can be further classified into non-diffractive and diffractive interactions. The diffractive scatterings are characterized by pomeron exchange(s) between the incoming protons. Pomerons are theoretical objects introduced in the Regge theory [105], which can be understood in the QCD framework as colorless multi-gluon objects.

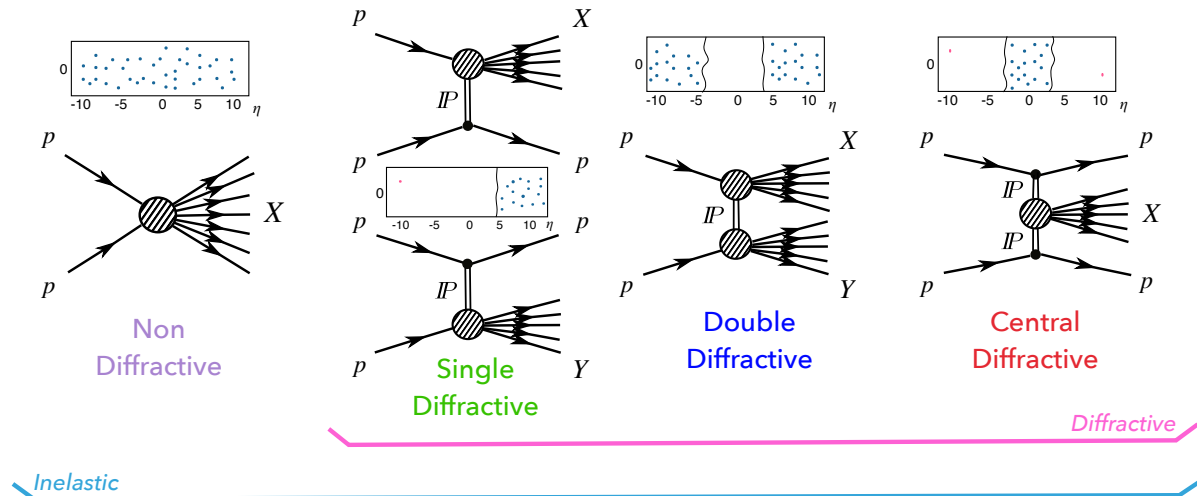


Figure 5.1: Different types of inelastic proton–proton collisions, with their corresponding interaction diagram and particle distribution in the pseudorapidity space. Diffractive events are characterized by Pomeron exchange. Figure adapted from [106].

Single and double-diffractive events correspond to 20% and 10% of the total inelastic cross-section, respectively [107]. In these events, most of the produced particles are emitted in the forward direction (see Figure 5.1). The central diffractive events are extremely rare at the LHC [108] and their impact on inclusive particle production studies is thus negligible. The effect of diffractive interactions and beam remnants are mainly visible at forward rapidity. These phenomena are not yet described with good accuracy by theoretical models, and the charged-particle pseudorapidity distribution can therefore provide a very valuable input. Indeed, model predictions at the LHC energies are generally more accurate in the midrapidity region, while the extrapolations towards forward pseudorapidities often suffer from large uncertainties. In this sense, measurements of particle production at forward rapidity are greatly beneficial for a better tuning, at forward rapidity, of the

models used to describe hadronic collisions at the LHC [109]. The study of final-state charged particles at forward rapidity is also crucial in cosmic ray physics to understand the distributions of the most energetic particles forming air showers, and thus to better constrain cosmic ray generators [110].

### 5.1.2 Previously published results at LHC

Several measurements of the charged-particle pseudorapidity distribution have been carried out at the LHC by the ALICE, ATLAS, CMS and LHCb collaborations in Run 1 and Run 2, at various center of mass energies and for various collision systems from p–p to Pb–Pb. In this section, we will focus on the available results in proton-proton collisions. The set of results presented here is not intended to be exhaustive, and mainly covers the results at forward rapidity or at the highest collision energy at the LHC.

The first measurement in this selection is the one of the charged-particle pseudorapidity distribution performed by LHCb in proton-proton collisions at  $\sqrt{s} = 7$  TeV. The result is shown in Figure 5.2.

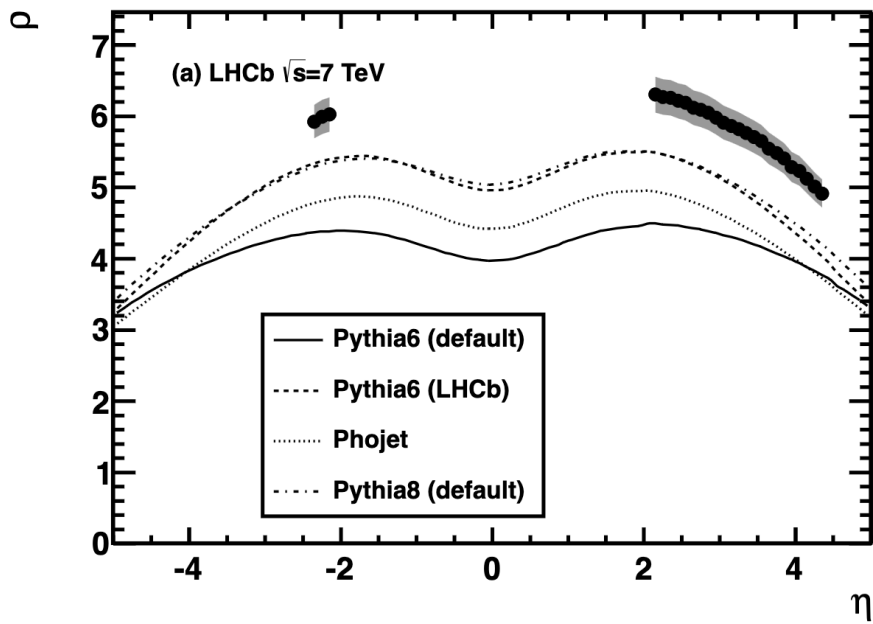


Figure 5.2: Charged particle pseudorapidity density (noted  $\rho$  in this figure) as a function of  $\eta$  obtained by the LHCb experiment, for events having at least one charged particle in the range  $2.0 < \eta < 4.5$ . Comparisons are shown with different PYTHIA generators with different tunes. Figure taken from [111].

At the time of this LHCb measurement, dating back to 2012, the default tune of PYTHIA8 failed to reproduce the results. The development of the Monash tune, which became the default tune in 2013, allowed to reproduce the measured  $dN_{\text{ch}}/d\eta$  significantly better (see for example [89]).

In 2014 and 2015, the TOTEM experiment measured the charged-particle pseudorapidity distribution as a function of  $\eta$  in the forward region, for p–p collisions at  $\sqrt{s} = 8$  TeV. This measurement, shown in Figure 5.3, spans a wide forward pseudorapidity range,

reaching almost  $\eta = 7$ . The PYTHIA8 tune 4C, EPOS-LHC, SYBILL and QGSJET-II predictions were found to be in agreement with the measurement, although the systematic uncertainties of the data were too large to draw firm conclusions. QGSJET-II is an event generator based upon the Reggeon field theory framework [112]. SYBILL is a cosmic-ray event generator based on the dual parton model [113].

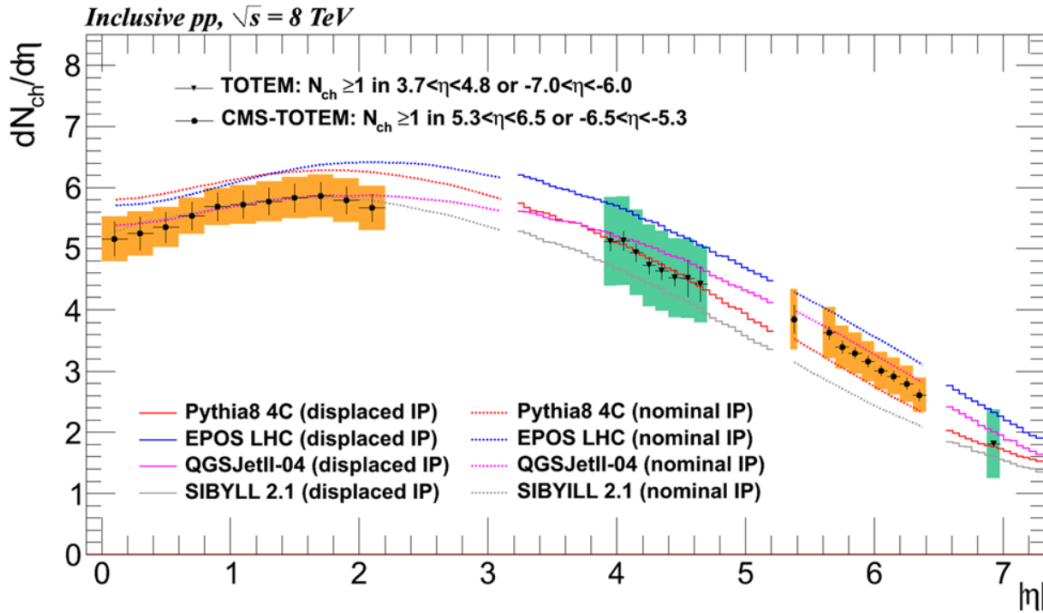


Figure 5.3: Charged-particle pseudorapidity distribution as a function of  $\eta$  for  $p-p$  collisions at  $\sqrt{s} = 8$  TeV, obtained by the TOTEM experiment considering both displaced (green band) and nominal interaction points (orange band). The results obtained considering the nominal interaction point are taken from [114]. Corresponding predictions from PYTHIA8 (tune 4C), SIBYLL, EPOS-LHC, and QGSJetII are also shown. Figure taken from [115].

More recently, a charged-particle pseudorapidity distribution measurement has been performed in  $p-p$  collisions at  $\sqrt{s} = 5.02$  TeV by the ALICE collaboration in the pseudorapidity interval  $-5 < \eta < 5$ , using the FMD and SPD detectors [116]. The corresponding results are shown in Figure 5.4. Despite the wide rapidity coverage, the result has significant systematic uncertainties in the forward region. So far, this is the only available measurement of forward charged-particle pseudorapidity distribution in  $p-p$  collisions in ALICE.

The aforementioned results cover, to the author's knowledge, the currently available measurements of forward charged-particle pseudorapidity distribution in proton-proton collisions at LHC energies.

Measurements of midrapidity charged-particle multiplicity at  $\sqrt{s} = 13$  TeV have also been performed by various LHC collaborations. Among the most recent results are the ones published by CMS and ALICE on the charged-particle pseudorapidity distribution in inelastic (INEL)  $pp$  collisions at  $\sqrt{s} = 13$  TeV. The two sets of results are shown, superimposed, in Figure 5.5. A measurement of the charged-particle pseudorapidity distribution in the  $INEL > 0$  event class is also presented, corresponding to inelastic events

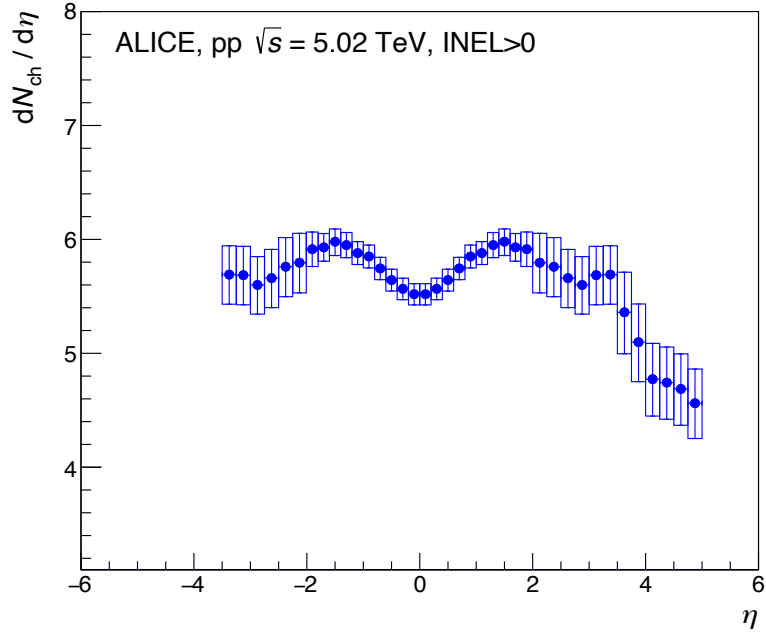


Figure 5.4: Charged-particle pseudorapidity distribution as a function of  $\eta$  for p-p collisions at  $\sqrt{s} = 5.02$  TeV obtained by the ALICE experiment [116].

producing at least one charged particle in  $|\eta| < 1$ . The CMS and ALICE results for inelastic collisions agree within the systematic uncertainty. Moreover, the measurements qualitatively agree with the available MC predictions.

The most recent ATLAS and CMS results of the charged-particle pseudorapidity distribution at midrapidity were obtained in pp collisions at  $\sqrt{s} = 13$  TeV in 2016 and 2018, respectively. These results are reported in Figures 5.6a and 5.6b.

The ATLAS results are compared with predictions from PYTHIA8 Monash and PYTHIA8 A2 tunes as well as with EPOS-LHC and QGSJET-II models. The measured charged-particle multiplicity distribution is in good agreement with PYTHIA8 Monash, EPOS-LHC and QGSJET-II. The best agreement over the whole  $\eta$  range is reached with PYTHIA8 Monash. Similarly, the CMS result is compared with different PYTHIA8 tunes and EPOS-LHC, the best agreement being reached with EPOS-LHC. It is worth noting that even though the measurements are similar, they differ in the type of events and particles considered. Indeed, in the ATLAS measurement, only events with at least two charged particles in  $|\eta| < 2.5$  are considered, and the charged primary particles must have a lifetime  $\tau > 300$  ps, and  $p_T > 100$  MeV/c. In the CMS measurement, events must be inelastic, with at least one charged particle in  $|\eta| < 2.4$ , and the charged primary particles must have a  $p_T > 0.5$  GeV/c. When using the same event and particle selections, ATLAS, ALICE and CMS results of charged particle pseudorapidity distributions were found to be compatible within the systematic uncertainties [120].

The predictions of the different models evolve when moving from the oldest to the most recent results, providing more and more accurate predictions over time. This, once again, suggests the importance of such measurements in constraining MC generators. In this context, contrary to the plethora of results available at midrapidity, forward rapidity

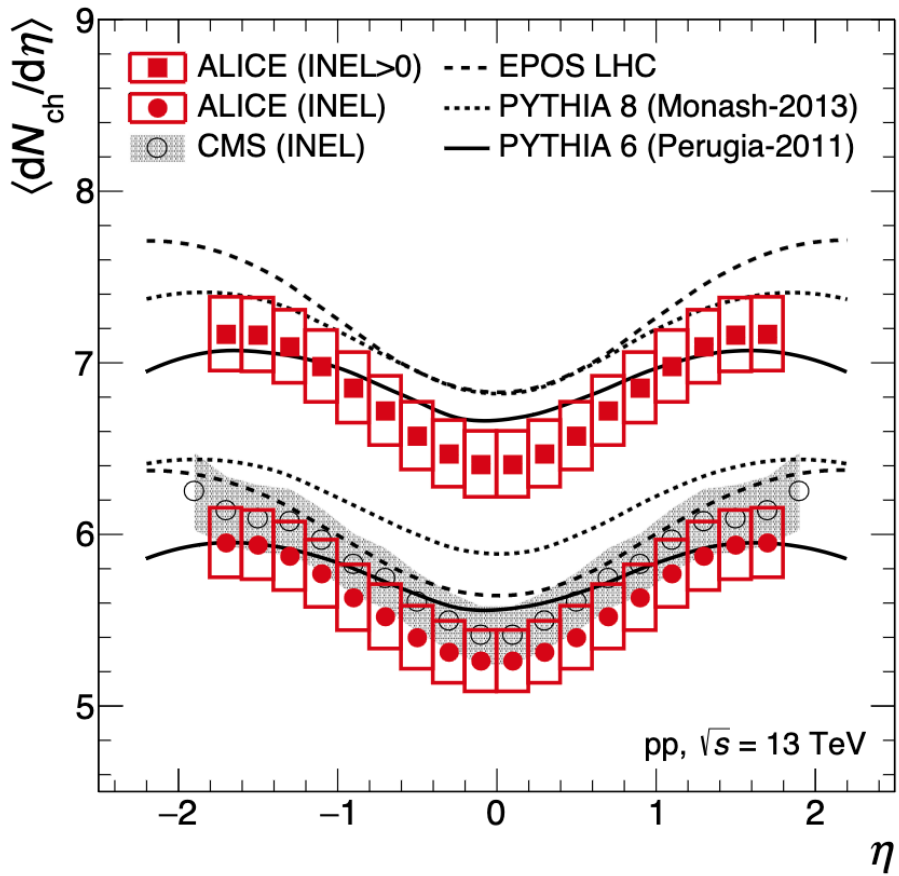
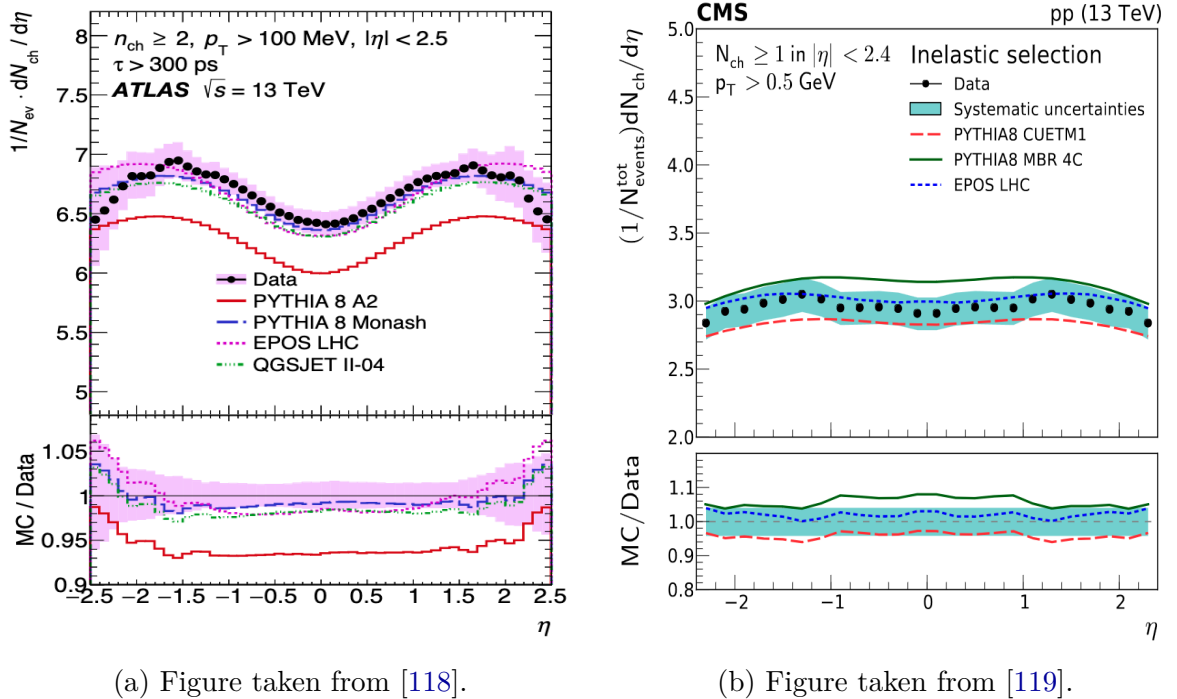


Figure 5.5: Charged-particle pseudorapidity distribution as a function of  $\eta$  produced in pp collisions at  $\sqrt{s} = 13$  TeV. The ALICE results are shown for the event classes INEL and INEL  $> 0$  and compared to Monte Carlo predictions and to the results from the CMS Collaboration [117]. Figure taken from [89].

results are very few and usually suffer from significant systematic uncertainties. This makes them less useful for constraining the models. In this sense, the ALICE experiment in Run 3 offers a great advantage thanks to the presence of the MFT detector in the forward region. This detector is capable of inclusive charged particle tracking in the region  $-3.6 < \eta < -2.5$ , which was not previously possible in ALICE. This provides a unique opportunity for precise measurements of particle multiplicity at forward rapidity at the LHC. Moreover, in addition to its value as a physics observable, the measurement of the forward charged-particle multiplicity in pp collisions is well-suited as a benchmark to perform crucial quality checks on the data provided by the newly installed MFT detector.



(a) Figure taken from [118].

(b) Figure taken from [119].

Figure 5.6: Charged-particle pseudorapidity density at  $\sqrt{s} = 13 \text{ TeV}$  measured by the CMS and ATLAS collaborations and compared with different models such as PYTHIA8, EPOS-LHC, and QGSJET-II.

## 5.2 Analysis procedure and selections

To carry out the charged-particle pseudorapidity measurement, two inputs have been considered:

- the number of tracks as a function of  $\eta$  and  $z_{\text{vtx}}$ ;
- the number of (selected) events as a function of  $z_{\text{vtx}}$ ,

where  $z_{\text{vtx}}$  is defined as the longitudinal coordinate of the primary vertex of the considered event. These observables are computed as 2D and 1D histograms by analyzing the data in the `A02D` format with `O2Physics`. The analysis includes various correction steps, that are based on MC simulations.

### 5.2.1 Datasets and MC simulations

The datasets used for this analysis are the following ones:

- run 517685 of the data taking period LHC22c for the measurement in p–p collisions at  $\sqrt{s} = 0.9$  TeV;
- run 526641 of the data taking period LHC22o for the measurement in p–p collisions at  $\sqrt{s} = 13.6$  TeV.

The MC simulations used for the corrections and the comparisons with data are the following:

- run 517685 of the MC production LHC22h1c1, anchored to the corresponding run of the data taking period LHC22c
- run 526641 of the MC production LHC23f4b2, anchored to the corresponding run of the data taking period LHC22o
- run 526641 of the MC production LHC24b1b, anchored to the corresponding run of the data taking period LHC22o.

All the employed MC productions exploit PYTHIA8 simulations for particle generation and GEANT4 for the particle transport through the experimental setup.

These MC simulations are anchored to the aforementioned datasets, which means that they are tuned to reproduce the data as well as possible at the reconstruction stage. The energy of the collisions and the bunch filling scheme are identical to those of the data, and the  $z_{\text{vtx}}$  distribution of collisions in the MC is based on the width and the most probable value extracted from the data. Furthermore, in the most recent MC simulations, the distribution of the reconstructed MFT tracks in simulation versus  $\eta$  and  $\varphi$  has been tuned to the data (see section 5.3).

### 5.2.2 Track selection

As no standard selection on the MFT reconstructed tracks is yet available, all the MFT standalone tracks stored in the analyzed `A02D` files are used in this analysis. By definition, an MFT track is a track that left hits in at least 4 MFT disks. The tracks are reconstructed within the nominal  $\eta$  acceptance  $[-3.6, -2.5]$  covered by the detector.

### 5.2.3 Event selection

The events selected in this analysis are required to have the sel8 tag, based on the FTOVTX trigger. This trigger ensures that the collisions occurred in BC slots in which a coincidence is found within a narrow window of 2.5 ns between at least one hit in the FT0-A detector and at least one hit in the FT0-C detector. Other selections are also implemented such as the exclusion of BCs close to the ITS readout frame boundaries and the BCs located on the borders of Time Frames [121]. The selected events are also required to have at least one track in the pseudorapidity region  $|\eta| < 1$  in order to match the  $\text{INEL} > 0$  event definition. Finally, only collisions having  $|z_{\text{vtx}}| < 10$  cm are considered.

## 5.3 Comparison between MC and data

The analysis of the charged-particle pseudorapidity distribution is particularly sensitive to the distribution of the number of tracks in  $\eta$  and  $\varphi$ . An accurate description of the detector in the MC simulation is thus needed to ensure that the reconstructed MC closely reproduces the real data.

This section summarizes the checks performed to compare the analyzed data and the corresponding MC simulations. As it will be shown in the following, some discrepancies persist between data and MC even with the most recent simulations. The comparison is expected to improve as soon as a tuning of the active chips of the MFT becomes available for every MC. The simulations are nevertheless already in sufficiently good agreement with the chosen datasets to allow for the derivation of the preliminary results.

### 5.3.1 p–p collisions at $\sqrt{s} = 0.9$ TeV

The only MC production for p–p collisions at  $\sqrt{s} = 0.9$  TeV suitable for this analysis is based on a simulation which does not have a tuning of the active and inactive chips of the MFT. However, since the chosen run in the considered dataset has a limited number of inactive chips, the corresponding acceptance for MFT tracks in  $\eta$  and  $\varphi$  is close to the ideal one.

The first check in comparing data and MC is performed considering the number of MFT tracks normalized to the total number of selected event. This distribution is extracted for both data and reconstructed MC, and represented as a function of  $\eta$  in Figure 5.7a, and as a function of  $\varphi$  in Figure 5.7b. The difference between reconstructed MC and data is less than 5% in the nominal  $\eta$  range of MFT, and the difference in  $\varphi$  is less than 10% over the whole range except close to  $\varphi = 0, \pi, 2\pi$  and in the region  $0.1 < \varphi < 0.8$ . The discrepancies at  $0, \pi, 2\pi$  are most likely due to a misalignment of the two half-cones of the MFT which is not reproduced in the MC simulations. The discrepancies in the region  $0.1 < \varphi < 0.8$  are due to the presence of dead chips in the data taking which were not reproduced by this MC simulation (since the tuning of the active and inactive MFT chips was not implemented at the time the MC was produced).

The  $z_{\text{vtx}}$  distributions of events in data and MC are also compared, see Figure 5.8. As one can see, the MC has not been tuned precisely enough, resulting in a shift of approximately 1 cm between the data and MC distributions. This shift, in turn, results in a discrepancy

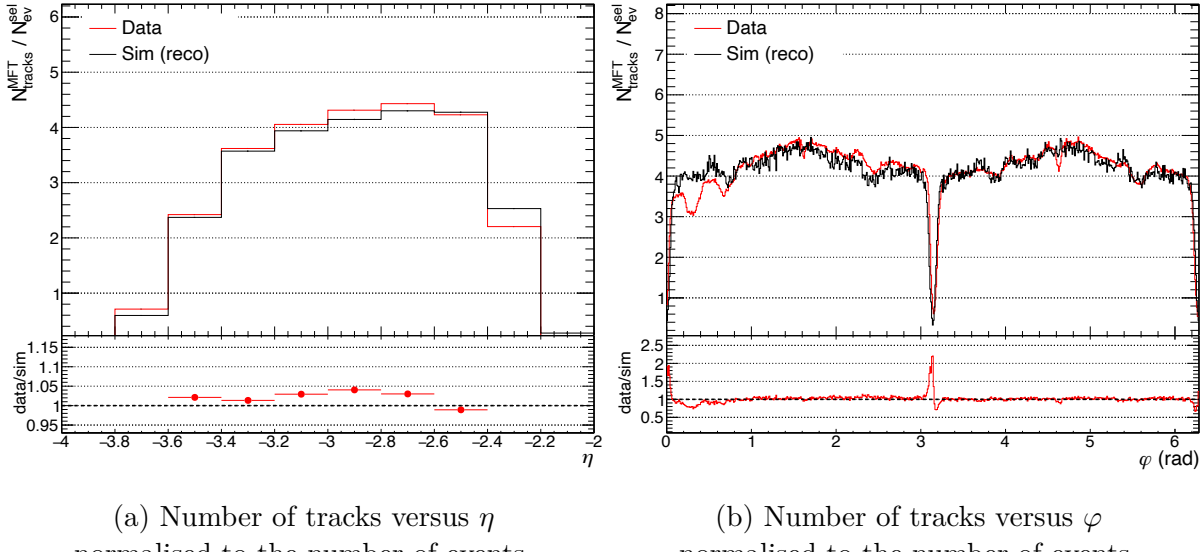


Figure 5.7: Comparison of the number of MFT tracks versus  $\eta$  and  $\varphi$  in data (LHC22c in red) and reconstructed MC (LHC22h1c1 in black).

of up to  $\pm 20\%$  between the data and MC distributions within  $|z_{\text{vtx}}| < 10$  cm, as shown in the bottom panel of Figure 5.8.

Although it is clear that the MC simulation can be further improved, the quality of the comparison to the data is nevertheless sufficient to derive reliable corrections for preliminary results. The comparison of the distribution of MFT tracks as a function of pseudorapidity, in particular, the most important one for the analysis, is found to be satisfactory.

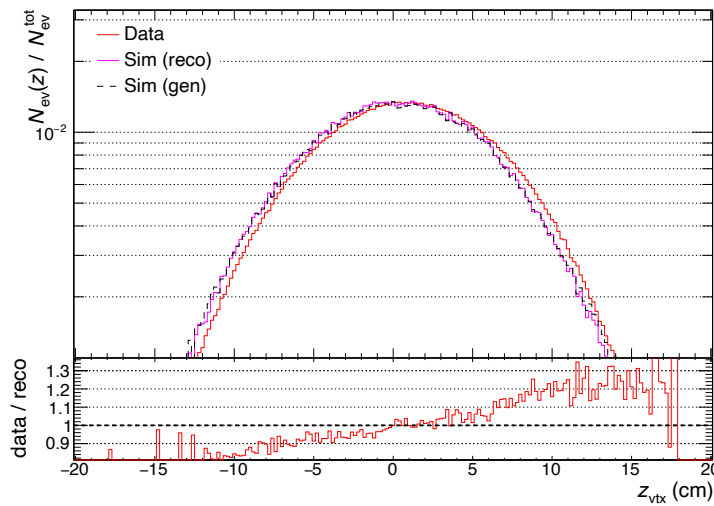


Figure 5.8: Distribution of  $z_{\text{vtx}}$  of events in data, reconstructed MC and generated MC.

### 5.3.2 p–p collisions at $\sqrt{s} = 13.6$ TeV

#### MC anchoring

It was demonstrated that the MFT acceptance varies according to which of the chips are inactive, especially if the inactive chips are located in the first MFT layers (i.e. the layers closest to the IP). However, at the time the MC corrections were estimated, no automatic survey of the inactive chips and their number over time was implemented in the software. The time dependence for this information is an important feature, as inactive chips could be reactivated at some point during the data taking: in the Detector Control System of MFT, a procedure called *chip recovery* is indeed automatically launched when more than 15 chips are not sending data. This procedure resets the chips and allows to recover some of them. As a result, the list of inactive chips is in general time dependent.

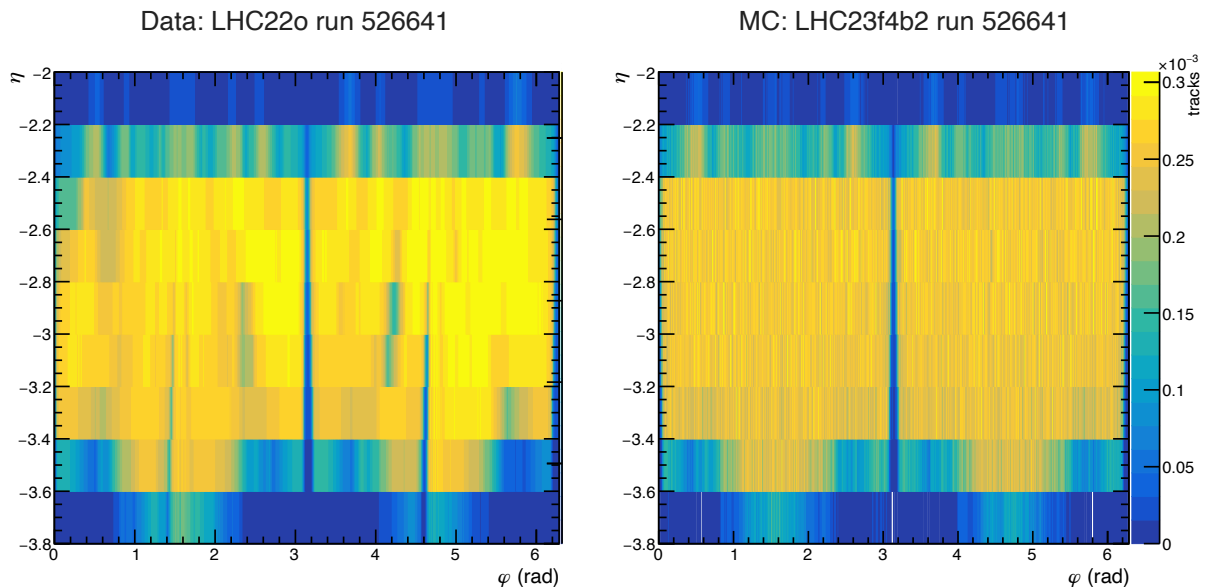


Figure 5.9: Distribution of  $\eta$  and  $\varphi$  of MFT tracks compared between data (left) and 2023 MC (right).

Since the very first steps of the analysis, it became clear that the information about the inactive chips had to be provided in order to have a reliable description of the MFT detector response in the MC simulations. This was finally implemented at the end of 2023, allowing for a new MC to be produced in 2024, that included a time-dependent disabling of the inactive chips. As one can see in Figure 5.10, this MC simulation provides significantly better description of the data compared to previous MC simulations which did not take into account the information of the inactive chips (Figure 5.9). In Figure 5.9, obtained considering the 2023 version of the MC, several differences can indeed be spotted between data and simulations: for instance, the hole around  $\varphi = 4$  and  $-3.2 < \eta < -2.8$  seen in the data is not reproduced by the MC. In the most recent MC, considered for the distributions in Figure 5.10, this hole is reproduced. Many other areas where less tracks were present in the data are also well reproduced in the newly generated MC.

In addition to the comparison of distributions of MFT tracks as a function of  $\eta$  and  $\varphi$ , one should also compare the distributions of the number of MFT tracks normalized to

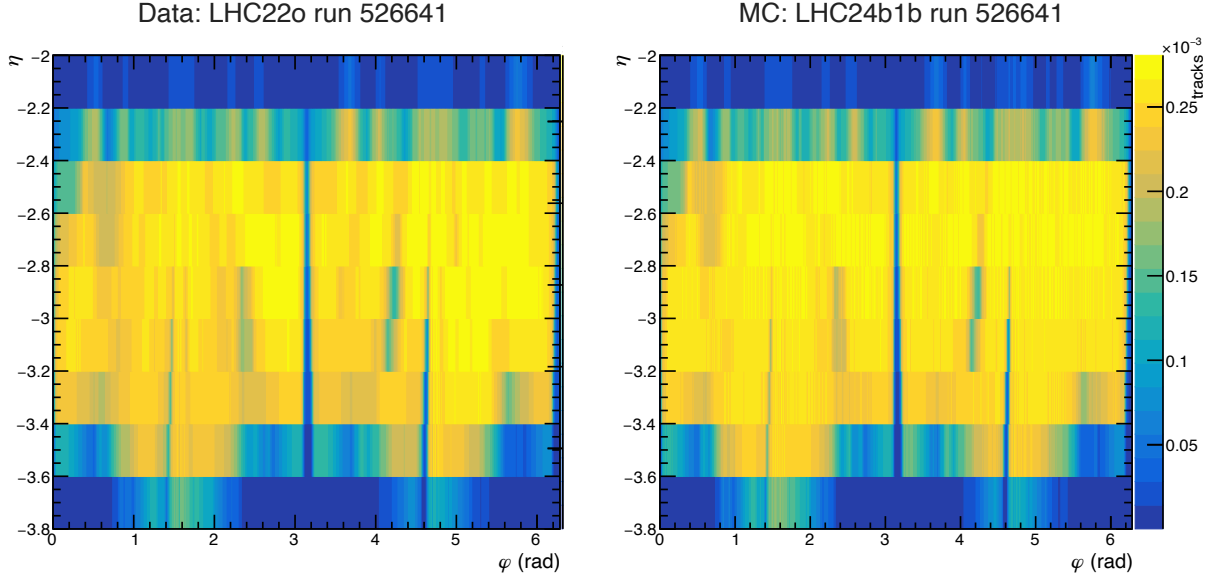


Figure 5.10: Distribution of  $\eta$  and  $\varphi$  of MFT tracks compared between data (left) and 2024 MC implementing the update in the description of the detector response (right).

the total number of selected events. This is done, in the present analysis, by projecting the distributions on the  $\eta$  and  $\varphi$  axes. For the 2023 MC, these comparisons (Figure 5.11) show differences above 5% in the central range of the  $\eta$  distribution and differences above 10% in the  $\varphi$  distribution. This MC was thus not exploitable to derive reliable corrections for the analysis of the charged-particle pseudorapidity distribution.

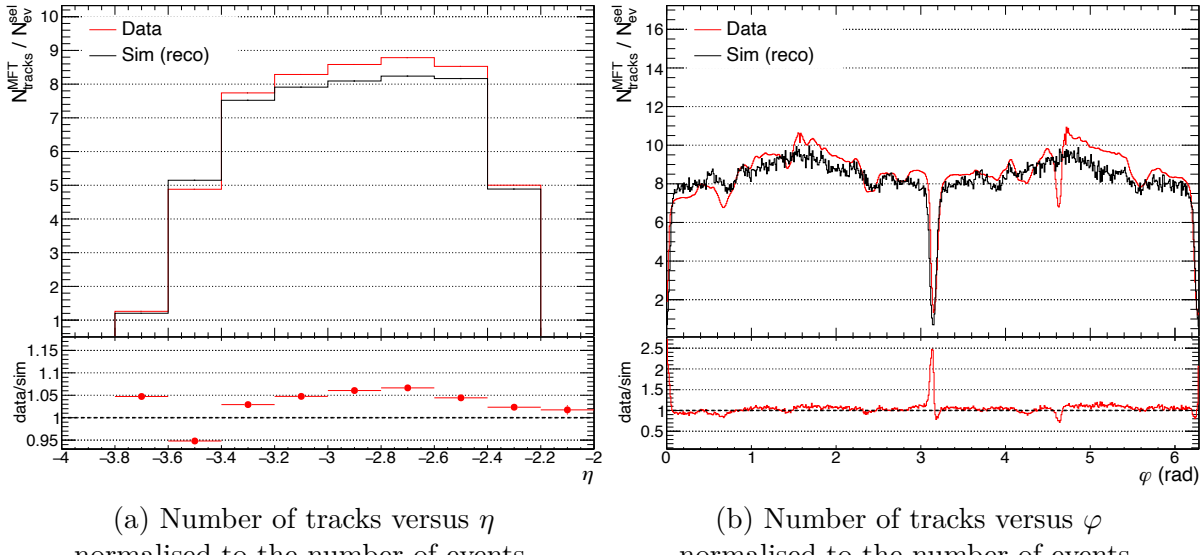


Figure 5.11: Comparison of the number of MFT tracks versus  $\eta$  and  $\varphi$  in data (LHC22o run 526641 in red) and reconstructed MC (LHC23f4b2 run 526641 in black).

However, for the most recent available MC simulation produced in 2024, the comparison between data and MC is significantly better. As one can see from Figures 5.12a and 5.12b,

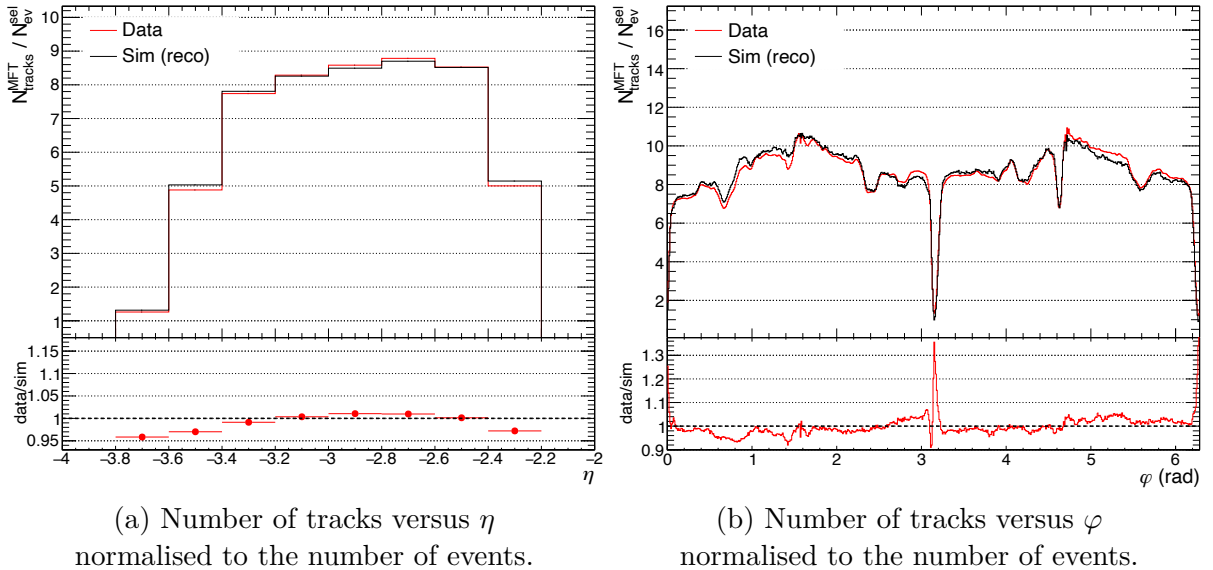


Figure 5.12: Comparison of the number of MFT tracks versus  $\eta$  and  $\varphi$  in data (LHC22o run 526641 in red) and reconstructed MC (LHC24b1b run 526641 in black).

the distributions of MFT tracks in data and MC are in a significantly better agreement with respect to the comparison with the 2023 MC. For the  $\eta$  distribution the difference is now less than 1% in the range  $-3.4 < \eta < -2.4$ , and for the azimuthal angle  $\varphi$  distribution the difference is less than  $\pm 5\%$  (except in the proximity of  $\varphi = 0, \pi, 2\pi$ ). The distribution of events along the  $z$  axis has also been compared in data and MC, and the difference is found to be less than 5% in the range  $|z_{\text{vtx}}| < 10$  cm. These differences are small enough to allow for a reliable estimation of the corrections based on the new MC.

## 5.4 Correction procedure

The correction procedure is similar to the one described in [122] where the *track-to-particle correction* and *triggering efficiency correction* (also called *trigger-bias correction*) are presented. This procedure has been used in ALICE to measure charged-particle pseudorapidity distributions since the first data were available.

The *vertex reconstruction efficiency correction* also presented in [122] is not implemented in this analysis since, contrarily to Run 2, in Run 3 each event has an associated primary vertex.

In Run 3, as the data are continuously readout in a triggerless scheme, the *triggering efficiency correction* is actually a *selection efficiency correction*. We will use this new notation in the following.

Each correction will be illustrated with the corresponding two- or one-dimensional distribution, obtained from MC simulations anchored to p–p collisions at  $\sqrt{s} = 13.6$  TeV taken in 2022.

### 5.4.1 Track-to-particle correction

It is worth reminding that the charged-particle pseudorapidity distribution is, by definition, the number of primary charged particles per collision and unit of pseudorapidity. Since the MFT is a tracking detector, MFT tracks can be reconstructed and are used as a proxy for the physical particles. As a result, a correction needs to be implemented to account for the difference between the number of reconstructed tracks and the number of primary charged particles: this is the *track-to-particle correction*.

This correction is described in more details in the following. For the sake of clarity, the following notations will be used:

- $G$  - number of generated primary particles in the MC simulation;
- $M$  - number of reconstructed tracks in the MC simulation.

To shorten mathematical expressions, in the following  $z_{\text{vtx}}$  will be noted as  $z$ .

The track-to-particle correction  $C_{\text{trk}}(\eta, z)$  is then computed as:

$$C_{\text{trk}}(\eta, z) = \frac{G_{\text{sel}}(\eta, z)}{M_{\text{sel}}(\eta, z)}, \quad (5.1)$$

where the subscript *sel* indicates that these quantities are computed considering the selected event sample in MC. The track reconstruction efficiency is defined as the number of reconstructed tracks divided by the number of generated primary particles, i.e.  $1/C_{\text{trk}}(\eta, z)$ . This quantity is represented in Figure 5.13 as a function of the  $\eta$  of the track, and of the longitudinal coordinate of the primary vertex of the collision,  $z_{\text{vtx}}$ .

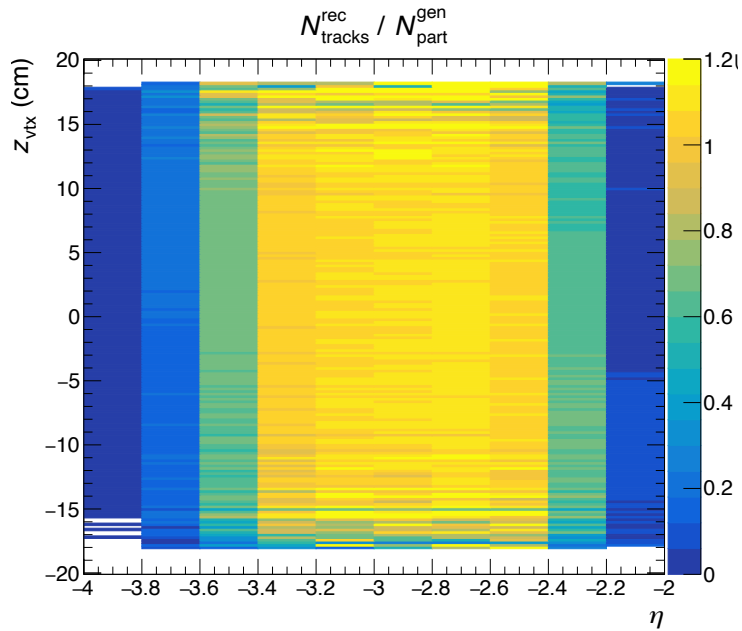


Figure 5.13: Track reconstruction efficiency of MFT tracks, computed using MC simulation.

As it can be deduced from Figure 5.13, the track reconstruction efficiency of the MFT is higher than 90% in central part of the pseudorapidity region covered by the detector,

namely  $-3.4 < \eta < -2.4$ , within the whole  $z_{\text{vtx}}$  range. Another important remark is that in some regions the reconstruction efficiency is higher than 100%. There are two main reasons for this. The first one is that the  $z_{\text{vtx}}$  in this distribution is the  $z$  coordinate of the collision associated to a given MFT track in A02D, which is the first one in the list of collisions time-compatible with the track and is not necessarily the collision from which the track originated. This association biases the distribution, because every track from a given MFT ROF will be associated in the A02D to exactly the same collision (see chapter 4 for more details), and therefore all these tracks will share the same  $z_{\text{vtx}}$  coordinate. The second reason is that the MFT tracking algorithm can reconstruct two different tracks corresponding to one single particle (track splitting). The influence of this reconstruction bias can be reduced by applying stricter requirements for the selection of MFT tracks. For example, one could consider excluding tracks with only 4 clusters in the MFT layers.

### 5.4.2 Selection efficiency correction

In addition to the *track-to-particle correction*, a so-called *selection efficiency correction* has to be applied in order to correct for the difference between the selected and the generated sample of events. This correction must be applied at both track and event levels.

#### Selection efficiency correction at track level

The selection efficiency correction at track level can be computed as:

$$C_{\text{sel}}(\eta, z) = \frac{G_{\text{all}}(\eta, z)}{G_{\text{sel}}(\eta, z)}, \quad (5.2)$$

with  $G_{\text{all}}$  being the total number of generated primary charged particles in  $\text{INEL} > 0$  events, and  $G_{\text{sel}}$  the number of generated primary charged particles belonging to selected events (events passing the event selection described above).

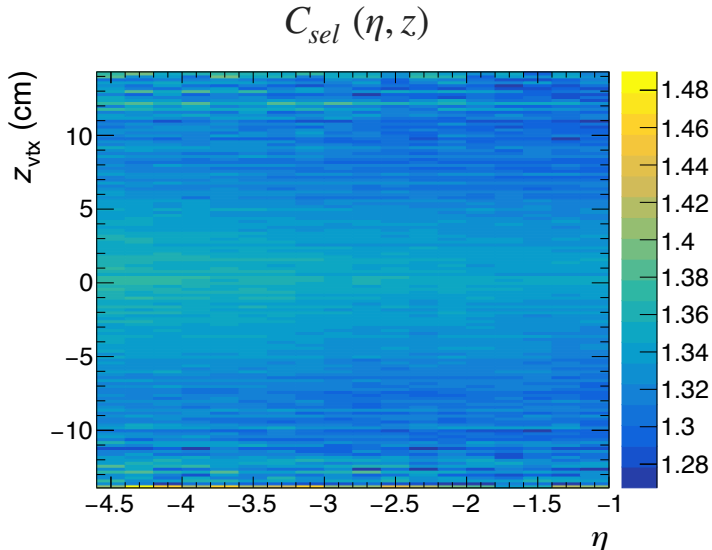


Figure 5.14: Selection efficiency correction at track level.

The correction is illustrated in Figure 5.14. As one can see, it depends only mildly on  $z_{\text{vtx}}$  and is almost independent of  $\eta$ .

### Selection efficiency correction at event level

Let's define  $E_{\text{all}}$  as the total number of generated events in the MC simulation having at least one primary charged particle in  $|\eta| < 1$  (this condition corresponds to the definition of INEL  $> 0$  event class), and  $E_{\text{sel}}^{\text{reco}}$  as the number of MC reconstructed events that have been selected. The selection efficiency correction at event level  $\tilde{C}_{\text{sel}}(z)$  is then defined as:

$$\tilde{C}_{\text{sel}}(z) = \frac{E_{\text{all}}(z)}{E_{\text{sel}}^{\text{reco}}(z)}. \quad (5.3)$$

This correction includes both the effect of event selection on the number of generated events, and the efficiency of event (i.e. primary vertex) reconstruction. The 2D correction profile is shown in Figure 5.15.

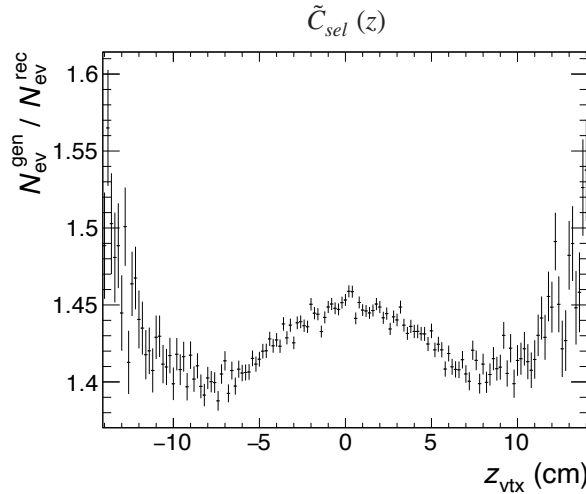


Figure 5.15: Selection efficiency correction at event level.

### 5.4.3 Calculation of the corrected result

The corrected result for the charged-particle multiplicity density is computed based on all the aforementioned corrections, using the following formula:

$$\left. \frac{1}{N_{\text{evt}}} \frac{dN}{d\eta} \right|_{\eta=\eta'} \sim \frac{\int_{z_{\min}(\eta')}^{z_{\max}(\eta')} N_{\text{trk}}^*(\eta', z) \times C_{\text{trk}}(\eta', z) \times C_{\text{sel}}(\eta', z)}{\int_{z_{\min}(\eta')}^{z_{\max}(\eta')} N_{\text{evt}}^*(z) \times \tilde{C}_{\text{sel}}(z)}, \quad (5.4)$$

where  $N_{\text{trk}}^*$  and  $N_{\text{evt}}^*$  are number of tracks and events in the data, respectively.

### 5.4.4 MC closure tests

MC closure tests are performed to check the correct implementation of the corrections described in the previous sections. The general idea behind the closure test is to ensure

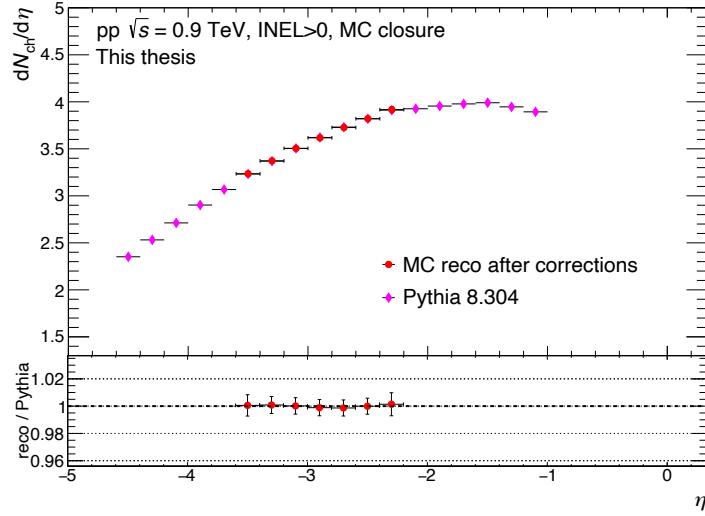


Figure 5.16: MC closure of LHC22h1c1.

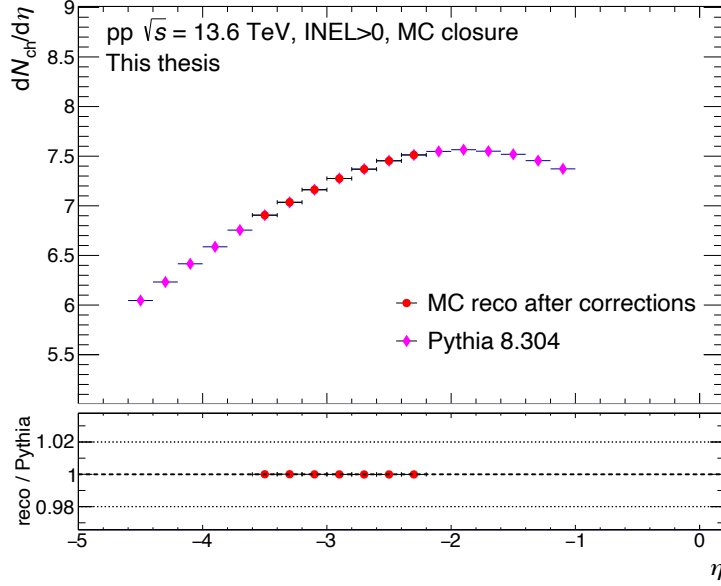


Figure 5.17: MC closure of LHC24b1b.

that whenever the reconstructed tracks and events in a MC simulation are corrected using the correction profiles established with the same simulation, the obtained result matches the generated distribution. It is worth noting that the closure test is meaningful only in case all the corrections involved in the analysis are applied. MC closure tests have been performed on MC simulations of p-p collisions at both  $\sqrt{s} = 0.9$  TeV and  $\sqrt{s} = 13.6$  TeV. The corresponding results are shown in Figures 5.16 and 5.17, respectively. As one can see, both MC closure tests result in a very good matching between the reconstructed distribution after correction and the generated distribution, well within the statistical uncertainties. This means that the corrections are working as expected and can be applied on the data.

## 5.5 Systematic uncertainties

### 5.5.1 Ambiguous tracks

In Run 3, the ALICE interaction rate is significantly higher with respect to the data taking during Runs 1 and 2. As a consequence, a sizable fraction of the reconstructed tracks can be “ambiguous”, i.e. time-associated to more than one collision (each collision being defined by the existence of a corresponding primary vertex). The percentage of ambiguous tracks in a dataset is highly dependent on its interaction rate and on the length of the readout window of the detector. The MFT detector, for instance, has a default readout window corresponding to 198 BC.

A specific task has been written in `O2Physics` to identify these ambiguous tracks and associate them to a list of compatible collisions that occurred within the track readout time window: this task is called the `track-to-collision-associator` for the central tracks, and the `fwdtrack-to-collision-associator` for MFT and muon tracks. The idea behind the task has been described in details in Chapter 4, section 4.3.1. Using this task one can estimate the percentage of ambiguous tracks for each dataset, reported in Table 5.1.

Dataset	$\sqrt{s}$ (TeV)	IR (kHz)	Fraction of ambiguous MFT tracks (%)
LHC22o run 526641	13.6	658	89
LHC22c run 517685	0.9	0.462	3.2

Table 5.1: Percentage of ambiguous tracks in the datasets used in this analysis.

As it was already mentioned, in the `A02D` files the reconstructed tracks are arbitrarily associated to their first compatible collision in time, and therefore some tracks can be wrongly associated to a collision they did not originate from.

In order to evaluate the uncertainty associated to ambiguous tracks, the number of MFT tracks normalized to the number of events (equivalent to an uncorrected  $dN_{\text{ch}}/d\eta$ ) is derived in two cases:

1. All tracks are associated to their first compatible collision in time, i.e. the default association in `A02D`;
2. Tracks are associated to the compatible collision that leads to the smallest  $DCA_{xy}$  (using the track-to-collision reassociation tool described in 4.3.2).

For the collisions at  $\sqrt{s} = 0.9$  TeV, which occurred at low IR, the fraction of ambiguous MFT tracks is small. The difference between the distributions of tracks versus pseudorapidity in the two cases cited above was evaluated, and found to be less than 0.1%: the systematic uncertainty due to ambiguous tracks is then negligible in this dataset.

For the collisions at  $\sqrt{s} = 13.6$  TeV, however, the fraction of ambiguous MFT tracks is much higher, as reported in Table 5.1, and the corresponding systematic uncertainty can become sizable. The comparison between the pseudorapidity distributions corresponding to the two track-to-collision association criteria for the 13.6 TeV dataset is shown in Figure 5.18. The difference stays within 2% for all the points, with only the last one at  $\eta = -2.3$  reaching 2.3%.

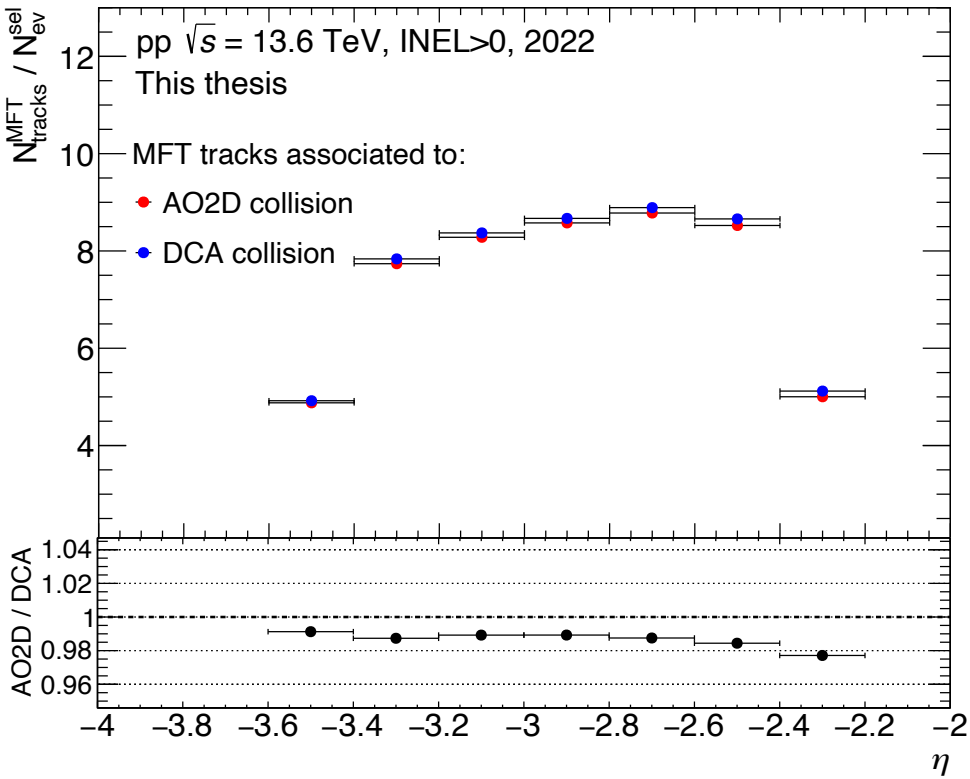


Figure 5.18: Distribution of the number of MFT tracks as a function of  $\eta$  normalized to the number of selected events, in p-p collisions at  $\sqrt{s} = 13.6$  TeV, using the two track-to-collision association criteria mentioned in the text.

To understand where this difference comes from, let us consider the case in which, using the first track-to-collision association criterion, a fraction of MFT tracks are initially associated to a collision  $coll_{\text{AO2D}}$ , which did not pass the event selection. All these tracks are then not counted in the uncorrected result. Now let us consider the second track-to-collision association criterion: in this case, some of the MFT tracks previously associated to the collisions  $coll_{\text{AO2D}}$  discarded by the event selection could be reassigned to another collision,  $coll_{\text{DCA}}$ , which passed the event selection. This time, these tracks would then be counted in the uncorrected result. The number of selected events does not vary in the two cases, but the number of MFT tracks can, depending on the selection tag of the collision they are associated to.

The systematic uncertainty resulting from the ambiguous tracks would be greatly reduced if one requires MFT tracks to be matched with FT0-C signal.

### 5.5.2 Other systematic uncertainties

Other sources of systematic uncertainty enter the analysis: they could not be implemented within the work developed in this thesis, but were nevertheless studied and, when possible, the corresponding analysis code was developed. They are briefly mentioned in what follows.

## Diffractive content and model dependence

In general, Monte Carlo event generators like PYTHIA8 differ from the data in the description of single and double-diffractive events. As such events correspond to 20% and 10% of total inelastic cross-section, respectively [107], and have very low midrapidity multiplicity, this difference has a considerable effect on the overall normalization and needs to be corrected for. As explained in section 5.1.1, the impact of single and double-diffractive events on the number of forward tracks also needs to be considered.

The correction is done by re-weighting the diffractive mass distribution in MC, the diffractive mass  $M_X$  being the invariant mass of the diffractively produced system. Diffractive mass distributions cannot be measured directly, thus the values are taken from a dedicated model calculation [123].

The corresponding systematic uncertainty is then evaluated by varying the diffractive mass distributions and fractions of single- and double-diffractive events. The procedure is similar to the one previously used in [89].

Even though the procedure is well established, it could not be employed for the present analysis because no MC simulations with reweighted diffraction content are available so far. Similarly, the uncertainty related to the model dependence is not evaluated since PYTHIA8 is the only generator currently implemented in simulations with particle transport and A02D production. One would need at least one additional generator to compute the different corrections up to the final result. The difference with PYTHIA8 could then be taken as systematic uncertainty.

In previous analyses at midrapidity, these uncertainty amount to 2% at  $\sqrt{s} = 13$  TeV [89] and represent the major systematic uncertainty of the measurement. It is expected that in the case of forward multiplicity measurement these uncertainties could be even larger.

## Extrapolation to zero $p_T$

All the detectors used in this analysis have a  $p_T$  threshold below which the particles are not detected. This threshold is around 50 MeV/ $c$ .

This means that the obtained particle yields below the threshold entirely depend on the assumptions made in the MC simulations, i.e. the generator chosen for the simulation. The corresponding uncertainty can be obtained by varying the amount of particles below that threshold.

## Detector simulation: material budget

The detector volumes are described with some limited precision in the geometry used by GEANT. This can lead to an imperfect description of the acceptance profile for primary charged particles. In order to account for this effect, the corresponding systematic uncertainty is evaluated by considering MC simulations with increased and decreased material budget. It is worth noting that this systematic uncertainty is expected to be significantly smaller for the MFT detector with respect to the forward detectors used in Runs 1 and 2, the main reason being that in Runs 1 and 2 some heavy ITS services were located in front of the forward detectors.

## 5.6 Results

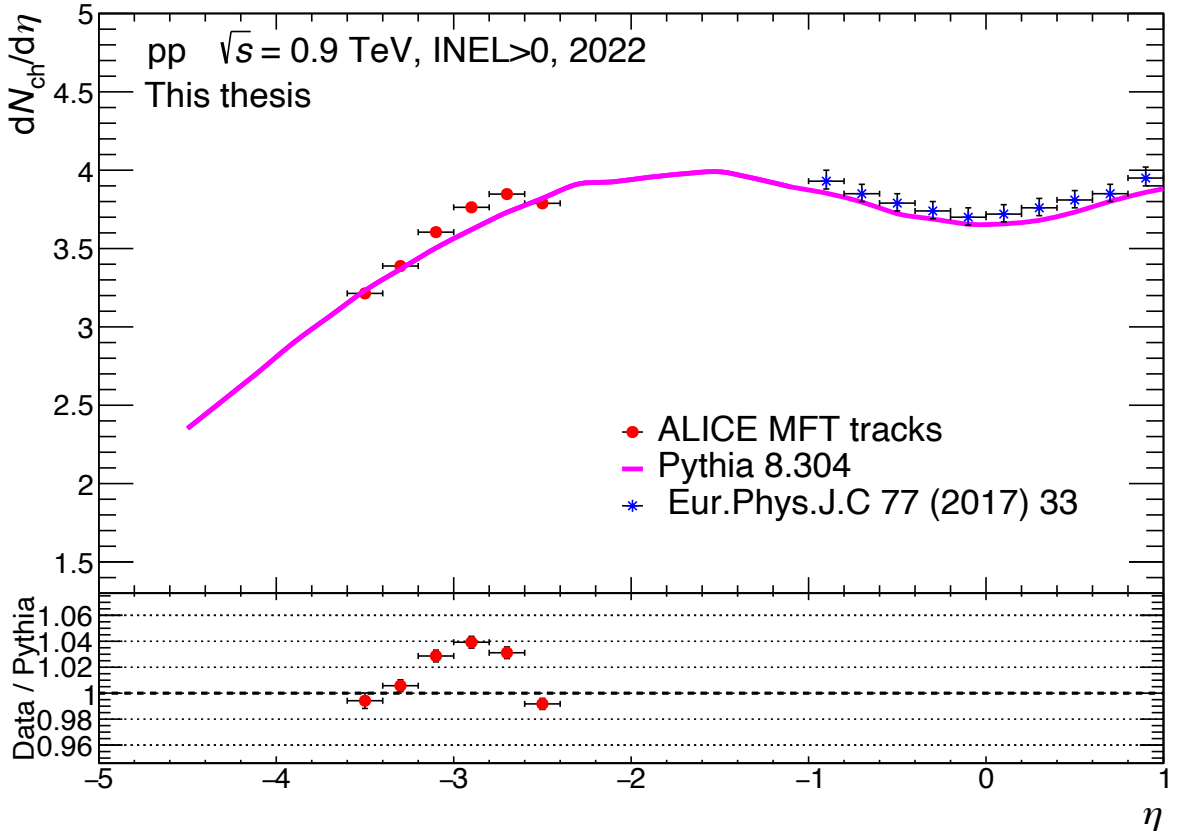


Figure 5.19: Charged-particle pseudorapidity distribution for proton-proton collisions at  $\sqrt{s} = 0.9$  TeV obtained with the MFT (in red) compared with the PYTHIA8 prediction and the central barrel results (in blue). The central barrel results are extracted from [124]. The statistical uncertainties are the only one represented in this figure, but they are too small to be noticeable.

The preliminary result for p-p collisions at  $\sqrt{s} = 0.9$  TeV, reported in Figure 5.19, shows a good agreement with the PYTHIA8 predictions. It is also compatible, despite the sizable gap between the two rapidity ranges, with the previously published ALICE result at midrapidity. It is worth noting the decreasing trend of the ratio between data and PYTHIA8 towards the edges of the MFT acceptance and the fact that the data points are above the PYTHIA8 prediction in the region  $-3.2 < \eta < -2.6$ . This can be explained by the discrepancy in the number of reconstructed MFT tracks in data and MC in this region (see Figure 5.7a). One can expect this result to become closer to PYTHIA8 whenever a new MC with tuning of MFT inactive chips becomes available.

The preliminary result at  $\sqrt{s} = 13.6$  TeV in Figure 5.20 also shows a very good agreement with the PYTHIA8 prediction. As in case of the  $\sqrt{s} = 0.9$  TeV analysis, one can notice the decreasing trend of the ratio between data and MC towards the edges of the MFT acceptance. In the regions  $\eta < -3.4$  and  $\eta > -2.4$ , in particular, data are found to be lower than MC by up to 3%, which can be also seen in Figure 5.12a.

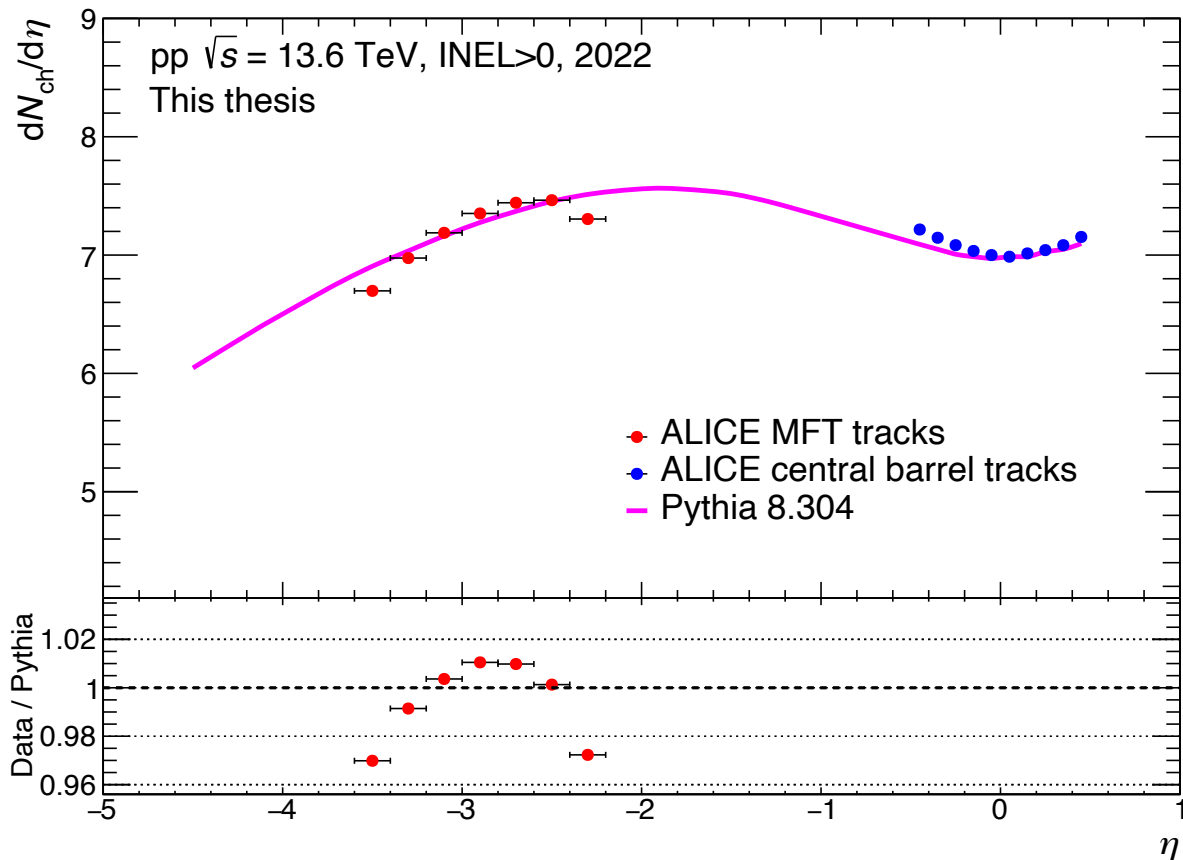


Figure 5.20: Charged-particle pseudorapidity distributions for proton-proton collisions at  $\sqrt{s} = 13.6$  TeV obtained with the MFT (in red) compared with PYTHIA8 predictions and the central barrel results (in blue). The statistical uncertainties are the only one represented in this figure, but they are too small to be noticeable. The central barrel results are taken from [125].

When comparing the results at  $\sqrt{s} = 0.9$  and  $13.6$  TeV with PYTHIA8 simulations, one has to keep in mind that some of the major systematic uncertainties, like the one arising from the contribution of diffractive events, have not yet been evaluated. A final, quantitative comparison with the theoretical predictions will only be possible when all the sources of systematic uncertainty will be computed.

## 5.7 Summary and outlook

In this chapter, the first analysis of the pseudorapidity distribution of charged particles in p-p collisions at  $\sqrt{s} = 0.9$  and  $13$  TeV has been presented, exploiting the tracks reconstructed by the MFT detector, based on the ALICE Run 3 data. This analysis allows to extend the midrapidity results towards the forward regions, the preliminary results showing a good agreement with the PYTHIA8 predictions both at  $\sqrt{s} = 0.9$  TeV and  $\sqrt{s} = 13.6$  TeV.

This study also allowed to pinpoint the need for anchored MC with tuning of MFT active/inactive chips during data taking. The quality of the available MC simulations

was evaluated, by comparing reconstructed MC and data, and the number of MFT tracks versus  $\eta$  and  $\phi$  was shown to be quite different in 2022 and 2023 MC productions. The latest MC quality was deemed good enough to calculate the needed correction profiles for the measurement. The uncertainty due to the presence of ambiguous tracks was found to be negligible for p-p collisions at  $\sqrt{s} = 0.9$  TeV, while for p-p collisions at  $\sqrt{s} = 13.6$  TeV it was shown to be smaller than 2.3%.

As an outlook, the charged-particle pseudorapidity measurement would need a complete systematic uncertainty evaluation in order to be published. This is not achievable at the moment of the writing of this manuscript since the specific MC simulations necessary to calculate several systematic uncertainties are not yet available.



# Conclusion

$J/\psi$  yield and inclusive charged-particle multiplicity are powerful observables to probe QCD, crucial to better understand mechanisms such as MPIs, non-perturbative QCD and more in general to constrain theoretical models. Studying the forward  $J/\psi$  yield as a function of charged-particle multiplicity at forward pseudorapidity in proton-proton collisions provides insights into  $J/\psi$  production and its correlation with the underlying event activity. It was shown that the forward relative  $J/\psi$  yield displays a steeper than linear increase as a function of relative charged-particle multiplicity at forward pseudorapidity, similar to the increase observed in a previous measurement of midrapidity relative  $J/\psi$  yield as a function of relative charged-particle multiplicity at midrapidity. Within the PYTHIA event generator, this effect suggests that Color Reconnection is at play. The measurement also shows a good agreement with EPOS4HQ and 3-Pomeron CGC models. In this thesis, the forward  $J/\psi$  yield as a function of charged-particle multiplicity at forward pseudorapidity was measured for the first time in proton-proton collisions at  $\sqrt{s} = 13$  TeV, based on the Run 2 data taking. I was responsible for the full analysis chain and the gathering of model comparisons.

Moving to the more recent Run 3 data taking, I worked on the software developments needed for the MFT quality control and data readiness, developing specific codes to reduce track-to-collision ambiguity, and to match MFT tracks to FT0-C signals. This matching displayed excellent performance on simulations and opened the way for a time-alignment between MFT and the CTP, for which I estimated a time offset of  $1.5 \pm 0.23 \mu\text{s}$ . Finally, the first physics results derived with the MFT were presented, i.e. the measurement of charged-particle pseudorapidity distribution in the forward region in proton-proton collisions at  $\sqrt{s} = 0.9$  and  $\sqrt{s} = 13.6$  TeV, found to be compatible with the available PYTHIA8 predictions.



# Appendix A

## Appendix

### A.1 Fit functions

#### A.1.1 Double Crystal Ball (CB2)

This function has 7 parameters, a normalization factor N, two Gaussian core parameters ( $\bar{x}$  and  $\sigma$ ) and four tail parameters ( $\alpha$ ,  $n$ ,  $\alpha'$  and  $n'$ ). This function is defined by [126] :

$$\text{CB2}(x) = N \times \begin{cases} \exp\left(\frac{-(x-\bar{x})^2}{2\sigma^2}\right) & \text{if } -\alpha < \frac{x-\bar{x}}{\sigma} < \alpha' \\ A \times (B - \frac{x-\bar{x}}{\sigma})^{-n} & \text{if } \frac{x-\bar{x}}{\sigma} \leq -\alpha \\ C \times (D + \frac{x-\bar{x}}{\sigma})^{-n'} & \text{if } \frac{x-\bar{x}}{\sigma} \geq \alpha' \end{cases}$$

with

$$A = \left(\frac{n}{|\alpha|}\right)^n \exp\left(-\frac{|\alpha|^2}{2}\right), \quad B = \frac{n}{|\alpha|} - |\alpha|$$

$$C = \left(\frac{n'}{|\alpha'|}\right)^{n'} \exp\left(-\frac{|\alpha'|^2}{2}\right), \quad D = \frac{n'}{|\alpha'|} - |\alpha'|$$

#### A.1.2 Variable Width Gaussian (VWG)

This 4-parameter function can be used to describe the background of the invariant mass spectra, and is defined as follows [126]

$$\text{VWG}(x; N, \bar{x}, A, B) = N \times \exp\left(-\frac{(x - \bar{x})^2}{2\sigma_{VWG}^2}\right)$$

with

$$\sigma_{VWG} = A + B \times \frac{(x - \bar{x})}{\bar{x}}$$

#### A.1.3 Pol2 $\times$ Exp

Another common function [126] used to describe the background of the invariant mass spectra is the multiplication of a 2nd order polynomial by an exponential, which can be defined as follows:

$$f(x; A, B, C, \lambda) = (A + Bx + Cx^2) \times e^{\lambda x}$$

## A.2 Corrections to the number of selected events

In the following the way to correct the measured number of events  $N_{ev}((kINT7 + PS) + vtxQA)$  into  $N_{ev}(INEL > 0)$  is described step by step.

$$\begin{aligned} N_{ev}(INEL > 0) &= \frac{N_{ev}(INEL > 0) \times N_{ev}(INEL > 0 + (kINT7 + PS))}{N_{ev}(INEL > 0 + (kINT7 + PS))} \\ &= \frac{1}{\epsilon_{INEL>0}^{MB}} \frac{N_{ev}(INEL > 0 + (kINT7 + PS))}{N_{ev}((kINT7 + PS) + vtxQA)} \times N_{ev}((kINT7 + PS) + vtxQA) \\ &= \frac{1}{\epsilon_{INEL>0}^{MB}} \frac{N_{ev}((kINT7 + PS)) - N_{ev}(INEL = 0 + (kINT7 + PS))}{N_{ev}((kINT7 + PS) + vtxQA)} \times N_{ev}((kINT7 + PS) + vtxQA) \\ &= \frac{N_{ev}((kINT7 + PS) + vtxQA)}{\epsilon_{INEL>0}^{MB}} \times \left( \frac{1}{\epsilon_{vtxQA}} - \frac{N_{ev}(INEL = 0 + (kINT7 + PS))}{N_{ev}((kINT7 + PS) + vtxQA)} \right) \\ &= \frac{N_{ev}((kINT7 + PS) + vtxQA)}{\epsilon_{INEL>0}^{MB}} \times \left( \frac{1}{\epsilon_{vtxQA}} - \frac{N_{ev}((kINT7 + PS))}{N_{ev}((kINT7 + PS) + vtxQA)} \frac{N_{ev}(INEL = 0 + (kINT7 + PS))}{N_{ev}((kINT7 + PS))} \right) \\ &= \frac{N_{ev}((kINT7 + PS) + vtxQA)}{\epsilon_{INEL>0}^{MB}} \times \frac{1}{\epsilon_{vtxQA}} \left( 1 - \frac{N_{ev}(INEL = 0 + (kINT7 + PS))}{N_{ev}((kINT7 + PS))} \right) \\ &= \frac{1}{\epsilon_{INEL>0}^{MB}} \frac{1}{\epsilon_{vtxQA}} \times (1 - C_{INEL=0}) \times N_{ev}((kINT7 + PS) + vtxQA) \end{aligned}$$

# Bibliography

- [1] A. Obertelli and H. Sagawa, *Modern nuclear physics*. Springer, 2021.
- [2] E. P. P. Aurenche, J.-Ph Guillet, *QED, QCD en pratique*. 2016. 3ème cycle. Beyrouth, Liban, cel-01440544v2.
- [3] S. Bethke, G. Dissertori and G. Salam, *Quantum Chromodynamics*. in K.A. Olive et al. (Particle Data Group), Chinese Physics C38 (2014) 090001.
- [4] M. Durante, P. Indelicato, B. Jonson, V. Koch, K. Langanke, U.-G. Meißner, E. Nappi, T. Nilsson, T. Stöhlker, E. Widmann, and M. Wiescher, “All the fun of the fair: fundamental physics at the facility for antiproton and ion research,” *Physica Scripta*, vol. 94, no. 3, 2019.
- [5] Y. M. Kohsuke Yagi, Tetsuo Hatsuda, *Quark-Gluon plasma: from big bang to little bang*. Cambridge University Press, 2005.
- [6] W. Busza, K. Rajagopal, and W. van der Schee, “Heavy ion collisions: The big picture and the big questions,” *Annual Review of Nuclear and Particle Science*, vol. 68, no. 1, pp. 339–376, 2018.
- [7] P. Braun-Munzinger and B. Dönigus, “Loosely-bound objects produced in nuclear collisions at the LHC,” *Nuclear Physics A*, vol. 987, p. 144–201, Jul 2019.
- [8] A. K. Chaudhuri, “Viscous hydrodynamic model for relativistic heavy ion collisions,” *Advances in High Energy Physics*, 2013.
- [9] M. E. Tejeda-Yeomans, “Heavy-ion physics: freedom to do hot, dense, exciting QCD,” 2020.
- [10] F. Becattini, “An introduction to the statistical hadronization model,” 2009.
- [11] A. Andronic, P. Braun-Munzinger, K. Redlich, and J. Stachel, “Decoding the phase structure of QCD via particle production at high energy,” *Nature*, vol. 561, p. 321–330, Sept. 2018.
- [12] A. Collaboration, “Measurements of chemical potentials in Pb-Pb collisions at  $\sqrt{s_{\text{NN}}} = 5.02 \text{ TeV}$ ,” 2024.

## BIBLIOGRAPHY

---

- [13] J. Stachel, A. Andronic, P. Braun-Munzinger, and K. Redlich, “Confronting LHC data with the statistical hadronization model,” *Journal of Physics: Conference Series*, vol. 509, p. 012019, may 2014.
- [14] ALICE collaboration, “Enhanced production of multi-strange hadrons in high-multiplicity proton–proton collisions,” *Nature Physics*, vol. 13, p. 535–539, Apr. 2017.
- [15] S. Hamieh, K. Redlich, and A. Tounsi, “Canonical description of strangeness enhancement from p–A to Pb–Pb collisions,” *Physics Letters B*, vol. 486, p. 61–66, July 2000.
- [16] P. Foka and M. A. Janik, “An overview of experimental results from ultra-relativistic heavy-ion collisions at the CERN LHC: Bulk properties and dynamical evolution,” *Reviews in Physics*, vol. 1, pp. 154–171, 2016.
- [17] T. Matsui and H. Satz, “ $J/\psi$  Suppression by Quark-Gluon Plasma Formation,” *Phys. Lett. B*, vol. 178, pp. 416–422, 1986.
- [18] E. G. Ferreiro, “Upsilon: the new golden probe?,” 2013. Workshop AFTER@ETC, Trento.
- [19] Mócsy, “Potential models for quarkonia: What can we learn from potential models at finite temperature?,” *The European Physical Journal C*, vol. 61, p. 705–710, Jan. 2009.
- [20] R. L. Thews, M. Schroedter, and J. Rafelski, “Enhanced  $J/\psi$  production in deconfined quark matter,” *Physical Review C*, vol. 63, Apr. 2001.
- [21] ALICE collaboration, “Direct photon production in Pb–Pb collisions at  $\sqrt{s_{NN}} = 2.76$  TeV,” *Physics Letters B*, vol. 754, p. 235–248, Mar. 2016.
- [22] G. e. a. Aad, “Observation of Long-Range Elliptic Azimuthal Anisotropies in  $\sqrt{s}=13$  and 2.76 TeV pp Collisions with the ATLAS Detector,” *Physical Review Letters*, vol. 116, p. 172301, Apr. 2016.
- [23] CMS collaboration, “Elliptic Flow of Charm and Strange Hadrons in High-Multiplicity pPb collisions at  $\sqrt{s_{NN}} = 8.16$  TeV,” *Physical Review Letters*, vol. 121, Aug. 2018.
- [24] Y. Kanakubo, Y. Tachibana, and T. Hirano, “Unified description of hadron yield ratios from dynamical core-corona initialization,” *Physical Review C*, vol. 101, Feb. 2020.
- [25] E. Eichten, K. Gottfried, T. Kinoshita, J. B. Kogut, K. D. Lane, and T.-M. Yan, “The Spectrum of Charmonium,” *Phys. Rev. Lett.*, vol. 34, pp. 369–372, 1975. [Erratum: Phys.Rev.Lett. 36, 1276 (1976)].
- [26] E. Eichten, S. Godfrey, H. Mahlke, and J. L. Rosner, “Quarkonia and their transitions,” *Reviews of Modern Physics*, vol. 80, p. 1161–1193, Sept. 2008.

- [27] G. Abbas, M. A. Khan, and V. Singh, “Rl workman et al.(particle data group),  
prog. theor,” *Exp. Phys*, 2022.
- [28] Brambilla, N., Krämer, M., Musса, R., Vairo, A., Bali, G., Bodwin and others,  
“Heavy quarkonium physics,” *arXiv preprint hep-ph/0412158*, 2004.
- [29] M. Bedjidian, D. Blaschke, G. T. Bodwin, N. Carrer, B. Cole, P. Crochet,  
A. Dainese, A. Deandrea, S. Frixione, P. Hoyer, D. Kharzeev, O. L. Kodolova,  
R. Kvätadze, J. Lee, I. P. Lokhtin, M. Mangano, N. Marchal, M. Nardi, G. Nardulli,  
H. Niemi, S. Peigne’, P. Petreczky, A. D. Polosa, H. Satz, H. Takai, S. Taprogge,  
R. L. Thews, E. Vercellin, and R. Vogt, “Hard probes in heavy ion collisions at the  
LHC: heavy flavour physics,” 2003.
- [30] C. Chao-Hsi, “Hadronic production of  $J/\psi$  associated with a gluon,” *Nuclear Physics B*, vol. 172, pp. 425–434, 1980.
- [31] R. Baier and R. Rückl, “Hadronic collisions: a quarkonium factory,” *Zeitschrift für  
Physik C Particles and Fields*, vol. 19, pp. 251–266, 1983.
- [32] A. Andronic, F. Arleo, R. Arnaldi, A. Beraudo, E. Bruna, D. Caffarri, Z. C.  
del Valle, J. G. Contreras, T. Dahms, A. Dainese, M. Djordjevic, E. G. Ferreiro,  
H. Fujii, P.-B. Gossiaux, R. G. de Cassagnac, C. Hadjidakis, M. He, H. van Hees,  
W. A. Horowitz, R. Kolevatov, B. Z. Kopeliovich, J.-P. Lansberg, M. P. Lombardo,  
C. Lourenço, G. Martinez-Garcia, L. Massacrier, C. Mironov, A. Mischke,  
M. Nahrgang, M. Nguyen, J. Nystrand, S. Peigné, S. Porteboeuf-Houssais, I. K.  
Potashnikova, A. Rakotozafindrabe, R. Rapp, P. Robbe, M. Rosati, P. Rosnet,  
H. Satz, R. Schicker, I. Schienbein, I. Schmidt, E. Scomparin, R. Sharma, J. Stachel,  
D. Stocco, M. Strickland, R. Tieulent, B. A. Trzeciak, J. Uphoff, I. Vitev, R. Vogt,  
K. Watanabe, H. Woehri, and P. Zhuang, “Heavy-flavour and quarkonium produc-  
tion in the LHC era: from proton–proton to heavy-ion collisions,” *The European  
Physical Journal C*, vol. 76, Feb. 2016.
- [33] G. T. Bodwin, E. Braaten, and G. P. Lepage, “Rigorous QCD analysis of inclusive  
annihilation and production of heavy quarkonium,” *Phys. Rev. D*, vol. 51, pp. 1125–  
1171, 1995. [Erratum: Phys.Rev.D 55, 5853 (1997)].
- [34] J. Soto, “Overview of Non-Relativistic QCD,” *The European Physical Journal A*,  
vol. 31, p. 705–710, Mar. 2007.
- [35] S. S. Biswal, S. S. Mishra, and K. Sridhar, “Understanding  $J/\psi$  and  $\psi'$  production  
using a modified version of non-relativistic quantum chromodynamics,” *Physics Let-  
ters B*, vol. 832, p. 137221, 2022.
- [36] G. T. Bodwin, E. Braaten, and G. P. Lepage, “Rigorous QCD analysis of inclusive  
annihilation and production of heavy quarkonium,” *Physical Review D*, vol. 51,  
no. 3, 1995.
- [37] M. Tarhini, *Measurement of Z-boson and  $J/\psi$  Production in  $p$ -Pb and Pb-Pb Col-  
lections at  $\sqrt{s_{NN}} = 5.02$  TeV with ALICE at the LHC*. Theses, Université Paris  
Saclay (COmUE), June 2017.

## BIBLIOGRAPHY

---

- [38] ALICE collaboration, “Prompt and non-prompt  $J/\psi$  production and nuclear modification at mid-rapidity in p–Pb collisions at  $\sqrt{s_{NN}} = 5.02$  TeV,” *The European Physical Journal C*, vol. 78, no. 6, 2018.
- [39] R. Pasechnik, A. Szczerba, and O. Teryaev, “Polarization effects in the central exclusive  $c$  production and the angular  $J/\psi$  distributions,” *Physical Review D*, vol. 83, Apr. 2011.
- [40] M. Butenschoen and B. A. Kniehl, “ $J/\psi$  Polarization at the Tevatron and the LHC: Nonrelativistic-QCD Factorization at the Crossroads,” *Phys. Rev. Lett.*, vol. 108, p. 172002, Apr 2012.
- [41] K.-T. Chao, Y.-Q. Ma, H.-S. Shao, K. Wang, and Y.-J. Zhang, “ $J/\psi$  polarization at Hadron Colliders in Nonrelativistic QCD,” *Physical Review Letters*, vol. 108, June 2012.
- [42] ALICE collaboration, “ $J/\psi$  polarization in pp collisions at  $\sqrt{s} = 7$  TeV,” *Physical Review Letters*, vol. 108, Feb. 2012.
- [43] LHCb Collaboration, “Measurement of  $J/\psi$  polarization in pp collisions at  $\sqrt{s} = 7$  TeV,” *Eur. Phys. J. C*, vol. 73, no. 11, p. 2631, 2013.
- [44] CMS collaboration, “Measurement of the prompt  $J/\psi$  and  $\psi(2S)$  polarizations in pp collisions at  $\sqrt{s} = 7$  TeV,” *Physics Letters B*, vol. 727, p. 381–402, Dec. 2013.
- [45] S. Porteboeuf and R. Granier de Cassagnac, “ $J/\psi$  yield vs. multiplicity in proton-proton collisions at the LHC,” *Nuclear Physics B - Proceedings Supplements*, vol. 214, p. 181–184, May 2011.
- [46] P. Bartalini, E. L. Berger, B. Blok, G. Calucci, R. Corke, M. Diehl, Y. Dokshitzer, L. Fano, L. Frankfurt, J. R. Gaunt, S. Gieseke, G. Gustafson, D. Kar, C. H. Kom, A. Kulesza, E. Maina, Z. Nagy, C. Roehr, A. Siodmok, M. Schmelling, W. J. Stirling, M. Strikman, and D. Treleani, “Multi-Parton Interactions at the LHC,” 2011.
- [47] ALICE collaboration, “ $J/\psi$  production as a function of charged particle multiplicity in pp collisions at  $\sqrt{s} = 7$  TeV,” *Physics Letters B*, vol. 712, p. 165–175, June 2012.
- [48] ALICE collaboration, “Multiplicity dependence of inclusive  $J/\psi$  production at midrapidity in pp collisions at  $\sqrt{s} = 13$  TeV,” *Physics Letters B*, vol. 810, p. 135758, Nov. 2020.
- [49] ALICE collaboration, “Forward rapidity  $J/\psi$  production as a function of charged-particle multiplicity in pp collisions at  $\sqrt{s} = 5.02$  and 13 TeV,” *Journal of High Energy Physics*, vol. 2022, June 2022.
- [50] S. Agostinelli, J. Allison, and *al*, “Geant4 — a simulation toolkit,” *Nuclear Instruments and Methods in Physics Research Section A: Accelerators, Spectrometers, Detectors and Associated Equipment*, vol. 506, no. 3, pp. 250–303, 2003.

- [51] T. Sjöstrand, S. Ask, J. R. Christiansen, R. Corke, N. Desai, P. Ilten, S. Mrenna, S. Prestel, C. O. Rasmussen, and P. Z. Skands, “An introduction to PYTHIA 8.2,” *Computer Physics Communications*, vol. 191, p. 159–177, June 2015.
- [52] T. Sjostrand, “Status and developments of event generators,” p. 007, 09 2016.
- [53] C. Bierlich, S. Chakraborty, N. Desai, L. Gellersen, I. Helenius, P. Ilten, L. Lönnblad, S. Mrenna, S. Prestel, C. T. Preuss, *et al.*, “A comprehensive guide to the physics and usage of PYTHIA 8.3,” *SciPost Physics Codebases*, p. 008, 2022.
- [54] S. Porteboeuf, T. Pierog, and K. Werner, “Producing Hard Processes Regarding the Complete Event: The EPOS Event Generator,” 2010.
- [55] K. Werner, F.-M. Liu, and T. Pierog, “Parton ladder splitting and the rapidity dependence of transverse momentum spectra in deuteron-gold collisions at the BNL Relativistic Heavy Ion Collider,” *Physical Review C*, vol. 74, Oct. 2006.
- [56] T. Pierog, I. Karpenko, J. M. Katzy, E. Yatsenko, and K. Werner, “EPOS LHC: Test of collective hadronization with data measured at the CERN Large Hadron Collider,” *Physical Review C*, vol. 92, Sept. 2015.
- [57] K. Werner, M. Bleicher, B. Guiot, I. Karpenko, and T. Pierog, “Evidence for Flow from Hydrodynamic Simulations of p-Pb Collisions at 5.02 TeV from v(2) Mass Splitting,” *Physical review letters*, vol. 112, p. 232301, 06 2014.
- [58] K. Werner, B. Guiot, I. Karpenko, and T. Pierog, “Analyzing radial flow features in p-Pb and p-p collisions at several TeV by studying identified-particle production with the event generator EPOS3,” *Physical Review C*, vol. 89, June 2014.
- [59] E. Lopienska, “The CERN accelerator complex, layout in 2022. Complexe des accélérateurs du CERN en janvier 2022,” 2022.
- [60] A. Dainese, E. Scomparin, G. Usai, P. Antonioli, R. Arnaldi, A. Beraudo, E. Bruna, G. Bruno, S. Bufalino, P. Nezza, M. Lombardo, R. Nania, F. Noferini, C. Oppedisano, S. Piano, F. Prino, A. Rossi, M. Agnello, W. Alberico, and C. Zampolli, “INFN What Next: Ultra-relativistic Heavy-Ion Collisions,” 02 2016.
- [61] E. Botta, “Particle identification performance at ALICE. Particle identification performance at ALICE,” tech. rep., 2017.
- [62] B. Cheynis, “ALICE VZERO detector.” <https://cds.cern.ch/record/1623370/files/>.
- [63] The ALICE collaboration, “*Technical Design Report on Forward Detectors: FMD, T0 and V0*, cern-lhcc-2004-025 alice-tdr-011(2004),” <https://cds.cern.ch/record/781854/files/lhcc-2004-025.pdf>.
- [64] C. Finck, “The muon spectrometer of the alice,” *Journal of Physics: Conference Series*, vol. 50, p. 397, nov 2006.

## BIBLIOGRAPHY

---

- [65] Christian Finck for the ALICE MS collaboration, “*The Muon Spectrometer of ALICE*,” J. Phys.:Conf. Ser. 50 397 (2006).
- [66] W. Shaikh, “Bottomonium studies at LHC energy using ALICE muon spectrometer,” 2020.
- [67] The ALICE collaboration, “The Muon Spectrometer.” [https://alice-collaboration.web.cern.ch/menu\\_proj\\_items/Muon-Spect](https://alice-collaboration.web.cern.ch/menu_proj_items/Muon-Spect).
- [68] “Upgrade of the ALICE Experiment: Letter of Intent,” tech. rep., CERN, Geneva, 2014.
- [69] “LHC long term schedule.” <https://lhc-commissioning.web.cern.ch/schedule/LHC-long-term.htm>.
- [70] The ALICE collaboration, “*Technical Design Report for the Upgrade of the ALICE Inner Tracking System*,” 2014.
- [71] F. Landua, “ALICE detector LS2 upgrade in four languages,” 2022. General Photo.
- [72] W. H. Trzaska, “New Fast Interaction Trigger for ALICE,” *Nucl. Instrum. Meth. A* 845 (2017)., vol. Ed. by G. Badurek et al., pp. 463–466.
- [73] S. Bysiak, “The Fast Interaction Trigger Upgrade for ALICE,” *PoS*, vol. LHCP2020, p. 251, 2021.
- [74] “Addendum of the Letter of Intent for the upgrade of the ALICE experiment : The Muon Forward Tracker,” tech. rep., CERN, Geneva, 2013.
- [75] The ALICE collaboration, “Technical Design Report for the Muon Forward Tracker,” 2015. <https://cds.cern.ch/record/1981898>.
- [76] L. C. Migliorin, *Measurement of incoherently produced  $J/\psi$  polarisation in ultra-peripheral Pb-Pb collisions with ALICE and characterisation of the Muon Forward Tracker*. PhD thesis, 2022.
- [77] J. Kvapil, A. Bhasin, M. Bombara, D. Evans, A. Jusko, A. Kluge, M. Krivda, I. Kralik, R. Lietava, S. K. Nayak, S. Ragoni, and O. Villalobos Baillie, “ALICE Central Trigger System for LHC Run 3,” *EPJ Web of Conferences*, vol. 251, p. 04022, 2021.
- [78] C. W. Fabjan, L. Jirdén, V. Lindestruth, L. Riccati, D. Rorich, P. Van de Vyvre, O. Villalobos Baillie, and H. de Groot, *ALICE trigger data-acquisition high-level trigger and control system: Technical Design Report*. Technical design report. ALICE, Geneva: CERN, 2004.
- [79] P. Buncic, M. Krzewicki, and P. Vande Vyvre, “Technical Design Report for the Upgrade of the Online-Offline Computing System,” tech. rep., 2015.
- [80] A. Alkin, G. Eulisse, J. F. Grosse-Oetringhaus, P. Hristov, M. Kabus, “ALICE Run 3 Analysis Framework.” 25th International Conference on Computing in High-Energy and Nuclear Physics, 17-21 May 2021.

- [81] Chiara Zampolli on behalf of the ALICE collaboration, “ALICE data processing for Run 3 and Run 4 at the LHC.” 40th International Conference on High Energy Physics, 28 July – 6 August 2020.
- [82] FairRoot Group, “FairMQ documentation website.” <https://github.com/FairRootGroup/FairMQ#documentation>.
- [83] O. Bourrion et al, “ALICE Run 3 Analysis Framework.” 2021 JINST 16 P05019.
- [84] R. Brun and F. Rademakers, “Root - an object-oriented data analysis framework,” *Nucl. Inst. & Meth. in Phys. Res. A*, vol. 389, pp. 81–86, 1997.
- [85] The ALICE collaboration, “The ALICE definition of primary particles,” 2017.
- [86] Steffen G. Weber, “Inclusive  $J/\psi$  production as a function of charged particle density at mid-rapidity in pp collisions at  $\sqrt{s} = 13$  TeV,” ALICE internal note ANA-594.
- [87] C.Cheshkov, Private communication.
- [88] ALICE collaboration, “Charged-particle multiplicities in proton–proton collisions at  $\sqrt{s} = 0.9$  to 8 TeV,” *The European Physical Journal C*, vol. 77, Jan. 2017.
- [89] ALICE collaboration, “Pseudorapidity and transverse-momentum distributions of charged particles in proton–proton collisions at  $\sqrt{s} = 13$  TeV,” *Physics Letters B*, vol. 753, p. 319–329, Feb. 2016.
- [90] J. Zhao, J. Aichelin, P. B. Gossiaux, and K. Werner, “Heavy flavor as a probe of hot QCD matter produced in proton-proton collisions,” 2024.
- [91] M. Siddikov, E. Levin, and I. Schmidt, “Multiplicity distributions as probes of quarkonia production mechanisms,” 2019.
- [92] E. Gotsman and E. Levin, “High energy QCD: multiplicity dependence of quarkonia production,” *The European Physical Journal C*, vol. 81, Feb. 2021.
- [93] E. Iancu and R. Venugopalan, *The Color Glass Condensate and high energy scattering in QCD*, p. 249–363. WORLD SCIENTIFIC, Jan. 2004.
- [94] S. G. Weber, A. Dubla, A. Andronic, and A. Morsch, “Elucidating the multiplicity dependence of  $J/\psi$  production in proton–proton collisions with PYTHIA8,” *The European Physical Journal C*, vol. 79, no. 1, p. 36, 2019.
- [95] ALICE collaboration, “Centrality dependence of particle production in p–Pb collisions at  $\sqrt{s_{NN}} = 5.02$  TeV,” *Physical Review C*, vol. 91, June 2015.
- [96] A. Ortiz, A. Paz, J. D. Romo, S. Tripathy, E. A. Zepeda, and I. Bautista, “Multi-parton interactions in pp collisions from machine learning-based regression,” *Physical Review D*, vol. 102, Oct. 2020.
- [97] ALICE collaboration, “Search for jet quenching effects in high-multiplicity pp collisions at  $\sqrt{s} = 13$  TeV via di-jet acoplanarity,” *Journal of High Energy Physics*, vol. 2024, May 2024.

## BIBLIOGRAPHY

---

- [98] LHCb collaboration, “Study of  $J/\psi$  production in jets,” *Physical Review Letters*, vol. 118, May 2017.
- [99] CMS Collaboration, “Fragmentation of jets containing a prompt  $J/\psi$  meson in PbPb and pp collisions at  $\sqrt{s_{NN}} = 5.02$  TeV,” *Physics Letters B*, vol. 825, p. 136842, Feb. 2022.
- [100] A. Ortiz, A. Khuntia, O. V. Rueda, S. Tripathy, G. Bencédi, S. Prasad, and F. Fan, “Unveiling the effects of multiple soft partonic interactions in pp collisions at  $\sqrt{s} = 13.6$  TeV using a new event classifier,” *Physical Review D*, vol. 107, Apr. 2023.
- [101] ALICE  $O^2$  group, “The  $O^2$  Analysis framework documentation.” <https://aliceo2group.github.io/analysis-framework/docs/>.
- [102] P. Antonioli, A. Kluge, and W. Riegler, “Upgrade of the ALICE Readout and Trigger System,” tech. rep., 2013.
- [103] A. Maevskaya, “Fast Interaction Trigger for the upgrade of the ALICE experiment at CERN: design and performance. The Fast Interaction Trigger detector for the upgrade of the ALICE experiment at CERN: design and performance,” *EPJ Web Conf.*, vol. 204, p. 11003, 2019.
- [104] D. Evans, A. Jusko, M. Krivda, L. Lietava, L. A. Perez Moreno, and O. Villalobos Baillie, “Trigger system design review,” technical report, University of Birmingham, May 2016.
- [105] P. D. B. Collins, *An Introduction to Regge Theory and High Energy Physics*. Cambridge Monographs on Mathematical Physics, Cambridge University Press, 7 2023.
- [106] P. Teles, “Diffraction forward physics in cms: Results and perspectives,” *EPJ Web of Conferences*, vol. 90, p. 06004, 03 2015.
- [107] The ALICE collaboration, “Measurement of inelastic, single- and double-diffraction cross sections in proton–proton collisions at the LHC with ALICE,” *The European Physical Journal C*, vol. 73, no. 6, p. 2456, 2013.
- [108] F. Reidt, “Central Diffraction in Proton-Proton Collisions at  $\sqrt{s} = 7$  TeV with ALICE at LHC,” *AIP Conf. Proc.*, vol. 1523, pp. 17–20, 2013. Comments: 4 pages, 2 figures, Proceedings Diffraction 2012 - International Workshop on Diffraction in High-Energy Physics, Puerto del Carmen, Sept. 10-15, 2012.
- [109] A. C. Ene, A. Jipa, and L.-E. Giubega, “Study of Monte Carlo event generators for proton-proton collisions at LHC energies in the forward region,” *Chinese Physics C*, vol. 43, p. 083001, Aug. 2019.
- [110] D. d’Enterria, R. Engel, T. Pierog, S. Ostapchenko, and K. Werner, “Constraints from the first LHC data on hadronic event generators for ultra-high energy cosmic-ray physics,” *Astroparticle Physics*, vol. 35, p. 98–113, Sept. 2011.

- [111] LHCb collaboration, “Measurement of charged particle multiplicities in pp collisions at  $\sqrt{s} = 7$  TeV in the forward region,” *The European Physical Journal C*, vol. 72, Apr. 2012.
- [112] S. Ostapchenko, “Monte Carlo treatment of hadronic interactions in enhanced Pomeron scheme: QGSJET-II model,” *Physical Review D*, vol. 83, Jan. 2011.
- [113] E.-J. Ahn, R. Engel, T. K. Gaisser, P. Lipari, and T. Stanev, “Cosmic ray interaction event generator SIBYLL 2.1,” *Physical Review D*, vol. 80, Nov. 2009.
- [114] C.-T. collaboration, “Measurement of pseudorapidity distributions of charged particles in proton-proton collisions at  $\sqrt{s} = 8$  TeV by the CMS and TOTEM experiments,” *Eur. Phys. J. C*, vol. 74, p. 3053, 2014. Comments: Submitted to the European Physical Journal C; updated to published version.
- [115] TOTEM collaboration, “Measurement of the forward charged particle pseudorapidity density in pp collisions at  $\sqrt{s} = 8$  TeV using a displaced interaction point,” *The European Physical Journal C*, vol. 75, no. 3, p. 126, 2015.
- [116] ALICE collaboration, “System-size dependence of the charged-particle pseudorapidity density at  $\sqrt{s_{NN}} = 5.02$  TeV for pp, p Pb, and Pb Pb collisions,” *Physics Letters B*, vol. 845, p. 137730, Oct. 2023.
- [117] CMS collaboration, “Pseudorapidity distribution of charged hadrons in proton–proton collisions at  $\sqrt{s} = 13$  TeV,” *Physics Letters B*, vol. 751, p. 143–163, Dec. 2015.
- [118] The ATLAS collaboration, “Charged-particle distributions at low transverse momentum in  $\sqrt{s} = 13$  TeV pp interactions measured with the ATLAS detector at the LHC,” *The European Physical Journal C*, vol. 76, Sept. 2016.
- [119] CMS collaboration, “Measurement of charged particle spectra in minimum-bias events from proton–proton collisions at  $\sqrt{s} = 13$  TeV,” *The European Physical Journal C*, vol. 78, Aug. 2018.
- [120] ALICE collaboration, “Pseudorapidity densities of charged particles with transverse momentum thresholds in pp collisions at  $\sqrt{s} = 5.02$  and 13 TeV,” *Physical Review D*, vol. 108, Oct. 2023.
- [121] GitHub, “O2physics framework, the event selection task,” 2024. Accessed: 27/06/2024.
- [122] J. F. Grosse-Oetringhaus, “Measurement of the Charged-Particle Multiplicity in Proton-Proton Collisions with the ALICE Detector,” 2009. Presented on 17 Apr 2009.
- [123] M. G. Poghosyan, “Predictions for pp single diffractive cross section at LHC,” 2012.
- [124] ALICE collaboration, “Charged-particle multiplicities in proton–proton collisions at  $\sqrt{s} = 0.9$  to 8 TeV,” *The European Physical Journal C*, vol. 77, Jan. 2017.

## BIBLIOGRAPHY

---

- [125] A. Hutson, “Particle production and entropy measurement in ALICE,” tech. rep., 2024. Quark Matter 2023 Conference Proceedings, 2 figures, 4 pages.
- [126] ALICE collaboration, “Quarkonium signal extraction in ALICE,” 2015.

# List of Figures

1.1	Classification of the elementary particles in the Standard Model. . . . .	4
1.2	A consequence of the confinement phenomenon in QCD [1]. . . . .	5
1.3	Feynman vertices in QCD. . . . .	6
1.4	The evolution of the strong coupling constant $\alpha_s$ as a function of the energy scale $Q$ [3] . . . . .	6
1.5	QCD phase diagram, from [4]. . . . .	7
1.6	Two scenarios of QGP formation, adapted from [5]. Top: at high temperature; bottom: at high net baryon density. . . . .	8
1.7	Evolution of an heavy-ion collision - adapted from [MADAI collaboration, Hannah Petersen and Jonah Bernhard]. . . . .	9
1.8	Spatio-temporal diagram of the evolution of a heavy-ion collision. [7]. . . .	10
1.9	A semi-central collision, with some nucleons participating in the collision, and others being spectators. Figure from [9]. . . . .	11
1.10	Elliptic flow: spatial anisotropies in the initial state are transferred to a momentum anisotropy of the final state particles. . . . .	12
1.11	J/ $\psi$ state dissociation at increasing temperature due to the Debye screening effect, $T_d$ being the dissociation temperature at which $\lambda_D < r$ . Figure adapted from [18]. . . . .	13
1.12	Charmonium resonances, their quantum numbers $J^{PC}$ and decays. Adapted from [26] by Batoul Diab. . . . .	15
1.13	Feynman diagram of a B hadron weak decay into a J/ $\psi$ [37]. . . . .	17
1.14	Fraction of non-prompt J/ $\psi$ as a function of $p_T$ for different collision energy and systems [38]. . . . .	18
1.15	Forward and mid-rapidity J/ $\psi$ relative yield as a function of relative multiplicity at mid-rapidity at $\sqrt{s} = 7$ TeV, for inelastic events [47]. . . . .	20
1.16	Forward and mid-rapidity J/ $\psi$ relative yield as a function of relative multiplicity at mid-rapidity [49]. . . . .	20
1.17	View of a hadron-hadron collision in PYTHIA [52]. . . . .	21
1.18	Schematic view of the parton ladder and the beam remnants in EPOS [55].	22
2.1	The layout of the LHC and the CERN accelerator complex [59] . . . . .	24
2.2	The ALICE detector (solenoid magnet not shown) with its coordinate system. . . . .	25
2.3	The ALICE detector in Run 2 [61]. . . . .	26
2.4	The V0 detector with its two detection disks, adapted from [62]. . . . .	28
2.5	V0-C channels and their numbering. . . . .	28
2.6	The Muon Spectrometer and its different parts [67]. . . . .	29
2.7	The LHC timeline from Run 2 to Run 3, adapted from [69]. . . . .	30

## LIST OF FIGURES

---

2.8	The ALICE detector in Run 3 . . . . .	31
2.9	The different detector upgrades implemented during Long Shutdown 2 (LS2) [71]. . . . .	31
2.10	The FIT detectors [73]. . . . .	32
2.11	Muon tracks with (right) and without (left) the MFT matching. . . . .	33
2.12	The MFT geometry and location. . . . .	34
2.13	Linear Track Finder schematic using the RCut parameter (maximum distance for a cluster to be attached to a straight line) [75]. . . . .	35
2.14	The Cellular Automaton method [75]. . . . .	35
2.15	The Central Trigger System in Run 3, adapted from [77]. . . . .	36
2.16	The different roles of $O^2$ and O2Physics. . . . .	37
2.17	The synchronous and asynchronous part of the data flow in ALICE $O^2$ [80].	38
2.18	The role of the Data Processing Layer (DPL) in the analysis framework of ALICE [81]. . . . .	39
3.1	$N_{V0C}$ distribution in MB events. . . . .	45
3.2	Ratio of V0C distributions per period over merged V0C distribution. The distributions are normalized by their integrals. . . . .	46
3.3	Average $N_{V0C}$ versus $z_{\text{vtx}}$ before the corrections for the residual $z_{\text{vtx}}$ dependence in period LHC18m. The red curve represents the fit used to obtain the correction function described in the text. . . . .	47
3.4	Average signal in the V0C channels in events where a single muon has hit channel 16. The bin framed in red corresponds to the V0C channel 3. . . . .	49
3.5	Channels $k = 18$ and $j = 22$ are located in the same ring as channel $i = 16$ , but at $\varphi \pm \frac{\pi}{2}$ in the azimuthal direction. . . . .	49
3.6	$N_{V0C}$ distributions in LHC17d18 MC (PYTHIA8 event generator) and in data (top), and ratio of data over MC (bottom). . . . .	51
3.7	$N_{V0C}$ versus $N_{\text{ch}}$ in MC simulations generated with PYTHIA8 (left panel) and EPOS-LHC (right panel). . . . .	51
3.8	$\langle N_{\text{ch}} \rangle$ versus $N_{V0C}$ in PYTHIA8 (left panel) and EPOS-LHC (right panel) fitted with the function $g$ (see text). . . . .	52
3.9	$J/\psi$ Acceptance $\times$ Efficiency for the $J/\psi$ measurement in the dimuon channel. . . . .	56
3.10	Fit of the dimuon invariant mass spectra for the multiplicity-integrated sample (top), in multiplicity interval 5 (middle), and in multiplicity interval 12 (bottom). The CB2 tails are taken from the anchored MC. The background is fitted with a VWG function. The fit range is defined between 2.1 and 4.7 $\text{GeV}/c^2$ . . . . .	57
3.11	$J/\psi$ relative yields and their uncertainties in the multiplicity interval 3 (top) and 12 (bottom). . . . .	59
3.12	Excess signal due to the passage of a muon in the different V0C channels. The excess averaged over the analyzed periods is in dark blue, the other histograms are the excess in different runs of the LHC18m period. . . . .	61
3.13	$J/\psi$ relative yield as a function of the relative multiplicity measured in the V0C acceptance $-3.7 < \eta < -1.7$ . . . . .	63

3.14	$J/\psi$ relative yield as a function of the relative multiplicity in the V0C acceptance $-3.7 < \eta < -1.7$ compared with PYTHIA 8.2, EPOS4HQ [90] and two 3-Pomeron CGC (Color Glass Condensate) model predictions [91,92]. . . . .	64
3.15	$J/\psi$ relative yield as a function of the relative multiplicity in the V0C acceptance $-3.7 < \eta < -1.7$ with and without the dimuon correction. . . . .	66
3.16	$J/\psi$ relative yield as a function of the relative multiplicity in the V0C acceptance $-3.7 < \eta < -1.7$ obtained with PYTHIA 8.2 simulations with including or excluding the $J/\psi$ daughters from the multiplicity estimation, and with a different multiplicity selection based on the number of charged particles in $ \eta  < 1$ . . . . .	67
3.17	Forward and midrapidity $J/\psi$ relative yields as a function of relative multiplicity in $ \eta  < 1$ (blue and green) [49], compared with forward $J/\psi$ relative yields as a function of relative multiplicity in $-3.7 < \eta < -1.7$ (red). The bottom panel shows the ratio of each result to the linear $y = x$ reference. . . . .	68
4.1	Cluster positions in disk 3 . . . . .	72
4.2	More histograms obtained with the MFT assessment workflow. . . . .	73
4.3	Picture of the support structures of the ITS and the MFT, the Interaction Point (IP) is represented with a white star, the flange volume is circled in red and represented on the right panel. The particles going towards the MFT cross this volume, which is 1.5 mm thick. . . . .	74
4.4	The different configurations of the detector used for the simulations . . . . .	74
4.5	Distribution of residuals (offsets) along $x$ for the MFT standalone tracks, for the simulations with no flange and no end-wheels. . . . .	75
4.6	Offset resolution for standalone MFT tracks (unidentified charged particles) along the $x$ (left) and $y$ axis (right) as a function of the true $p_T$ , with the default detector geometry. . . . .	76
4.7	Offset resolution for standalone MFT tracks (unidentified charged particles) along the $x$ (left) and $y$ axis (right) as a function of the true $p_T$ , with the detector geometry without the flange. . . . .	76
4.8	Offset resolution for standalone MFT tracks (unidentified charged particles) along the $x$ (left) and $y$ axis (right) as a function of the true $p_T$ , with the detector geometry without the flange and the end-wheels. . . . .	77
4.9	Offset resolution for global muon tracks (combining the information of the MFT and the Muon Spectrometer) along the $x$ (left) and $y$ axis (right) as a function of the true $p_T$ , with the default detector geometry. . . . .	77
4.10	Offset resolution for global muon tracks (combining the information of the MFT and the Muon Spectrometer) along the $x$ (left) and $y$ axis (right) as a function of the true $p_T$ , with the detector geometry without the flange. . . . .	78
4.11	Offset resolution for global muon tracks (combining the information of the MFT and the Muon Spectrometer) along the $x$ (left) and $y$ axis (right) as a function of the true $p_T$ , with the detector geometry without the flange and the end-wheels. . . . .	78

## LIST OF FIGURES

---

4.12 DCA <sub>x</sub> of MFT tracks from primary particles and only non-ambiguous tracks, fitted with the sum of 2 Gaussians. The wider gaussian is used to better describe the distribution tails, while the narrower one is used for the resolution determination. . . . .	80
4.13 MFT offset resolution along the $x$ axis as a function of the $p_T$ of the MC particle. . . . .	80
4.14 Track time for detectors characterized by a sharp readout window, and collision time. . . . .	83
4.15 Track time for detectors characterized by a gaussian resolution, and collision time. . . . .	83
4.16 Histogram of the number of compatible collisions per standalone MFT track for one run of the LHC22o data taking period (pp collisions at $\sqrt{s} = 13.6$ TeV). The total number of processed MFT tracks is $3.23 \times 10^{10}$ . . . . .	84
4.17 Schematic of the different steps of the algorithm leading to the reassociation of an MFT track to the collision with the smallest $DCA_{xy}$ . “col1”, “col2” and “col3” are the collisions compatible with this track, obtained with the <code>fwdtrack-to-collision-associator</code> . . . . .	85
4.18 FT0-C channel map (view from IP) . . . . .	86
4.19 Extrapolation of one MFT track towards FT0-C . . . . .	87
4.20 Distribution of the distance $D$ (in cm) between the extrapolated MFT track and the center of the FT0-C channel sharing the same MC-label as the track	89
4.21 Probability for MFT tracks <b>not</b> to match with any FT0-C signal. The central rectangular FT0-C hole is clearly visible in pink, together with the inefficient peripheral zones of the different FT0-C modules. The white areas correspond to zones without MFT tracks (the shape of the MFT detection planes results in the circular hole at the center). . . . .	89
4.22 MFT-FT0-C MC-matching efficiency as a function of the extrapolated $x$ position of the track: the $x$ regions highlighted in red are the regions that will be excluded. . . . .	90
4.23 MFT-FT0-C matching efficiency before and after excluding inefficient regions	91
4.24 On the left: Extrapolation of one MFT track towards FT0-C, the FT0-C and extrapolated MFT track coordinates (marked by a red star) are visible in the $xy$ plane of $z$ coordinate $-82.6$ cm. On the right: reduction of that MFT track time window. . . . .	92
4.25 Fraction of matchable tracks as a function of the number of BC matched with FT0-C signal per MFT track . . . . .	94
4.26 MFT-FT0-C time alignment, the green arrow representing the time shift added between the two detectors to recover a correct time alignment. . . . .	97
4.27 Fraction of unmatched tracks as a function of the shift in BC applied to the beginning of the MFT ROFs for two different runs, at relatively low IR compared to the nominal IR in Run 3. . . . .	99
4.28 Fraction of unmatched tracks as a function of the shift in BC applied to the beginning of the MFT ROF 2 in case of a sparse filling scheme. The legend is the same as in figure 4.26. In this figure one implicitly assumes that all BCs corresponding to FT0-C signals have an associated collision. . . . .	100
4.29 Filling schemes of two runs in Run 3 . . . . .	100

---

4.30 Fraction of unmatched tracks as a function of the shift in BC applied to the beginning of the MFT ROFs for two different runs of LHC22o, close to the nominal IR for p-p collisions in Run 3 . . . . .	101
5.1 Different types of inelastic proton–proton collisions, with their corresponding interaction diagram and particle distribution in the pseudorapidity space. Diffractive events are characterized by Pomeron exchange. Figure adapted from [106]. . . . .	104
5.2 Charged particle pseudorapidity density (noted $\rho$ in this figure) as a function of $\eta$ obtained by the LHCb experiment, for events having at least one charged particle in the range $2.0 < \eta < 4.5$ . Comparisons are shown with different PYTHIA generators with different tunes. Figure taken from [111].	105
5.3 Charged-particle pseudorapidity distribution as a function of $\eta$ for p-p collisions at $\sqrt{s} = 8$ TeV, obtained by the TOTEM experiment considering both displaced (green band) and nominal interaction points (orange band). The results obtained considering the nominal interaction point are taken from [114]. Corresponding predictions from PYTHIA8 (tune 4C), SIBYLL, EPOS-LHC, and QGSJetII are also shown. Figure taken from [115]. . . . .	106
5.4 Charged-particle pseudorapidity distribution as a function of $\eta$ for p-p collisions at $\sqrt{s} = 5.02$ TeV obtained by the ALICE experiment [116]. . . . .	107
5.5 Charged-particle pseudorapidity distribution as a function of $\eta$ produced in pp collisions at $\sqrt{s} = 13$ TeV. The ALICE results are shown for the event classes INEL and $INEL > 0$ and compared to Monte Carlo predictions and to the results from the CMS Collaboration [117]. Figure taken from [89]. . . . .	108
5.6 Charged-particle pseudorapidity density at $\sqrt{s} = 13$ TeV measured by the CMS and ATLAS collaborations and compared with different models such as PYTHIA8, EPOS-LHC, and QGSJET-II. . . . .	109
5.7 Comparison of the number of MFT tracks versus $\eta$ and $\varphi$ in data (LHC22c in red) and reconstructed MC (LHC22h1c1 in black). . . . .	112
5.8 Distribution of $z_{\text{vtx}}$ of events in data, reconstructed MC and generated MC. . . . .	112
5.9 Distribution of $\eta$ and $\varphi$ of MFT tracks compared between data (left) and 2023 MC (right). . . . .	113
5.10 Distribution of $\eta$ and $\varphi$ of MFT tracks compared between data (left) and 2024 MC implementing the update in the description of the detector response(right). . . . .	114
5.11 Comparison of the number of MFT tracks versus $\eta$ and $\varphi$ in data (LHC22o run 526641 in red) and reconstructed MC (LHC23f4b2 run 526641 in black). . . . .	114
5.12 Comparison of the number of MFT tracks versus $\eta$ and $\varphi$ in data (LHC22o run 526641 in red) and reconstructed MC (LHC24b1b run 526641 in black). . . . .	115
5.13 Track reconstruction efficiency of MFT tracks, computed using MC simulation. . . . .	116
5.14 Selection efficiency correction at track level. . . . .	117
5.15 Selection efficiency correction at event level. . . . .	118
5.16 MC closure of LHC22h1c1. . . . .	119
5.17 MC closure of LHC24b1b. . . . .	119

5.18	Distribution of the number of MFT tracks as a function of $\eta$ normalized to the number of selected events, in p-p collisions at $\sqrt{s} = 13.6$ TeV, using the two track-to-collision association criteria mentioned in the text. . . . .	121
5.19	Charged-particle pseudorapidity distribution for proton-proton collisions at $\sqrt{s} = 0.9$ TeV obtained with the MFT (in red) compared with the PYTHIA8 prediction and the central barrel results (in blue). The central barrel results are extracted from [124]. The statistical uncertainties are the only one represented in this figure, but they are too small to be noticeable. . . . .	123
5.20	Charged-particle pseudorapidity distributions for proton-proton collisions at $\sqrt{s} = 13.6$ TeV obtained with the MFT (in red) compared with PYTHIA8 predictions and the central barrel results (in blue). The statistical uncertainties are the only one represented in this figure, but they are too small to be noticeable. The central barrel results are taken from [125]. . . . .	124

## List of Tables

3.1	Multiplicity intervals obtained from the V0C signal $N_{\text{V0C}}$ distribution. . . . .	46
3.2	The $\epsilon_{N_{ch}}$ and $\epsilon_{N_{ch}}^i$ correction factors as obtained using MC. . . . .	53
3.3	Summary of the relative V0C signal, the relative charged-particle multiplicity and its statistical and systematic uncertainties for the multiplicity intervals considered in the analysis. . . . .	54
3.4	Tail parameters extracted from a fit to all available Run 2 dimuon data and from the corresponding anchored MC. . . . .	56
3.5	Correction factors applied on the $J/\psi$ yields. . . . .	60
3.6	Summary of the systematic uncertainties of the relative $J/\psi$ yield. . . . .	62
4.1	Summary table of the results for the time alignment between MFT and FT0-C for various IR conditions characterizing the ALICE pp data taking in Run 3 . . . . .	101
5.1	Percentage of ambiguous tracks in the datasets used in this analysis. . . . .	120